
JSR A
JOURNAL OF
SCIENTIFIC REPORTS A
E-ISSN:2687-6167
Number 61
June 2025
Journal of Scientific Reports-A, June 2025, Number 61

Kütahya Dumlupınar University
Institute of Graduate Studies

Journal of Scientific
Reports-A
E-ISSN: 2687-6167
Number 61, June 2025

JSR A
Journal of Scientific Reports

Journal of Scientific Reports-A, Number 61, June 2025

Journal of Scientific Reports-A started its publication life in 2000 as name of Journal of Science and Technology of Dumlupınar University and is a national peer-reviewed journal published regularly four times a year in March, June, September and December. The language of the journal is English. Articles submitted to the journal are evaluated by at least two referees who are experts in the subject and selected by the editorial board. All articles submitted to the journal are evaluated by the double-blind method. Articles submitted to our journal for review should not be previously published, accepted for publication and in the process of being evaluated for publication in another journal. All responsibility for the articles published in the journal belongs to the author(s).

The journal aims to share scientific studies carried out in the fields of science and engineering at national and international level with scientists and the public. Original research articles, review articles and short notes in science and engineering disciplines are accepted for the journal. Original research articles are expected to contain theoretical and experimental results and should not be published in other journals. In the review articles, it is expected that scientific, technological and current developments on a specific subject are reflected by using an extensive bibliography and made a satisfying evaluation of these. Short notes should be brief writings prepared to announce the first findings of an original study.

Editorial Policy

The journal is open access and the article evaluation period is between 1-2 months.

Correspondence Address: Kütahya Dumlupınar Üniversitesi Evliya Çelebi Yerleşkesi Fen Bilimleri Enstitüsü 43270 KÜTAHYA
E-mail: joursra@gmail.com
Webpage: gsjsra.com
Phone: 0 274 443 19 42
Fax: 0 274 265 20 60

JSR A
Journal of Scientific Reports

JSR A
Journal of Scientific Reports

JSR A
Journal of Scientific Reports

JOURNAL OF SCIENTIFIC REPORTS-A
E-ISSN: 2687-6167

CONTENTS

RESEARCH ARTICLES

JSR A
Journal of Scientific Reports

Contents lists available at *Dergipark*

Journal of Scientific Reports-A

journal homepage: *https://dergipark.org.tr/tr/pub/jsr-a*

E-ISSN: 2687-6167 ***Number 61, June 2025***

RESEARCH ARTICLE

Receive Date: 31.10.2024 *Accepted Date: 24.03.2025*

The role of active and conductive layer thickness in maximizing power conversion efficiency of perovskite solar cells

Enes Nayman[a]*, Mehmet Fatih Gözükızıl[b]

[a]*Bilecik Şeyh Edebali University, Söğüt Vocational School, Bilecik, 11600, Türkiye, ORCID: 0000-0002-3656-3126*
[b]*Bilecik Şeyh Edebali University, Söğüt Vocational School, Bilecik, 11600, Türkiye, ORCID: 0000-0003-1719-959X*

Abstract

This study investigates the effect of active and conductive layer thickness on photovoltaic performance in perovskite solar cells, addressing the need for efficient and sustainable energy solutions in light of current environmental challenges. Using OghmaNano software, we analyzed how variations in thickness of the perovskite, fluorine-doped tin oxide (FTO), and gold (Au) layers influence key performance metrics, including power conversion efficiency (PCE), fill factor (FF), open-circuit voltage (Voc), and short-circuit current density (Jsc). The ideal thicknesses identified for achieving maximum PCE are 775 nm for the perovskite layer, 50 nm for the FTO layer, and 100 nm for the Au layer. This study underscores the complex relationship between light absorption and charge transport in perovskite solar cells and highlights the importance of fine-tuning layer thickness for enhanced efficiency. The simulation-based approach used here proves valuable for its practical efficiency, reducing both time and cost compared to experimental fabrication.

Keywords: Perovskite solar cells; layer thickness; OghmaNano software; power conversion efficiency; photovoltaics; sustainable development; nanomaterials

* Corresponding author. Tel.: +90 (228) 214 21 70;
E-mail address: enes.nayman@bilecik.edu.tr

.

1. Introduction

Worldwide problems such as rapidly increasing environmental pollution, overuse of natural resources and climate change further emphasize the importance of sustainable solutions in the energy sector as in every field [1]. Renewable energy sources reduce environmental pollution and meet energy needs in a sustainable way. Carbon emissions from the use of fossil fuels have increased the interest in renewable energy sources [2, 3]. Especially solar energy systems minimize the negative impacts on the environment. They also have the potential to generate significant amounts of energy [4, 5, 6]. Recently, technologies such as perovskite solar cells have increased the efficiency of solar energy systems. This has led to significant progress in the field of sustainable energy [7, 8, 9].

Perovskite solar cells have gained an important place in photovoltaic technologies [10]. These cells are in high demand due to their high energy conversion efficiency, low manufacturing costs and flexible design [11]. The rapid advancement of perovskite solar cells in thin film technology allows them to be integrated harmoniously with more flexible and lightweight substrates [12]. This makes perovskite solar cells usable in a wide range of applications, from wearable technologies to sustainable building materials [13, 14]. Perovskite solar cells consist of layers such as FTO, perovskite and metal materials. Each layer is important in determining the overall performance of the solar cell. Therefore, each layer should have an ideal thickness.

OghmaNano software was used in this study. Within the application, the ideal solar cell power conversion efficiency was determined by changing the active and conductive layer thicknesses in the perovskite solar cell structure. Fill factor, open circuit current density and open circuit voltage were also analyzed as efficiency criteria. Perovskite solar cells have high energy conversion efficiency and flexibility of use. They have a significant potential to meet future energy needs [15, 16]. However, in order for this technology to be more widely used in commercial applications, the thickness of each layer needs to be continuously studied and idealized. This study demonstrates the potential to improve the performance of perovskite solar cells. It is also expected to make significant contributions to the future evolution of solar energy technologies.

2. Material and Method

Perovskite solar cells consist of a light-absorbing perovskite layer, electron-hole carrier layers and conductive contacts. TiO_2 is used as the electron carrier layer. Thanks to its high electron mobility and optical transparency, it plays an important role in the charge transport process. Spiro-OMeTAD which is used as a hole carrier layer, supports hole transport thanks to its conductivity which is enhanced by suitable energy levels and doping. The main objective of the study is to determine the ideal thickness of the active and conductive core layers in perovskite solar cells. In this way, the effect of thickness on power conversion efficiency can be understood. These main layers include FTO (fluorine-doped tin oxide), perovskite and Au layers. By varying the thickness of each layer over a certain range, the changes in the performance of the solar cell were investigated. The layer structure of the perovskite solar cell is shown in Figure 1.

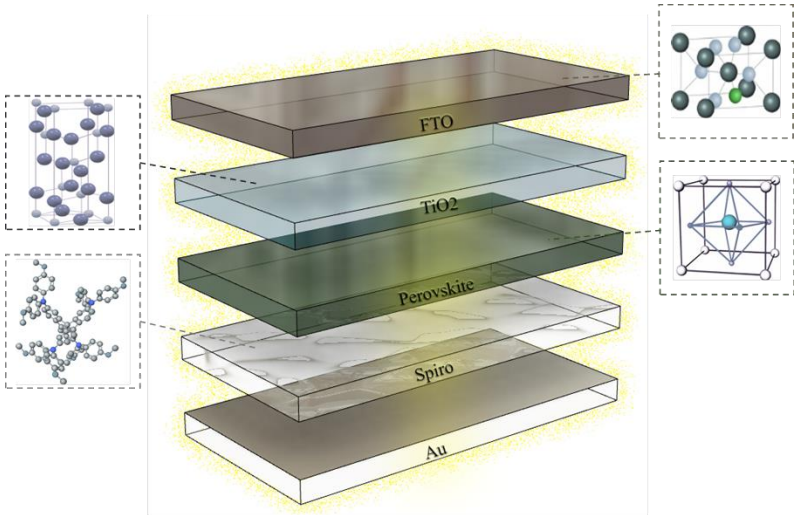

Fig. 1. Layer Structure of Perovskite Solar Cell

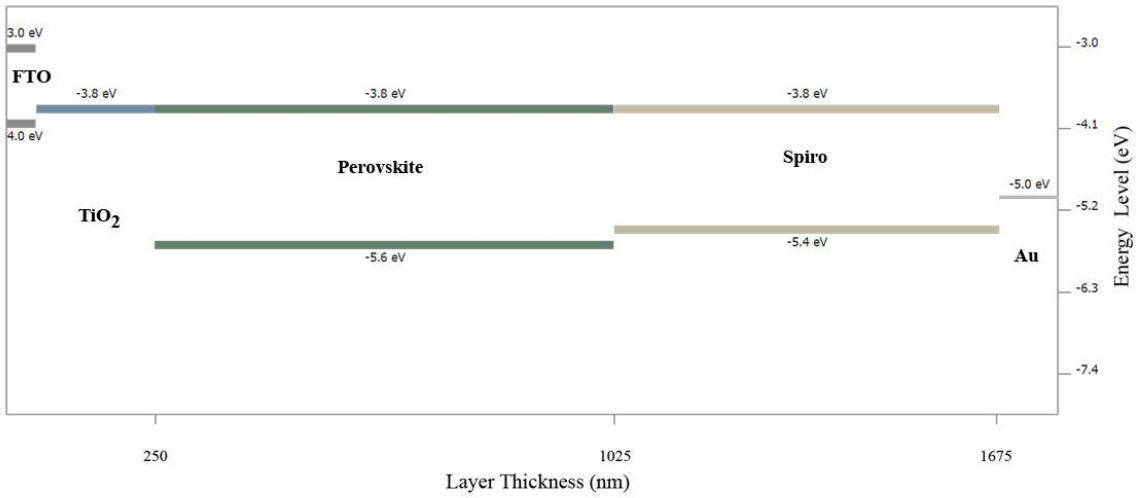

Fig. 2. Energy Levels of Perovskite Solar Cell Layers

Perovskite solar cells consist of basic layers, each playing a different role in the energy conversion process. The perovskite layer absorbs sunlight and generates charge carriers [17, 18]. FTO acts as a transparent conductor. It allows light to reach the perovskite layer [19]. The Au layer acts as an electrode, assisting the electron collection [20, 21]. This strategic combination of layers maximizes light absorption, charge transport and storage, contributing to the overall performance and efficiency of the solar cell.

The layer arrangement and energy levels in perovskite solar cells are shown in Figure 2. The energy levels of the layers created for solar cells vary depending on the operating conditions, the structure of the active layers and the electron carrying capacity. The efficiency of the solar cell should be selected in such a way that these factors will get the best value. There are differences between the energy levels of the cell layers. These differences will allow the electrons excited by the effect of sunlight to create an electric current.

2.1. Perovskite Solar Cell Simulation Indicators

The Fill Factor in the context of a solar cell refers to a critical parameter reflecting the efficiency of the device in converting incident sunlight into electrical energy. It is a quantity that quantifies the extent to which the solar cell operates within the maximum power point of its current-voltage characteristic.

Mathematically, the Fill Factor is defined as the ratio of the maximum power output of the solar cell (P_{max}) to the product of the V_{oc} and J_{sc} [22]. It is shown in the equation (1).

$$Fill\ Factor\ (FF) = \frac{P_{max}}{V_{oc} \cdot J_{sc}} \tag{1}$$

The FF essentially encapsulates losses and deviations from ideality within the solar cell's performance. Factors such as resistive losses, non-ideal diode behavior, and recombination losses contribute to deviations from the ideal behavior. Therefore, a lower FF may indicate inefficiencies or obstructions within the device. A higher FF indicates a more efficient conversion of sunlight into usable electrical power [23, 24, 25].

Power Conversion Efficiency is expressed as a percentage. It is calculated by dividing the electrical power output of the solar cell by the total power of the incident sunlight. The most important factor in determining the efficiency of a solar cell is the PCE percentage, which corresponds to the efficiency of the conversion from sunlight to electrical energy [26, 27]. Mathematically, PCE is given by the equation (2).

$$PCE = \frac{Electrical\ Power\ Output}{Incident\ Solar\ Power}\ x\ 100 \tag{2}$$

The light J-V characteristics were measured under AM 1.5G solar simulator. That is, 1 sun is simulated in AM 1.5G spectrum. P_{in} (1 sun) for AM1.5G is 1000 watts/m^2. Trials were carried out at 300K temperature.

Open-Circuit Voltage (V_{oc}), signifies the maximum voltage the solar cell can achieve in the absence of an external load [28]. Changes in V_{oc} are indicative of the impact of perovskite layer thickness on the cell's ability to maintain a potential difference. V_{oc} is essentially a measure of the potential difference across the solar cell in the absence of current flow, acting as a direct indicator of the built-in electric field within the device [29].

Short-Circuit Current Density (J_{sc}) is denoting the maximum current density attained when the solar cell is short-circuited, effectively acting as a current source [30]. The negative sign of Jsc indicates the direction of current flow. This means that when the cell is short-circuited, current flows through the perovskite layer towards the external circuit. [31, 32].

3. Results and Discussion

3.1. Perovskite Layer

Perovskite solar cells have attracted great interest in the field of photovoltaic technology. The performance of these cells is closely related to the thickness of the perovskite layer [33]. The perovskite layer efficiently absorbs sunlight and produces high-energy electron/hole pairs [34]. In addition, the high conductivity properties of perovskite support the efficient collection and delivery of the produced carriers to the electrodes. Moreover, the layer absorbs a broad

spectrum of sunlight by properly aligning the energy levels, improving the overall efficiency of the solar cell [35, 36, 37].

The J-V (current-voltage) graph in perovskite solar cells shows how the solar cell responds to changes in voltage (V) over current (J). This graph is often used to determine the performance of the solar cell. It shows key parameters such as short-circuit current (J_{sc}), open-circuit voltage (V_{oc}) and ultimately maximum power output (P_{max}). J-V curves of perovskite solar cells based on different perovskite layer thicknesses are shown in Figure 3.

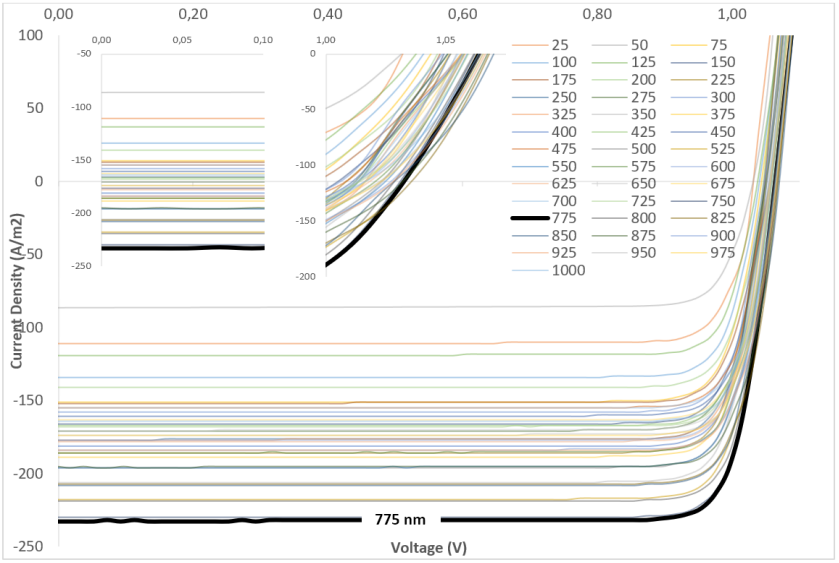

Fig. 3. J-V curves of perovskite solar cells based on different thicknesses of perovskite layers

When Figure 4 is examined, it is seen that the lowest Voc and the highest Jsc occur for the 50 nm thick perovskite layer. This indicates that thinner layers exhibit reduced current generation, which in turn limits light absorption and electron production. On the other hand, the highest Voc and the lowest Jsc values are observed for the 775 nm thick layer. This indicates that thicker layers can contribute to higher voltage and current outputs by increasing light absorption.

The changes in FF, PCE, Voc and Jsc of the perovskite layer are shown one by one in the figure. These parameters show the effect of thickness on the overall performance of the solar cell.

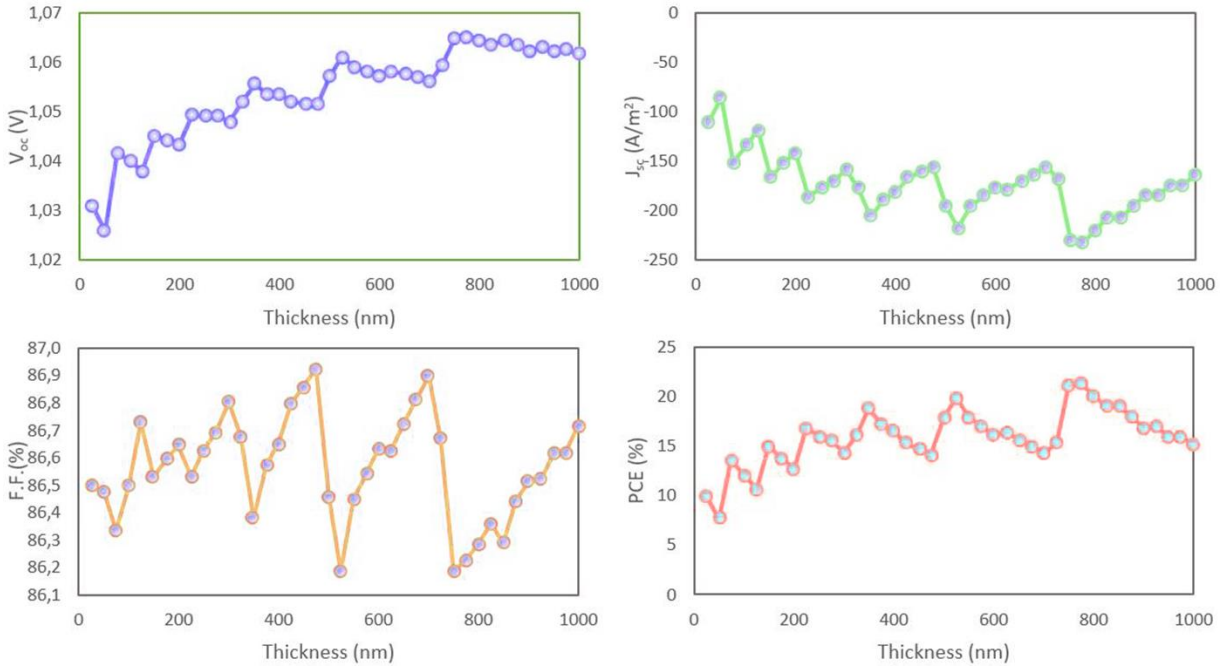

Fig. 4. Effect of change in layer thickness of perovskite on solar cell parameters (Voc, Jsc, F.F. and PCE)

According to the dataset, Voc fluctuates between 1.0259 V and 1.0654 V. Variations in Voc are closely linked to the thickness of the perovskite layer. It affects the cell's ability to maintain the potential difference under the changing layer.

The observed Jsc values range from 232.5062 mA/cm² to 86.3402 mA/cm² is remarkable. It shows the effect of perovskite layer thickness on the current conducting capacity of the cell under short circuit conditions. The fluctuation in Jsc values at different perovskite layer thicknesses shows the importance of the relationship between the optical and electrical properties of the layer.

Fill Factor values range from 0.8619 to 0.8692. These values indicate how effectively the perovskite solar cell uses incoming sunlight to produce electrical power. A higher FF is desirable because it means the solar cell is operating closer to its theoretical maximum power point. This means that overall efficiency is increased.

The observed PCE values range from 7.6594% to 21.3586%. The fluctuations in PCE may be due to various factors related to the perovskite layer. The thickness of the perovskite layer is a factor that determines the optical and electronic properties of the solar cell. When this layer is too thin, there may be insufficient absorption of sunlight. This may result in lower current production. Conversely, an excessively thick layer may lead to increased recombination losses and decreased charge removal efficiency. An ideal thickness is essential to achieve a balance between light absorption, charge carrier production and charge removal. In this study, the perovskite layer with the highest PCE value was measured at 775 nm thickness.

The aim was to evaluate the effects of the perovskite layer on PCE in perovskite solar cells. For this reason, an experimental study was carried out in a wide range between 25 nm and 100 nm by changing the thickness of the perovskite layer every 25 nm. The maximum PCE efficiency in the perovskite layer was determined as 775 nm.

3.2. FTO Layer

In perovskite solar cells, FTO allows light to penetrate the solar cell. It acts as a transparent conductor. It plays an important role in establishing a balance between optical transparency and conductivity. This directly affects the overall efficiency of the solar cell. It also acts as an electrode that actively collects electrons produced during the energy conversion process.

The efficiency parameters for each 25 nm thickness in the FTO layer have been obtained in the range of 25-500 nm. J-V curves of perovskite solar cells based on different FTO layer thicknesses are shown in Figure 5.

Notably, the 50 nm thickness stands out with the highest V_{oc} of 1.0907 V, indicating a potential for elevated open-circuit voltage output. Conversely, the 275 nm thickness demonstrates the lowest V_{oc} at 1.0741 V, suggesting a reduced voltage output. The J_{sc} values follow a similar trend, with the 275 nm thickness displaying the highest current density at 163.9843 mA/cm², for achieving optimal photovoltaic performance. Changes in FF, PCE, V_{oc} and J_{sc} values depending on the FTO layer thickness are shown in Figure 6.

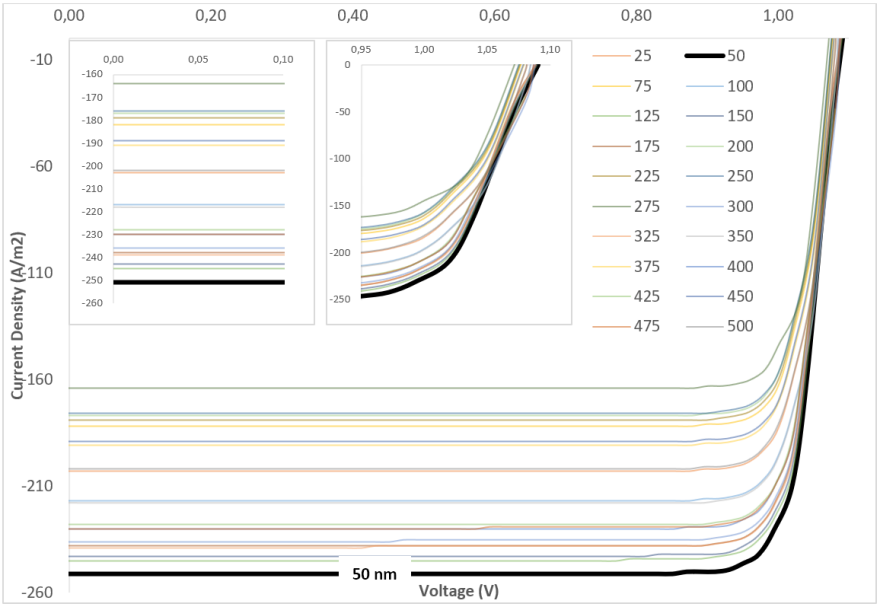

Fig. 5. J-V curves of perovskite solar cells based on different thicknesses of FTO layers

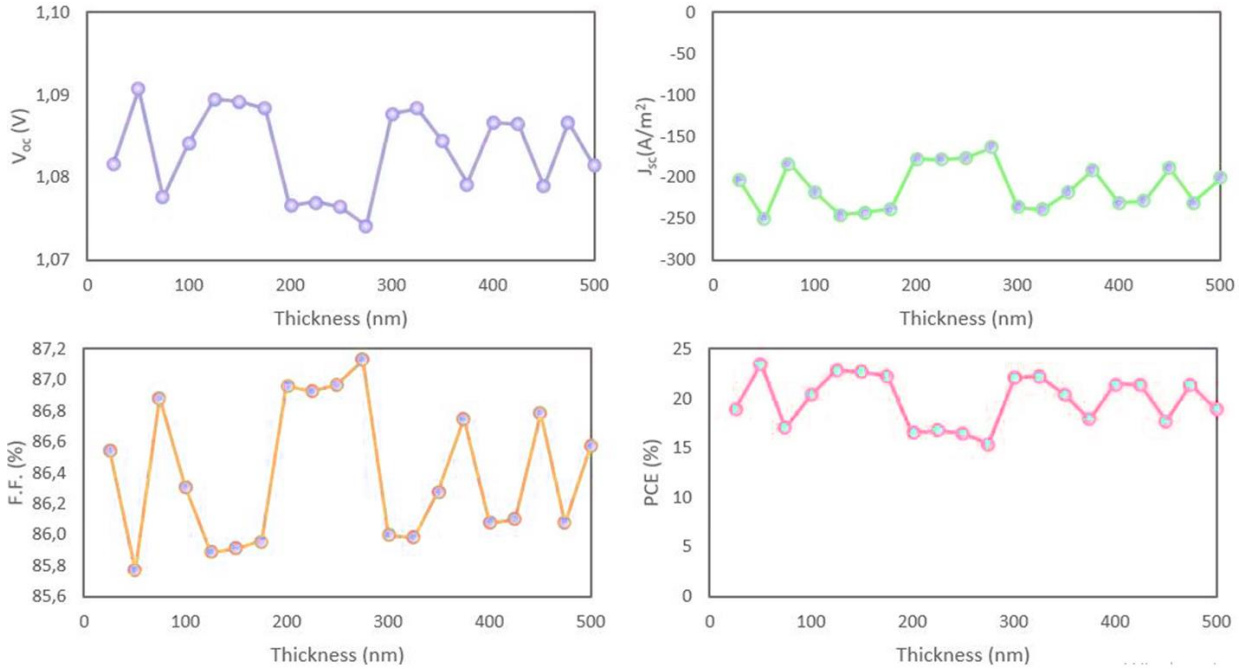

Fig. 6. Effect of change in layer thickness of FTO on solar cell parameters (Voc, Jsc, F.F. and PCE)

As the thickness of the FTO layer increases, the fill factor (FF) exhibits a fluctuating trend ranging between 0.8577 and 0.8713. The power conversion efficiency (PCE) experiences a gradual decrease from 23.4703% to 15.3471%, reflecting the complex interaction between layer thickness and overall cell efficiency. However, these stepwise intervals do not occur in relation to the sequence of thickness values. In other words, as the thickness increases, PCE values have not consistently increased, and occasional declines have occurred. The opposite situations can also occur. As a result, the ideal PCE value of 23.47% was obtained at 50 nm FTO thickness.

3.3. Au Layer

The Au layer in perovskite solar cells serves as an electrode, aiding in the collection of electrons. It plays a crucial role in completing the external circuit and facilitating electron extraction from the solar cell.

The efficiency parameters for each 25 nm thickness in the Au layer have been obtained in the range of 25-250 nm. J-V curves of perovskite solar cells based on different Au layer thicknesses are shown in Figure 7.

The graphical representation of V_{oc} and J_{sc} in relation to the thickness of the Au layer reveals distinctive lines. The 75 nm thick layer stands out with the lowest V_{oc} at 1.0783 V, indicating a notable decrease in voltage output for this particular thickness. In contrast, the 100 nm thick layer exhibits the highest V_{oc} at 1.0907 V, highlighting a positive correlation between increased thickness and elevated voltage. Moreover, the 100 nm thick layer records the lowest J_{sc} at 250.8915 mA/cm². Changes in FF, PCE, V_{oc} and J_{sc} values depending on the Au layer thickness are shown in Figure 8.

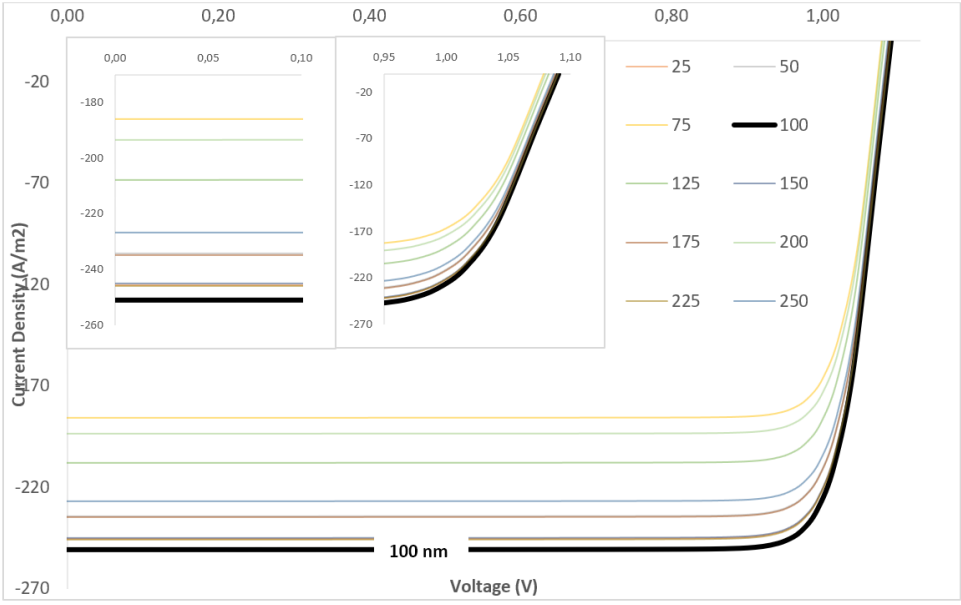

Fig. 7. J-V curves of perovskite solar cells based on different thicknesses of Au layers

The 75 nm thick layer demonstrates the highest FF at 0.8682, indicating an efficient charge transfer and collection for this particular thickness. Conversely, the 25, 100, 150 and 225 nm layer exhibits a slightly lower FF from the 0.8600, suggesting a potential decrease in charge collection efficiency for some other layers. In terms of PCE, the 100 nm thick layer stands out with the highest value at 23.4924%, emphasizing the ideal conversion efficiency achieved at this thickness. The 75 nm thick layer, despite having a high FF, records a lower PCE at 17.4155%, suggesting a potential trade-off between FF and PCE for certain thicknesses.

It is observed that, compared to the maximum PCE values obtained as 17.57% [38], 17,8% [39], 22,06% [40], 19,42% [41], 17,57% [42] and 21,98% [43], the 23.49% PCE value we obtained as a result of the study has a higher value than these studies examined in the literature.

Simulation results show how main performance parameters such as power conversion efficiency, fill factor, open circuit current density and open circuit voltage change depending on the change in the thickness of perovskite, FTO and metal layers. The data obtained emphasize that the optimization of each layer plays a significant role in determining the overall performance of perovskite solar cells.

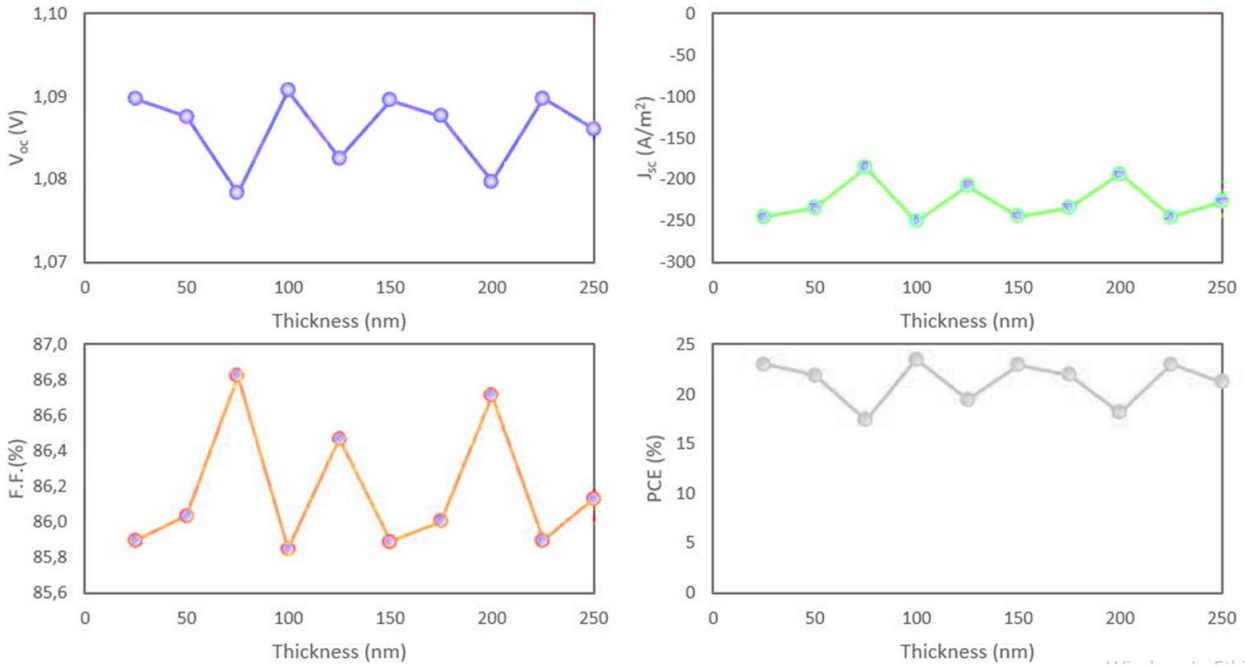

Fig. 8. Effect of change in layer thickness of FTO on solar cell parameters (Voc, Jsc, F.F. and PCE)

4. Conclusion

This study demonstrates that optimization of layer thicknesses in perovskite solar cells can significantly enhance PCE, thus contributing to the development of more sustainable and efficient energy technologies. Using OghmaNano software, we observed that each layer -the perovskite active layer, FTO conductive layer and the Au layer- has an ideal thickness for maximizing the photovoltaic performance of the solar cell.

The highest PCE recorded as 23.49% was obtained from the 775 nm perovskite layer, 50 nm FTO layer and 100 nm Au layers. These thicknesses also produced positive values for other important parameters such as FF, Voc and Jsc. In particular, the optimum 775 nm perovskite layer thickness produced a Voc of 1.0654 V and a Jsc of 86.3402 mA/cm². This indicates that increasing the thickness increases the light absorption and hence produces higher voltage output. However, exceeding this optimum thickness causes recombination losses that reduce the efficiency gains.

The highest PCE value was obtained with the FTO layer thickness of 50 nm. Voc also reached its maximum value at this thickness of 1.0907 V. The results show that thinner FTO layers are generally beneficial for achieving high Voc values due to improved electron mobility. On the other hand, increasing the FTO thickness beyond this value resulted in a decrease in PCE due to excessive material resistance.

The Au layer performed best at 100 nm thickness. It showed a peak Voc of 1.0907 V and a Jsc of 250.8915 mA/cm². At this thickness Au layer collects charges efficiently. Allowing electrons to flow smoothly without adding extra resistance.

This study aimed to find the ideal values of layer thickness in perovskite solar cells to improve PCE, Voc, Jsc, and FF. By fine-tuning these parameters, our findings not only exceed those of previous studies (17.57%, 22.06%, and 21.98%), but also underscore the potential of perovskite solar cells to advance toward practical, high-efficiency applications. This approach to achieving ideal layer properties can serve as a model for future solar cell designs and strengthen the role of photovoltaics in meeting the world's increasing energy demands in a sustainable manner.

Acknowledgements

There is no conflict of interest.

Author Contribution

E.N. and M.F.G. organized and performed all the analyses and wrote the manuscript.

References

[1] Z. Chen, X. Yiliang, Z. Hongxia, G. Yujie, and Z. Xiongwen, "Optimal design and performance assessment for a solar powered electricity, heating and hydrogen integrated energy system," *Energy*, vol. 262, pp. 125453, 2023.
[2] A. I. Osman *et al.*, "Cost, environmental impact, and resilience of renewable energy under a changing climate: a review," *Environ. Chem. Lett. 2022 212*, vol. 21, no. 2, pp. 741–764, 2022.
[3] O. Abedinia, A. Ghasemi-Marzbali, S. Gouran-Orimi, and M. Bagheri, "Presence of Renewable Resources in a Smart City for Supplying Clean and Sustainable Energy," *Decision Making Using AI in Energy and Sustainability* pp. 233–251, 2023.
[4] K. Dong, Q. Jiang, Y. Liu, Z. Shen, and M. Vardanyan, "Is energy aid allocated fairly? A global energy vulnerability perspective," *World Dev.*, vol. 173, pp. 106409, 2024.
[5] U. K. Pata, Q. Wang, M. T. Kartal, and A. Sharif, "The role of disaggregated renewable energy consumption on income and load capacity factor: A novel inclusive sustainable growth approach," *Geosci. Front.*, vol. 15, no. 1, pp. 101693, 2024.
[6] A. Sohrabi, M. Meratizaman, and S. Liu, "Comparative analysis of integrating standalone renewable energy sources with brackish water reverse osmosis plants: Technical and economic perspectives," *Desalination*, vol. 571, pp. 117106, 2024.
[7] N. A. N. Ouedraogo *et al.*, "Eco-friendly processing of perovskite solar cells in ambient air," *Renew. Sustain. Energy Rev.*, vol. 192, p. 114161, 2024.
[8] H. Si, X. Zhao, Z. Zhang, Q. Liao, and Y. Zhang, "Low-temperature electron-transporting materials for perovskite solar cells: Fundamentals, progress, and outlook," *Coord. Chem. Rev.*, vol. 500, pp. 215502, 2024.
[9] H. J. Kim, Y. J. Kim, G. S. Han, and H. S. Jung, "Green Solvent Strategies toward Sustainable Perovskite Solar Cell Fabrication," *Sol. RRL*, pp. 2300910, 2024.
[10] X. Li *et al.*, "Dimensional diversity (0D, 1D, 2D, and 3D) in perovskite solar cells: exploring the potential of mixed-dimensional integrations," *J. Mater. Chem. A*, 2024.
[11] P. Zhu *et al.*, "Toward the Commercialization of Perovskite Solar Modules," *Adv. Mater.*, pp. 2307357, 2024.
[12] R. Tian, S. Zhou, Y. Meng, C. Liu, and Z. Ge, "Material and Device Design of Flexible Perovskite Solar Cells for Next-Generation Power Supplies," *Adv. Mater.*, pp. 2311473, 2024.
[13] J. Qin *et al.*, "Towards operation-stabilizing perovskite solar cells: Fundamental materials, device designs, and commercial applications," *InfoMat*, pp. e12522, 2024.
[14] S. Wang *et al.*, "Efficient thermoelectric properties and high UV absorption of stable zinc-doped all-inorganic perovskite for BIPV applications in multiple scenarios," *Sol. Energy*, vol. 267, p. 112240, 2024.
[15] J. Zhang *et al.*, "Templated-seeding renders tailored crystallization in perovskite photovoltaics: path towards future efficient modules," *J. Mater. Chem. A*, vol. 12, no. 3, pp. 1407–1421, 2024.
[16] N. K. Elangovan, R. Kannadasan, B. B. Beenarani, M. H. Alsharif, M. K. Kim, and Z. Hasan Inamul, "Recent developments in perovskite materials, fabrication techniques, band gap engineering, and the stability of perovskite solar cells," *Energy Reports*, vol. 11, pp. 1171–1190, 2024.
[17] J. Cheng, H. Cao, S. Zhang, F. Yue, and Z. Zhou, "Reinforcing built-in electric field to enable efficient carrier extraction for high-performance perovskite solar cells," *Mater. Chem. Front.*, 2023.
[18] X. Dong *et al.*, "Improve the Charge Carrier Transporting in Two-Dimensional Ruddlesden-Popper Perovskite Solar Cells," *Adv. Mater.*, pp. 2313056, 2024.
[19] L. jing Huang, M. Zhang, Z. yan Wang, S. yu Zhao, H. Ji, and B. jia Li, "Fabrication of fractal Ag mesh/FTO transparent electrodes/heaters with enhanced electrical conductivity based on mesh hierarchy and shape optimization," *Opt. Laser Technol.*, vol. 168, pp. 109895, 2024.
[20] H.-J. Seok *et al.*, "Cost-Effective Transparent N-Doped Tin Oxide Electrodes with Excellent Thermal and Chemical Stabilities Enabling Stable Perovskite Photovoltaics Based on Tin Oxide Electron Transport Layer," *Adv. Energy Mater.*, pp. 2303859, 2024.
[21] Y. Sun, J. Zhang, B. Yu, S. Shi, and H. Yu, "Regulate defects and energy levels for perovskite solar cells by co-modification strategy," *Nano Energy*, vol. 121, pp. 109245, 2024.
[22] A. Sadhanala *et al.*, "Recent Advances and Challenges in Halide Perovskite Crystals in Optoelectronic Devices from Solar Cells to Other Applications," *Cryst. 2021, Vol. 11, Page 39*, vol. 11, no. 1, pp. 39, 2020.
[23] D. K. Sarkar *et al.*, "Numerical investigation of Aloe Vera-mediated green synthesized CuAlO2 as HTL in Pb-free perovskite solar cells," *J. Taibah Univ. Sci.*, vol. 18, no. 1, pp. 2300856, 2024.
[24] J. Maleki, M. Eskandari, and D. Fathi, "New design and optimization of half-tandem quantum dot solar cell: Over 30% power conversion efficiency using nanostructure oriented core-shell," *Renew. Energy*, vol. 222, pp. 119938, 2024.

[25] A. Mortadi, E. El Hafidi, M. Monkade, and R. El Moznine, "Investigating the influence of absorber layer thickness on the performance of perovskite solar cells: A combined simulation and impedance spectroscopy study," *Mater. Sci. Energy Technol.*, vol. 7, pp. 158–165, 2024.
[26] M. Sadullah and K. Ghosh, "Bandgap tuning and performance analysis of hybrid MAPb1−xSnxI3 perovskite solar cell: A numerical approach," *Optik (Stuttg).*, vol. 300, pp. 171644, 2024.
[27] J. Bisquert, *The physics of solar cells: Organic-Inorganic Halide Perovskite Photovoltaics*, vol. 50, no. 8. 2018.
[28] S. Adak and H. Cangi, "Development software program for finding photovoltaic cell open-circuit voltage and fill factor based on the photovoltaic cell one-diode equivalent circuit model," *Electr. Eng.*, pp. 1–14, 2024.
[29] A. K. K. Soopy *et al.*, "Towards High Performance: Solution-Processed Perovskite Solar Cells with Cu-Doped CH3NH3PbI3," *Nanomaterials*, vol. 14, no. 2, pp. 172, 2024.
[30] J. Kaur, S. Kumar, R. Basu, and A. K. Sharma, "Modelling and Simulation of Planar Heterojunction Perovskite Solar Cell featuring CH3NH3PbI3, CH3NH3SnI3, CH3NH3GeI3 Absorber Layers," *Silicon*, vol. 1, pp. 1–11, 2023.
[31] Y. Song, "Electrical and photovoltaic properties of metal/para-indium-phosphide Schottky barriers," 1988.
[32] H. A. Maddah, "Investigation of charge transport mechanism at TiO2/MAPbI3/β-Carotene heterostructure in natural dye sensitized solar cells," *Mater. Sci. Eng. B*, vol. 302, pp. 117197, 2024.
[33] V. Deswal, S. Kaushik, R. Kundara, and S. Baghel, "Numerical simulation of highly efficient Cs2AgInBr6-based double perovskite solar cell using SCAPS 1-D," *Mater. Sci. Eng. B*, vol. 299, pp. 117041, 2024.
[34] P. Ghosh, S. Sundaram, T. P. Nixon, and S. Krishnamurthy, "Influence of Nanostructures in Perovskite Solar Cells," *Encycl. Smart Mater.*, pp. 646–660, 2021.
[35] Q. Zhao, Y. Yang, Z. Hu, and H. Zhang, "A new full-spectrum solar power system based on perovskite solar cell and thermally regenerative electrochemical cycle: Influential mechanism and performance limit," *Energy Convers. Manag.*, vol. 302, pp. 118086, 2024.
[36] L. Mi, Y. Zhang, T. Chen, E. Xu, and Y. Jiang, "Carbon electrode engineering for high efficiency all-inorganic perovskite solar cells," *RSC Adv.*, vol. 10, no. 21, pp. 12298–12303, 2020.
[37] B. Nath, · Praveen, C. Ramamurthy, · Gopalkrishna Hegde, · Debiprosad, and R. Mahapatra, "Role of electrodes on perovskite solar cells performance: A review," *ISSS J. Micro Smart Syst. 2022 111*, vol. 11, no. 1, pp. 61–79, 2022.
[38] N. Chawki, R. Essajai, M. Rouchdi, M. Braiche, M. Al-Hattab, and B. Fares, "Efficacy analysis of BaZrS3-based perovskite solar cells: investigated through a numerical simulation," *Adv. Mater. Process. Technol.*, pp. 1–14, 2024.
[39] Z. S. Ismail, E. F. Sawires, F. Z. Amer, and S. O. Abdellatif, "Perovskites informatics: Studying the impact of thicknesses, doping, and defects on the perovskite solar cell efficiency using a machine learning algorithm," *Int. J. Numer. Model. Electron. Networks, Devices Fields*, vol. 37, no. 2, pp. e3164, 2024.
[40] J. Qi *et al.*, "Modulation of intermolecular interactions in hole transporting materials for improvement of perovskite solar cell efficiency: a strategy of trifluoromethoxy isomerization," *J. Mater. Chem. A*, vol. 12, no. 7, pp. 4067–4076, 2024.
[41] F. Xie *et al.*, "One-step hydrothermal synthesis of Zr-doped brookite TiO2 nanorods for highly efficient perovskite solar cells," *Mater. Res. Bull.*, vol. 173, pp. 112677, 2024.
[42] N. Chawki, R. Essajai, M. Rouchdi, M. Braiche, M. Al-Hattab, and B. Fares, "Efficacy analysis of BaZrS3-based perovskite solar cells: investigated through a numerical simulation," *Adv. Mater. Process. Technol.*, 2024.
[43] D. Shen *et al.*, "Tunable Photoluminescent Nitrogen-Doped Graphene Quantum Dots at the Interface for High-Efficiency Perovskite Solar Cells," *ACS Appl. Nano Mater.*, 2023.

Contents lists available at *Dergipark*

Journal of Scientific Reports-A

journal homepage: *https://dergipark.org.tr/tr/pub/jsr-a*

E-ISSN: 2687-6167 ***Number 61, June 2025***

RESEARCH ARTICLE

Receive Date: 11.12.2024 *Accepted Date: 05.05.2025*

Performance analysis of the most downloaded Turkish and English language models on the Hugging-Face platform

İnayet Hakkı Çizmeci[a,*], Kerem Gencer[b]

[a]"*Afyon Kocatepe University, Department of Computer Engineering, Afyonkarahisar 03030, Türkiye,*" *ORCID : 0000-0001-6202-4807*
[b]"*Afyon Kocatepe University, Department of Computer Engineering, Afyonkarahisar 03030, Türkiye,*" *ORCID : 0000-0002-2914-1056*

Abstract

This study analyzes the performance of the most popularly downloaded language models on the Hugging Face platform. For this purpose, the five most downloaded language models in Turkish and English were used. The analysis was evaluated in three phases. These stages were contextual learning, question and answer, and expert evaluation. ARC, Turkish sentiment analysis, Hellaswag, and MMLU datasets were used for contextual learning. For the question-and-answer test, the models trained with the text file created were asked questions from the text. Finally, six experts evaluated the answers given by the models from the developed mobile application. F1 score was used for context evaluation, Rouge-1, Rouge-2, and Rouge-L metrics were used for question and answer, and Elo and TrueSkill metrics were used for expert evaluations. The correlations of these metrics were calculated, and it was seen that there was a correlation of 0.74 between expert evaluations and question-answer performances. It was also observed that learning in context and question-answering performances were not correlated. When the language models were evaluated in general, the timpal0l/mdeberta-v3-base-squad2 language model performed the best. Turkish and English language models performed best on the sentiment analysis dataset with an F1 score above 0.85.

Keywords: Language Models; Fine-tune; Hugging Face; LLM

* Corresponding author. Tel.: +90 272 218 2364
E-mail address: icizmeci@aku.edu.tr

1. Introduction

In today's technology, it has become widespread to produce solutions by developing machine-based models (ML) for solving problems. Unique open-source platforms have been developed for sharing and developing these solutions. The primary reason for using open-source platforms is that machine learning models are large and expensive. To solve this problem, researchers have attempted to adapt pretrained models to open-source platforms. The presentation of model structures, including pre-trained weights, structures, and documentation, has made these platforms popular [1]. The most popular of these platforms is the 'Hugging Face Hub' [2]. The ecosystem of the Hugging Face Hub platform is given in Fig 1.

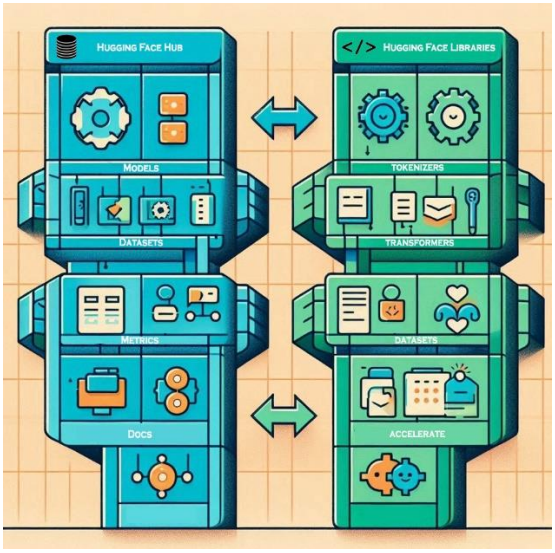

Fig. 1 Main components of the Hugging Face ecosystem [3]

The Hugging Face (HF) platform has become a hub for pretrained models. The HF platform allows language model developers to store the models they create and researchers to develop applications based on these models [4]. The HF platform makes frameworks such as Keras, Tensorflow, and PyTorch available to researchers via API [5]. As of August 2024, it hosts more than 820 thousand models, over 190 thousand data sets, and over 230 thousand demo applications [6]. It offers many public and online arguments that make the platform stand out. It allows everyone to develop natural language processing-based models and applications quickly. Large language models (LLM) such as GPT2, developed by OpenAI; BERT, developed by Google; and LLMA 3, developed by META, are offered to users via HF. If we make a metaphor for the HF platform, teaching mathematics to an illiterate student will take a lot of time and be difficult. However, for a literate student, learning mathematics will be both easier and less time-consuming. HF can be considered a platform through which literate students can obtain information.

Table 1. Some studies on language models

Study Name	Author(s)	Year	Subject	Results
Web Application for Solving Complex Artificial Intelligence Problems	Shen et al. [7]	2023	Use of the ChatGPT model	A web application was developed using ChatGPT, and artificial intelligence problems were solved.

Safety Analysis of Hugging Face Models	Kathikar et al. [8]	2023	Security vulnerabilities of the models	It is stated that the vulnerabilities of the models are 35.98%.
Predicting Early Diagnosis of Mental Disorders	Pourkeyvan et al. [9]	2024	BERT-based fine-tuned models	The prediction was made with four different fine-tuned models of BERT.
Quantitative Analysis of Hugging Face Models	Osborne et al. [10]	2024	Number of downloads of models and usage habits	The number of downloads of 70% of the models was found to be 0, and the number of downloads of 99% was found to be 1.
User and Community Analysis of Models	Castaño et al. [11]	2024	Communities and Model Care Situations	The communities' models, usage frameworks, and maintenance processes were analysed.
Performance Comparison of Turkish Language Models	Dogan et al. [12]	2024	Learning and question-answer performance of Turkish language models in context	In this context, it was found that learning and question-answering capabilities are not significantly related.

Platforms such as LLM Leaderboard [13] and datasets such as BigBench [14] and Big Glue [15] are used to compare the capabilities of language models. However, these platforms and data sets do not include Turkish language models and data sets. To address the deficiencies mentioned in this study, five Turkish and English language models popularly downloaded and fine-tuned on the HF platform were used. Structures such as the artificial intelligence evaluation scale [16] were not used to measure the effectiveness of these models. Although these scales provide an idea about the models, they are not sufficiently evaluated in detail. Therefore, more detailed evaluation and contextual learning approaches are required [17]. Contextual learning, expert evaluation, and question-answer methods were used to evaluate the effectiveness of the models. These evaluations were in the form of contextual learning, expert evaluation, and question-answer. A diagram summarizing the evaluation of the language models for this article is given in Fig. 2.

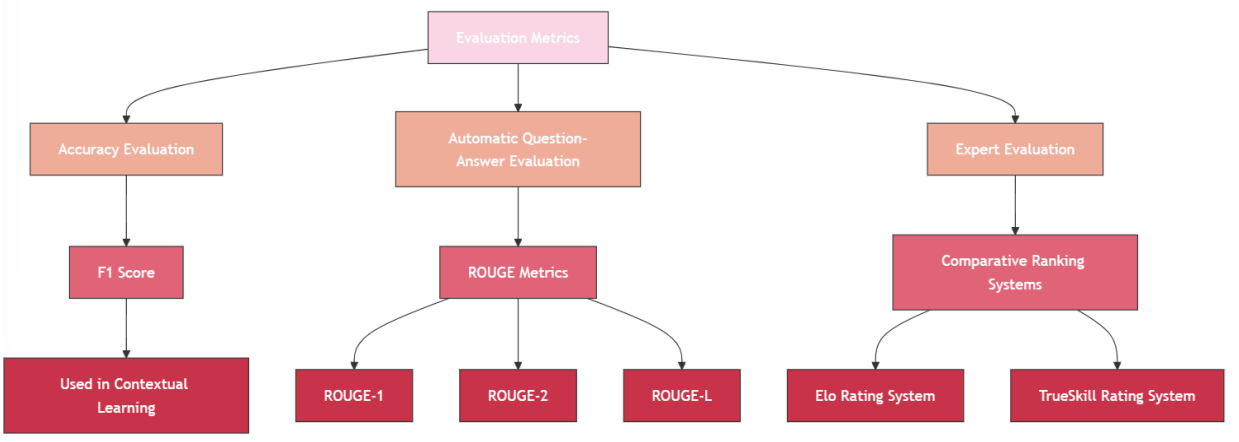

Fig. 2. Diagram summarizing the general structure of the article

The structure of this paper is as follows: In the first section, the purpose of the HF platform and the use of the language models it hosts are explained. The second section gives information about the data sets and methods used to analyze the models. The findings section presents the evaluation of the data obtained in the analysis, and the final section presents a discussion of the results.

2. Materials and Methods

2. 1. Language model (LM)

Language is the most important ability of humans to communicate. Unless the capabilities of machines are improved, they cannot communicate with and understand humans. Experts are constantly researching language models to achieve this goal. This research has led to language modeling methods. The missing parts in language modeling are provided by prediction. Four different methods are used for this modeling [18]. These methods are as follows:

- Statistical Language Model (SLM)
- Neural Language Model (NLM)
- Pre-Trained Language Model (PLM)
- Large Language Model (LLM)

In this study, pre-trained language models were used on the HF platform. The language models used are the platform's top five most downloaded models. As of 12 August 2024, the most downloaded Turkish language models are given in Table 2.

Table 2. Selected Turkish language models

Model Name	Base Model	Description
timpal0l/mdeberta-v3-base-squad2	BERT and RoBERTa	BERT and RoBERTa models were obtained by developing [19].
savasy/bert-base-turkish-squad	BERT	The capacity of the BERT-based model was increased by fine-tuning [20].
incidelen/bert-base-turkish-cased-qa	BERT	boun-tabi/squadtr (Budur et al., 2024) is a model developed using the dataset [21]
yunusemreemik/logo-qna-model	BERT	It is a model inspired by the Savasy/bert-base-turkish-squad model [22].
ozcangundes/mt5-multitask-qa-qg-turkish	Google T5-small	Google's multilingual T5-small model was fine-tuned with the Turkish question-answering dataset [23].

The most downloaded English language models on the same date are given in Table 3.

Table 3. Selected English language models

Model Name	Base Model	Description
deepset/roberta-base-squad2	RoBERTa	It is a model based on the Roberta-base model but gives faster results than this model [24].
bert-large-uncased-whole-word-masking-finetuned-squad	BERT	It is a fine-tuned language model based on the BERT language model developed by Google [25].
distilbert/distilbert-base-cased-distilled-squad	BERT	It is obtained by developing the BERT language model. It stands out with its 60% faster operation and smaller size [26].
distilbert/distilbert-base-uncased-distilled-squad	BERT	It was obtained by developing the BERT language model. 40% fewer parameters were used to make it work faster [26].

phiyodr/bert-large-finetuned-squad2	BERT	Using the large language model, BERT was fine-tuned on SQuAD2.0 [25].

2.2. Data set selection

To analyze the context learning performance of the selected language models, the ARC [27], Turkish Sentiment Analysis [28], Hellaswag, and MMLU [29] datasets were used. For the context evaluation of the models, data were used in both Turkish and English. English datasets were translated to English using the Helsinki-NLP/opus-mt-tc-big-en-tr [30] language model, and Turkish datasets were translated to English using the Helsinki-NLP/opus-mt-tc-big-en [30]. No operations, such as removing meaningless data or structuring, were performed on the existing data. Raw data was used. 200 question-answer data were used for testing in all models. The 200-test data were randomly selected. An example question-answer data set is presented in Table 4.

ARC is a multiple-choice question-answer dataset, easy and hard. The hard section contains difficult questions that require reasoning. Turkish sentiment analysis dataset contains positive, negative, and neutral sentences from various data sources. Hellaswag is a comprehensive dataset that measures the ability of natural language processing systems to complete sentences in a meaningful and logical manner. MMLU is a dataset designed to measure machines' knowledge and reasoning abilities. It contains multiple-choice questions from 57 different fields and topics.

Table 4. Question and answer example

Questions	Choices	Correct Answer
Stars are usually classified according to their brightness as seen in the night sky. Stars can be classified in many other ways. Which of these is least helpful in classifying stars?	A) visible colour, B) composition, C) surface texture D) temperature	C) surface texture
How long does it take for the Earth to rotate on its axis 7 times?	A) one day, B) a week, C) one month, D)one year	B) a week,

A text file containing information about the meta-heuristic algorithms was used for the question-answering performance. The Turkish version of this text file was tested on Turkish language models, and the English version was tested on English language models. A part of this text file is given in Table 5.

Table 5. Part of the Turkish and English texts

Turkish	English
### METASEZGİSEL ALGORİTMALAR	###METAHEURISTIC ALGORITHMS
### Karınca Koloni Algoritması	###Ant Colony Algorithm
Karıncalar besin kaynakları ile evlerinin arasındaki yolları belirlemektedir. İlk olarak geçen karınca feromon adı verilen koku yaymaktadır. Eğer yol kısa ise koku yoğun olmaktadır. Bu durum diğer karıncaların bu yoldan devam etmesini sağlamaktadır. Kesişen yol olursa koku yoğunluğuna göre rastgele seçim olmaktadır.	Ants mark the paths between food sources and their homes. The first ant to pass emits an odor called pheromone. If the path is short, the odor is intense. This ensures that other ants continue this path. If an intersecting path exists, a random selection is made according to the odor intensity.
### Bakteriyel arama besin arama optimizasyonu	###Bacterial search food search optimization
Ekolü bakterilerinin besin arama hareketlerinden esinlenilmiştir. Bakteriler beslenme davranışını örnek almışlardır. Bakteri besini ulaştığında salgı yaymakta ve diğer bakteriler de bu saygıya doğru grup olarak hareket	The foraging behavior of bacteria inspired the school. Bacteria are modeled on feeding behavior. When the bacterium reaches the food, it emits a secretion, and the other bacteria move as a

etmekte bir…	group towards this respect…

Questions were prepared from the text for each model's question-and-answer performance. The answers given automatically to these questions were compared with the answers the experts gave through voting. Examples of the question-and-answer dataset are given in Table 6.

Table 6. Sample questions and answers to the question-and-answer dataset

Turkish Questions	English Questions	Turkish Answers	English Answers
1- Dağ ceylanı optimizasyonunda 4 ana faktör nedir?	1- What are the 4 main factors in mountain gazelle optimization?	Bekar erkekler sürüsü, bölgesel erkekler, annelik sürüleri, yalnızlar	Swarm of single men, territorial men, swarm of mothers, loners
2- Ateş böceği sürüsünde fitness değeri neye göre belirlenmektedir?	2- How is the fitness value determined in a firefly swarm?	Parıldama derecelerine göre fitness değerleri belirlenmektedir.	According to the degree of scintillation
3- Feromon adlı salgı kim tarafından salgılanmaktadır?	3-Who secretes the secretion called pheromone?	İlk karınca tarafından salgılanmaktadır	The first ant to pass
4- Gri Kurt algoritması kaç katmandan oluşur?	4- How many layers does the grey wolf algorithm consist of?	4 katmandan oluşur	4 Layers
5- Yarasa algoritmasında yarasalar uzaklıklarını nasıl belirliyorlar?	5- How do bats determine their distance in the bat algorithm?	Seslere göre	According to sounds

2.3. Methods used in the analysis

2.3.1. Learning method in context

Learning in context is defined as the response of a language model based on the current context without additional training or with very little data. This shows the fast learning and adaptability of model [31]. ARC, Turkish sentiment analysis, Hellaswag, and MMLU datasets were used to determine the contextual capabilities of the popular models selected for this study. F1 scores were calculated based on the accuracy of the models' responses to these datasets. Thus, the strengths and weaknesses of the language models were determined.

2.3.2. Question and answer method

The model's ability to answer automatically is evaluated in the question-and-answer method. For this evaluation, the model was trained with a text file and tested with questions generated from this text. The answers given by the models were analyzed by comparing them with the reference answers. This analysis used ROUGE-1, ROUGE2, and ROUGE-L metrics [32]. They were also analyzed in terms of word order.

F1-Score: The F1 score, a one-dimensional indicator, has an important place in performance evaluation metrics. It is defined as the harmonic means of precision and recall. F1 score takes a value between 0 and 1. While a value of 1 indicates excellent precision and recall values, a value of 0 indicates the worst performance. F1 score is especially prominent in unbalanced data sets [33] [34].

ROUGE: It is a widely used metric in natural language processing. The metric measures numerically how closely an automatically generated summary matches human-generated reference texts. This metric is typically based on word

overlap. A high ROUGE score indicates that the generated text is more similar to the reference text. The ROUGE can be calculated using different methods depending on the level of detail. The most commonly used examples are [35]:

- ROUGE-N: Based on N-gram overlaps (like ROUGE-1, ROUGE-2)
- ROUGE-L: Based on Longest Common Subsequence (LCS) length.
- ROUGE-S: Based on Skip-bigram overlaps.
- ROUGE-SU: Based on Skip-bigram and unigram overlaps.

2.3.3 Expert assessment

In analyzing the performance of the models, the evaluation of the experts by voting method is important. The two models generate the answer to the question randomly selected from the question pool. The expert compares these two answers and chooses one of the four options. A mobile application was developed for this case. The application was developed using the React Native framework and JavaScript. Firebase database was used. The answers to the questions about the models to be compared are given in the mobile application in Fig. 3. It is not stated which answer belongs to the given model. A blind evaluation system has been created. The same questions were asked by all models. The score table for the model was created according to the experts' answers. If the answer of the model is good, the model receives a (+1) point, whereas the other model receives a (-1) point. If the expert chooses the option where both models are good, both models receive a value of (+1), and if both are bad, both models receive a value of (-1).

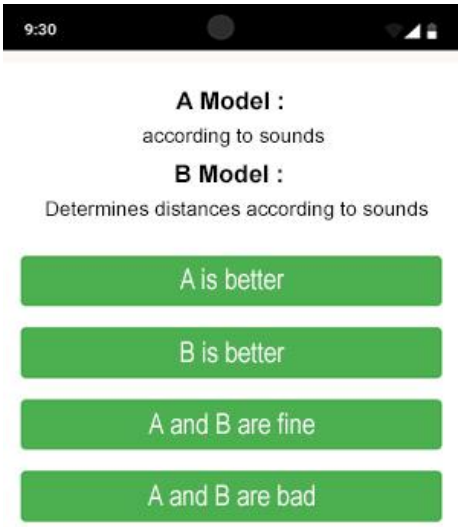

Fig. 3. Mobile App

Six experts can also reveal the semantic differences between the language used by humans and the language produced by the models. In this analysis, Elo [36] and TrueSkill [37] metrics, which are used to evaluate performances in competitive systems, were used. Elo indicates that one model wins, and the other model loses points.

The model with the most points stands out in the evaluation, which starts with a specific score. TrueSkill considers the uncertainties of both sides. Thus, it is considered in cases where A and B are good, or A and B are bad.

2.4 Hardware and Software Used in the Analysis

The experimental study used Google's Collaborative platform for the analysis. The hardware provided by this platform is 40 GB GPU and 107.7 GB storage space. Python was used as the programming language. HF used Transformers and torch libraries to integrate the models into the software. Transformers bring a fast architectural structure for natural language processing, leaving recurrent artificial neural networks behind. This architecture is scaled with training data and model size, enabling more efficient training [38]. PyTorch is an open-source Python-based machine-learning library [39]. The given texts need to be chunked for training. This process is called tokenization. Tokenization is dividing the body given in language models into units. Each unit consists of a token [40]. An example of the code block used for tokenization is given in Fig. 4.

```
model_name = "timpal0l/mdeberta-v3-base-squad2"
tokenizer = AutoTokenizer.from_pretrained(model_name)
model = AutoModelForQuestionAnswering.from_pretrained(model_name)
```

Fig. 4. Tokenization process

3. Results

The results of the analyses are given in Table 7. The F1 score was used for accuracy evaluation in contextual learning. ROUGE-1, ROUGE2 and ROUGE-L metrics were used for automatic question-and-answer evaluation, and Elo and TrueSkill were used for expert evaluation. In Elo, each model started with 500 points, while TrueSkill started with 25 points. In the expert evaluation, each expert voted on 70 questions, and 420 votes were used. The correlation matrix of the metrics with each other is shown in Fig. 5. As a result of the analyses, the best result obtained is the Turkish language model A (timpal0l/mdeberta-v3-base-squad2). This language model was developed based on the BERT and RoBERTa language models. Following language model A, language model N (distilbert/distilbert-base-uncased-distilled-squad) performed the second best. Among the other language models, K (deepest/Roberta-base-squad2), L (bert-large-uncased-whole-word-masking-finetuned-squad), and O (phiyodr/bert-large-finetuned-squad2) language models showed the third best performance. The remaining language models could not take the lead in any datasets.

Table 7. Evaluation of models

Criteria	A	B	C	D	E	K	L	M	N	O
ARC (F1 Score)	0.2605	0.2450	0.2559	0.2281	0.2504	0.2778	0.2784	0.2466	**0.2785**	0.2721
Turkish Sentiment Analysis (F1 Score)	**0.9500**	0.9049	0.4251	0.8997	0.8639	0.8486	0.8851	0.8750	0.8845	0.9000
MMLU (F1 Score)	0.2116	0.2183	0.2294	0.2674	0.2305	0.2314	0.2280	0.2289	0.2214	**0.3100**
Hellaswag (F1 Score)	0.1981	0.2170	0.2547	0.2128	0.1967	0.1910	**0.2218**	0.2025	0.1345	0.1799
ROUGE-1	**0.8750**	0.0952	0.3077	0.0952	0.1830	0.7500	0.8000	0.6667	0.7500	0.8000
ROUGE-2	**0.6667**	0.0000	0.1818	0.0000	0.1325	**0.6667**	0.4444	0.5714	**0.6667**	0.4444
ROUGE-L	**0.8750**	0.0952	0.3077	0.0952	0.1830	0.7500	0.8000	0.6667	0.7500	0.8000
ELO	**614**	382	534	407	462	488	514	437	566	593

TrueSkill	**29.5**	20.5	26.5	21.5	23.5	24.5	25.5	22.5	27.5	28.5

A: timpal0l/mdeberta-v3-base-squad2

B: savasy/bert-base-turkish-squad

C: incidelen/bert-base-turkish-cased-qa

D: yunusemreemik/logo-qna-model

E: ozcangundes/mt5-multitask-qa-qg-turkish

K: deepset/roberta-base-squad2

L: bert-large-uncased-whole-word-masking-finetuned-squad

M: distilbert/distilbert-base-cased-distilled-squad

N: distilbert/distilbert-base-uncased-distilled-squad

O: phiyodr/bert-large-finetuned-squad2

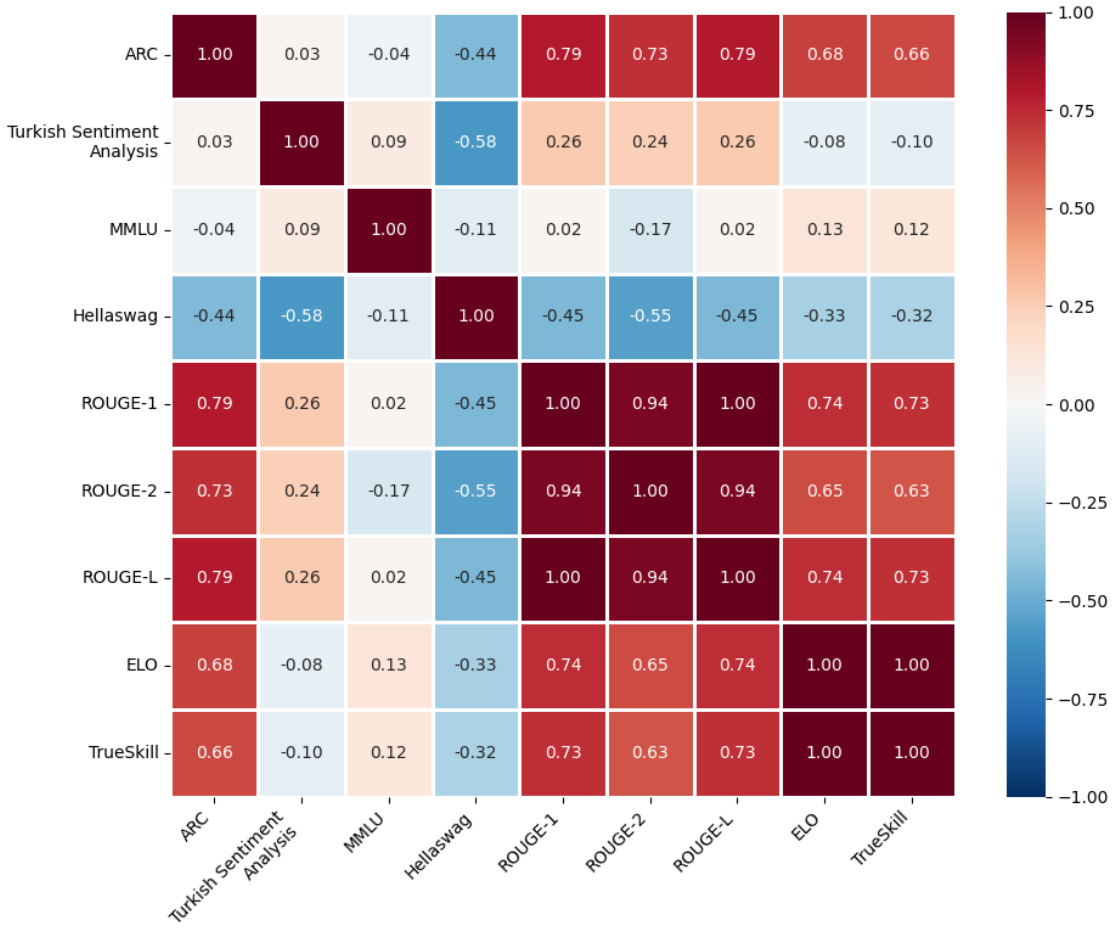

Fig 5. Correlation of Criteria

4. Conclusions and Discussion

The correlation matrix shown in Figure 5 reveals the relationships between different evaluation metrics. According to the analysis results, ROUGE metrics (ROUGE-1, ROUGE-2, and ROUGE-L) have very high correlations among themselves (0.94-1.00). It is also seen that ROUGE metrics show a strong positive correlation (0.73-0.79) with ARC values. An excellent correlation (1.00) is observed between expert evaluation metrics Elo and TrueSkill, indicating that the two methods produce similar results. Elo and TrueSkill also exhibit strong positive correlations (0.63-0.74) with ROUGE metrics. This proves that there is a significant agreement between automatic evaluation and expert evaluation. On the other hand, negative correlations (between -0.11 and -0.58) are observed between Hellaswag and other metrics. These findings suggest that Hellaswag, which measures the ability to learn in context, may be inversely related to question-answering performance. The MMLU metric showed weak correlations with other metrics (between -0.17 and 0.13), indicating that models that perform well on multiple-choice logic and comprehension tests may not perform as well on question-answering tasks. There is a low-to-moderate correlation (0.24-0.26) between Turkish Sentiment Analysis performance and ROUGE metrics, indicating that model performances on sentiment analysis and question-answering tasks may be partially related, but this relationship is not strong.

When we examined the most popular language models on Hugging Face and evaluated the results, we observed something different from what we expected. The most striking outcome was the success of the Turkish model timpal0l/mdeberta-v3-base-squad2. This result demonstrates the importance of combining the strengths of the BERT and RoBERTa models. Moreover, this model provided similarly good results regardless of the measurement method used.

On the other hand, we noticed a big difference between sentiment analysis and question-answer. Although the models achieved F1 scores above 0.85 in sentiment analysis, they scored lower in question-answer. This reminded us that we must select different models for different tasks. Question-answer is a much more complex task than sentiment analysis. In particular, the incidelen/bert-base-turkish-cased-qa model fell behind the others with a low F1 score of 0.42. This showed us that some BERT-based models have limitations in Turkish Question-Answer.

We were surprised to see that different measurement methods such as ROUGE-L, TrueSkill and Elo gave similar results. Therefore, there is less difference between automatic evaluation and expert evaluation than we thought. However, interestingly, we did not find a relationship between the success of a model in context learning and its success in question-answering. This was the case for both the Turkish and English models.

We learned lessons from these results for both researchers and practitioners. For researchers, it became clear that it is important to use different metrics for different tasks rather than a single metric when testing language models. Similar trends in Turkish and English models suggest that some results may be language-independent.

For those working on Turkish natural language projects, we provide practical information on which model to choose for which task. Although mdeberta-v3-base-squad2 is a good choice for general language understanding, other models may be more suitable for tasks focused on sentiment analysis.Finally, the size of the datasets we used in this study was a limitation.

In future, we plan to work with larger and more diverse datasets to increase the reliability of our results. In addition, investigating the reasons for the performance gap between sentiment analysis and question-answering can help us develop better models. Also, the transferability of fine-tuning across languages is an important area of research for multilingual applications.

Acknowledgements

The study did not receive specific financing from any grant agencies in the public, commercial, or non-profit sectors.

References

[1] J. Jones, W. Jiang, N. Synovic, G. Thiruvathukal, and J. Davis, "What do we know about Hugging Face? A systematic literature review and quantitative validation of qualitative claims," in *Proc. of the 18th ACM/IEEE International Symposium on Empirical Software Engineering and Measurement*. 2024, pp. 13–24.

[2] A. Ait, J. L. C. Izquierdo and J. Cabot, "HFCommunity: A Tool to Analyze the Hugging Face Hub Community," in *Proc. 2023 IEEE International Conference on Software Analysis, Evolution and Reengineering (SANER)*. Taipa, Macao, 2023, pp. 728-732, doi:10.1109/SANER56733.2023.00080

[3] Z. Hussain, M. Binz, R. Mata *et al.* "A tutorial on open-source large language models for behavioural science," *Behav Res* 56, pp. 8214–8237, 2024. doi:10.3758/s13428-024-02455-8

[4] S. M. Jain, "Introduction to Transformers for NLP: With the Hugging Face Library and Models to Solve Problems," *Apress Media LLC*, pp. 51-53, 2022, doi: 10.1007/978-1-4842-8844-3

[5] F. Pepe, V. Nardone, A. Mastropaolo, G. Bavota, G. Canfora, and M. Di Penta, "How do Hugging Face Models Document Datasets, Bias, and Licenses? An Empirical Study," in *Proc. of the 32nd IEEE/ACM International Conference on Program Comprehension*. 2024, pp. 370–381.

[6] Hugging Face Inc., https://Huggingface.Co/ (accessed August. 13, 2024)

[7] Y. Shen, K. Song, X. Tan, D. Li, W. Lu and Y. Zhuang, "HuggingGPT: Solving AI Tasks with ChatGPT and its Friends in Hugging Face. Advances in Neural Information," in *Proc. Systems 36*, New Orleans, USA, 2023, pp. 38154—38180, doi: 10.48550/arXiv.2303.17580.

[8] A. Kathikar, A. Nair, B. Lazarine, A. Sachdeva and S. Samtani, "Assessing the Vulnerabilities of the Open-Source Artificial Intelligence (AI) Landscape: A Large-Scale Analysis of the Hugging Face Platform," in *Proc. 2023 IEEE International Conference on Intelligence and Security Informatics*, Charlotte, NC, USA, 2023, pp.1-6, doi: 10.1109/ISI58743.2023.10297271.

[9] A. Pourkeyvan, R. Safa and A. Sorourkhah, "Harnessing the Power of Hugging Face Transformers for Predicting Mental Health Disorders in Social Networks," IEEE Access, 12, pp. 28025-28035, 2024, doi: 10.1109/ACCESS.2024.3366653

[10] C. Osborne, J. Ding and H. R. Kirk, "The AI community building the future? A quantitative analysis of development activity on Hugging Face Hub," *Journal of Computational Social Science*, vol.7, no.1, pp. 2432-2725, 2024, doi https://doi.org/10.1007/s42001-024-00300-8

[11] J. Castaño, M. F. Silverio, X. Franch and J. Bogner, "Analyzing the Evolution and Maintenance of ML Models on Hugging Face," in *Proc. of the 21st International Conference on Mining Software Repositories*, New York, NY, USA, 2024, pp. 607–618, doi: 10.1145/3643991.3644898

[12] E. Dogan, M. E. Uzun, A. Uz, H. Seyrek, A. Zeer, E. Sevi et al. "Performance Comparison of Turkish Language Models," *arXiv e-prints*, 2024, arXiv:2404.17010.

[13] Open llm leaderboard, a hugging face space by huggingfaceh4, https://huggingface.co/open-llm-leaderboard. (accessed August. 13, 2024)

[14] A. Srivastava, A. Rastogi, A. Rao, A. A. M. Shoeb, A. Abid, A. Fisch and et al, "Beyond the Imitation Game: Quantifying and extrapolating the capabilities of language models", *Transactions on Machine Learning Research, 2023*.

[15] A. Wang, A. Singh, J. Michael, F. Hill, O. Levy, and S. R. Bowman, "GLUE: A multi-task benchmark and analysis platform for natural language understanding", *arXiv [cs.CL]*, 20-Apr-2018, arXiv preprint arXiv:1804.07461.

[16] M. Perkins, L. Furze, J. Roe, and J. Macvaugh, "The Artificial Intelligence Assessment Scale (AIAS): a framework for ethical integration of generative AI in educational assessment," *Journal of University Teaching and Learning Practice*, 21(6), 2024. doi: 10.53761/q3azde36

[17] C. Gonsalves, "Contextual assessment design in the age of generative AI," *Journal of Learning Development in Higher Education*, (34), 2025. https://doi.org/10.47408/jldhe.vi34.1307

[18] W. X. Zhao, K. Zhao, J. Li, T. Tang, X. Wang and *et al.*, "A survey of large language models", *arXiv [cs.CL]*, 31-Mar-2023, doi: 10.48550/arXiv.2303.18223

[19] P. He and J. Gao, "DeBERTaV3: Improving DeBERTa using ELECTRA-Style Pre-Training with Gradient-Disentangled Embedding Sharing', in *Proc. The Eleventh International Conference on Learning Representations*, Kigali, Ruanda, 2023, pp. 1–16.

[20] S. Yildirim, "Fine-tuning Transformer-based encoder for Turkish Language understanding tasks", *arXiv [cs.CL]*, 30-Jan-2024, doi: 10.48550/arXiv.2401.17396

[21] M. İncidelen, Hugging Face Inc., https://Huggingface.Co/Incidelen/Bert-Base-Turkish-Cased-Qa (accessed August 13, 2024)

[22] Y. E. Emik, Hugging Face Inc., https://Huggingface.Co/Yunusemreemik/Logo-Qna-Model (accessed August 13, 2024)

[23] Ö. Gündeş, Hugging Face Inc., https://Huggingface.Co/Ozcangundes/Mt5-Multitask-Qa-Qg-Turkish (accessed August 13, 2024)

[24] Deepset, Hugging Face Inc., https://huggingface.co/deepset/roberta-base-squad2 (accessed August 13, 2024)

[25] J. Devlin, M. W. Chang, K. Lee, and K. Toutanova, "BERT: Pre-training of Deep Bidirectional Transformers for Language Understanding", in *Proc. of NAACL-HLT 2019*, Stroudsburg, PA, USA, 2019, pp. 4171–4186.

[26] V. Sanh, L. Debut, J. Chaumond, and T. Wolf, "DistilBERT, a distilled version of BERT: smaller, faster, cheaper and lighter", *arXiv [cs.CL]*, 2019, doi:10.48550/arXiv.1910.01108

[27] naytin, Hugging Face Inc. https://huggingface.co/datasets/naytin/ai2_arc_tr (accessed September 12, 2024)

[28] Hugging Face Inc. https://huggingface.co/datasets/winvoker/turkish-sentiment-analysis-dataset (accessed September 12, 2024)

[29] naytin, Hugging Face Inc. https://huggingface.co/datasets/naytin/hellaswag_tr (accessed September 12, 2024)

[30] J. Tiedemann and S. Thottingal, "OPUS-MT Building open translation services for the World", in *Proc. the 22nd Annual Conference of the European Association for Machine Translation*, 2020, pp. 479–480.

[31] Y. Gu, L. Dong, F. Wei, and M. Huang, "Pre-training to learn in context", *arXiv [cs.CL]*, 15-May-2023, doi: 10.48550/arXiv.2305.09137

[32] C. Y. Lin, "Rouge: A package for automatic evaluation of summaries", in *Text summarization branches out*, 2004, pp. 74–81.

[33] D. Chicco and G. Jurman, "The advantages of the Matthews correlation coefficient (MCC) over F1 score and accuracy in binary classification evaluation," *BMC Genomics* 21, 6, 2020. https://doi.org/10.1186/s12864-019-6413-7.

[34] H. Huang, H. Xu, X. Wang and W. Silamu, "Maximum F1-Score Discriminative Training Criterion for Automatic Mispronunciation Detection," in *IEEE/ACM Transactions on Audio, Speech, and Language Processing*, vol. 23, no. 4, pp. 787-797, April 2015, doi: 10.1109/TASLP.2015.2409733

[35] M. Barbella and G. Tortora, "Rouge metric evaluation for text summarization techniques," *Available at SSRN 4120317. http://dx.doi.org/10.2139/ssrn.4120317*

[36] A. E. Elo, *The Rating of Chessplayers, Past and Present*. New York: Arco Publishing, 1978.

[37] R. Herbrich and T. Graepel, *TrueSkillTM: A Bayesian skill rating system*. Microsoft Research, 2006.

[38] T. Wolf, L. Debut, V. Chaumond, *C.* Delangue, A.Moi, P. Cistac end *et al.*, "Transformers: State-of-the-Art Natural Language Processing*", The 2020 Conference on Empirical Methods in Natural Language Processing*. Stroudsburg, USA, pp. 38–45.

[39] Y. Zhang *et al*., "DIALOGPT: Large-scale generative pre-training for conversational response generation", in *Proceedings of the 58th Annual Meeting of the Association for Computational Linguistics: System Demonstrations*, Online, 2020, doi:10.18653/v1/2020.acl-demos.30

[40] S. Choo and W. Kim, "A study on the evaluation of tokenizer performance in natural language processing", *Appl. Artif. Intell.*, vol. 37, no. 1, Dec. 2023.

Contents lists available at *Dergipark*

Journal of Scientific Reports-A

journal homepage: *https://dergipark.org.tr/tr/pub/jsr-a*

E-ISSN: 2687-6167 ***Number 61, June 2025***

RESEARCH ARTICLE

Receive Date: 18.12.2024 *Accepted Date: 08.04.2025*

A useful utility program for all Gaussian version users: ZEKA

Zeki Kartal[a*], Kamil Kartal[b]

[a]*Retired Professor of Atomic and Molecular Physics, Kütahya Dumlupınar University, Kütahya, 43020, Türkiye, ORCID: 0000-0001-9739-0858*
[b]*Retired from TFKB (TÜRKİYE FINANCE PARTICIPATION BANK) Information Technologies, Assistant Manager, and IT Manager at TGS between 2011-2015, İstanbul, 34584, Türkiye, ORCID: 0009-0003-2157-1689*

Abstract

This study focuses on ZEKA, a time-saving utility calculation program for researchers using the Gaussian 03, Gaussian 09 and Gaussian 16 molecular modeling and calculation programs. The magnetic, vibrational, electro-optic, some NLO and NBO properties of the compound whose structure is resolved with the Gaussian program are calculated by taking the necessary data from its .log output file and placing them in the relevant formulas. The ZEKA utility program completes such calculations in a very short time interval of approximately **300-400 milliseconds (ms)** for an average-sized molecular structure, depending on the size of its log file. These processes require the researcher to spend a lot of time on this work. In addition, the fact that the calculations are performed by the human factor may cause some unwanted errors. The ZEKA utility program will enable researchers to both make the best use of their limited time and prevent errors caused by human factors.

Keywords: Gaussian molecular modeling program, Gaussian calculation program, structural properties of compounds, Gaussian output file (.log), ZEKA utility program

1. Introduction

Human beings began to watch the various events taking place around them in this world, first with fear, then with curiosity, and then with interest. As a result, humankind has gained insights into the events of interest. Later, human beings began to investigate the events around them, wondering why and how they happened. Thus, the foundation of the first scientific thought and scientific study in human history was laid.

As time passed, studies and developments in science reached a dizzying pace in every field. Especially in the last fifty years, developments in the fields of computers and software have enabled many physical and chemical events to be simulated in the computer environment and the results of the events to be obtained in the form of new data. For example, obtaining new compounds and investigating their physical, chemical, electronic and magnetic properties is one of the most important areas in this regard.

Quantum chemistry and solid-state physics computer programs apply quantum chemistry methods in these fields. These programs may also use Hartree-Fock (HF), Density Functional Theory (DFT), Molecular Mechanics (MM), Semi-Empirical Quantum Chemistry (SEQCM), and a number of other methods. Some of these programs are suitable for both free use and

* Corresponding author. Tel.: 05326831144
E-mail address: zekikartal52@gmail.com

commercial use. Many experts have made great contributions in bringing these programs to their current state. Programs such as AMPAC [1], CASTEP [2], CRYSTAL [3], GAMESS [4], GAUSSIAN [5], MOPAC [6], SIESTA [7] and SPARTAN [8] … etc. can be given as examples of such programs. Many researchers are increasingly using some of these programs in their own studies. Many researchers make decisions about which program to use in their scientific studies based on their own observations, sensations, and the results of using and testing various programs to the extent of their possibilities.

It is a well-known fact that there are many auxiliary programs such as GAUSSSUM, MULTIWFN and others that make it easier to understand the outputs of the computational molecular modeling programs mentioned above. None of the other programs provided as an auxiliary to the Gaussian program provide those who use it with the concrete calculated results that the ZEKA utility does. However, the ZEKA utility offers a new type of service that those programs do not provide, namely automatic calculation of μ, α_0, Δα, β_0 and γ values. Thus, it saves for researchers a significant amount of time.

Gaussian software easily indicates the most complex interactions in electronic structures, revealing even the smallest differences in them. Gaussian enables in-depth examination of electronic interactions in molecular structures, and presents the results accurately in the shortest possible time. Due to such features, it is widely used in academic studies. The purpose of this study is definitely not to compare similar programs with each other in terms of quality or functionality, but only to save time for researchers using various variants of the Gaussian program and to make their work easier on some issues.

Whichever program is used to determine the structural properties of a compound, the result gives the information in an output file as various file extensions (for example, chk, gjf and log etc. in the Gaussian program). These new outputs contain raw information used to calculate many properties of the compound of interest. Extracting this raw information from the file, applying it to the necessary formulas, and obtaining the desired result relies almost entirely on human effort. Especially in complex compounds formed by the combination of many atoms, the number of raw data in question can reach quite large values. Therefore, the number of human errors that can be made when using large amounts of raw data also increases.

2. Material and method

When conducting an experimental scientific study, various chemical substances such as ligands, different atoms and solvents are used. As a result of experimental studies, new synthesized products emerge in various forms. Some physical and chemical properties of these new products are investigated either with some technical instruments (for example: IR, Raman, NMR, powder and single crystal data analyzers ...) or with some quantum mechanical calculation programs mentioned earlier.

Like many researchers, we use the Gaussian program in computational chemistry studies. We calculated various properties of some of the compounds we examined with the help of the Gaussian program [9-12]. We wanted to create a utility that would save time and eliminate human errors for researchers who will use the Gaussian program in their future studies. Thus, as a result of long efforts, the "ZEKA" program emerged. The purpose of this study is to introduce the ZEKA utility to Gaussian users. Later, efforts will be made to improve it in line with the requests and suggestions that may come from the users.

2.1. Why the ZEKA utility was needed?

By using the data (mol or cif files) of a compound that has been theoretically designed or whose crystal structure has been analyzed experimentally, theoretical analyzes can be made about that compound with the Gaussian program. The Gaussian program saves theoretical calculation results as files with gjf, chk, and log extensions. The first two documents give the visual data of the relevant compound, and the last document gives the raw data as a txt file. The raw data to be taken from the txt file of the relevant compound is used in the formulae below (Eqs. 1-8) to calculate its magnetic, electrical or structural properties [13,14].

The values that can be calculated for the relevant compound; dipole moment (μ), mean polarizability (α_0), anisotropies of polarizability (Δα), first order static hyperpolarizability (β_0) and its components (β_x, β_y, β_z) and second order static hyperpolarizability (γ) values are given in Equations (1-8), respectively.

$$\mu = \sqrt{\mu_x^2 + \mu_y^2 + \mu_z^2} \tag{1}$$

$$\alpha_0 = \frac{\alpha_{xx}+\alpha_{yy}+\alpha_{zz}}{3} \tag{2}$$

$$\Delta\alpha = \sqrt{\frac{(\alpha_{xx}-\alpha_{yy})^2+(\alpha_{yy}-\alpha_{zz})^2+(\alpha_{zz}-\alpha_{xx})^2+6(\alpha_{xy}^2+\alpha_{xz}^2+\alpha_{zy}^2)}{2}} \tag{3}$$

$$\beta_x = \beta_{xxx} + \beta_{xyy} + \beta_{xzz} \quad (4)$$

$$\beta_y = \beta_{yyy} + \beta_{xxy} + \beta_{yzz} \quad (5)$$

$$\beta_z = \beta_{zzz} + \beta_{xxz} + \beta_{yyz} \quad (6)$$

$$\beta_0 = \sqrt{\beta_x^2 + \beta_y^2 + \beta_z^2} \quad (7)$$

$$\gamma = \frac{1}{5}\{\gamma_{xxxx} + \gamma_{yyyy} + \gamma_{zzzz} + 2[\gamma_{xxyy} + \gamma_{xxzz} + \gamma_{yyzz}]\} \quad (8)$$

Even the log file calculated by the Gaussian program for a small compound consisting of about five or six atoms has a very large volume. It would take a researcher a very long time to calculate some properties of the compound by taking the relevant values from this file and using them in equations (Eqs. 1-8). Small research on this subject will reveal the sizes of the log files of the relevant compounds (approximately between 100 – 10.000 KB or over 100.000 in terms of number of lines). Especially when some researchers want to calculate the various properties of different derivatives of a ligand or a large number of compounds formed by a ligand or ligands with different transition metals, the time required for this becomes much longer [15,16]. In addition to wasting time, this will also add possible errors caused by the human factor to the results. It can only be understood whether there is an error in the results obtained by repeating the process. This results in a significant waste of time. For this reason, the ZEKA utility program was created by us so that researchers can allocate their valuable time to new research topics.

All values calculated from the equations for the compounds are expressed in atomic units (au). These calculated values are converted into electrostatic units (esu) by multiplying them with appropriate coefficients [17,18]. The ZEKA utility simultaneously performs the unit conversions and presents the results in both systems.

2.2. Promotion and use of the ZEKA utility

ZEKA program is a utility that calculates and presents various properties of a compound by using the data calculated and presented by various versions of the Gaussian program in the relevant formulas. ZEKA program can run on any laptop or desktop computer with Windows operating system. When the needle at the bottom left of the ZEKA utility program is moved to the left, the program screen becomes increasingly transparent. This allows you to see and access any information in the background without leaving the program.

To easily obtain some features of a molecular structure analyzed in the Gaussian program, you can use the ZEKA utility in two ways, depending on the language selection, “TURKISH” or “ENGLISH”. To do this, all you have to do is select the language you want to use in the "ZEKA" utility, which you have made available for operation by performing the necessary operations on your computer (see Fig. 1).

An important tip: It is important that there are no programs running in the background when using the ZEKA utility, so that it can perform its operations smoothly and quickly.

Fig. 1. First boot view of the ZEKA utility program.

3. Results and discussion

If your ZEKA utility program language selection is English, it will turn into a new window as seen in the picture below (Fig. 2).

Fig. 2. View of the ZEKA utility program after selecting the user language as English.

When you select the log extension file of the compound you want to analyze among your Gaussian data, the appearance of the ZEKA utility is as shown in Fig. 3. If the selected log file is a file created by a higher version program such as Gaussian 09 or Gaussian 16, a green mark will appear inside the "SELECT LOG FILE" button. If the selected log file is a file created by a lower version program such as Gaussian 03, this green mark will not appear (see Fig. 3).

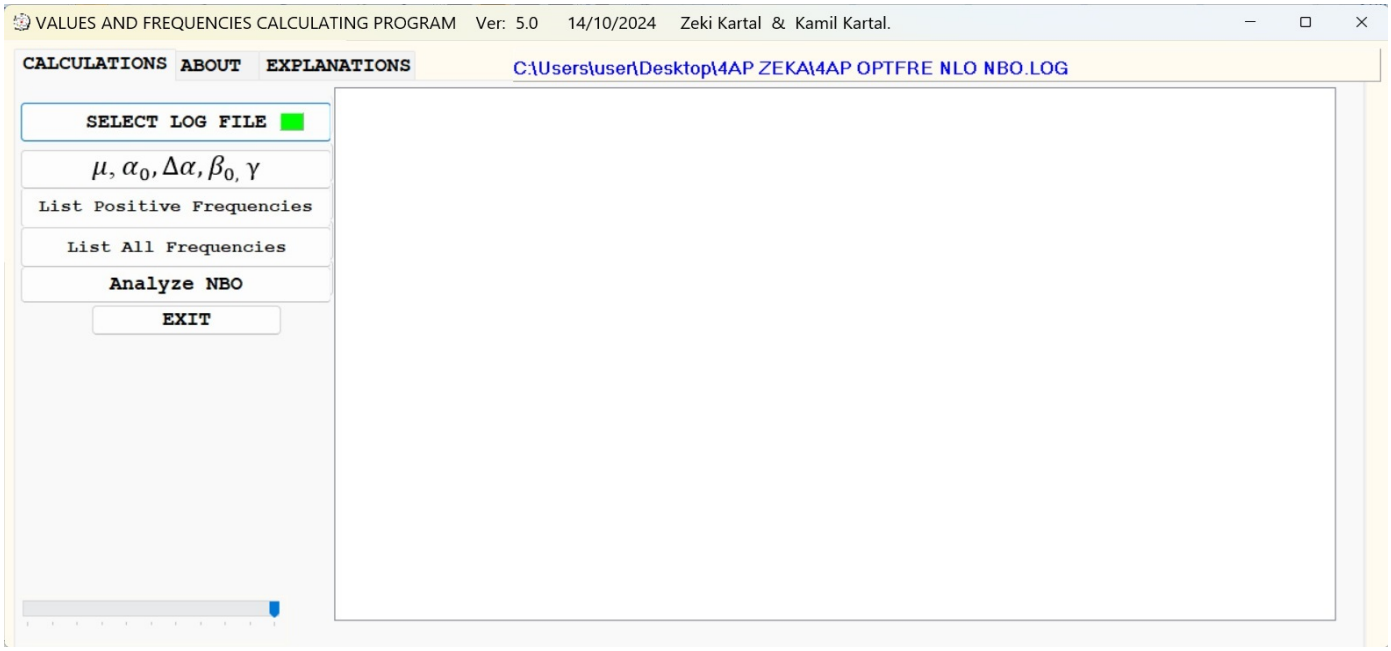

Fig. 3. View of the ZEKA utility after selecting the relevant log file.

3.1. Calculating the NLO values of a compound.

The ZEKA utility automatically displays in a window on the screen, at the moment a button is pressed for any task, the total number of lines in the relevant log file, the start and end times of the operation, the time taken to perform the operation and the number of operations performed.

When you ask the ZEKA utility to calculate the NLO values of the compound you are interested in (that is, when you touch the

button on which the μ, α_0, Δα, β_0 and γ values are written), the ZEKA utility lists the values calculated for all steps using the data in the log file of the relevant compound. Which of the values listed by the ZEKA utility will be taken will be found with the help of the values in the chk file of the relevant compound. When the relevant compound's chk file is opened in GaussView, the dipole moment value in the "Gaussian Calculation Summary" section of the "Results" tab seen in GaussView and the matching dipole moment value calculated by the ZEKA utility are found. The calculated values in the step where the matching dipole moment value is found are the correct values sought. Another benefit of these ranked values is that they help us understand how some of the properties of the compound change as its energy changes.

To better understand the use of the ZEKA utility, the calculation procedures for the 4-aminopyridine (4AP) ligand molecule [9,10 and 19,20], which we use in many of our studies, are given as examples in Figures (4-7). The GaussView image of the chk file created by the Gaussian program for the 4AP molecule is given in Fig. 4. Here, the dipole moment value of the 4AP molecule is seen as 4.017742 Debye. This value is found as 4.0177 Debye in the document calculated by the ZEKA utility. When the relative error value resulting from the representation of the relevant dipole moment value with only two different decimal places is calculated, it is seen that the result is 00105%. This result is also at a level that can be neglected within scientific limits. The all values in that step where this dipole moment value is located are the real values sought for the 4AP molecule. As can be seen from Fig. 5, the NLO values of the relevant compound calculated by the ZEKA utility are given in both atomic units (au) and electrostatic units (esu).

Then, the ZEKA utility will ask you to specify a file name to save the results as a docx file into the relevant file (Fig. 5). When you specify the file name, the results will be saved as a docx file into the relevant file. If desired and if the operating system on your computer is suitable, this docx file can be saved too in PDF format with the same name by clicking the PDF button seen under the analysis labels.

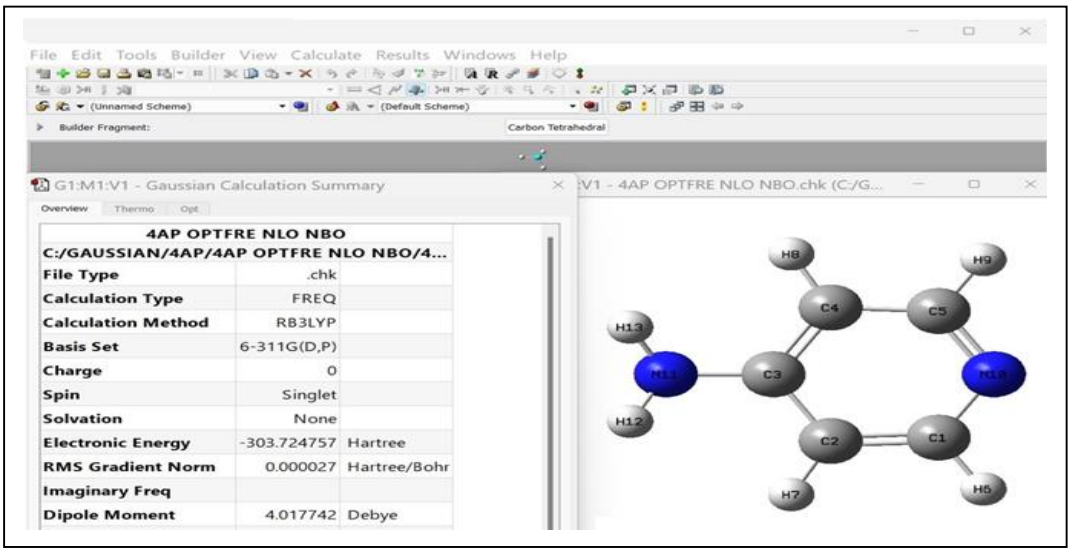

Fig. 4. The image of the chk file created by the Gaussian program for the 4AP molecule in GaussView.

The point that program users should pay attention to here is that the scientific notation of (esu) units is ($\times 10^{-30}$) or similar.

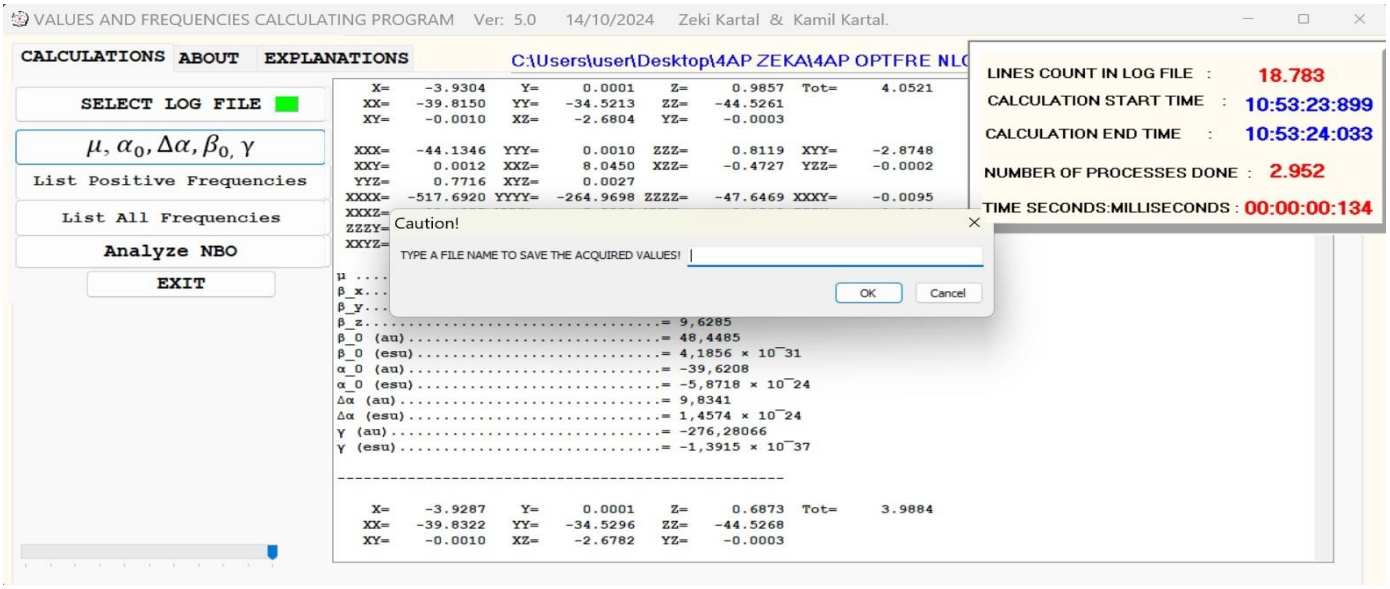

Fig. 5. View of the ZEKA utility after calculating the NLO values of the compound of interest.

The magnetic moment and NLO values obtained by the ZEKA utility for the 4AP molecule using the values in the .log file generated by the Gaussian program are given in Table 1 in terms of both (au) and (esu) values.

Table 1. Magnetic moment and NLO values obtained by the ZEKA utility for the 4AP molecule.

Symbols	In (au) unit	Symbols	In (au) unit	In (esu) unit
μ	4.0177 D	β_0	48.2372	4.1673×10^{-31}
$\boldsymbol{\beta_x}$	-47.432	α_0	-39.6249	-5.8724×10^{-24}
$\boldsymbol{\beta_y}$	0.002	$\Delta\alpha$	9.8302	1.4568×10^{-24}
$\boldsymbol{\beta_z}$	8.7772	γ	-276.33848	-1.3918×10^{-37}

Similar processes will be repeated to perform vibration (IR and Raman) frequencies (Fig. 6) and natural bond analysis (NBO) (Fig. 7) of the same compound.

3.2. Calculating the vibration (IR and Raman) values of a compound.

When some properties of a molecular structure are to be calculated with the Gaussian program, if the molecular structure is not optimized enough or if the appropriate basis set is not selected for the calculation, some vibration frequencies of that molecular structure may take negative values. If desired, only positive frequencies or all frequencies, both positive and negative, of the molecule of interest will be calculated. The calculated vibration frequencies along with the IR intensities and Raman activity values of the relevant molecule are listed by the ZEKA utility from the largest vibration to the smallest (Fig. 6).

When the "List all frequencies" button is used for a molecular structure, the ZEKA utility will warn "No negative frequency values found" if the molecular structure is fully optimized and the appropriate calculation basis set is selected.

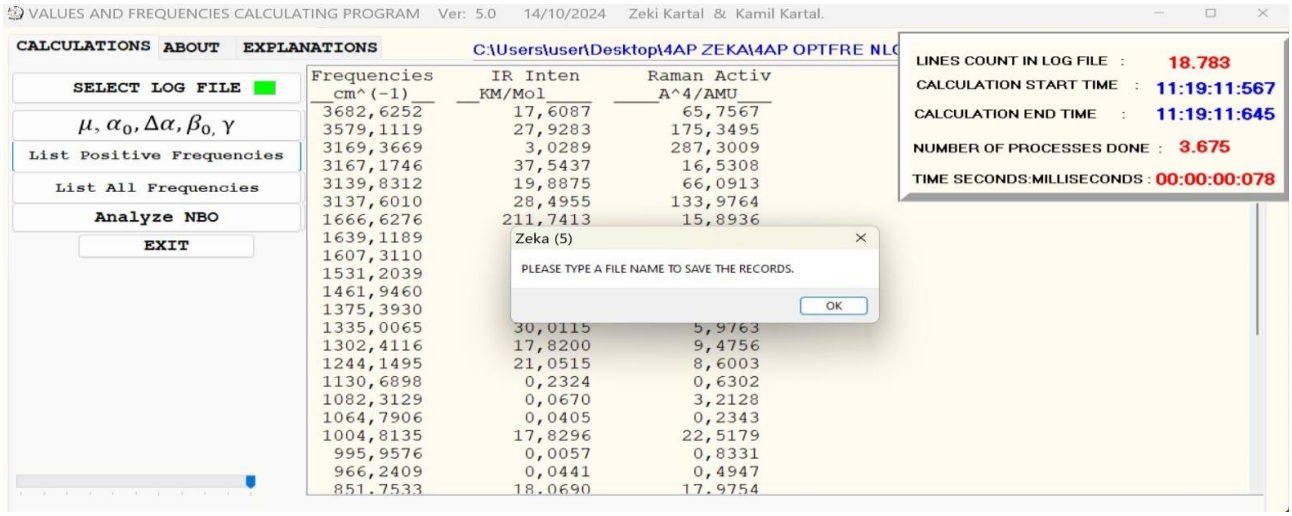

Fig. 6. View of the ZEKA utility after calculating the vibration frequencies of the compound of interest.

The values of vibrational frequencies in the .log file calculated by the Gaussian program were tabulated for the 4AP molecule by the ZEKA utility (see Table 2). In this table, the IR and Raman frequencies (cm^{-1}), IR intensities (KM/Mol) and Raman activities (A^4/AMU) are in units.

Table 2. Table of vibration frequency values arranged by the ZEKA utility for the 4AP molecule. The units of frequencies, IR intensities and Raman activities are (cm^{-1}), (KM/Mol) and (A^4/AMU), respectively.

Frequencies	IR intensities	Raman activities	Frequencies	IR intensities	Raman activities
3682.6252	17.6087	65.7567	1082.3129	0.067	3.2128
3579.1119	27.9283	175.3495	1064.7906	0.0405	0.2343
3169.3669	3.0289	287.3009	1004.8135	17.8296	22.5179
3167.1746	37.5437	16.5308	995.9576	0.0057	0.8331
3139.8312	19.8875	66.0913	966.2409	0.0441	0.4947
3137.601	28.4955	133.9764	851.7533	18.069	17.9754
1666.6276	211.7413	15.8936	840.5563	0.0702	1.3705
1639.1189	95.402	7.7507	822.6253	53.0769	1.8792
3682.6252	17.6087	65.7567	749.6183	0.278	0.1587
3579.1119	27.9283	175.3495	684.7527	0.0531	5.2105
1607.311	31.7898	0.6878	544.8463	18.3842	1.3007
1531.2039	34.6126	4.0246	532.0932	6.9096	5.932
1461.946	11.8774	1.6015	473.2431	324.8051	2.0192
1375.393	0.1127	1.232	394.8566	0.0092	0.0173
1335.0065	30.0115	5.9763	384.3669	0.5189	1.0215
1302.4116	17.82	9.4756	356.4313	14.245	0.6391
1244.1495	21.0515	8.6003	218.2846	1.5046	0.2216
1130.6898	0.2324	0.6302			

3.3. Calculating the NBO values of a compound.

The magnitude of the interaction energy between electron donor and electron acceptor parts in a molecular structure indicates the intensity of the interaction in that structure and is shown with the symbol $E^{(2)}$. The Gaussian program calculates the transitions of a compound separately for each different part of that compound. In the NBO analysis of a compound, the ZEKA utility lists all transition values of that compound from largest to smallest according to the $E^{(2)}$ energy value (Fig. 7). By taking the desired parts from this table, the parts that need to be drawn attention to in the study can be further emphasized.

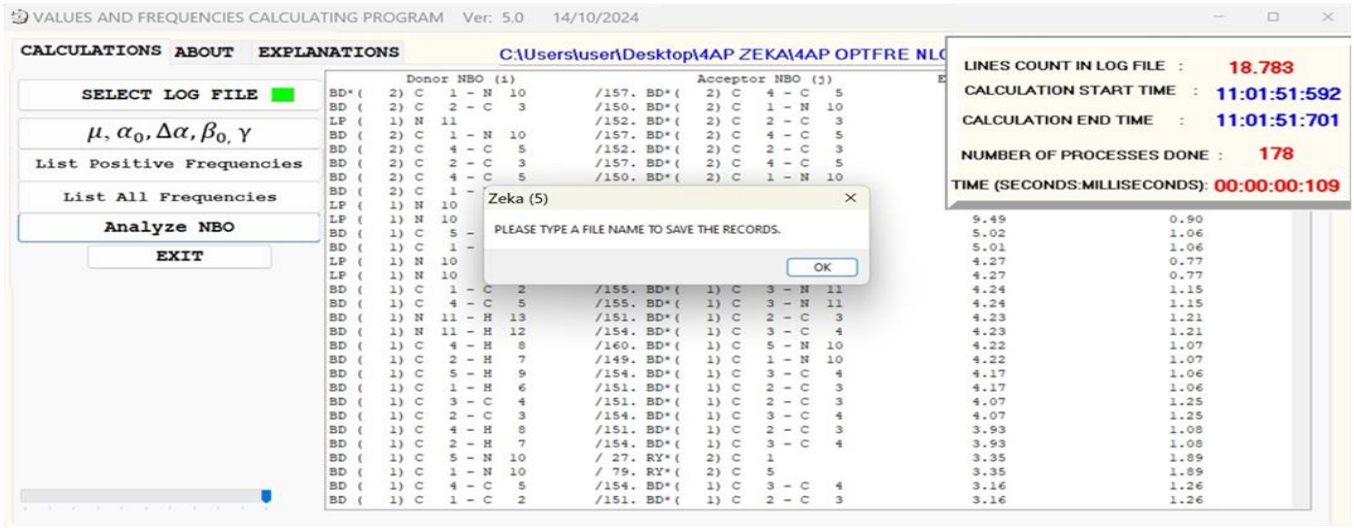

Fig. 7. View of the ZEKA utility after performing the NBO analysis of the compound of interest.

Both the results of the vibration frequencies and the NBO analysis were recorded in Excel table format by the ZEKA utility for easier conversion into tables by users. There are a total of 174 NBO transitions with different stabilization energies [$E^{(2)}$] calculated by the Gaussian program for the 4AP ligand molecule. The first ten NBO analysis results of the 4AP ligand molecule are listed in Table 3, sorted from largest to smallest, for the purpose of example.

Table 3. Ranking of the first ten values of the stabilization energy of the 4AP molecule by the ZEKA utility from largest to smallest.

Donor NBO(i)	Acceptor NBO(j)	$E^{(2)}$ [a] kcal/mol	E(j)-E(i) [b] (a.u.)	F(i,j) [c] (a.u.)
BD* (2) [d] C1 - N10	BD*(2) C4 - C5	221.43	0.01	0.08
BD (2) C2 - C3	BD*(2) C1 - N10	32.87	0.27	0.085
LP (1) N11	BD*(2) C2 - C3	32.45	0.32	0.096
BD (2) C1 - N10	BD*(2) C4 - C5	29.53	0.32	0.087
BD (2) C4 - C5	BD*(2) C2 - C3	24.93	0.28	0.077
BD (2) C2 - C3	BD*(2) C4 - C5	13.98	0.29	0.058
BD (2) C4 - C5	BD*(2) C1 - N10	13.12	0.27	0.055
BD (2) C1 - N10	BD*(2) C2 - C3	11.47	0.31	0.055
LP (1) N10	BD*(1) C4 - C5	9.49	0.9	0.084
LP (1) N10	BD*(1) C1 - C2	9.49	0.9	0.084

[a] $E^{(2)}$: stabilization energy, [b] Energy difference between i and j NBO orbitals, [c] F(i,j) is the Fock matrix elements, [d] (*) indicates anti-bonding, LP (A) is a valence lone pair orbital.

The accuracy and consistency of the all results obtained by the ZEKA utility have been confirmed by repeated calculations of the same results at different times by us and other people.

If it assumes that 30 minutes are required for each calculation step, it is seen that the time that should be spent on this part of an average article is approximately three or four hours. This situation shows how important the ZEKA utility is for a researcher in terms of using time effectively.

4. Conclusions

The biggest deficiency of people or groups doing scientific research is that they cannot spend enough time on the subjects they are working on. Because there are many research subjects today and the number of these subjects is increasing at a dizzying pace every day. In this case, researchers spend their valuable and limited time on subjects that can be solved in other ways. These expenditures are a great loss for the future of science. The ZEKA utility was prepared to save time for researchers working on molecular mechanics calculations theoretically or experimentally so that they can use it on new research topics. A problem can be solved by a human. The time required for this is a few hours. The same problem can be solved by ZEKA utility. The time required for this is a few hundred milliseconds (ms). When the times spent by humans and the ZEKA utility to solve the same problem are compared with each other, the importance of using the ZEKA utility becomes apparently. In future versions of the ZEKA utility, it is planned to add some properties obtained from the HOMO and LUMO states of the relevant compounds, some values of their thermochemical properties, and examinations of UV-visible region and NMR spectroscopic values. In addition, studies will be

carried out to make the program more functional in line with the suggestions or new requests of the researchers who use this ZEKA utility program.

Researchers who want to use the ZEKA utility can contact via e-mail and use it after completing the necessary procedures. Valuable researchers who use the ZEKA utility are requested to cite this article as a reference.

Acknowledgement

As the authors, we would like to express our greatest gratitude to our parents and all our teachers who provided us with this opportunity to deliver the ZEKA utility to the users.

Author contribution statement

The authors contributed equally to the preparation of this article.
Zeki Kartal: Research, Writing–review and editing, original draft.
Kamil Kartal: Research, program design, program creation, and program development.

References

[1] D. C. Young, *Computational Chemistry*. Wiley-Interscience, 2001, Appendix A. A.3.1 pp. 341, AMPAC, doi: 10.1002/0471220655.app1.

[2] S. J. Clark *et al.*, "First principles methods using CASTEP," *Z. Kristallog.*, vol. 220, no. 5-6, pp. 567-570, 2005, doi: 10.1524/zkri.220.5.567.65075.

[3] R. Dovesi *et al*., "Quantum-mechanical condensed matter simulations with crystal," *WIREs Comput. Mol. Sci.*, vol. 8, no. 4, 2018, doi: 10.1002/wcms.1360.

[4] G. M. J. Barca *et al*., "Recent developments in the general atomic and molecular electronic structure system," *J. Chem. Phys.*, vol. 152, no. 15, pp. 154102, 2020, doi: 10.1063/5.0005188.

[5] M. J. Frisch *et al.*, Gaussian 03 Revision D.01. Gaussian. Inc., Wallingford CT (2004).

[6] J. J. Stewart, "MOPAC: A semiempirical molecular orbital program." *J. Comput. Aided Mol. Des.*, vol. 4. no. 1, pp. 1-105, 1990, doi:10.1007/BF00128336.

[7] A. García *et al*., "Siesta: Recent developments and applications." *J. Chem. Phys.* vol. 152, no. 20, 2020. 204108, doi:10.1063/5.0005077.

[8] D. C. Young, *Computational Chemistry*, Wiley-Interscience, 2001, Appendix A. A. 1.6 pp 330, Spartan, doi: 10.1002/0471220655.app1.

[9] Z. Kartal and O. Şahin, "Synthesis. X-ray crystallography characterization and DFT theoretical studies of a new metal compound $[CdCl_2(4\text{-aminopyridine})_2]_n$," *J. Mol. Struct.*, vol. 1243, 2020, 130720, doi:10.1016/j.molstruc.2021.130720.

[10] Z. Kartal and O. Şahin, "Synthesis of two Hofmann type and Hofmann-type-like compounds in crystal form from 4-aminopyridine and their characterizations by various methods," *J. Mol. Struct.*, vol. 1252, 2022, 132088, doi: 10.1016/j.molstruc.2021.132088.

[11] Z. Kartal and Z. S. Şahin, "Synthesis and characterization of two new Hofmann-Type-Like compounds from some alkali metal atoms and glycine anhydride," *JOTCSA*, vol. 11, no. 1, pp. 125-36, 2024, doi: 10.18596/jotcsa.1368425.

[12] Z. Kartal and Z. S. Şahin, "Crystal structure and Hirshfeld surface analysis of a heterometallic Hofmann-type-like compound," *Sinop Univ. J. Nat. Sci.*, vol. 9, no. 1, pp. 72-95, 2024, doi: 10.33484/sinopfbd.1370598.

[13] D. A. Kleinman, "Nonlinear Dielectric Polarization in Optical Media," *Phys. Rev.*, vol. 126, no. 6, pp. 1977-1979, 1962, doi: 10.1103/PhysRev.126.1977.

[14] H. A. Kurtz D. S. Dudis, "Quantum Mechanical Methods for Predicting Nonlinear Optical Properties," *Reviews in Computational Chemistry*, vol. 12, K. B. Lipkowitz. D. B. Boyd. Ed., New York. USA: VCH Publishers, 1998, pp 241-279.

[15] M. G. Vivas D. L. da Silva, C. R. Mendonca, L. De Boni, "Chapter 8 - First-order hyperpolarizability of organic molecules: hyper-Rayleigh scattering and applications." *Molecular and Laser Spectroscopy*. V.P. Gupta. Yukihiro Ozaki. Ed., Elsevier, 2020, pp. 275-314, doi: 10.1016/B978-0-12-818870-5.00008-3.

[16] Ö. Tamer *et al*., "First and second order hyperpolarizabilities of flavonol derivatives: A density functional theory study," *Spectrochim. Acta. Part A*, 283, 2022, 121728, doi: 10.1016/j.saa.2022.121728.

[17] A. B. Ahmed, H. Feki, Y. Abid, H. Boughzala, A. Mlayah, "Structural. vibrational and theoretical studies of l-histidine bromide," *J. Mol. Struct.*, vol. 888, no. (1-3), pp. 180–186, 2008, doi:10.1016/j.molstruc.2007.11.056.

[18] M. Nakano *et al*., "Second hyperpolarizability (gamma) of singlet diradical system: dependence of gamma on the diradical character," *J Phys Chem A*., vol. 109, no. 5, pp. 885-891, 2005, doi:10.1021/jp046322x.

[19] Z. Kartal and O. Şahin, "Synthesis, spectroscopic, thermal, crystal structure properties and characterization of new Hofmann-type-like clathrates with 4-aminopyridine and water," *Turk. J. Chem.*, vol. 45, no. 3, pp. 616–633, 2021, doi:10.3906/ kim-2011-29.

[20] Z. Kartal and O. Şahin, "The synthesis of heteroleptic cyanometallate aminopyridine complexes and an investigation into their structural properties with various spectroscopic methods." *J. Mol. Struct.*, 2021, 1227, 129514, doi:10.1016/j.molstruc.2020.129514.

Contents lists available at *Dergipark*

Journal of Scientific Reports-A

journal homepage: *https://dergipark.org.tr/tr/pub/jsr-a*

E-ISSN: 2687-6167 ***Number 61, June 2025***

RESEARCH ARTICLE

Receive Date: 24.12.2024 *Accepted Date: 21.03.2025*

Cost optimization in microgrids: A scenario-based analysis by using polar the fox optimization algorithm

Nisa NACAR ÇIKAN [a*]

[a] *Çukurova University, Department of Electrical and Electronics Engineering, Adana, 01330, Türkiye*
ORCID:0000-0002-9641-4616

Abstract

Microgrids have come up as a promising solution for ensuring efficient, reliable, and sustainable energy management through the distributed energy resources integration. However, some challenges such as integration of distributed generators, economic efficacy and operational constraints cause the management and operation of microgrids remain as a complex problem. In this work, a comprehensive analysis is realized by using the Polar Fox Optimization algorithm to find solutions to these problems. Four different scenarios are analyzed to examine the effects of operational constraints on system performance and economic costs. In the first case, all distributed energy resources are operated within the specified limits and all power from renewable sources is injected into the microgrid. This scenario results in an operating cost of 269.76 €/day. In the second case, the output power of the renewable distributed energy sources is optimized. This case, a cost reduction of 42.5% is obtained when compared to the first scenario. In the third case, the energy exchange constraint between the grid and the microgrid is removed. Thus, a cost reduction of 74.7% is obtained when compared to the first case. In the fourth case, a detailed battery energy storage system model is added by considering technical parameters such as battery efficiency, state-of-charge limits, and charge/discharge rates. This case an operating cost of €107.08/day is obtained. Thus, a cost reduction of 60.3% is obtained when compared to the first case. The results show that changing the operational constraints significantly affects both system performance and economic efficiency. The proposed approach presents valuable perception for microgrid operators and planners. It points out the importance of the optimization algorithm in achieving economically efficient and reliable energy management.

Keywords: Microgrid optimization; Energy management; Renewable integration; Battery storage systems; Grid exchange; Operational constraints

[*] Corresponding author. Tel.: +90-0322-338-6868 Ext: 124
E-mail address: ncikan@cu.edu.tr

1. Introduction

Microgrids (MGs) integrate various distributed energy resources (DERs) to provide reliable, efficient, and sustainable energy solutions. These systems typically consist of distributed generators (DGs) such as photovoltaic (PV) panels, wind turbines (WT), and energy storage systems like batteries, capacitors, and controllable loads [1-3]. These systems offer efficient, reliable, and environmentally friendly solutions for energy management with the integration of renewable DGs [4]. MGs operate in both islanded mode and grid-connected mode unlike traditional centralized power grids. In grid-connected mode, MGs can exchange power with the main grid to optimize energy costs and stability. In islanded mode, they can independently supply power to critical loads during grid outages or in remote areas without grid access [5]. These operations make MGs a key component of modern energy infrastructure in areas with limited grid access. The renewable energy sources (RES) penetration in MGs not only reduces greenhouse gas emissions but also mitigates the dependency on fossil fuels. Furthermore, MGs show a pivotal duty in modern energy infrastructure by supporting the intermittent renewable energy sources integration, improving energy efficiency, and providing backup power during emergencies. For instance, the Santa Rita Jail microgrid in California includes solar PV, fuel cells, and battery storage. Thus, it provides uninterrupted power supply during grid failures and reduces energy costs [6]. Another example is the Bornholm Island microgrid in Denmark. It ensures over 50% of the island's energy demand by wind power and other RES [7]. These examples show the importance of MGs in addressing contemporary energy challenges. It also highlights the need for advanced energy management strategies to optimize the MGs performance.

Previous studies on MGs are mainly focused on energy optimization, control strategies, and economic analysis. Energy optimization techniques aim to minimize operational costs while meeting energy demand. Control strategies focus on maintaining system stability and reliability [8]. Economic analyses evaluate the cost-effectiveness of MGs and their potential for reducing energy expenses [8]. There are many studies in the literature investigating the effective operation of MGs [9-11]. These studies are used different optimization methodologies and considered different cases to find the optimal operating range. Optimization methods are analyzed as deterministic and non-deterministic (metaheuristic) approaches [12,13]. Deterministic methods rely on mathematical models and require a continuous, differentiable objective function along with its gradient information to guide the search process. These methods are efficient for problems where such functions are available, offering fast convergence and high accuracy. However, many real-world engineering and scientific problems involve complex, non-linear, or discontinuous objective functions, making deterministic approaches less applicable. This limitation has led to the development of non-deterministic methods, which do not require gradient information and are better suited for handling complex, multi-modal, and high-dimensional optimization problems [13]. Non-deterministic methods, particularly metaheuristic algorithms, are inspired by natural phenomena and employ probabilistic rules to explore the search space. These algorithms can be further classified into several categories based on their inspiration sources. Evolutionary algorithms imitates the principles of natural selection and evolution. Swarm intelligence algorithms simulate the collective behavior of animal groups. Social-based methods, including Teaching-Learning-Based Optimization (TLBO), model human learning and social interactions, while physics-based methods, such as Simulated Annealing (SA) and Gravitational Search Algorithm (GSA), are inspired by physical laws. Each of these methods has unique and different advantages. For instance, swarm-based algorithms show success in exploration. Evolutionary methods are effective in balancing exploration and exploitation. Thus, the algorithm should be chosen depending on the problem. This is provided comprehensive research on improving the performance and adaptability of metaheuristic algorithms [13].

For an effective energy operation management (EOM) in MGs, different novel algorithms have been implemented in recent years. It is tried to find out which algorithm provides the most effective solution to the applied problem. In [14], different metaheuristic algorithms applied to MGs. The study revealed the increasing need for renewable energy

sources. The study also discussed the problems arising from the intermittent energy supply of DGs and their impact on cost analysis. This review paper also emphasizes the importance of metaheuristic algorithms applied to find optimal solutions for the economic operation of MGs and, in fact, sets the direction for future research. In [15], a cost analysis is performed by solving the sizing problem in MGs using PSO algorithm. In the paper, different PSO-based models are considered to see the effectiveness of the algorithm in cost analysis. The impact of these models on energy management, economic dispatch and unit commitment is analyzed. In [16], the application of a dynamic cost penalty is analyzed by taking into account the cost function in case of any battery degradation in the EOM. PSO algorithm was used in the study and savings of up to 44.50% were achieved. In [17], battery energy storage system (BESS)'s optimal size is determined by taking into account the uncertainties due to market prices, load demand, and DGs, and it is also aimed to minimize the grid cost by reducing it. The study employs the 2m point estimate method for uncertainty modeling and uses Whale Optimization Algorithm and Swine Influenza Model Based Optimization with Quarantine (SIMBO-Q) for cost reduction. The results show that incorporating BESS at an optimal size significantly reduces the MG's operation cost.

Early approaches to MG optimization primarily relied on conventional numerical techniques, including interior-point methods, linear programming, quadratic programming, nonlinear programming, and dynamic programming [18]. These classical methods are effective for finding solutions to optimization problems. These are characterized by continuous variables, and differentiable, low dimensionality, single objectives, or simple constraints. Nevertheless, as MG optimization problems have grown in complexity featuring high dimensionality, large-scale systems, multi-objective requirements, mixed constraints, and multiple control variables. These traditional techniques have proven inadequate or require significant preprocessing to yield results. Moreover, they struggle to address dynamic or robust optimization challenges. In contrast, meta-heuristic methods, which are inspired by social adaptation processes or natural selection, employ a combination of random and local search strategies. Metaheuristic algorithms have been widely applied to various engineering problems, demonstrating their versatility and effectiveness in solving complex optimization tasks [12,13,19-24]. Unlike classical techniques, meta-heuristic approaches are less prone to becoming trapped in local optima, do not rely on specific problem structures or domains, and demonstrate strong adaptability to diverse environments and problem types. They are capable of providing effective solutions in most scenarios [18, 25-26]. Additionally, meta-heuristic methods can dynamically adjust algorithm parameters and encoding precision during the optimization process, making them suitable for solving dynamic optimization problems [18,27]. They also find solutions for discontinuous, non-convex, and multi-objective optimization tasks. As a result, meta-heuristic methods show significant performance in solving complex MG management problems [18, 28-29]. In [30], microgrid contains photovoltaic, wind, and fuel cell generation along with energy storage devices. This method utilizes the 2m point estimate method (PEM) to solve uncertainties by applying self-adaptive gravitational search algorithm (SGSA). The study aims to optimize the operational costs of the microgrid by considering uncertainties in market prices, load demand, and the generated power by DGs. In this work, Polar Fox Optimization (PFO) algorithm is used for the optimal operation of microgrids [31]. A metaheuristic approach is chosen due to its flexibility and ability to handle the non-linear and complex problems. The algorithm shows a balance between exploration and exploitation which is critical for achieving optimal solutions. This research proposes a detailed BESS model. Unlike previous studies, technical parameters such as battery efficiency, state of charge limits, and charging/discharging rates are considered. Furthermore, the study systematically evaluates the impact of different operational constraints and control strategies through four progressive scenarios: (1) a baseline scenario where all distributed generation units are operational, and the full power output from renewable sources (PV and WT) must be injected into the grid; (2) The scenario in which the power generated from DGs is optimally injected into the grid in accordance with the objective function (there is no obligation to supply all the generated energy to the grid); (3) a scenario removing power exchange limitations with the main grid (utility) to evaluate the impact of MG constraints on system economics; and (4) a scenario incorporating detailed battery storage characteristics and constraints into the optimization framework. In summary, this study investigates four different scenarios. In comparison with previous studies (cases 1-3), improvements have been made numerically in terms of cost and reliability. The main contribution of the study is presented in Case 4. By adding a

detailed BESS model, more realistic optimization results have been achieved. The inclusion of BESS constraints in the optimization with a realistic approach has proven its importance for grid operation. The proposed approach not only enhances the economic efficiency of microgrids but also provides a robust solution for managing complex operational constraints, making a significant advancement in the field of microgrid energy management.

Section 2 introduces the problem formulation; section 3 outlines the algorithm used in the paper. In Section 4, simulation results are presented and discussed. Furthermore, 4 different scenarios are presented to show the impact of the PFO algorithm on the cost minimization problem. The last section is the conclusion.

2. Formulation part

The studied MG system consists of multiple DERs and operates in a grid-connected mode at a voltage level of 400V. The primary goal of the MG is to optimize energy dispatch and cost minimization while ensuring reliable power supply to different types of consumers. The parameters are as follows:

- The system includes DGs such as microturbines (MT), PV, fuel cells (FC), and WT.
- A BESS is integrated into the MG to manage load fluctuations and store excess renewable energy.
- The MG can import and export electricity from the utility depending on market prices and operational constraints.

Figure 1 shows the MGs architecture.

In this section, cost is chosen as the objective function. The mathematical formulas are presented for minimization of the total operating cost. The constraints for system reliability and stability are also provided. Additionally, mathematical models for each DG are presented.

2.1. Objective function

The objective function of this study is the minimization of the total operational cost. For this purpose, the generation units and storage systems must be operated optimally within a certain period. The minimum cost function formula is shown in Eq. 1[32].

$$\min_{q}(\text{Cost}) = \min_{q} \sum_{t=1}^{T_{\text{Horizon}}} \text{Cost}(q^t, r^t) = \min_{q} \sum_{t=1}^{T_{\text{Horizon}}} \sum_{i=1}^{N_{DG}} [f_{DG}(P_{Gi}^t) + \lambda_t . P_{\text{Grid}}^t] \quad (1)$$

where p^t is the vector of control variables at time t. It includes the active power outputs of the storage units and generation. This can be written as in Eq. 2.

$$q^t = \left[P_{G1}^t, P_{G2}^t, \dots, P_{GN_G}^t\right] \quad (2)$$

Additionally, r^t denotes the amount of active power exchanged with the utility at time t. It is shown in Eq. 3.

$$r^t = P_{\text{Grid}}^t \quad (3)$$

Here, T_{Horizon} is the time intervals in the optimization period. N_{DG} demonstrated the number of DGs. P_{Gi}^t is active power output of the i-th DG unit at time t. $f_{DG}(P_{Gi}^t)$ is the cost associated with the power generation of the i-th unit. P_{Grid}^t is the power exchanged with the utility at time t. λ_t shows the market price of electricity. The function $f_{DG}(P_{Gi}^t)$ is typically nonlinear, reflecting the complex nature of generation cost functions. The term $\lambda_t . P_{\text{Grid}}^t$ represents the economic cost of purchasing or selling electricity with the utility at time t.

The objective function in Eq. 1 is inherently nonlinear. Specifically, $f_{DG}(P_{Gi}^t)$ shows the complex nature of

generation cost functions. It includes quadratic terms (e.g.,$c(P_{Gi}^{t})^2$) or other nonlinear components. Additionally, the cost associated with power exchange with the grid (λ_t. P_{Grid}^{t}) introduces a piecewise linear component. These nonlinearities are resulted from the complex interactions between generation units, storage systems, and grid exchange.

2.2. Operational constraints

The optimal operation of the microgrid system must satisfy various technical and operational constraints to ensure reliable and stable performance. These constraints include power balance requirements, generation limits of distributed energy resources, energy storage system limitations, and grid power exchange boundaries. The following constraints are considered in the optimization framework for secure and efficient operation of the microgrid.

2.2.1. Micro turbine

The operational constraints of the microturbine are defined by Eq. 4.
Power output limits:

$$P_{MT,min} \leq P_{MT} \leq P_{MT,max} \tag{4}$$

where $P_{MT,min}$ and $P_{MT,max}$ represent the minimum and maximum power outputs respectively. As specified in Table 1, the MT operates within a power range of 6-30 kW with an associated cost coefficient of 0.457 €/kWh. The dynamic operation of MT must respect these power limits while maintaining system stability and meeting demand requirements. These constraints ensure that the MT operates within its technical capabilities while providing reliable power output for microgrid operation.
RD_{MT} and RU_{MT}, is given Eq. 5, represent the ramp-down and ramp-up rates respectively, and t denotes the time interval.

$$-RD_{MT} \leq P_{MT}^{(t)} - P_{MT}^{t-1} \leq RU_{MT} \tag{5}$$

2.2.2. Pem Fuel Cell

Power output limits:

$$P_{FC,min} \leq P_{FC} \leq P_{FC,max} \tag{6}$$

Ramp rate constraints:

$$-RD_{FC} \leq P_{FC}^{t} - P_{FC}^{t-1} \leq RU_{FC} \tag{7}$$

where $P_{FC,min}$ and $P_{FC,max}$ are the minimum and maximum power outputs (3-30 kW in the current study) RD_{FC} and RU_{FC} represent ramp-down and ramp-up rates respectively, as shown in Eq. 6. The dynamic operation of the fuel cell is constrained by its ramp rates as expressed in Eq. 7, where t denotes the time interval.

2.2.3. Energy storage system

The BESS power output is constrained by its rated capacity as shown in Eq. 8, where P_{rated} represents the maximum charging/discharging power capability (±30 kW).
Power limits:

$$-P_{Rated} \leq P_b(t) \leq P_{rated} \quad (8)$$

The state of charge must be maintained within operational limits as defined in Eq. 9, where SoC_{min} and SoC_{max} are set to 20% and 90% respectively to protect battery life and ensure reliable operation. For initialization purposes, the initial state of charge ($SoC_{initial}$) is defined as 50% of the total capacity.
State of charge limits:

$$SoC_{min} \leq SoC(t) \leq SoC_{max} \quad (9)$$

2.2.4. Photovoltaic panels

The power output of the PV system is bounded by the constraints expressed in Eq. 10, where the lower bound represents zero output during periods of no solar irradiance, and $P_{PV,max}$ represents the maximum power output capacity of 25 kW. This constraint ensures that the PV generation remains within its physical limitations while accounting for the intermittent nature of solar resources. Note that the actual power output at any time t depends on the available solar irradiance and ambient temperature conditions but cannot exceed the rated capacity defined in Eq. 10.
Power output limits:

$$0 \leq P_{PV}(t) \leq P_{PV,max} \quad (10)$$

where $P_{PV,max}$ is equal 25 kW (rated capacity) in this study.

2.2.5. Utility

The power exchange between the microgrid and utility grid is subject to constraints as defined in Eq. 11, where $P_{grid,min}$ and $P_{grid,max}$ are set to -30 kW and +30 kW respectively for Case-1 and Case-2. The negative value indicates power export to the utility grid, while positive value represents power import from the utility grid. It should be noted that in Cases 3-4, these power exchange limitations are removed, allowing unrestricted power transactions with the main grid. This constraint plays a crucial role in determining the optimal operation strategy and overall system economics, particularly during periods of high price differentials or significant renewable generation fluctuations.
Power exchange limits for Case-1 and Case-2:

$$-30\,\text{kW} \leq P_{grid}(t) \leq 30\,\text{kW} \quad (11)$$

The limitation specified in Eq.11 is not taken into account in case 3 and case 4. The constraints in the optimization model include both linear and nonlinear components. The power exchange constraint (Eq. 11) is linear, as it defines a simple range for power import/export between the microgrid and the utility grid. However, the battery storage system constraints (Eqs. 8, 9, and 18) introduce nonlinearity due to the inclusion of charging/discharging efficiencies (η_{charge} and $\eta_{discharge}$) and the state of charge dynamics (SoC(t)). These nonlinear constraints significantly affect the overall

structure of the optimization problem, making it more complex and requiring advanced optimization techniques for effective solution.

2.3. DG's model

The MG studied in this study includes DGs such as PV and WT, generators such as MT and FC, and energy storage systems. Each DG unit needs to be properly modeled to operate optimally. In this section, mathematical models of operational characteristics and constraints of DGs are presented.

2.3.1. Micro turbine

Microturbines are tiny gas turbines that can creates both heat and electricity. Their electrical output ranges from about 25-250 kW. The reasons why microturbines are preferred in MGs include their high efficiency and low emission release. The MT consists of a compressor, turbine, combustor, and permanent magnet generator operating at high speeds (typically 50,000-120,000 rpm).

I. Cost function

Eq. 12 shows the operational cost calculation of the MT [33]:

$$C_{MT}(P_{MT}) = a + bP_{MT} + c(P_{MT})^2 \quad (12)$$

where P_{MT} is the output power(kW), C_{MT} is the operational cost (€/h), and a, b, c are the cost coefficients.

II. Fuel cost

The calculation of the fuel cost is demonstrated in Eq.13.

$$C_{fuel} = F \times HR \times P_{MT} \quad (13)$$

where F is the fuel price (€/m³), C_{fuel} is the fuel cost (€/kWh), HR is the heat rate (m³/kWh), and P_{MT} is the power output (kW).

III. Operation & maintenance cost

The costs calculation for maintenance and operation are shown in Eq.14.

$$C_{O\&M} = K_{O\&M} \times P_{MT} \quad (14)$$

where $K_{O\&M}$ is the O&M coefficient (€/kWh) and $C_{O\&M}$ is the O&M cost (€/kWh).

IV. Start-up/Shut-down Cost

Eq. 15 shows the cost calculation for Start-up/shut-down.

$$\frac{C_{SU}}{SD} = \frac{K_{SU}}{SD} \times \frac{N_{SU}}{SD} \quad (15)$$

where the $\frac{N_{SU}}{SD}$ is the number of start-ups/shut-downs events and the $\frac{K_{SU}}{SD}$ is the start-up/shut-down cost coefficient.

V. Total bid calculation:

Eq. 16 shows the total bid calculation.

$$\mathrm{Bid_{MT}} = (\mathrm{C_{fuel}} + \mathrm{C_{O\&M}}) \times (1 + \mathrm{P_{margin}}) \quad (16)$$

Here, $\mathrm{P_{margin}}$ is the profit margin (typically taken as 10-20%).

In order to optimally price MTs, analysis of many components is required. The main one among these components is the fuel cost. This cost is calculated by multiplication of the heat rate, fuel price and power output of the MT unit. The production of the heat rate (m^3/kWh), fuel price(€/m^3), and the MT power output (kW) give the fuel cost in terms of €/h. Another component is the operation and maintenance (O&M) cost, which takes into account component wear, routine maintenance, and so on. Shutdown and start-up costs are important, especially in high-cycle operations. Especially in frequent cycle operations, the closing and start-up costs are important. The cost here is obtained by multiplying the closing/start-up coefficients by the number of cycles. In the final price offer, all costs are added and formulated by adding a profit margin, usually between 10% and 20%.

In this study, considering the local market conditions and the operational characteristics of the MT system and taking all costs into account, it was determined as 0.457 €/kWh.

2.3.2. Pem fuel cell

Proton exchange membrane fuel cells (PEM FC) directly and efficiently convert chemical energy stored in fuel into electrical energy. In MG applications, PEMFCs offer several advantages including high efficiency, quick start-up capability, and environmental benefits due to zero emissions during operation. PEMFCs typically operate at low temperatures (60-80°C) which makes them suitable for power generation applications.

The cost of the PEM FCs can be calculated as in Eq. 17.

$$\mathrm{C_{FC}}(\mathrm{P_{FC}}) = \alpha_{\mathrm{FC}} + \beta_{\mathrm{FC}} \times \mathrm{P_{FC}} + \gamma_{\mathrm{FC}} \times (\mathrm{P_{FC}})^2 \quad (17)$$

Here, $\mathrm{P_{FC}}$ is the power output (kW), $\mathrm{C_{FC}}$is the operational cost (€/h), α_{FC}, β_{FC}, γ_{FC} are the cost coefficients.

In this work, the cost of PEMFC is determined as 0.294 €/kWh. This price is lower than the MT price, indicating that PEMFCs operate at high efficiency and low operating costs. This cost advantage makes PEMFC an economically attractive option for MG operations, particularly during periods of high energy demand or when renewable sources are unavailable.

2.3.3. Energy storage systems

The BESS plays an important role in MG operation by providing power balance, peak shaving capabilities, and economic optimization through energy arbitrage. In this study, a NiMH battery system is implemented with a rated power capacity of 30 kW and energy capacity of 400 kWh, enabling efficient energy management and grid support functionalities.

I. Mathematical model:

The state of charge (SoC) dynamics can be expressed as [34]:

$$\mathrm{SoC(t)} = \mathrm{SoC(t-1)} + \left(\eta_{\mathrm{charge}}.\mathrm{P_{charge}(t)} - \frac{\mathrm{P_{discharge}(t)}}{\eta_{\mathrm{discharge}}}\right)\left(\frac{\Delta \mathrm{t}}{\mathrm{C_b}}\right) \quad (18)$$

where SoC(t) is the state of charge at time t, η_{charge} and $\eta_{\mathrm{discharge}}$ are charging and discharging efficiencies (95% and 92% respectively). $\mathrm{P_{charge}(t)}$ and $\mathrm{P_{discharge}(t)}$ represent charging and discharging power, $C_b$is the battery capacity (400 kWh), and $\Delta \mathrm{t}$ is the time interval.

II. Cost function:

The operational cost of BESS is shown in Eq. 19.

$$C_{BESS} = C_{deg} \times |P_b(t)| + C_{O\&M} \quad (19)$$

Here, $C_{O\&M}$ is operation and maintenance cost and C_{deg} indicates the degradation cost. The total bid cost is set at 0.38 €/kWh. Here, the total cost is determined as 0.38 €/kWh. BESS works bidirectionally, allowing both injection and absorption of power. Thus, it responds more flexibly to the changing load demands of the MG and the changing price signals accordingly.

2.3.4. Photovoltaic panels

PVs are an important renewal DG in MGs. They convert solar radiation directly into electrical energy through semiconductor materials. The power output produced depends entirely on solar radiation. In this work, the PV system has a rated capacity of 25 kW, with its actual power output varying throughout the day based on solar radiation intensity.

I. Mathematical model:

The PV output power can be calculated as in Eq. 20.

$$P_{PV}(t) = \eta_{PV} \times A \times G(t) \times \left(1 - \beta(T_c(t) - T_{ref})\right) \quad (20)$$

where η_{PV} is the overall system efficiency, A is the total area of PV panels (m²), G(t) is the solar irradiance (kW/m²), β is the temperature coefficient (%/°C), $T_c(t)$ is the cell temperature, and T_{ref} is the reference temperature (25°C)

II. The generation cost structure includes:

$$C_{PV} = \frac{C_{capital}}{N} + C_{O\&M} \quad (21)$$

where $C_{capital}$ is the annualized capital cost, N is the number of operational hours per year, $C_{O\&M}$ represents operation and maintenance costs. The total bid cost is set at 2.584 €/kWh.

The PV system's output exhibits daily and seasonal variations, with peak generation occurring around 13:00 hours in the current study, reaching approximately 23.9 kW. Despite having no fuel costs, the relatively high bid price reflects the capital investment and maintenance requirements. The system's intermittent nature necessitates coordination with other microgrid components, particularly the battery storage system and conventional generators, to ensure reliable power supply. The optimization algorithm considers both mandatory full power injection (Case-1) and flexible power injection (Cases 2-4) scenarios, allowing for comprehensive evaluation of different operational strategies while maintaining system stability and economic efficiency.

2.3.5. Utility

The microgrid maintains continuous power exchange with the main grid (utility), enabling both power import during high demand or low local generation periods and power export during excess generation. The bidirectional power flow is governed by economic and technical constraints.

Given the nonlinearity of the objective function and the presence of nonlinear constraints, the proposed optimization problem is classified as a nonlinear optimization model. Although the problem is solved using a metaheuristic algorithm (Polar Fox Optimization), the mathematical structure of the problem remains nonlinear due to the quadratic cost terms of distributed generation units and the efficiency-based constraints of the battery storage system. This classification is essential for understanding the complexity of the problem and the need for advanced optimization techniques to achieve an effective solution.

I. Mathematical model:

The power exchange with utility can be expressed as [1,35]:

$$P_{grid}(t) = P_{load}(t) - [P_{MT}(t) + P_{FC}(t) + P_{PV}(t) + P_{WT}(t) \pm P_{BAT}(t)] \quad (22)$$

where $P_{grid}(t) > 0$ represents power import from utility, $P_{grid}(t) < 0$ represents power export to utility.

II. Cost/Revenue Function:

$$C_{grid}(t) = P_{grid}(t) \times B_{grid}(t) \quad (23)$$

Here, $C_{grid}(t) > 0$ denotes the cost (import), $B_{grid}(t)$ is the time-varying utility bid price, and $C_{grid}(t) < 0$ indicates the revenue (export).

Utility bid cost varies according to the peak hours of the day. For example, it is 0.12 €/kWh in the early morning hours, while it becomes 4.00 €/kWh during the peak hours, which include the 10:00-14:00 period. The change here once again shows the importance and necessity of the optimization study. During peak hours, it maximizes power export by using all the DERs available in the MG. During low-price periods, it imports power for consumption and battery charging. Thus, this bidirectional change is important in cost function optimization studies.

3. Polar fox optimization algorithm

PFO is a metaheuristic algorithm inspired by hunting behaviours and movements of arctic foxes [31]. In the PFO algorithm, a group of "arctic foxes" explore a solution space to find the global optimum of the objective function. The location of each fox is represented as a vector in the solution space, represented as $X_i = [x_{i1}, x_{i2}, \dots, x_{id}]$, where i refers to the fox index and d represents the dimension of the problem. The PFO algorithm uses two main strategies for movement: global exploration (random movement) and local exploitation (interactions between individuals). The algorithm employs two main strategies for movement: a global exploration strategy (simulating random movement) and a local exploitation strategy (based on interactions between individuals). Mathematically, the position of each fox is updated iteratively using the Eq. 24.

$$X_i^{new} = X_i^{old} + \alpha.(X_{best} - X_i) + \beta.(X_{rand} - X_i) \quad (24)$$

where, X_{best} is the best-known solution (global best), X_{rand} is a randomly selected fox, α and β are scaling factors that control the exploration and exploitation behaviors, X_i^{new} and X_i^{old} are the updated and previous positions of the fox, respectively. These movements allow the foxes to converge towards the optimal solution, balancing exploration, and exploitation throughout the search process. The PFO algorithm has been shown to effectively solve complex and nonlinear problems, outperforming many traditional optimization methods in terms of both accuracy and convergence speed.

4. Simulation results

The structure of the proposed system for optimal operation of microgrids is shown in Figure 1. The test system is a typical low-voltage microgrid containing DGs including a fuel cell (FC), micro-turbine (MT), WT, and PV. Additionally, the system includes a battery as an energy storage unit. The microgrid operates in grid-connected mode at 400V level and serves three different load zones (industrial, commercial, and residential). The technical specifications and cost data of the generation units in the system are presented in Tables 1 and 2. The minimum-maximum generation capacities and operating costs (€/kWh) of each unit are specified. The battery system has a ±30 kW power capacity and can perform charging/discharging operations. Power exchange with the main grid is also limited to ±30 kW. Figure 2 shows the load demand, PV and WT generation, and grid price variations during the 24-hour operation period of the system. The load demand varies between 50-90 kW throughout the day. While PV generation reaches its peak value of approximately 24 kW at 13:00 due to maximum solar radiation intensity, WT generation shows variability depending on wind speed. Grid electricity prices remain particularly high during peak hours (between 9:00-16:00). In light of this data, minimum-cost generation planning has been performed for optimal MG operation under different scenarios. The operation strategy has been developed considering the technical constraints of all units and system reliability. The suggested approach aims to minimize the total operating cost while maintaining power balance and satisfying various operational constraints such as generation limits, battery storage characteristics, and grid exchange limitations.

The mathematical formulation and detailed analysis of different operational scenarios will be presented in the following sections to show the proposed optimization technique's effectiveness in achieving economical and reliable microgrid operation. In this study, four different operational scenarios are investigated to analyse the optimal operation management of the microgrid system:

- Case-1 represents the baseline scenario where all distributed generation units are operational, and the full power output from renewable sources (PV and WT) must be injected into the grid. This case serves as a reference point for comparing other operational strategies.
- Case-2 maintains the same system configuration as Case-1 but introduces flexibility in renewable power integration. Instead of mandatory full power injection, PV and WT outputs are treated as optimization variables, allowing the system to determine the optimal level of renewable power utilization.
- Case-3 extends Case-2 by removing the power exchange limitations with the main grid. While Case-1 and Case-2 operate under strict grid power exchange constraints (±30 kW), this case allows unrestricted power exchange to evaluate the impact of grid constraints on system economics.
- Case-4 builds upon Case-3 by incorporating detailed battery storage characteristics into the optimization framework. This scenario considers technical parameters such as battery efficiency, state of charge limits, and charging/discharging rates to provide a more realistic assessment of storage system integration.

Through these progressive scenarios, it is aimed to systematically evaluate the impact of different operational constraints and control strategies on microgrid performance and economic efficiency. This framework helps identify the most effective operational strategy considering various technical and economic factors affecting microgrid operation.

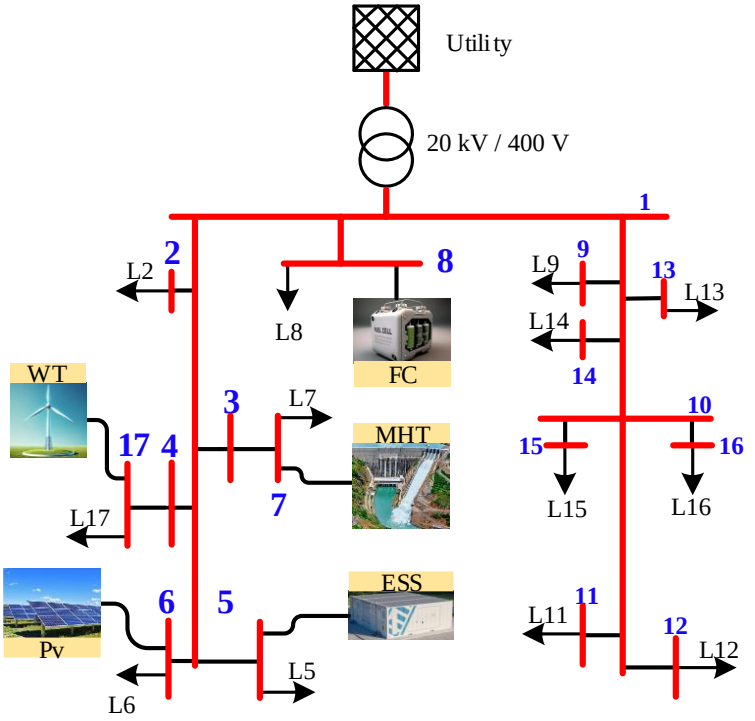

Fig. 1. Single-line diagram of the proposed low-voltage microgrid with distributed generation units [36]

Table 1. Power output limitations and cost parameters of generation units [1]

ID	Generator Type	Min Power Generation [kW]	Max Power Generation [kW]	Bid (€/kWh)
1	Battery	-30	30	0.380
2	PEM FC	3.0	30	0.294
3	PV	0.0	25	2.584
4	WT	0.0	15	1.073
5	MT	6.0	30	0.457
6	Utility	-30	30	In Table (2) Column (5)

Table 2. Technical specifications of distributed generation units in the microgrid [1,35,36]

Hour	Photovoltaic [kW]	Wind Turbine [kW]	Load [kW]	Utility (€/kWh)
1	0.0000	1.7850	52.000	0.2300
2	0.0000	1.7850	50.000	0.1900
3	0.0000	1.7850	50.000	0.1400

4	0.0000	1.7850	51.000	0.1200
5	0.0000	1.7850	56.000	0.1200
6	0.0000	0.9150	63.000	0.2000
7	0.0000	1.7850	70.000	0.2300
8	0.2000	1.3050	75.000	0.3800
9	3.7500	1.7850	76.000	1.5000
10	7.5250	3.0900	80.000	4.0000
11	10.4500	8.7750	78.000	4.0000
12	11.9500	10.4100	74.000	4.0000
13	23.9000	3.9150	72.000	1.5000
14	21.0500	2.3700	72.000	4.0000
15	7.8750	1.7850	76.000	2.0000
16	4.2250	1.3050	80.000	1.9500
17	0.5500	1.7850	85.000	0.6000
18	0.0000	1.7850	88.000	0.4100
19	0.0000	1.3020	90.000	0.3500
20	0.0000	1.7850	87.000	0.4300
21	0.0000	1.3005	78.000	1.1700
22	0.0000	1.3005	71.000	0.5400
23	0.0000	0.9150	65.000	0.3000
24	0.0000	0.6150	56.000	0.2600

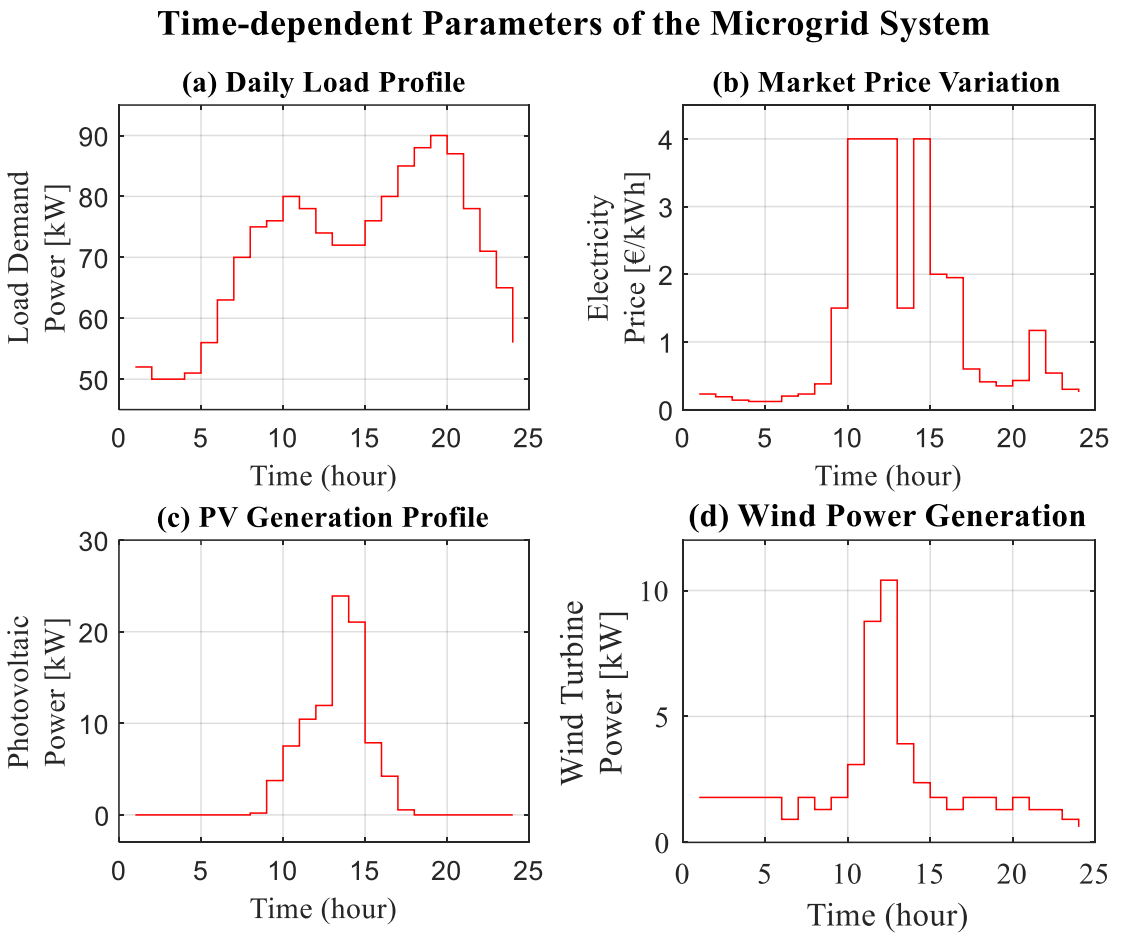

Fig. 2. Time-dependent parameters of the microgrid over 24 hours: (a) Load demand, (b) Grid electricity prices (c) PV power availability and, (d) WT power availability.

4.1. Case-1: system operation under complete renewable power injection

The performance analysis of Case-1, where all DG units are operational and full power from PV and WT is injected into the grid, is presented in Table 3 and Figure 3. The results demonstrate several key operational characteristics over the 24-hour period, revealing distinct patterns in different time intervals.

During early morning hours (00:00-06:00), the system operates under low grid prices ranging from 0.12 to 0.23 €/kWh. In this period, the battery system operates in charging mode, storing energy between -11.7 to -17.7 kW. Simultaneously, both MT and FC maintain their minimum output levels of 6 kW and 30 kW respectively, responding to the combination of low demand and prices.

The operational strategy undergoes a significant shift during peak hours (09:00-14:00) when grid prices surge to 4.0 €/kWh. During these hours, the MT outputs maximum capacity, while the battery goes into maximum discharge mode. MG efficiently exports excess power to the grid and reaches up to -30 kW. This shows that the stored energy is used efficiently during peak hours. Renewable DGs contribute at different rates throughout the day. For example, PV generation reaches its maximum level at 23.9 kW around 13:00, while WT produces between 0.61-10.41 kW. By

applying the PFO algorithm to the optimization problem, the system is operated stably. During the evening hours (17:00-21:00), the power demand in the system increases. However, during the same hours, there is a decrease in the power production of renewable DGs. Therefore, the grid is supported by the power provided by MT, FC and battery during the evening hours.

The total operating cost for Case-1 is calculated as 269.76 €/day. This baseline scenario effectively demonstrates system operation under full renewable power injection constraints, showcasing successful coordination between dispatchable units (MT, FC), storage system, and grid exchanges while minimizing operational costs and meeting demand requirements. The effectiveness of this operational strategy can be further evaluated through comparison with subsequent cases to assess potential improvements in operational efficiency and cost reduction.

Table 3. Hourly optimal dispatch results and operational costs for Case-1 with full renewable power integration

Time Hour	Fuel Cell [kW]	Micro Turbine [kW]	Wind Turbine [kW]	PV [kW]	Utility (€/kWh)	Cost (€/kWh)	Energy Storage [kW]
1	30.0000	6.0000	1.7850	0.0000	30.0000	14.3790	-15.7850
2	30.0000	6.0000	1.7850	0.0000	30.0000	12.4190	-17.7850
3	30.0000	6.0000	1.7850	0.0000	30.0000	10.9190	-17.7850
4	30.0000	6.0000	1.7850	0.0000	30.0000	10.6990	-16.7850
5	30.0000	6.0000	1.7850	0.0000	30.0000	12.5990	-11.7850
6	30.0000	6.0000	0.9150	0.0000	30.0000	17.0561	-3.9150
7	30.0000	6.0000	1.7850	0.0000	30.0000	21.2190	2.2150
8	30.0000	6.0000	1.3050	0.2000	10.3031	27.7272	27.1919
9	30.0000	30.0000	1.7850	3.7500	-19.5350	16.2328	30.0000
10	30.0000	30.0000	3.0900	7.5250	-20.6150	-25.7698	30.0000
11	30.0000	28.7750	8.7750	10.4500	-30.0000	-50.2115	30.0000
12	30.0000	21.6400	10.4100	11.9500	-30.0000	-47.8418	30.0000
13	30.0000	14.1850	3.9150	23.9000	-30.0000	47.6609	30.0000
14	30.0000	18.5800	2.3700	21.0500	-30.0000	-34.3527	30.0000
15	30.0000	30.0000	1.7850	7.8750	-23.6600	8.8743	30.0000
16	30.0000	30.0000	1.3050	4.2250	-15.5300	15.9642	30.0000
17	30.0000	30.0000	1.7850	0.5500	-7.3350	32.8655	30.0000
18	30.0000	6.0000	1.7850	0.0000	20.2150	33.1655	30.0000
19	30.0000	6.0000	1.3020	0.0000	30.0000	32.0843	22.6980
20	30.0000	6.0000	1.7850	0.0000	19.2150	33.1398	30.0000
21	30.0000	30.0000	1.3005	0.0000	-13.3005	19.7639	30.0000
22	30.0000	30.0000	1.3005	0.0000	-20.3005	24.3632	30.0000
23	30.0000	6.0000	0.9150	0.0000	30.0000	20.8161	-1.9150
24	30.0000	6.0000	0.6150	0.0000	30.0000	15.9882	-10.6150
---	---	---	---	---	**Total Cost:**	**269.7599**	---

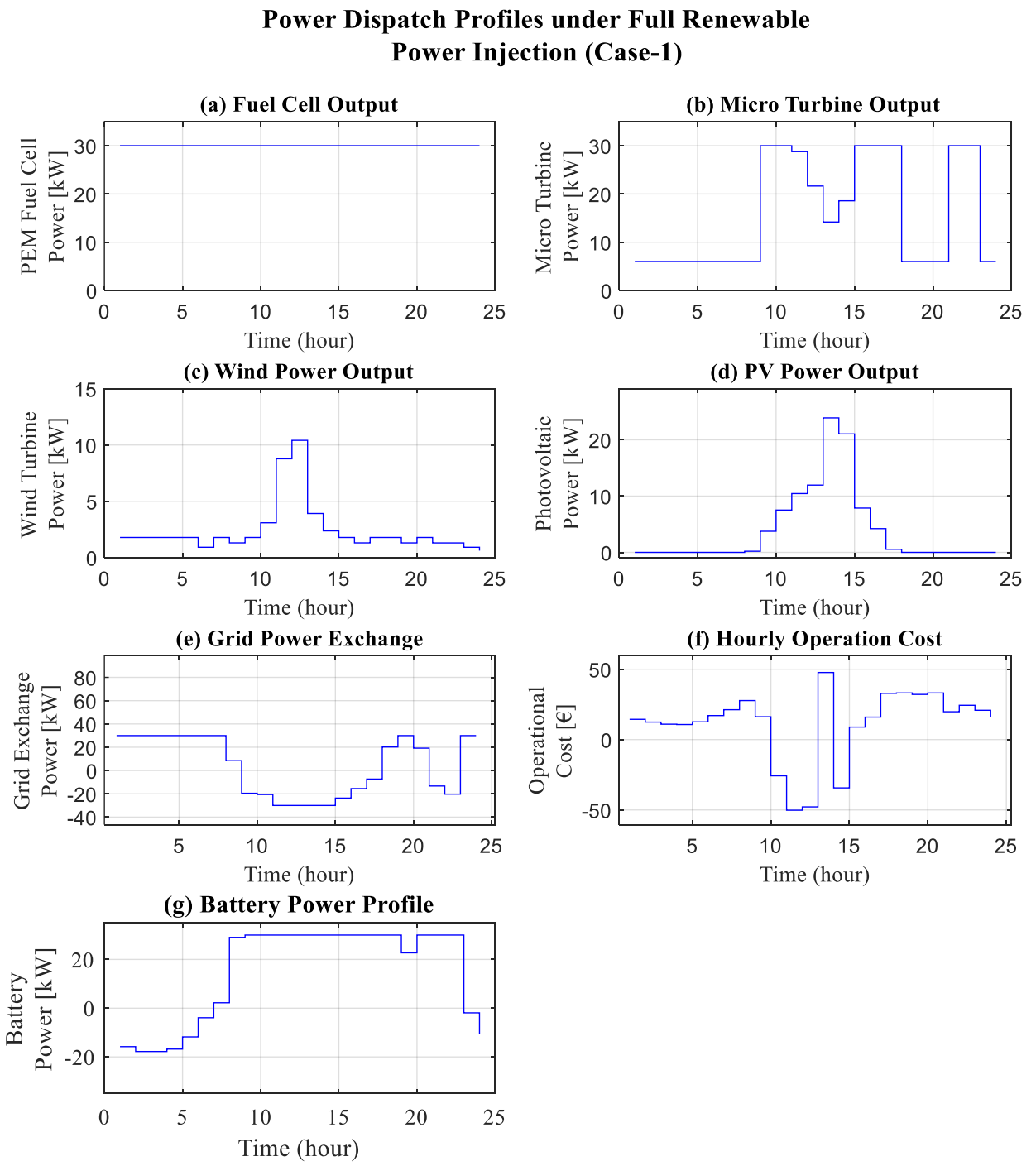

Fig. 3. Power dispatch profiles and system performance under full renewable injection (Case-1: Generation unit outputs a-FC, b-MT, c-WT, d-PV, e-Grid exchange power, f-Hourly operational cost, and g-Battery power.)

4.2. Case-2: operational optimization with controllable renewable integration

In this study, Case-2 examines the operational optimization where renewable power (PV and WT) injection is considered as a decision variable, unlike Case-1 where complete injection of renewable generation was mandatory. The optimization results, presented in Table 4 and Figure 4, reveal several significant findings.

The total operational cost decreased to 155.01 €/day, representing a substantial 42.5% reduction compared to Case-1 (269.76 €/day). This remarkable improvement demonstrates the advantages of flexible renewable power integration. During low-price periods (00:00-07:00), the optimization strategy-maintained MT and FC at their minimum outputs (6 kW and 30 kW respectively) while completely curtailing PV and WT generation. Throughout this period, the battery operated in charging mode with values ranging from -3 to -16 kW, storing energy for high-price periods.

During peak price hours (09:00-14:00), the system implemented various strategies to maximize economic benefits. These strategies included operating MT and FC at full capacity (30 kW each), selectively utilizing renewable generation (e.g., 7.52 kW from PV and 3.09 kW from WT at 10:00), maintaining battery discharge at maximum capacity (30 kW), and exporting power to the grid when profitable.

In the evening period (17:00-22:00), the system coordinated battery discharge and conventional generation (MT, FC) in a balanced manner to minimize grid power import during moderate price periods. This case study demonstrates that optimal scheduling of renewable power injection can significantly enhance economic performance while maintaining system stability and meeting demand requirements. The results clearly indicate that allowing flexibility in renewable power integration can lead to more cost-effective operation of the microgrid system.

Table 4. Optimal dispatch results for Case-2: flexible renewable power integration strategy

Time Hour	Fuel Cell [kW]	Micro Turbine [kW]	Wind Turbine [kW]	PV [kW]	Utility (€/kWh)	Cost (€/kWh)	Energy Storage [kW]
1	30.0000	6.0000	0.0000	0.0000	30.0000	13.1420	-14.0000
2	30.0000	6.0000	0.0000	0.0000	30.0000	11.1820	-16.0000
3	30.0000	6.0000	0.0000	0.0000	30.0000	9.6820	-16.0000
4	30.0000	6.0000	0.0000	0.0000	30.0000	9.4620	-15.0000
5	30.0000	6.0000	0.0000	0.0000	30.0000	11.3620	-10.0000
6	30.0000	6.0000	0.0000	0.0000	30.0000	16.4220	-3.0000
7	30.0000	6.0000	0.0000	0.0000	30.0000	19.9820	4.0000
8	30.0000	6.0000	0.0000	0.0000	9.3328	26.3820	29.6672
9	30.0000	30.0000	1.7850	0.0500	-15.7850	12.1678	30.0000
10	30.0000	30.0000	3.0900	7.5250	-20.6150	-25.7698	30.0000
11	30.0000	30.0000	8.7750	9.2250	-30.0000	-52.8170	30.0000
12	30.0000	30.0000	10.4100	3.5900	-30.0000	-65.6235	30.0000
13	30.0000	30.0000	3.9150	0.0000	-21.9150	5.2583	30.0000
14	30.0000	30.0000	2.3700	9.6300	-30.0000	-58.6431	30.0000
15	30.0000	30.0000	1.7850	7.8750	-15.7850	4.2753	30.0000
16	30.0000	30.0000	1.3050	4.2250	-11.3050	13.2855	30.0000
17	30.0000	30.0000	0.0000	0.5500	-5.0000	30.9300	30.0000
18	30.0000	6.0000	0.0000	0.0000	22.0000	31.9820	30.0000
19	30.0000	6.0000	0.0000	0.0000	30.0000	31.1820	24.0000
20	30.0000	6.0000	0.0000	0.0000	21.0000	31.9920	30.0000

21	30.0000	30.0000	1.3005	0.0000	-13.3005	19.7639	30.0000
22	30.0000	30.0000	0.0000	0.0000	-19.0000	23.6700	30.0000
23	30.0000	6.0000	0.0000	0.0000	30.0000	20.1820	-1.0000
24	30.0000	6.0000	0.0000	0.0000	30.0000	15.5620	-10.0000
---	---	---	---	---	**Total Cost:**	**155.0133**	---

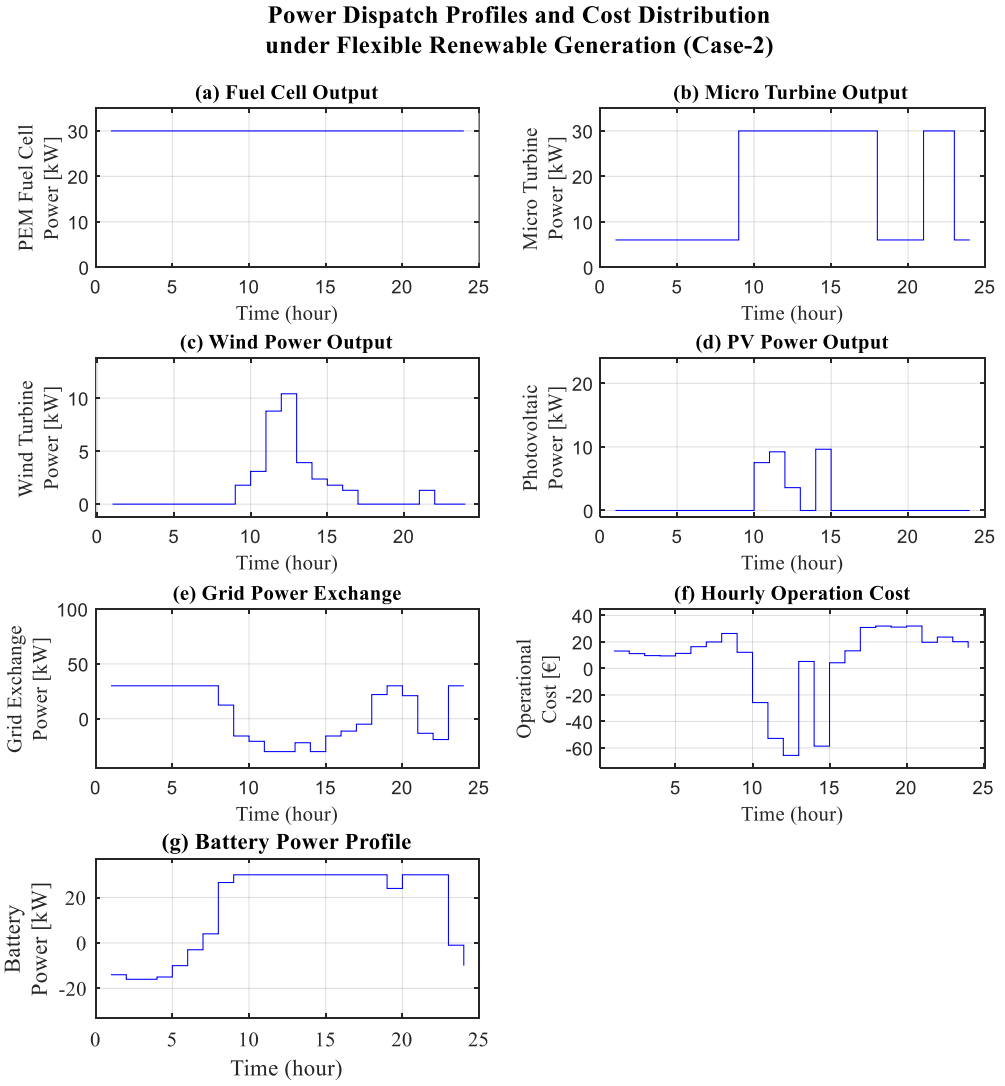

Fig. 4. Optimal power dispatch profiles and cost distribution under flexible renewable generation control (Case-2: Generation unit outputs a-FC, b-MT, c-WT, d-PV, e-Grid exchange power, f-Hourly operational cost, and g-Battery power.)

4.3. Case-3: unrestricted grid exchange with flexible renewable integration

This study examines the impact of removing grid power exchange limitations while maintaining flexible renewable

power integration. The results, presented in Table 5 and Figure 5, demonstrate significant improvements in system economics and operational flexibility. The total operational cost decreased to 68.18 €/day, representing a substantial reduction of 74.7% and 56.0% compared to Case-1 (269.76 €/day) and Case-2 (155.01 €/day), respectively. This remarkable cost reduction highlights the significant economic impact of grid exchange constraints on microgrid operation. During low-price periods (00:00-07:00), the optimization strategy exhibited distinct characteristics. The MT and FC operated at minimum outputs (6 kW and 3 kW respectively), while renewable generation was completely curtailed. The battery maintained maximum charging rate (-30 kW), and significant power import from the grid (up to 91 kW) was utilized to meet demand when prices were low. The peak price period (09:00-14:00) demonstrated aggressive economic optimization through several strategies. These included maximum utilization of all DG units, strategic deployment of renewable resources (e.g., 11.95 kW from PV and 10.41 kW from WT at 12:00), battery discharging at maximum capacity (30 kW), and substantial power export to grid (up to -41.42 kW at 14:00) to capitalize on high prices. Evening operations (17:00-24:00) revealed dynamic switching between import and export modes based on price signals, with grid exchange power varying from -19 kW to 84 kW, demonstrating the benefits of unrestricted grid interaction. The results clearly indicate that removing grid exchange limitations enables more aggressive economic optimization, although practical implementation would require careful consideration of grid stability and infrastructure capabilities. This case effectively illustrates how grid exchange constraints significantly impact the economic efficiency of microgrid operations, where the ability to freely exchange power with the main grid enables the system to better capitalize on price differentials and optimize resource utilization.

Table 5. Optimization results for Case-3: unrestricted grid exchange with flexible renewable integration

Time	Fuel Cell	Micro Turbine	Wind Turbine	PV	Utility	Cost	Energy Storage
Hour	[kW]	[kW]	[kW]	[kW]	(€/kWh)	(€/kWh)	[kW]
1	3.0000	6.0000	0.0000	0.0000	73.0000	9.0140	-30.0000
2	3.0000	6.0000	0.0000	0.0000	71.0000	5.7140	-30.0000
3	3.0000	6.0000	0.0000	0.0000	71.0000	2.1640	-30.0000
4	3.0000	6.0000	0.0000	0.0000	72.0000	0.8640	-30.0000
5	3.0000	6.0000	0.0000	0.0000	77.0000	1.4640	-30.0000
6	3.0000	6.0000	0.0000	0.0000	84.0000	9.0240	-30.0000
7	3.0000	6.0000	0.0000	0.0000	91.0000	13.1540	-30.0000
8	30.0000	6.0000	0.0000	0.0000	22.6887	26.3820	16.3113
9	30.0000	30.0000	1.7850	0.0000	-15.7850	12.1678	30.0000
10	30.0000	30.0000	3.0900	7.5250	-20.6150	-25.7698	30.0000
11	30.0000	30.0000	8.7750	10.4500	-31.2250	-54.5516	30.0000
12	30.0000	30.0000	10.4100	11.9500	-38.3600	-77.4613	30.0000
13	30.0000	30.0000	3.9150	0.0000	-21.9150	5.2583	30.0000
14	30.0000	30.0000	2.3700	21.0500	-41.4200	-74.8138	30.0000
15	30.0000	30.0000	1.7850	0.0000	-15.7850	4.2753	30.0000
16	30.0000	30.0000	1.3050	0.0000	-11.3050	13.2855	30.0000
17	30.0000	30.0000	0.0000	0.0000	-5.0000	30.9300	30.0000
18	30.0000	6.0000	0.0000	0.0000	22.0000	31.9820	30.0000
19	30.0000	6.0000	0.0000	0.0000	84.0000	29.5620	-30.0000
20	30.0000	6.0000	0.0000	0.0000	21.0000	31.9920	30.0000
21	30.0000	30.0000	1.3005	0.0000	-13.3005	19.7639	30.0000

22	30.0000	30.0000	0.0000	0.0000	-19.0000	23.6700	30.0000
23	30.0000	6.0000	0.0000	0.0000	59.0000	17.8620	-30.0000
24	3.0000	6.0000	0.0000	0.0000	77.0000	12.2440	-30.0000
---	---	---	---	---	**Total Cost:**	**68.17626**	---

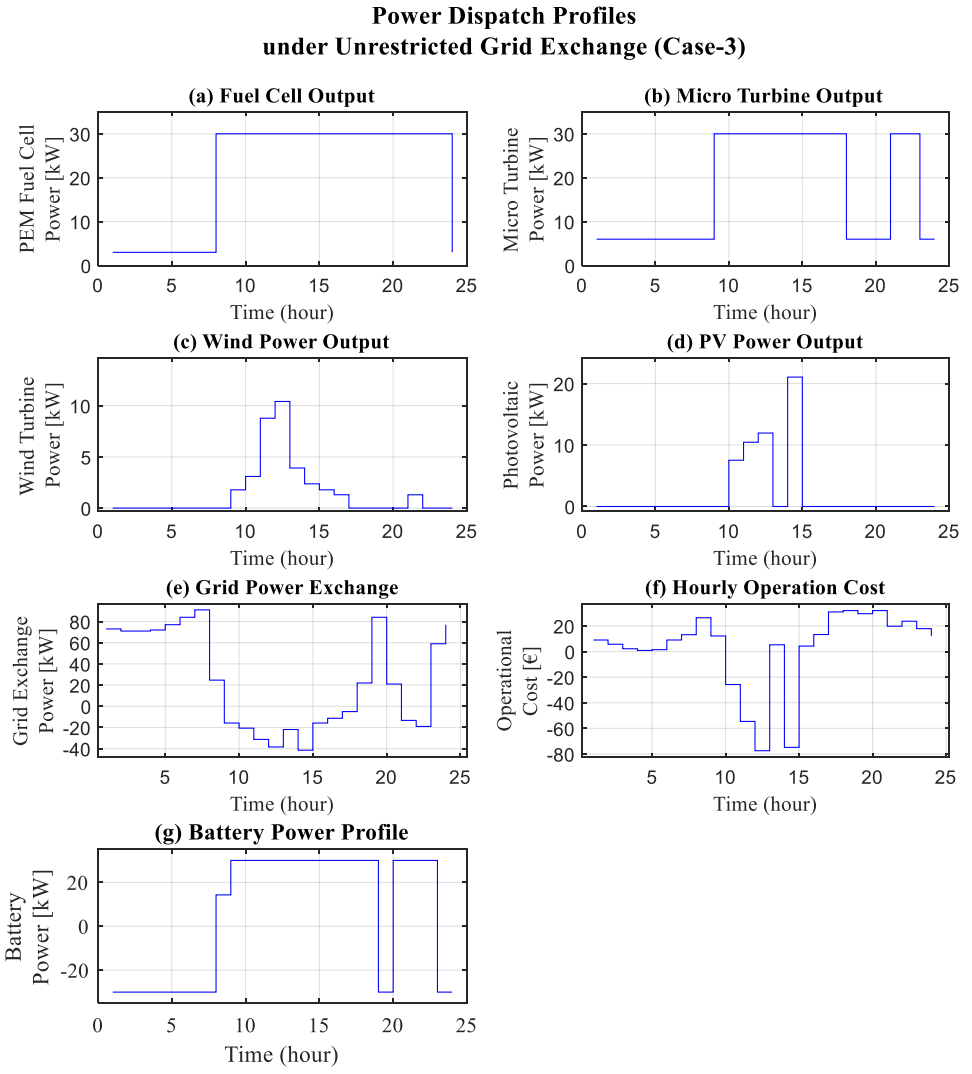

Fig. 5. Power dispatch profiles and economic performance under unrestricted grid exchange conditions (Case-3: Generation unit outputs a-FC, b-MT, c-WT, d-PV, e-Grid exchange power, f-Hourly operational cost, and g-Battery power.)

4.4. Case-4: analysis of microgrid operation with detailed battery energy storage system model

This case study incorporates a detailed BESS model to achieve more realistic optimization results. The BESS is

characterized using Equations 8, 9, and 18. The implementation of detailed battery constraints while maintaining unrestricted grid exchange reveals several significant operational characteristics.

The optimization results demonstrate that the total operational cost amounts to 107.08 €/day. Although this cost is higher than Case-3 (68.18 €/day), it represents a more realistic operational scenario and still achieves substantial cost reductions compared to Cases 1 and 2. This cost differential primarily stems from the incorporation of practical battery constraints, including efficiency losses and state of charge limitations. Analysis of the early morning period (00:00-05:00) demonstrates an optimization strategy focused on leveraging low electricity prices. During these hours, the battery system operates at maximum charging capacity (-30 kW), while distributed generation units maintain minimal output levels with MT and FC operating at 6 kW and 3 kW respectively. This period is characterized by significant grid power imports, serving both the load demand and battery charging requirements efficiently. The system behaviour during peak price periods (09:00-14:00) exhibits sophisticated optimization characteristics. The distributed generation units operate at full capacity, with both MT and FC delivering their maximum output of 30 kW. Renewable power sources are strategically deployed based on availability and economic considerations. Battery discharge operations are carefully optimized while respecting efficiency parameters and SoC constraints, complementing the system's ability to export power to the grid during high-price intervals.

Table 6. Optimal dispatch results for Case-4: integration of detailed battery storage constraints with unrestricted grid exchange

Time	Fuel Cell	Micro Turbine	Wind Turbine	PV	Utility	Cost	Energy Storage
Hour	[kW]	[kW]	[kW]	[kW]	(€/kWh)	(€/kWh)	[kW]
1	3.0000	6.0000	0.0000	0.0000	73.0000	9.0140	-30.0000
2	3.0000	6.0000	0.0000	0.0000	71.0000	5.7140	-30.0000
3	3.0000	6.0000	0.0000	0.0000	71.0000	2.1640	-30.0000
4	3.0000	6.0000	0.0000	0.0000	72.0000	0.8640	-30.0000
5	3.0000	6.0000	0.0000	0.0000	77.0000	1.4640	-30.0000
6	3.0000	6.0000	0.0000	0.0000	72.4211	11.1082	-18.4211
7	3.0000	6.0000	0.0000	0.0000	61.0000	17.6540	-0.0000
8	30.0000	6.0000	0.0000	0.0000	39.0000	26.3820	-0.0000
9	30.0000	30.0000	1.7850	0.0000	-15.7850	12.1678	30.0000
10	30.0000	30.0000	3.0900	7.5250	-20.6150	-25.7698	30.0000
11	30.0000	30.0000	8.7750	10.4500	-31.2250	-54.5516	30.0000
12	30.0000	30.0000	10.4100	11.9500	-38.3600	-77.4613	30.0000
13	30.0000	30.0000	3.9150	0.0000	-21.9150	5.2583	30.0000
14	30.0000	30.0000	2.3700	21.0500	-41.4200	-74.8138	30.0000
15	30.0000	30.0000	1.7850	0.0000	-15.7850	4.2753	30.0000
16	30.0000	30.0000	1.3050	0.0000	-11.3050	13.2855	30.0000
17	30.0000	30.0000	0.0000	0.0000	7.4000	33.6580	17.6000
18	30.0000	6.0000	0.0000	0.0000	52.0000	32.8820	-0.0000
19	30.0000	6.0000	0.0000	0.0000	84.0000	29.5620	-30.0000
20	30.0000	6.0000	0.0000	0.0000	24.7800	32.1810	26.2200
21	30.0000	30.0000	1.3005	0.0000	16.6995	43.4639	0.0000
22	30.0000	30.0000	0.0000	0.0000	11.0000	28.4700	0.0000
23	30.0000	6.0000	0.0000	0.0000	59.0000	17.8620	-30.0000

24	3.0000	6.0000	0.0000	0.0000	77.0000	12.2440	-30.0000
---	---	---	---	---	**Total Cost:**	**107.07747**	---

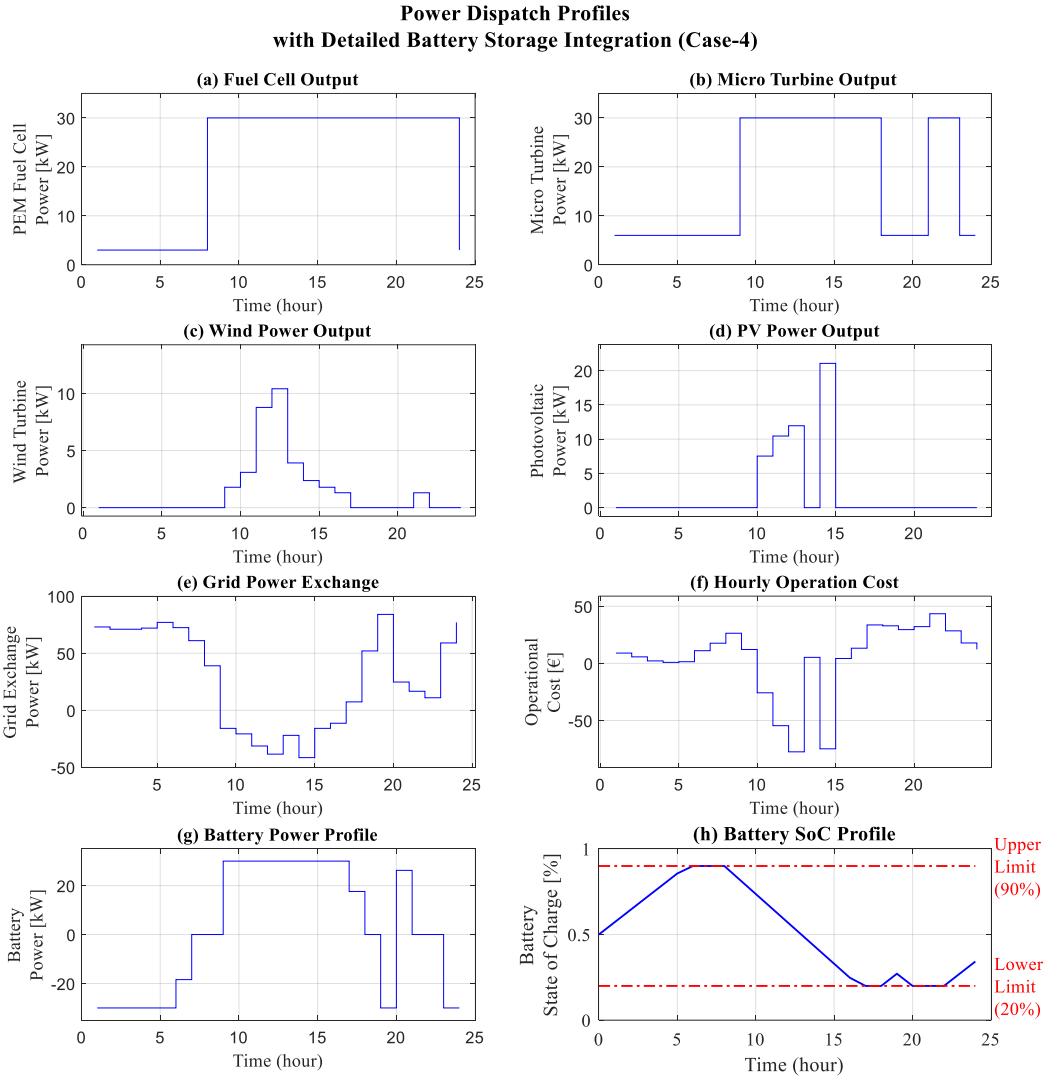

Fig. 6. 24-hour optimal power dispatch profiles considering detailed battery storage constraints (Case-4: Generation unit outputs a-FC, b-MT, c-WT, d-PV, e-Grid exchange power, f-Hourly operational cost, g-Battery power and h-Battery state of charge)

The evening operational pattern (17:00-24:00) showcases the system's ability to maintain stable and efficient operation. The battery system operates dynamically while strictly adhering to SoC limitations, facilitating balanced power exchange with the grid. This shows that there is effective coordination between all units of DERs. Thus, a good level is achieved in economic terms and system stability is also ensured.

The results obtained in this study demonstrate the importance of including realistic battery constraints in the operational planning of the MGs. It also highlights that storage system characteristics should be considered in cost

function calculations.

5. Conclusion

In this study, an optimization study is conducted using PFO algorithm for effective operation and management of MGs. In the study, cost minimization is considered as the objective function. This study presents a nonlinear optimization model for the optimal operation of MGs, considering both nonlinear objective functions and constraints. The use of a metaheuristic algorithm (Polar Fox Optimization) is justified by the complex and nonlinear nature of the problem, which cannot be effectively solved using traditional deterministic methods. The proposed approach provides a robust framework for handling the nonlinear interactions between distributed energy resources, storage systems, and grid exchange, ensuring both economic efficiency and system reliability. The study is conducted on four different scenarios. The effects on system performance and economics are investigated by modifying the constraints. In Case 1, it is assumed that all DERs are operating within the specified limits. In this case, all the energy produced by renewable DGs is injected into the MG. Case 1 served as a reference point for the other cases. As a result of the optimization study, the cost value is found to be €269.76/day. The value found is compatible with the literature. In Case 2, the output power of renewable DGs is accepted as the optimization variable. A 42.5% decrease in cost is occurred and the cost function is found to be 155.01 €/day. In case 3, the same conditions as in case 2 are valid. However, the utility power restriction (+30- and -30-kW limitation) is removed. The cost function for case 3 is calculated as 68.18 €/day. This result shows a reduction of 74.7% compared to the first case 1. Furthermore, the improvement in cost shows the impact of utility constraints on the operation costs and system efficiency. In Case 4, unlike the other cases, an optimization study was conducted by considering technical parameters such as battery efficiency, charge states, battery capacity and battery charge/discharge in order to solve the integration of the BES system to the grid with a more realistic approach. As a result of the study, the operating cost was calculated as 107.08 €/day. Although this cost is higher than the cost in Case 3, it allows the system to operate in a more realistic way since it takes into account practical battery limitations and battery efficiency.

This study shows the critical results obtained regarding the EOM of MGs. Firstly, optimizing the output power of renewable DGs contributed to the improvement of performance in economic terms. Secondly, removing constraints between MG and utility caused a significant decrease in costs. This situation showed the importance of grid infrastructure capacity. Thirdly, adding BESS constraints to the optimization with a realistic approach proved its importance for grid operation in daily life.

Future research can focus on enhancing the proposed optimization framework by incorporating multi-objective optimization to balance cost, environmental impact, and system resilience. Real-time optimization techniques using adaptive control and machine learning could improve decision-making under dynamic conditions. Additionally, integrating hybrid energy storage systems and exploring large-scale microgrid applications would enhance scalability and flexibility. Lastly, integrating the model with smart grid technologies, such as demand-side management and blockchain-based energy trading, could further optimize microgrid operations for sustainable and cost-effective energy management.

Acknowledgement

The author gratefully acknowledges the support provided by TÜBİTAK within the scope of the 1001 project under grant number 124E002.

Author Contribution

The writing of the manuscript and all analyses were conducted solely by the corresponding author.

Appendix A.

The following tables summarize the sets, indices, parameters, and decision variables used in the optimization framework.

A.1. Sets and indices

Symbol	Description
$t \in T$	Time periods (hours) in the planning horizon
$i \in I$	Set of distributed generation units
$s \in S$	Set of energy storage systems
$r \in R$	Set of renewable generation units (PV, WT)
X_i	Solution vector for i^{th} fox
X_{best}	Global best solution vector
X_{rand}	Randomly selected solution vector

A.2. Distributed/renewable power generation parameters

Symbol	Description	Unit
P_{MT}^{min} , P_{MT}^{max}	Min/max power output of microturbine	kW
P_{FC}^{min} , P_{FC}^{max}	Min/max power output of fuel cell	kW
P_{PV}^{max}	Maximum power output of PV system	kW
P_{WT}^{max}	Maximum power output of wind turbine	kW
P_{rated}	Rated power of battery system	kW
RD_{MT}, RU_{MT}	Ramp down/up rates of microturbine	kW/h
RD_{FC}, RU_{FC}	Ramp down/up rates of fuel cell	kW/h

A.3. Cost parameters

Symbol	Description	Unit
$\alpha_{FC}, \beta_{FC}, \gamma_{FC}$	Cost coefficients for fuel cell	€/kWh
a, b, c	Cost coefficients for microturbine	€/kWh
λt	Time-varying electricity price	€/kWh
C_{deg}	Battery degradation cost	€/kWh

A.4. Battery parameters

Symbol	Description	Unit
η_{charge}	Battery charging efficiency	%
$\eta_{discharge}$	Battery discharging efficiency	%
SoC_{min}	Minimum state of charge	%

SoC_{max}	Maximum state of charge	%
C_b	Battery capacity	kWh

A.5. Decision variables

Symbol	Description	Unit
$P_{MT}(t)$	Microturbine power output at time t	kW
$P_{FC}(t)$	Fuel cell power output at time t	kW
$P_{PV}(t)$	PV power output at time t	kW
$P_{WT}(t)$	Wind turbine power output at time t	kW
$P_b(t)$	Battery power (+ discharge, - charge) at time t	kW
$P_{grid}(t)$	Grid exchange power at time t	kW
SoC(t)	Battery state of charge at time t	%

References

[1] S. Mohammadi, B. Mozafari, S. Solimani, and T. Niknam, ‘‘An adaptive modified firefly optimisation algorithm based on hong's point estimate method to optimal operation management in a microgrid with consideration of uncertainties,’’ Energy, vol.51, pp.339-348, March. 2013, doi: 10.1016/j.energy.2012.12.013.
[2] M. Cikan and N. N.Cikan, ‘‘Optimum allocation of multiple type and number of DG units based on IEEE 123-bus unbalanced multi-phase power distribution system’’ International Journal of Electrical Power & Energy Systems, vol.144, pp.1-17, Jan. 2023, doi: 10.1016/j.ijepes.2022.108564.
[3] M. Çıkan, “Çita optimizasyon algoritması kullanarak kısmi gölgelenme altındaki fotovoltaik sistemlerde maksimum güç noktası izleyicisinin tasarlanması,” Gazi Üniversitesi Mühendislik Mimarlık Fakültesi Dergisi, vol.40, no.1, pp. 555–572, Jan. 2025, doi: 10.17341/gazimmfd.1183267.
[4] M. Çıkan and N.N. Çıkan, ‘‘Elektrikli araç şarj istasyonlarının enerji dağıtım hatlarına optimum şekilde konumlandırılması’’ Kahramanmaraş Sütçü İmam Üniversitesi Mühendislik Bilimleri Dergisi, vol.27, no.2, pp. 340-363, Jun. 2024, doi:10.17780/ksujes.1365209.
[5] M.Cikan, N.N. Cikan, B. Kekezoglu, “Determination of optimal island regions with simultaneous DG allocation and reconfiguration in power distribution networks,” IET Renewable Power Generation, vol.19, pp. e12942, 2025, doi:10.1049/rpg2.12942.
[6] C. Marnay, N. DeForest and J. Lai, “A green prison: The Santa Rita Jail campus microgrid,’’ IEEE Power and Energy Society General Meeting, 2012, pp.1-2, doi: 10.1109/PESGM.2012.6345235.
[7] T. Gabderakhmanova et al., “Demonstrations of DC Microgrid and Virtual Power Plant Technologies on the Danish Island of Bornholm,’’ 55th International Universities Power Engineering Conference (UPEC), 2020, pp. 1-6, doi: 10.1109/UPEC49904.2020.9209853.
[8] S. Ahmad, M. Shafiullah, C. B. Ahmed and M. Alowaifeer, “A Review of Microgrid Energy Management and Control Strategies,’’ IEEE Access, vol. 11, pp. 21729-21757, 2023, doi: 10.1109/ACCESS.2023.3248511
[9] N.N. Cikan and M. Cikan, ‘‘Reconfiguration of 123-bus unbalanced power distribution network analysis by considering minimization of current & voltage unbalanced indexes and power loss,’’ International Journal of Electrical Power & Energy Systems, vol.157, pp.1-15, Jun.2024, doi: 10.1016/j.ijepes.2024.109796.
[10] M. Cikan and B. Kekezoglu, ‘‘Comparison of metaheuristic optimization techniques including Equilibrium optimizer algorithm in power distribution network reconfiguration,’’ Alexandria Engineering Journal, vol.61, no.2, pp. 991-1031, Feb. 2022, doi: 10.1016/j.aej.2021.06.079.
[11] K. Doğanşahin and M. Çıkan, ‘‘A new line stability index for voltage stability analysis based on line loading,’’ Clean Energy Technologies Journal, vol.1, no.1, pp.23-30, 2023.
[12] A. Mortazavi, “Comparative assessment of five metaheuristic methods on distinct problems,” Dicle Üniversitesi Mühendislik Fakültesi Mühendislik Dergisi (DUJE), vol. 10, pp. 879–898, 2019, doi: 10.24012/dumf.585790.
[13] A. Mortazavi, “A fuzzy reinforced Jaya algorithm for solving mathematical and structural optimization problems,’’ Soft Computing, vol. 28, pp. 2181–2206, 2024, doi:10.1007/s00500-023-09206-5.
[14] A. Akter et al., ‘‘A review on microgrid optimization with meta-heuristic techniques: Scopes, trends and recommendation,’’ Energy Strategy Reviews, vol. 51, pp. 1-27, Jan. 2024, doi: 10.1016/j.esr.2024.101298.
[15] S. Phommixay, M.L. Doumbia, and D. Lupien St-Pierre, ‘‘Review on the cost optimization of microgrids via particle swarm optimization,’’ International Journal of Energy and Environmental Engineering, vol. 11, pp. 73-89, 2020, doi: 0.1007/s40095-019-00332-1.
[16] M. A. Hossain, H. R. Pota, S. Squartini, F. Zaman, and K.M. Muttaqi, ‘‘Energy management of community microgrids considering degradation cost of battery,’’ Journal of Energy Storage, vol.22, pp.257-269, April 2019, doi: 10.1016/j.est.2018.12.021.
[17] S. Sharma, S. Bhattacharjee, and A. Bhattacharya, ‘‘Probabilistic operation cost minimization of Micro-Grid,’’ Energy, vol.148, pp. 1116-1139, 2018, doi: 10.1016/j.energy.2018.01.164.

[18] Z. Zheng, S.Yang, Y. Guo, X. Jin, and R. Wang, "Meta-heuristic Techniques in Microgrid Management: A Survey'' Swarm and Evolutionary Computation, vol.78, pp.101256, 2023, doi: 10.1016/j.swevo.2023.101256.
[19] A. Mortazavi, "Marathon runner algorithm: theory and application in mathematical, mechanical and structural optimization problems,'' Materials Testing, vol. 66, pp. 1267-1291,2024, doi: 10.1515/mt-2023-009.
[20] M. Moloodpoor, A. Mortazavi, and N. Ozbalta, "Thermo-economic optimization of double-pipe heat exchanger using a compound swarm intelligence,'' Heat Transfer Research, vol.52, pp.1-20,2021, doi: 10.1615/HeatTransRes.2021037293.
[21] E. C. Kandemir, and A. Mortazavi, "Optimization of Seismic Base Isolation System Using a Fuzzy Reinforced Swarm Intelligence,'' Advances in Engineering Software, vol.174, pp. 103323, 2022, doi: 10.1016/j.advengsoft.2022.103323.
[22] M. Cikan, and K. Dogansahin, "A Comprehensive Evaluation of Up-to-Date Optimization Algorithms on MPPT Application for Photovoltaic Systems," Energy Sources, Part A: Recovery, Utilization, and Environmental Effects, vol.45, pp.10381–10407, 2023, doi:10.1080/15567036.2023.2245771.
[23] N.N. Cikan, "Optimization of PV, Capacitor Bank, and EV Charging Station Allocation in a 33-Bus Power Distribution System Using the Slime Mould Algorithm" European Journal of Engineering and Natural Sciences (EJENS), vol.9, pp.55-60, 2024.
[24] N.N. Cikan, "Optimization of a 33-Bus Power Distribution System Using Artificial Hummingbird Algorithm for Power Loss and Voltage Stability Enhancement," European Journal of Engineering and Natural Sciences (EJENS), vol.9, pp.41-46, 2024.
[25] M.Gendreau, and JY. Potvin, "Metaheuristics in Combinatorial Optimization,'' Annals of Operation Research, vol. 140, pp.189–213, 2005, doi:10.1007/s10479-005-3971-7.
[26] I. Boussaïd, J. Lepagnot, and P. Siarry, "A survey on optimization metaheuristics,'' Information Sciences, vol. 237, pp.82-117, 2013, doi: 10.1016/j.ins.2013.02.041.
[27] S. Yang, Y. Jiang, and T.T. Nguyen, "Metaheuristics for dynamic combinatorial optimization problems,'' IMA Journal of Management Mathematics, vol.24, pp.451–480, 2013, doi: 10.1093/imaman/dps021.
[28] C. Gamarra, and J. M. Guerrero, "Computational optimization techniques applied to microgrids planning: A review,'' Renewable and Sustainable Energy Reviews, vol. 48, pp. 413-424, 2015, doi: 10.1016/j.rser.2015.04.025.
[29] M. F. Zia, E. Elbouchikhi, and M. Benbouzid, "Microgrids energy management systems: A critical review on methods, solutions, and prospects,'' Applied Energy, vol. 222, pp. 1033-1055, 2018, doi: 10.1016/j.apenergy.2018.04.103.
[30] T. Niknam, F. Golestaneh, and A. Malekpour, ''Probabilistic energy and operation management of a microgrid containing wind/photovoltaic/fuel cell generation and energy storage devices based on point estimate method and self-adaptive gravitational search algorithm,'' Energy, vol.43, no.1, pp. 427-437, July 2012, 10.1016/j.energy.2012.03.064.
[31] A. Ghiaskar, A. Amiri, S. Mirjalili, ''Polar fox optimization algorithm: a novel meta-heuristic algorithm,'' Neural Computing and Applications, vol.36, pp. 20983–21022, Aug. 2024, doi: 10.1007/s00521-024-10346-4.
[32] J. Radosavljevic, ''Optimal energy and operation management of microgrids,'' in Metaheuristic Optimization in Power Engineering, 1st ed. London, England: IET, ch.12, pp. 407-447.
[33] H. Saadat, Power system analysis. New York, NY, USA: McGraw-Hill,1999.
[34] J. Radosavljevic, ''Optimal power flow in transmission networks,'' in Metaheuristic Optimization in Power Engineering, 1st ed. London, England: IET, ch.6, pp. 177-233.
[35] S. Mohammadi, S. Soleymani, and B. Mozafari, ''Scenario-based stochastic operation management of microgrid including wind, photovoltaic, micro-turbine, fuel cell and energy storage devices,'' International Journal of Electrical Power & Energy Systems, vol. 54, pp.525-535, Jan.2014, doi: 10.1016/j.ijepes.2013.08.004.
[36] A. A. Moghaddam, A. Seifi, T. Niknam, and M. R. A. Pahlavani, ''Multi-objective operation management of a renewable MG (micro-grid) with back-up micro-turbine/fuel cell/battery hybrid power source,'' Energy, vol.36, no.11, pp. 6490-6507, Nov.2011, doi: 10.1016/j.energy.2011.09.017.

Contents lists available at *Dergipark*

Journal of Scientific Reports-A

journal homepage: *https://dergipark.org.tr/tr/pub/jsr-a*

E-ISSN: 2687-6167 ***Number 61, June 2025***

RESEARCH ARTICLE

Receive Date: 06.01.2025 *Accepted Date: 28.04.2025*

Development and characterization of gelatin-based scaffolds for 3D cancer cell culture

Bahar Yılmaz[a,*], Esra Armağan[b], Mukaddes Keskinateş[c], Ziya Aydın[d], Mevlüt Bayrakcı[e]

[a]*Karamanoğlu Mehmetbey University, Department of Bioengineering, Karaman, 70200, Turkey, ORCID: 0000-0002-6315-3018*
[b]*Karamanoğlu Mehmetbey University, Ermenek Uysal and Hasan Kalan Health Services Vocational School, Department of Pharmacy Services, Karaman, 70200, Turkey, ORCID: 0000-0002-5414-2392*
[c]*Karamanoğlu Mehmetbey University, Kazım Karabekir Vocational School, Department of Medical Services and Techniques, Karaman, 70200, Turkey, ORCID: 0000-0002-1799-7180*
[d]*Karamanoğlu Mehmetbey University, Vocational School of Technical Sciences, Karaman, 70200, Turkey, ORCID: 0000-0001-8074-9510*
[e]*Karamanoğlu Mehmetbey University, Department of Bioengineering, Karaman, 70200, Turkey, ORCID: 0000-0002-0416-2870*

Abstract

Two-dimensional (2D) cell culture is a commonly utilized method in laboratories for growing and maintaining cells, particularly in cancer research under controlled conditions. A critical factor in cancer cell culture is preserving cell viability and functionality, as cancer cells are highly sensitive to changes in their environment. However, the three-dimensional (3D) structure of tumors cannot be effectively replicated in 2D cell culture. In contrast, 3D cell culture provides significant advantages over traditional 2D systems, primarily by cultivating cancer cells in an environment that more accurately resembles the 3D architecture and complexity of tumors in vivo. This study is designed to develop cancer-specific gelatin-based scaffolds for developing a 3D (spheroid) culture model. These scaffolds were prepared reproducibly using pig skin gelatin, cold-water fish gelatin, and bovine skin gelatin. Phytagel and agarose-based gels (control groups) were used for comparison. The scaffold structures were characterized by Fourier transform infrared (FT-IR) spectroscopy and scanning electron microscopy (SEM). MCF-7, HeLa, and HT-29 cancer cells were seeded on gelatin substrates and imaged by inverted microscopy. FT-IR analysis showed that the scaffolds were successfully prepared, while SEM analysis showed that the scaffolds were highly porous. The cancer cell lines were successfully grown on scaffolds and were shown to aggregate to form spherical structures. In this study, for the first time, 3D structures were generated from monolayer cell structures by using different gelatin structures. Many 3D cell studies will benefit from the fact that the resulting gelatin scaffolds are biocompatible and support infiltration and proliferation.

Keywords: Spheroid; Gelatin; Scaffold; Biomaterial; 3D culture; Cancer

* Corresponding author. Tel.: +90 338 226 2200; fax: +90 338 226 2214.
E-mail address: baharyilmaz@kmu.edu.tr

1. Introduction

Cancer refers to a group of diseases marked by the uncontrolled growth and spread of abnormal cells within the body. Advancing cancer research is essential for developing new and effective treatments, enhancing patient outcomes, and ultimately finding a cure for this disease [1].

For a wide range of basic and preclinical studies, cell culture systems are essential [2]. This system is popular among cancer researchers because it allows them to cultivate cells on a plane and examine the essential media for cell maintenance and development under a well-controlled setting [1]. Traditional cell culture methods utilize 2D monolayers that enable in vitro investigation of cellular processes [2–3]. However, with further investigation of the cellular environment, it has become clear that cellular functions in 2D culture systems are significantly different from those observed in the living organism [4]. In this way, it can be said that cells cultivated on 2D surfaces, as compared to the cells that grow in an in vivo environment, are different in terms of morphology, signaling, proliferation, cell-matrix and cell-cell interactions, differentiation and many other parameters [5]. For this reason, it appears that the next frontier in cell biology research is the development and employment of three-dimensional (3D) culture technology that aims to further replicate the in vivo cell microenvironment [6]. A wide range of detailed studies have been conducted in recent years in the direction of advanced 3D culture techniques to achieve a nurturing environment. Their biodegradability further makes them advantageous for tissue engineering applications [7]. Conventional 2D cell cultures cannot adapt to the cellular diversity of both normal and cancerous tissues, making them inadequate for studying tissue-specific processes or diseases such as cancer [2]. 3D cell cultures provide more refined models by simulating cell-cell and extracellular matrix (ECM) interactions and enhancing cell signaling and proliferation [8]. 3D cell culture allows cells to grow in an environment that closely mimics their natural environment, allowing them to interact within a supporting matrix [9].

Scaffolds are essential in 3D cell culture systems as they provide a 3D environment for cells to grow and interact with each other and their environment. Many biomaterials including natural polymers (such as collagen, fibrin), synthetic polymers, decellularized tissues, hydrogels, and microfluids are used to create scaffold-based 3D culture models [1]. Properties of biopolymers such as wall morphology, pore structure and surface area enable the production of scaffolds that support cell seeding, growth and tissue development. Natural polymers function as bioadhesive and biofunctional materials by offering advantages such as biocompatibility, biodegradability, low toxicity and increased cellular interaction [10]. These materials have some advantages and disadvantages. While natural polymers promote cell attachment, proliferation and differentiation with their ECM-like structure, they may have limitations in terms of mechanical strength and stability. Synthetic polymers may require surface modifications for biocompatibility while providing precise control over porosity, degradation rate and mechanical strength. Decellularized tissues retain tissue-specific signals and mechanical properties, but their preparation can be complex and costly [1]. Organoids, another model used to create 3D structures, are clusters of cells derived from stem cells or organ-specific progenitor cells that exhibit organ-like properties. However, these systems have some limitations: lack of vascular structure prevents oxygen and nutrients from reaching the center of the organoids, lack of blood vessels limits the size of the organoids and prevents them from meeting the needs of the tissues, immune and stromal cell interactions in the tumor microenvironment cannot be adequately mimicked [8]. Encapsulating cells within hydrogels is a widely used method for 3D culture. These hydrogels are composed of loosely cross-linked natural materials, such as collagen, agarose, fibrin, or hyaluronic acid, and feature a high water content [11]. Often regarded as the 3D equivalent of native ECM, hydrogels exhibit swelling properties, low elasticity, and high water content. Hydrogels are hydrophilic, three-dimensional cross-linked polymer networks featuring interconnected microscopic pores, allowing them to absorb up to 99% of their volume in biological fluids. As synthetic extracellular matrix scaffolds, they offer structural support and promote spatial organization, enhancing cellular interactions with their surrounding environment [12]. Due to their porous structure, hydrogels support nutrient and oxygen diffusion and ensure cell survival. Their mechanical properties, degradation rate and transport capacity for bioactive molecules can be easily tuned. However, their lack of long-term stability requires careful design and optimization [1].

Gelatin is a gelling agent derived from animal collagen, characterized by its tasteless, translucent, and pale yellow or colorless appearance. It is a high molecular weight biopolymer produced through protein hydrolysis. Its unique amino acid composition, rich in Gly-Pro-Hyp (glycine, L-proline and 3-hydroxy-L-prolin), grants gelatin distinctive functional properties, including gelling, binding, viscosity enhancement, and film-forming abilities [13]. Since the emergence of biomaterials for tissue regeneration, gelatin has been incorporated into various systems, such as injectable hydrogels, scaffolds, and drug delivery platforms [14]. Its advantageous features–such as low toxicity, biocompatibility, and biodegradability–support enhanced differentiation, cell proliferation, and adhesion by body enzymes (e.g., metalloproteinases) without eliciting an immune response. Additionally, its cost–effectiveness has facilitated its use in diverse applications, including hydrogels for sustained chemotherapeutic drug delivery and for promoting bone regeneration across tissues like bone, neural, and skeletal systems. Gelatin's properties, such as water absorption, porosity, support for healthy cell growth, and oxygen transport, are critical for successful tissue regeneration [15].

Phytagel is a polysaccharide with various functions in the production of hydrogels and scaffolds [16]. Phytagel is derived from a bacterial substrate composed of rhamnose, glucuronic acid, and glucose. This polymer consists of repeating tetrasaccharide units that gelate in the presence of mono- or divalent cations [17].

Agarose is a biocompatible and biodegradable biomaterial due to its neutral polysaccharide structure based on D-galactose. These properties make it advantageous for use in tissue engineering and drug delivery. It can be mixed with other biomaterials to create biological scaffolds that can adapt to different soft tissues and can be used in clinical applications such as human skin and organ production [10]. Since its size and stiffness are adjustable, it can mimic natural tissue stiffness in tumor engineering. It also supports cell proliferation, maintains phenotype, and provides a stable cellular environment by increasing ECM secretion [18].

Gelatin can be crosslinked by chemical or enzymatic methods; however, these methods require non-physiological conditions and are not suitable for 3D cell encapsulation. Therefore, practical methods to obtain gelatin-based hydrogels are being investigated, especially to regulate the pore size, degradation, swelling, and mechanical properties of the scaffold [19]. Gelatins from different sources contain various protein and biopolymer components that can optimize cell adhesion and growth, allowing the production of hydrogels with various physical, chemical and biological properties [19–20]. Biomaterials such as cold-water fish gelatin are immunogenic, non-toxic and biodegradable [20]. Hydrogels derived from bovine skin gelatin have favorable mechanical properties that support cell growth, migration and proliferation and offer tunability for the culture of different cell types. Gel stiffness differs between bovine and porcine skin gelatin. While the gel strength of BSG increases proportionally with pH, this increase is inconsistent for pigskin gelatin. Lower stiffness bovine skin gelatin hydrogels are expected to promote cell spreading [19].

The scaffold materials selected for this study are known to exhibit high porosity, thus increasing cell infiltration and enhancing intercellular interactions [20]. In this study, for the first time, 3D structures were formed from monolayered cell structures by using three different gelatin structures obtained from different organisms that contain gelling properties in their structure. These gelatin structures were layered on 96- well plates at specific concentrations, and the most suitable ground for 3D cell structures was prepared and characterized. We fabricated gelatin-based scaffolds with highly homogeneous pore size and biocompatibility using different base materials in this study. Compared to other gel systems previously used for tumor models, the materials used in present study combine the advantages of both natural and synthetic biomaterials, aiming to create more realistic and reliable 3D environments for cell culture studies.

2. Materials and methods

2.1. Materials

Sigma-Aldrich, Merck (Darmstadt, Germany) and/or Fluka (Milwaukee, USA) were purchased for the chemical solvents and substances used in the study. Purified water from a water purifier (Millipore Milli-Q Plus) was used for all aqueous solutions. The pH measurements were carried out using a digital pH meter (Orion 2 Star pH Benchtop). Spheroid cells were photographed with a digital camera (Leica 475) under an inverted microscope (Leica DMI 4000B, Germany).

2.2. Preparation of TAE (Tris-Acetic Acid-EDTA) buffer

First, 48.4 g of Tris was dissolved in 800 mL of distilled water. 11.4 mL of acetic acid was added to the mixture under a fume hood. Add 3.72 g of EDTA and mix well. Finally, 1 L of distilled water was added [21].

2.3. Preparation of basic gelatin for spheroid cell formation

To produce spheroids, we added 80 µL of different gelatin, phytagel and agarose solutions to the bottom of a 96-well plate. We first dissolved 1% phytagel [22], 1% agarose [22], and 1.5% bovine skin, 5% cold water fish, and 10% pig skin gelatin solutions in TAE buffer prepared specifically for this procedure. After preparation, we sterilized the solutions under UV light. To avoid air bubbles, we carefully dispensed the sterilized gel solutions into the wells and evenly spread them across the bottom surfaces. Finally, we placed the plates at 4°C for 10 minutes to allow gel formation [23–24].

2.4. Fourier transform infrared (FT-IR) spectroscopy

The structure of five different gelatin scaffolds prepared for 3D cell formation was analyzed using FT-IR (PerkinElmer FT-IR Spectrum One, USA). The scaffolds were placed in the FT-IR device for analysis, and scanning was conducted across a range of 400 cm^{-1} to 4000 cm^{-1} to detect changes in the functional groups within the 3D gelatin scaffolds [21].

2.5. Scanning electron microscopy (SEM)

We used SEM to understand the morphology and surface properties of agarose, phytagel, and other gelatin structures. For the SEM images, we first coated the materials with a 5 nm layer of Au and then imaged them at a distance of about 1 micron. We used the images to evaluate morphology, porosity, structure, and other important features of the sample [25]. We then analyzed the obtained images with ImageJ image processing software and measured the average porosity and pore size [26]. Using the software, we calculated the pore size by measuring the pore diameters of each scaffold type and the percentage porosity by measuring the area occupied by the pores.

2.6. Preparation of monolayer cell lines

Cell culture studies were performed with MCF-7 (breast cancer line) (ATCC® HTB-22™), HeLa (uterine cancer line) (ACC 733, DSMZ) and HT-29 (colon cancer line) (ATCC® CRL1573™). Cells stored frozen at -80 °C and/or in liquid nitrogen in cold stabilized vials were thawed rapidly in a water bath (at 37 °C). They were placed in the medium after centrifugation for 5 minutes at 1300 rpm. The cancer cells were then incubated in flasks with 1%

penicillin-streptomycin, 10% FBS, 0.01% gentamicin and DMEM with 10% FBS, 1% penicillin-streptomycin and RPMI with 0.01% gentamicin in humidity-controlled incubators at 37 °C with a 5% CO_2 atmosphere. Cells that reached 80-90% confluence in culture were passaged and reseeded [25–27].

2.7. Spheroid cell formation from monolayer cell lines

In spheroid cell studies, passaged cell pellets were seeded in fresh medium at same concentrations (5.0×10^4 cells per mL). This seeding density has been reported as optimal for initiating spheroid formation, allowing sufficient cell–cell contact to promote aggregation [28]. Furthermore, maintaining this moderate cell density ensures that the scaffold porosity and surface area are not overwhelmed, allowing for uniform spheroid morphology and facilitating comparative analyses among different scaffold types. These cells were seeded in well plates containing phytagel, agarose, and different gelatins. In general, in 3D cell culture studies, at least 3 to 7 days are required for cells to attach to the scaffold, proliferate, and form spherical structures [29]. Therefore, cells were cultured for a period of seven days and samples were then analyzed on day 7. Images of the spheroidal cells were captured and recorded using a digital camera (Leica 475) under an inverted microscope (Leica DMI4000B, Germany) [27].

2.8. Statistical analysis

Multiple samples (n=3–6) were collected in each experiment and expressed as mean ± SD. Each experiment was replicated three times. One-way analysis of variance (ANOVA) was used to evaluate statistical significance. *P* values ≤ 0.05 were considered significant.

3. Results and discussion

In this study, we used only physical gelation method for 3D encapsulation of cells and did not resort to chemical cross-linking agents. Agarose, gelatin, and phytagel scaffolds of homogeneous size and shape were successfully and reproducibly produced (Figure 1). It has been observed that the structures obtained by physical gelation have high biocompatibility and provide sufficient support for cell proliferation and global organization.

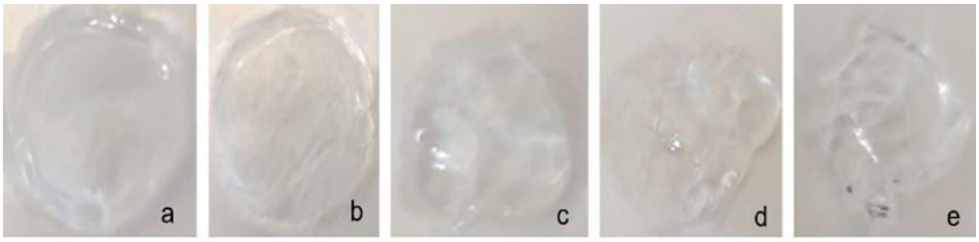

Fig. 1. Macroscopic images of the scaffold structures composed of different sources. (a) Agarose; (b) Phytagel; (c) Bovine skin gelatin; (d) Cold water fish gelatin; (e) Pig skin gelatin.

FT-IR spectroscopy clearly reported the structure of each gelatin composition, and the FT-IR spectrum of each structure obtained is shown in Figure 2. In the FT-IR spectra of gelatin, the C=O stretching at 1630–1635 cm^{-1} was for amide I and the N–H deformation at 1500–1540 cm^{-1} was for amide II. The absorption of amide I was mainly due to the stretching vibration of C–O bond, and the band of amide II was due to the combination of bending of -NH bond and stretching of C–N bond. The band due to N–H stretching was scattered at 3250–3300 cm^{-1} [30–31]. The amide structures obtained by FT-IR analysis indicate that the gelation process has been successful. The agarose hydrogel

(black line in Fig. 2) showed typical signals at 1043 cm^{-1}, corresponding to the C–H bending and C–O stretching of glycosidic bonds, and two broad peaks at 1625 and 3350 cm^{-1}, characteristic of the H–O–H bonded water and O–H hydrogen-bonded hydroxylic groups of carbohydrates, respectively [32]. The FT-IR spectrum of phytagel (red line in Fig. 2) shows a broad absorption band registered at 3320 cm^{-1} specific to the stretching vibrations of the OH groups of the glucopyranose ring. The absorption bands at 1603 cm^{-1} is assigned to asymmetric and symmetric stretching of the COO^- group. Also the vibrations of C–O and C–O–C bonds are present in the region of 1300–1020 cm^{-1} [33].

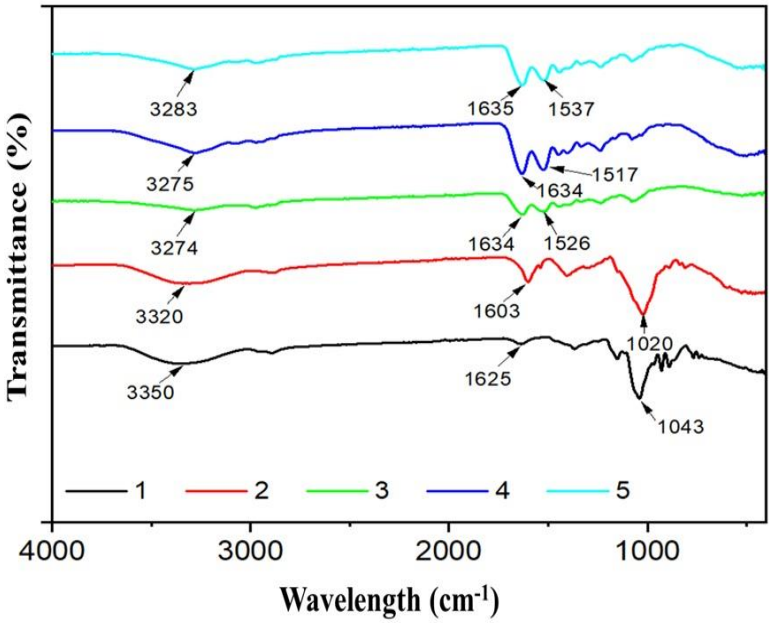

Fig. 2. Fourier-transform infrared (FT-IR) spectra of the fabricated 3D scaffold structures. FT-IR analysis was performed to evaluate the chemical composition and functional groups present in the scaffolds prepared from five different biopolymer sources: (1) Agarose; (2) Phytagel; (3) Bovine skin gelatin; (4) Cold water fish gelatin; (5) Pig skin gelatin. Characteristic absorption peaks corresponding to hydroxyl (–OH), amide (–CO–NH), and carboxyl (–COOH) groups were observed, confirming the presence of expected functional groups inherent to polysaccharide- and protein-based materials. The results validate the successful incorporation of each biopolymer into the scaffold matrix.

Different pore sizes and interconnecting shapes affect the physicochemical properties of the scaffold [34]. Previous studies have shown that the greater the variation in pore size of 3D tissue engineering scaffolds, the more difficult it is for cells to seed and proliferate [35]. SEM was used to observe the morphological changes of the 3D scaffolds. SEM images showed that the scaffolds had an isotropic pore structure and were highly porous (Figure 3). Homogenous microstructure and high porosity of the scaffolds were observed for all scaffold groups. There is a good connection between the pores and the pores have an optimum distribution all over the scaffold surfaces. The inherently interconnected structure of the pores, without a closed-cell configuration, ensured connectivity between adjacent pores.

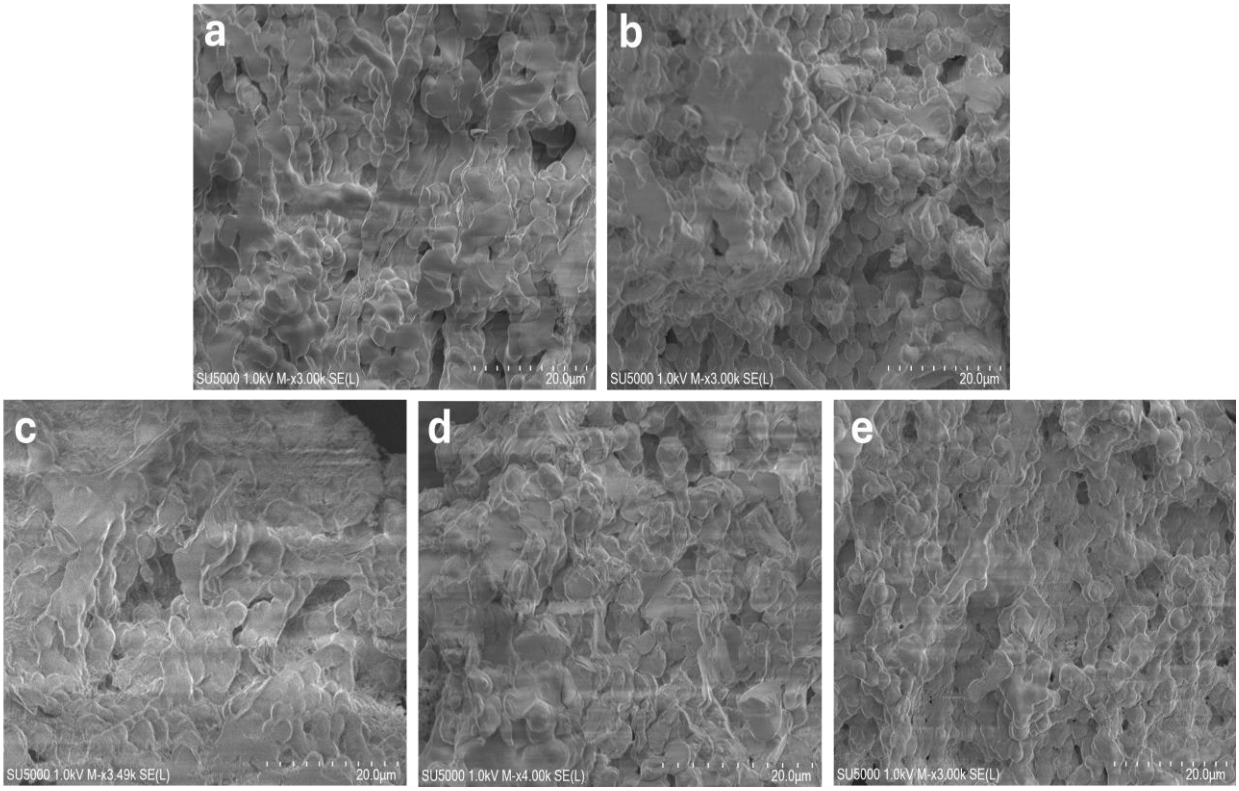

Fig. 3. Scanning electron microscopy (SEM) images of the surface morphology of the prepared 3D scaffolds at ×3000 magnification. All scaffold structures exhibited a highly porous and interconnected morphology with an isotropic pore distribution. The micrographs reveal homogenous pore organization across the surfaces of the scaffolds. The pore interconnectivity and uniform size distribution observed in all groups indicate successful scaffold fabrication under controlled conditions. (a) Agarose; (b) Phytagel; (c) Bovine skin gelatin; (d) Cold water fish gelatin; (e) Pig skin gelatin.

Pores larger than 100 μm enable tissue growth, while extremely large pores (> 400 μm) reduce the cell-cell contact rate because cells exhibit a 2D growth pattern instead of a 3D organization on the substrate [36]. The pore sizes of agarose, phytagel, bovine skin gelatin, cold water fish gelatin and pig skin gelatin were 262.6±39, 237.0±22, 313.0±26, 273.0±39, and 264.4±37 μm, respectively (Figure 4), and these pore sizes are suitable for the formation of 3D cells. The data obtained showed that there was no statistically significant difference between the different scaffolds in terms of mean pore size ($P > 0.05$). Pore sizes were uniform across both transverse and longitudinal planes, with no significant differences observed. However, pore sizes along the longitudinal axis were significantly larger ($P \leq 0.05$) than those in the transverse plane, resulting in oval-shaped pores. This structure may allow cells to be more easily oriented (cell alignment) and may have a potential impact on tissue organization. These findings are consistent with previous findings [37]. Porosity analysis (Figure 4) revealed that all compositions exhibited high porosity levels (> 90%) across all groups (agarose 91.62±1.05, phytagel 90.58±1.25, bovin skin gelatin 91.4±2.13, cold water fish gelatin 91.42±1.381, and pig skin gelatin 91.06±0.823%) with no statistical significance ($P > 0.05$). The findings show that 3D scaffolds with an isotropic pore structure and high porosity create a favorable microenvironment for intercellular connections. The strong intercellular connectivity and the absence of a closed cell structure allow cells to move freely within the scaffold, resulting in highly compliant scaffold [38]. Compared to other studies, these findings are

consistent with some important design principles widely recognized in the literature. For example, Liu et al. showed that scaffolds with high porosity allow for better cellular proliferation and differentiation [39]. Similarly, Jones et al. highlight that the pore structure, pore diameter and connectivity of scaffolds are critical for cells to successfully settle on the scaffold surface and penetrate deep into the scaffold [40]. Additionally, porous scaffolds formed with the combination of fish gelatin and hyaluronic acid had porosity values ranging from 71.72% to 91.17% and supported the proliferation and infiltration of human fibroblast and keratinocyte cells [41]. In conclusion, these findings reveal that scaffolds with high porosity and homogeneous pore structure can potentially outperform in tissue engineering applications and support the successful integration of cells into the scaffold. Consistent with other studies, these results provide important clues for improving cellular performance and designing more functional 3D scaffolds for biomedical applications.

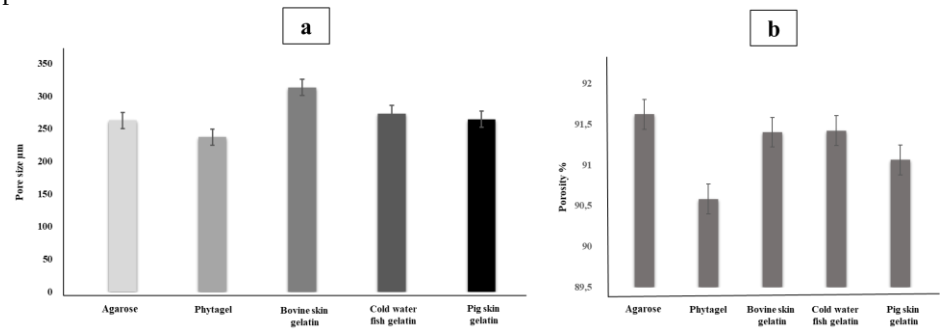

Fig. 4. Quantitative comparison of (a) average pore sizes, and (b) porosity % among different scaffold types used for 3D cell culture applications. Statistical analysis revealed no significant difference in average pore size, and porosity % between the scaffold types ($P > 0.05$), indicating that all scaffold groups exhibit comparable high porosity in terms of dimensional characteristics.

3D cell culture is achieved by embedding cells within artificial matrices, which can consist of solid scaffolds (like foams or sponges), hydrogels, fibers, or beads. These matrices are designed with adjustable porosities and mechanical characteristics to mimic the ECM of tumors in vivo [42]. After seeding, cells adhere to the matrix material and migrate inward, creating microstructures within its cavities.

Artificial matrices for 3D spheroid formation are typically composed of non-adhesive polymers, such as agarose or hyaluronic acid, or a combination of non-adhesive polymers with other biomaterials. Non-adhesive properties are essential for promoting spheroid formation, as they allow cell-cell adhesive forces to dominate over cell-matrix interactions, thereby driving cell aggregation [43]. Researchers have developed and utilized numerous scaffold-based materials for 3D cell culture. In this study, for the first time, we used pig skin gelatin, cold-water fish gelatin, and bovine skin gelatin as base materials for spheroid cell formation. Researchers have employed various base materials such as agar, agarose, and polymer structures for 3D cell formation, and they consider these materials among the most promising for promoting spheroid cell growth. Nevertheless, materials that rely on spheroid formation on flat, non-adhesive surfaces face challenges, such as limited reproducibility. As a result, researchers are exploring different gelatin-based materials to enhance spheroid production and optimize their suitability as base materials.

For comparison, three different cancer cell lines were seeded on these scaffolds. After 7 days, all cell lines formed multicellular spheres. Figure 5 illustrates the 3D structures formed by MCF-7 (4A), HT-29 (4B), and HeLa (4C) cell lines. The reasons for choosing these cancer cell lines are that they each represent common cancer types of different tissue origins and that the behavior of these cells in 2D and 3D cultures is well described in the literature. Thus, the general applicability of the 3D culture model for different cancer types could be evaluated. Morphological analysis using an inverted microscope revealed that the cells predominantly displayed a 3D round morphology (multicellular spheroids), with evident 3D cell-cell and cell-matrix interactions. When we compared gelatin-based scaffolds, we found that bovine skin gelatin-based scaffolds showed the best performance. The possible reason for this may be that

bovine skin gelatin supports cell spreading due to its lower hardness [19]. All grown tumor spheroids are of similar shape with different sizes. The difference could be attributed to the preferences of different cell lines in the tumor microenvironment [44]. Furthermore, the most optimal 3D scaffold structures occurred in the MCF-7 cell line (bovine skin gelatin-based scaffold) compared to other cancer cells. MCF-7 cells adhere better on this scaffold, proliferate and form a spheroid structure. HeLa and HT-29 cells, on the other hand, may exhibit lower adhesion properties and therefore perform poorly in bovine skin gelatin-based scaffolds compared to MCF-7 [45]. MCF-7 cells are cells that can better penetrate porous structures and are prone to form spheroids with more cell-cell interactions. This porous structure contributed to better proliferation and infiltration of MCF-7 cells [1]. Breast cancer cells (especially MCF-7) are one of the cell lines that can mimic the 3D tumor microenvironment by forming spheroid structures. The homogeneous pore structure and optimal mechanical strength of bovin skin gelatin-based scaffolds supported the organization of these cells into 3D spheroid structures. HeLa and HT-29 cells, on the other hand, tend to grow in a monolayer planar manner and may not have formed strong spheroid structures like MCF-7. The better performance of MCF-7 cancer cell line on bovine skin gelatin-based scaffolds is associated with the high biocompatibility of bovin skin gelatin, its protein structure that enhances cell adhesion, its homogeneous porous structure and its microenvironment suitable for MCF-7's capacity to form spheroid structures. This created a tumor-like environment for MCF-7 cells, allowing the cells to show better proliferation, adhesion and 3D organization. HeLa and HT-29 cells were found to perform less well on these scaffolds due to their different cellular characteristics. Similarly, when we look at the literature, gelatin-based scaffolds give successful results especially with MCF-7 cell line. For example, Arya et al. reported that gelatin-based scaffolds provided a favorable environment for the growth of MCF-7 breast cancer cells and the cells showed good adhesion and proliferation [46]. Azar et al. found that fish gelatin showed lower thermal stability and mechanical strength, which may affect structural integrity in long-term cultures [47]. In our study, bovine gelatin offered a more stable and more suitable microenvironment for the cells in these aspects.

Cell culture is a widely used in vitro tool for the development of cell biology, tissue morphology and disease mechanisms, drug action, protein production and tissue engineering. Most cancer-related research is based on experiments using in vitro 2D cell cultures. However, 2D cultures have many limitations, such as changes in cell polarity, morphology and division method, and interaction imbalances between cellular and extracellular environments. These disadvantages led to the development of 3D culture models that can better mimic in vivo conditions [48]. Chen et al. found that MCF-7 cells were flat with triangular and polygonal morphologies after growing on 2D culture, while cells grown on collagen scaffolds had various morphologies including more rounded, spread out and elongated [49]. Findings obtained from studies conducted with cancer cell lines show that 3D systems are more advantageous in terms of proliferation and viability of cancer cells compared to 2D cultures [50–51]. The formation of cell aggregates or spheroids has been shown to better mimic tissue structure, although not all cells can come into direct contact with the medium due to limitations in nutrient and waste exchange [52]. The formation of these cell clusters and spheres in the studied 3D cultures may provide advantages to the models by providing different microenvironments for the cells [53].

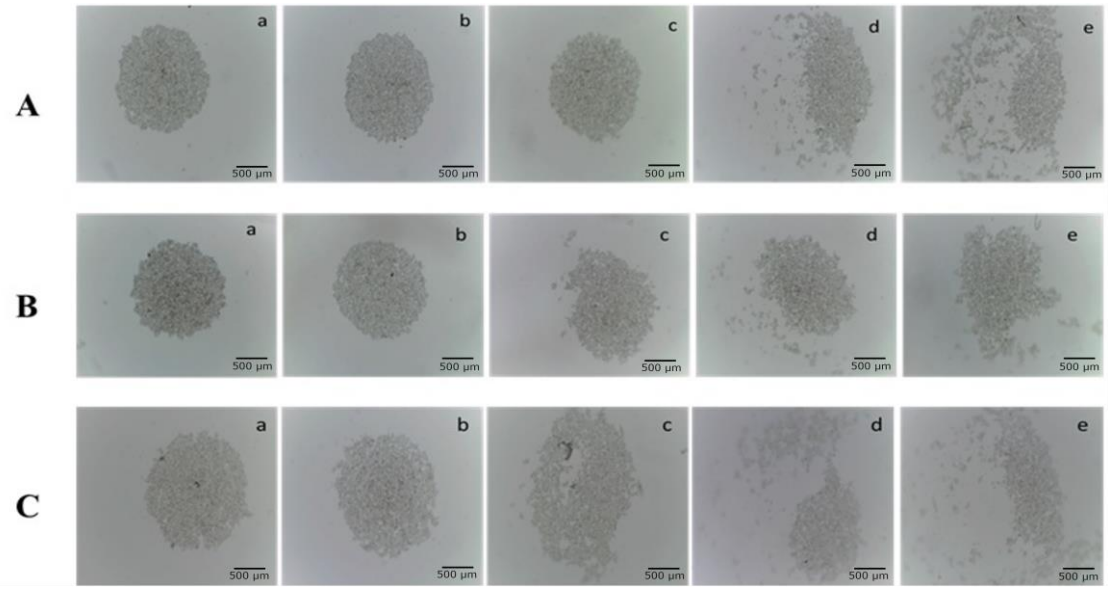

Fig. 5. Representative inverted microscopy images showing 3D spheroid formation of (A) MCF-7, (B) HT-29, and (C) HeLa cell lines cultured on various scaffold types after 7 days of incubation. All three cancer cell lines formed multicellular spheroid structures on the scaffolds. Morphological evaluation via inverted microscopy demonstrated that the cells predominantly exhibited a rounded, 3D architecture characteristic of spheroid morphology. (a) Agarose; (b) Phytagel; (c) Bovine skin gelatin; (d) Cold water fish gelatin; (e) Pig skin gelatin.

4. Conclusion

3D scaffold-based cell culture has become a crucial method in cancer research, offering a more accurate model to study tumor behavior, assess drug effectiveness, and explore interactions within the tumor microenvironment. Diverse scaffold materials such as hydrogels, polymers, decellularized matrices, and hybrid systems integrated with microfluidics have been engineered to create advanced and biomimetic 3D models. Notably, polymer-based scaffolds are distinguished by their adaptability, attributed to customizable mechanical properties and straightforward production methods.

This study focused on the development and characterization of innovative gelatin-based scaffolds for 3D cell culture. The analysis revealed a highly porous architecture with appropriate pore sizes in all compositions, promoting effective cell infiltration as well as nutrient and waste exchange. Additionally, in vitro evaluations confirmed that these scaffolds effectively support the formation of 3D cell spheroids.

Spheroid formation experiments were performed using HT-29, MCF-7, and HeLa cancer cell lines, all of which successfully grew on scaffolds, forming well-defined spheroid structures. Morphological analysis through inverted microscopy revealed predominantly 3D round cell morphologies, along with clear evidence of 3D cell-cell and cell-matrix interactions. Among the gelatin-based scaffolds, those prepared with bovine skin gelatin demonstrated the highest performance. The possible reason for this may be that bovine skin gelatin supports cell spreading due to its lower hardness. Furthermore, this study revealed that bovine skin gelatin-based scaffolds provide a more favorable microenvironment for optimal growth of MCF-7 cells in 3D culture compared to other cancer cell lines. This may be related to the stable pore structure, biocompatibility, mechanical strength and rich protein content of bovine skin gelatin, which promotes cell adhesion. Such scaffolds offer significant potential for biomedical applications such as 3D tumor modeling and drug testing. These results highlight that gelatin scaffolds offer an enhanced microenvironment for cancer cell proliferation. Collectively, the observed growth, proliferation, and spheroid

formation across all scaffold compositions demonstrate their promise for cell culture studies. Because these scaffolds can mimic the 3D structure of tumors, they can be used to more accurately study the natural behavior of cancer cells (proliferation, migration and invasion). They can be used in drug discovery processes by providing a more realistic environment to test the efficacy and side effects of anticancer drugs. Due to their biocompatible structures, they can be evaluated in drug delivery and controlled release systems and drug formulations due to their porosity. The developed scaffolds can promote cell infiltration, proliferation and ECM secretion to support regeneration of soft tissues (e.g. skin, muscle or connective tissue). These scaffolds enable the development of organoid models by preserving the phenotype of the cells and creating long-term biological structures. As a result, these scaffolds provide a promising platform for cell growth and tissue regeneration in biological and pharmaceutical research, preclinical testing, and tissue engineering applications.

Although this study successfully demonstrated the formation of 3D spheroid structures using various gelatin-based scaffolds, it has certain limitations that should be acknowledged. Firstly, the findings are based solely on in vitro assays, and in vivo validation has not yet been performed to confirm the physiological relevance and tumor-mimicking potential of the developed scaffolds within a living system. Secondly, while morphological observations and spheroid formation were assessed, no functional analyses such as apoptosis, cell viability (e.g., live/dead or metabolic activity assays like MTT), or gene/protein expression profiling were conducted to further elucidate the biological behavior of the cancer cells within the 3D microenvironment. Additionally, comparative evaluation was limited to traditional 2D monolayer culture in a general context, without detailed quantitative or functional benchmarking against 2D systems. In addition, using only MCF-7, HeLa, and HT-29 cell lines in this study does not sufficiently represent all cancer types or the biological diversity of tumors. Furthermore, since long-term culture results were not evaluated, it does not provide sufficient information about important parameters such as phenotypic stability, growth dynamics, and viability of the cells. These limitations indicate that the study's findings should be supported by more comprehensive tests in the future. Future research may explore the use of these scaffolds in therapeutic screening, in different types of cancer, in long-term 3D cultures, and broader research applications for validation.

Acknowledgements

We would like to thank Karamanoğlu Mehmetbey University Scientific Research Projects Commission for supporting this project numbered 06-M-23.

Ethical Approval

This study does not require study-specific approval by the appropriate ethics committee for research involving human subjects and/or animals.

Author Contribution

All authors contributed to the study conception and design. Material preparation, data collection and analysis were performed by Bahar Yılmaz and Mukaddes Keskinateş. Bahar Yılmaz: investigation, methodology, data curation, writing original draft, and validation. Esra Armağan: investigation, methodology, data curation, and writing original draft. Mukaddes Keskinateş: investigation, methodology, data curation, and writing original draft. Ziya Aydın: investigation, methodology, data curation, writing original draft, and validation. Mevlüt Bayrakcı: investigation, methodology, data curation, writing original draft, and validation. All authors read and approved the final manuscript.

References

[1] W. H. Abuwatfa, W. G. Pitt, and G. A. Husseini, "Scaffold-based 3D cell culture models in cancer research," *J Biomed Sci*, vol. 31, no. 1, pp. 7, 2024, doi: 10.1186/s12929-024-00994-y.

[2] E. D'Imprima *et al.*, "Light and Electron Microscopy Continuum-Resolution Imaging of 3D Cell Cultures," *Developmental cell*, vol. 58, no. 7, pp. 616-632.e6., 2023, doi: 10.1016/j.devcel.2023.03.001.

[3] K. Duval *et al.*, "Modeling Physiological Events in 2D vs. 3D Cell Culture," *Physiology (Bethesda, Md.)*, vol. 32, no. 4, pp. 266–277, 2017, doi: 10.1152/physiol.00036.2016.

[4] M. Sun *et al.*, "3D Cell Culture-Can It Be As Popular as 2D Cell Culture?," *Advanced NanoBiomed Research*, vol. 1, no. 5, 2021, doi: 10.1002/anbr.202000066.

[5] B. Weigelt, C. M. Ghajar, and M. J. Bissell, "The Need for Complex 3D Culture Models to Unravel Novel Pathways and Identify Accurate Biomarkers in Breast Cancer," *Advanced drug delivery reviews*, vol. 69–70, pp. 42–51, 2014, doi: 10.1016/j.addr.2014.01.001.

[6] D. Lv, Z. Hu, L. Lu, H. Lu, and X. Xu, "Three-dimensional Cell Culture: A Powerful Tool in Tumor Research and Drug Discovery," *Oncology Letters*, vol. 14, no. 6, pp. 6999–7010, 2017, doi: 10.3892/ol.2017.7134.

[7] E. Knight and S. Przyborski, "Advances in 3D Cell Culture Technologies Enabling Tissue-Like Structures to be Created in vitro," *Journal of Anatomy*, vol. 227, no. 6, pp. 746–756, 2015, doi: 10.1111/joa.12257.

[8] K. Kretzschmar and H. Clevers, "Organoids: Modeling Development and the Stem Cell Niche in a Dish," *Developmental cell*, vol. 38, no. 6, pp. 590–600, 2016, doi: 10.1016/j.devcel.2016.08.014.

[9] D. Erden Gönenmiş, "Hibrit Nanobiyomalzemeler İçeren Kemik Doku İskelelerinin Geliştirilmesi ve Karakterizasyonu", Yüksek lisans tezi, Pamukkale Üniversitesi Fen Bilimleri Enstitüsü, Türkiye, 2021.

[10] A. V. Samrot *et al*., "Scaffold using chitosan, agarose, cellulose, dextran and protein for tissue engineering—A review," *Polymers*, vol. 15, no. 6, pp. 1525, 2023, doi: 10.3390/polym15061525.

[11] M. W. Tibbitt and K. S. Anseth, "Hydrogels as Extracellular Matrix Mimics for 3D Cell Culture," *Biotechnology and bioengineering*, vol. 103, no. 4, pp. 655–663, 2009, doi: 10.1002/bit.22361.

[12] F. Akther, P. Little, Z. Li, N. T. Nguyen, and H. T. Ta, "Hydrogels as artificial matrices for cell seeding in microfluidic devices," *RSC Advances*, vol.10, no. 71, pp. 43682–43703, 2020, doi: 10.1039/d0ra08566a.

[13] B. A. Rashid, N. N. Showva, and M. E. Hoque, "Gelatin-Based Scaffolds: An Intuitive Support Structure for Regenerative Therapy," *Current Opinion in Biomedical Engineering*, vol. 26, no. 100452, 2023, doi: 10.1016/j.cobme.2023.100452.

[14] T. Nuge, K. Y. Tshai, S. S. Lim, N. Nordin, and M. E. Hoque, "Preparation and Characterization of Cu, Fe-, Ag-, Zn- and Ni- Doped Gelatin Nanofibers for Possible Applications in Antibacterial Nanomedicine," *Journal of Engineering Science and Technology*, vol. 12, no. 1, pp. 68–81, 2017.

[15] R. R. Besser *et al.*, "Enzymatically Crosslinked Gelatin-Laminin Hydrogels for Applications in Neuromuscular Tissue Engineering," *Biomaterials science*, vol. 8, no. 2, pp. 591–606, 2020, doi: 10.1039/c9bm01430f.

[16] M. Băbuțan and I. Botiz, "Morphological Characteristics of Biopolymer Thin Films Swollen-Rich in Solvent Vapors," *Biomimetics*, vol. 9, no. 7, pp. 396, 2024, doi: 10.3390/biomimetics9070396.

[17] A. Tejo-Otero *et al.*, "Soft-Tissue-Mimicking Using Hydrogels for the Development of Phantoms," *Gels*, vol. 8, no. 1, pp. 40, 2022, doi: 10.3390/gels8010040.

[18] G. Xu, F. Yin, H. Wu, X. Hu, L. Zheng, and J. Zhao, "In vitro ovarian cancer model based on three-dimensional agarose hydrogel," *Journal of tissue engineering*, vol. 5, 2041731413520438, 2014, doi: 10.1177/2041731413520438.

[19] S. Suvarnapathaki, M. A. Nguyen, X. Wu, S. P. Nukavarapu, and G. Camci-Unal, "Synthesis and characterization of photocrosslinkable hydrogels from bovine skin gelatin," *RSC advances*, vol. 9, no. 23, pp. 13016–13025, 2019, doi: 10.1039/C9RA00655A.

[20] A. Maihemuti *et al*., "3D-printed fish gelatin scaffolds for cartilage tissue engineering," *Bioactive Materials*, vol. 26, pp. 77–87, 2023, doi: 10.1016/j.bioactmat.2023.02.007.

[21] B. Yilmaz, "Spektroskopik Teknikler Kullanılarak Furosemid ile DNA Etkileşimlerinin İncelenmesi," *Bitlis Eren Üniversitesi Fen Bilimleri Dergisi*, vol. 10, no. 2, pp. 325–331, 2021, doi: 10.17798/bitlisfen.856526.

[22] S. Asim, E. Hayhurst, R. Callaghan, and M. Rizwan, "Ultra-low content physio-chemically crosslinked gelatin hydrogel improves encapsulated 3D cell culture," *International Journal of Biological Macromolecules*, vol. 264, 130657, 2024, doi: 10.1016/j.ijbiomac.2024.130657.

[23] S. Al-Ghadban, I. A. Pursell, Z. T. Diaz, K. L. Herbst, and B. A. Bunnell, "3D Spheroids Derived from Human Lipedema ASCs Demonstrated Similar Adipogenic Differentiation Potential and ECM Remodeling to Non-Lipedema ASCs In Vitro," *International Journal of Molecular Sciences*, vol. 21, no. 21, pp. 8350, 2020, doi: 10.3390/ijms21218350.

[24] H. A. Awad, M. Q. Wickham, H. A. Leddy, J. M. Gimble, and F. Guilak, "Chondrogenic Differentiation of Adipose-Derived Adult Stem Cells in Agarose, Alginate, and Gelatin Scaffolds," *Biomaterials*, vol. 25, no. 16, pp. 3211–3222, 2004, doi: 10.1016/j.biomaterials.2003.10.045.

[25] B. Altinok Yilmaz, M. Keskinates, and M. Bayrakci, "Protein Adsorpsiyon Çalışmaları için Metal Şelat Grupları İçeren pHEMA-GMA Kolon Dolgu Malzemelerinin Hazırlanması," *Niğde Ömer Halisdemir Üniversitesi Mühendislik Bilimleri Dergisi*, vol.13, no. 2, pp. 1–1, 2024, doi: 10.28948/ngumuh.1382364.

[26] H. Mohammadi, M. Sepantafar, N. Muhamad, and A. Bakar Sulong, "How does scaffold porosity conduct bone tissue regeneration?," *Advanced Engineering Materials*, vol. 23, no. 10, 2100463, 2021, doi: 10.1002/adem.202100463.

[27] B. Yilmaz, A. T. Bayrac, and M. Bayrakci, "Evaluation of Anticancer Activities of Novel Facile Synthesized Calix[n]arene Sulfonamide Analogs," *Applied Biochemistry and Biotechnology*, vol. 190, no. 4, pp. 1484–1497, 2020, doi: 10.1007/s12010-019-03184-x.

[28] J. Friedrich, C. Seidel, R. Ebner, and L. A. Kunz-Schughart, "Spheroid-based drug screen: considerations and practical approach,"*Nature protocols*, vol. 4, no. 3, pp. 309–324, 2009, doi: 10.1038/nprot.2008.226.
[29] S. Melissaridou *et al*., "The effect of 2D and 3D cell cultures on treatment response, EMT profile and stem cell features in head and neck cancer," *Cancer cell international*, vol. 19, pp. 1–10, 2019, doi: 10.1186/s12935-019-0733-1.
[30] M. N. Khan, J. M. Islam, and M. A. Khan, "Fabrication and characterization of gelatin-based biocompatible porous composite scaffold for bone tissue engineering," *Journal of biomedical materials research Part A*, vol. 100, no. 11, pp. 3020–3028, 2012, doi: 10.1002/jbm.a.34248.
[31] N. Kartikasari *et al*., "Characteristic of bovine hydroxyapatite-gelatin-chitosan scaffolds as biomaterial candidate for bone tissue engineering," *2016 IEEE EMBS Conference on Biomedical Engineering and Sciences (IECBES*), Kuala Lumpur, Malaysia, 2016, pp. 623–626, doi: 10.1109/IECBES.2016.7843524.
[32] A. Quarta *et al*., "Investigation on the composition of agarose–collagen i blended hydrogels as matrices for the growth of spheroids from breast cancer cell lines," *Pharmaceutics*, vol. 13, no. 7, pp. 963, 2021, doi: 10.3390/pharmaceutics13070963.
[33] L. E. Nita *et al*., "New hydrogels based on agarose/phytagel and peptides," *Macromolecular Bioscience*, vol. 23, no. 3, 2200451, 2023, doi: 10.1002/mabi.202200451.
[34] W. Dai, N. Kawazoe, X. Lin, J. Dong, and G. Chen, "The Influence of Structural Design of PLGA/Collagen Hybrid Scaffolds in Cartilage Tissue Engineering," *Biomaterials*, vol. 31, no. 8, pp. 2141–2152, 2010, doi: 10.1016/j.biomaterials.2009.11.070.
[35] H. W. Liu, W. T. Su, C. Y. Liu, and C. C. Huang, "Highly Organized Porous Gelatin-Based Scaffold by Microfluidic 3D-Foaming Technology and Dynamic Culture for Cartilage Tissue Engineering," *International Journal of Molecular Sciences*, vol. 23, no. 15, pp. 8449, 2022, doi: 10.3390/ijms23158449.
[36] M. P. Nikolova and M. S. Chavali, "Recent advances in biomaterials for 3D scaffolds: A review," *Bioactive materials*, vol. 4, pp. 271–292, 2019, doi: 10.1016/j.bioactmat.2019.10.005.
[37] A. Oryan, P. Sharifi, A. Moshiri, and I. A. Silver, "The role of three-dimensional pure bovine gelatin scaffolds in tendon healing, modeling, and remodeling: an in vivo investigation with potential clinical value," *Connective Tissue Research*, vol. 58, no. 5, pp. 424–437, 2016, doi: 10.1080/03008207.2016.1238468.
[38] M. C. Varley *et al*., "Cell structure, stiffness and permeability of freeze-dried collagen scaffolds in dry and hydrated states," *Acta biomaterialia*, vol. 33, pp. 166–175, 2016, doi: 10.1016/j.actbio.2016.01.041.
[39] X. Liu and P. X. Ma, "Polymeric scaffolds for bone tissue engineering," *Annals of biomedical engineering*, vol. 32, pp. 477-486, 2004, doi: 10.1023/B:ABME.0000017544.36001.8e.
[40] A. C. Jones *et al*., "The correlation of pore morphology, interconnectivity and physical properties of 3D ceramic scaffolds with bone ingrowth," *Biomaterials*, vol. 30, no. 7, pp. 1440–1451, 2009, doi: 10.1016/j.biomaterials.2008.10.056.
[41] P. Chailom, T. Pattarakankul, T. Palaga, and V. P. Hoven, "Fish Gelatin-Hyaluronic Acid Scaffold for Construction of an Artificial Three-Dimensional Skin Model,".*ACS omega*, vol. 10, no. 8, pp. 8172–8181, 2025, doi: 10.1021/acsomega.4c09708.
[42] A. Asti and L. Gioglio, "Natural and Synthetic Biodegradable Polymers: Different Scaffolds for Cell Expansion and Tissue Formation," *The International Journal of Artificial Organs*, vol. 37, no. 3, pp. 187–205, 2014, doi: 10.530/ijao.5000307.
[43] E. C. Costa, D. de Melo-Diogo, A. F. Moreira, M. P. Carvalho, and I. J. Correia, "Spheroids Formation on Non-Adhesive Surfaces by Liquid Overlay Technique: Considerations and Practical Approaches," *Biotechnology Journal*, vol. 13, no. 1, 10.1002/biot.201700417, 2018, doi: 10.1002/biot.201700417.
[44] B. Thongrom, P. Tang, S. Arora, and R. Haag, "Polyglycerol-Based Hydrogel as Versatile Support Matrix for 3D Multicellular Tumor Spheroid Formation," *Gels*, vol. 9, no.12, pp. 938, 2023, doi: 10.3390/gels9120938.
[45] A. A. Haroun, M. A. Abo-Zeid, A. M. Youssef, and A. Gamal-Eldeen, "In vitro biological study of gelatin/PLG nanocomposite using MCF-7 breast cancer cells," *Journal of Biomedical Materials Research Part A*, vol. 101, no. 5, pp. 1388-1396, 2013, doi: 10.1002/jbm.a.34441.
[46] N. Arya, V. Sardana, M. Saxena, A. Rangarajan, and D. S. Katti, "Recapitulating tumour microenvironment in chitosan-gelatin three-dimensional scaffolds: an improved in vitro tumour model," *J R Soc Interface*, vol. 9, no. 77, pp. 3288–302, 2012, doi: 10.1098/rsif.2012.0564.
[47] M. Ghafouri Azar *et al*., "Optimizing PCL/PLGA Scaffold Biocompatibility Using Gelatin from Bovine, Porcine, and Fish Origin," *Gels*, vol. 9, no. 11, pp. 900, 2023, doi: 10.3390/gels9110900.
[48] M. Kapałczyńska *et al*., "2D and 3D cell cultures–a comparison of different types of cancer cell cultures," *Archives of medical science*, vol. 14, no. 4, 910–919, 2018, doi: 10.5114/aoms.2016.63743.
[49] L. Chen *et al*., "The enhancement of cancer stem cell properties of MCF-7 cells in 3D collagen scaffolds for modeling of cancer and anti-cancer drugs," *Biomaterials*, vol. 33, no. 5, 1437–1444, 2012, doi: 10.1016/j.biomaterials.2011.10.056.
[50] J. L. Horning *et al*., "3-D tumor model for in vitro evaluation of anticancer drugs," *Molecular pharmaceutics*, vol. 5, no. 5, 849–862, 2008, doi: 10.1021/mp800047v.
[51] C. Godugu, A. R. Patel, U. Desai, T. Andey, A. Sams, and M. Singh, "AlgiMatrix™ based 3D cell culture system as an in-vitro tumor model for anticancer studies," *PloS one*, vol. 8, no. 1, e53708, 2013, doi: 10.1371/journal.pone.0053708.
[52] M. Zanoni *et al*., "3D tumor spheroid models for in vitro therapeutic screening: a systematic approach to enhance the biological relevance of data obtained," *Scientific reports*, vol. 6, no. 1, 19103, 2016, doi: 10.1038/srep19103.
[53] J. C. Fontoura *et al*., "Comparison of 2D and 3D cell culture models for cell growth, gene expression and drug resistance," *Materials Science and Engineering: C*, vol. 107, 110264 , 2020, doi: 10.1016/j.msec.2019.110264.

Contents lists available at *Dergipark*

Journal of Scientific Reports-A

journal homepage: *https://dergipark.org.tr/tr/pub/jsr-a*

E-ISSN: 2687-6167 ***Number 61, June 2025***

RESEARCH ARTICLE

Receive Date: 16.01.2025 *Accepted Date: 29.05.2025*

Analysis of LiDAR system performance through analogy with FSO communication systems

Bünyamin Kaya[a]* , Ahmet Altuncu[b]

[a]*Kütahya Dumlupınar University, Department of Electric- Electronic Engineering, Kütahya*
Nursan Kablo Donanımları San. ve Tic. A.Ş. Kütahya 43300, Türkiye
ORCID: 0000-0002-9907-2826
[b]*Afyon Kocatepe University, Department of Electric-Electronic engineering, Afyonkarahisar, Türkiye*
ORCID: 0000-0002-3753-9515

Abstract

LiDAR (Light Detection and Ranging) systems are used in autonomous vehicle technology and environmental sensing applications. In this study, the performance of LiDAR systems is simulated by adapting it to a free space optical (FSO) communication system and analyzed using this approach. OptiSystem software was used in the simulation studies and different atmospheric conditions such as clear, rainy and extremely foggy weather conditions were considered. The performance of LiDAR systems under these conditions was evaluated; the effects of features on the backscattering ratios of the backscattered signals from the target surface and the effects of these outputs on system performance were evaluated. The results were analyzed to show that atmospheric conditions and target reflection rates affect the LiDAR system performance and that the received pulse quality is negatively affected by increasing the detection distance.

Keywords: LiDAR; Free-Space Optical Communication; FSO; BER Analysis; OptiSystem Simulation; Performance Analysis.

1. Introduction

Optical communication systems have attracted significant attention due to their ability to provide high-speed data transmission with low latency and high reliability. In addition to conventional fiber-optic systems, Free Space Optical

* Corresponding author. Tel.: +0 555-641-23-77;
E-mail address: bunyasacademy@gmail.com

(FSO) systems have emerged as a flexible, energy-efficient [1] and high-bandwidth an alternatives that operate without the need for fiber waveguides, relying instead on FSO-based propagation principles [2,3,4].

However, the performance of FSO systems is significantly affected by absorption, scattering and turbulence-induced degradation [5,6,7,8], and the stability and reliability of FSO links are also adversely impacted by environmental factors such as rain, fog, snow, dust and high particulate concentrations in the atmosphere [9,10].

Specifically, in low density foggy and dusty environments, the system can provide successful transmission over longer distances, while the transmission distance is significantly shortened in medium and high density foggy and dusty conditions [11,12]. Consequently, the Bit Error Rate (BER) increases while the Q-Factor decreases.

Similarly, LiDAR (Light Detection and Ranging) is a technology that uses laser beams to perform high-resolution and precise distance measurements and can operate under various atmospheric conditions. Therefore, LiDAR systems are widely used in applications such as environmental sensing and object recognition in next-generation autonomous vehicles [13].

Due to the propagation of laser beams through the atmosphere and their reliance on reflections from objects, LiDAR systems, like FSO systems, are affected by atmospheric conditions. This leads to performance degradation in terms of detection range and accuracy [8,14,15,16].

For instance, in [17], sensitivity and accuracy evaluations were carried out using different reflective targets in the range of 5 to 180 m, and it was shown that in many systems, the detection capability decreases with increasing distance depending on the reflectivity.

Similarly, [13] also emphasises the effect of atmospheric conditions on detection accuracy and the importance of signal processing methods. In [18], Optical Code Division Multiple Access (OCDMA) technology was proposed to mitigate mutual interference effects in LiDAR systems, reducing the false alarm rate from 90% to 2%. Additionally, using a Lambert surface model and a theoretical analysis method, the effects of parameters such as interference distance and angle on detection and false alarm performance were examined in detail [19].

The optical similarities between LiDAR and FSO systems—including shared components and atmospheric behavior—are key to enabling accurate cross-domain modeling and performance prediction. Therefore, the analogy between LiDAR system parameters and FSO communication systems offers opportunities for both the performance evaluation of existing systems and the development of next-generation technologies.

In this study, unlike the communication-oriented FSO analyses in the literature, the FSO channel structure is analysed by analogy to evaluate the LiDAR detection performance. The analogy relates FSO and LiDAR systems from both a performance-based evaluation perspective and a sensing performance enhancement perspective. In this context, the performance parameters of LiDAR systems are compared with those of FSO communication systems, and analyses were conducted using the OptiSystem V21 software. In this simulation, a lens-free LiDAR system is implemented by inserting a coreless fiber tip spliced at the end of optical transmission fiber cable with 0.125 mm cladding diameter to serve as optical transmitter and receiver pairs with a constant aperture diameter in the given FSO channel. Although there are several experimental studies showing the channel behavior of FSO systems under different atmospheric conditions, studies conducted by drawing an analogy to LiDAR systems are very limited. The aim of this study is both to develop a simulation model that resembles a LiDAR system using the FSO model and to use this model for a lens-free, fully optical fiber based LiDAR design capable of short-range detection, by employing coreless fiber tips spliced to fiber cables as transmitter and receiver apertures. In the simulations conducted using the proposed LiDAR design, various atmospheric conditions (clear, rainy, and foggy weather conditions) and target reflectivity levels (10%, 35%, 60%, 90%) were considered, and the results have shown the critical factors affecting the performance of LiDAR systems.

2. Method

The LiDAR-FSO system model used in the simulations is given schematically in Figure 1. The LiDAR-FSO system model created in OptiSystem V21 software is also shown in Figure 2. Detailed information about the subsystem parameters used in OptiSystem V21 software is given in Table 1.

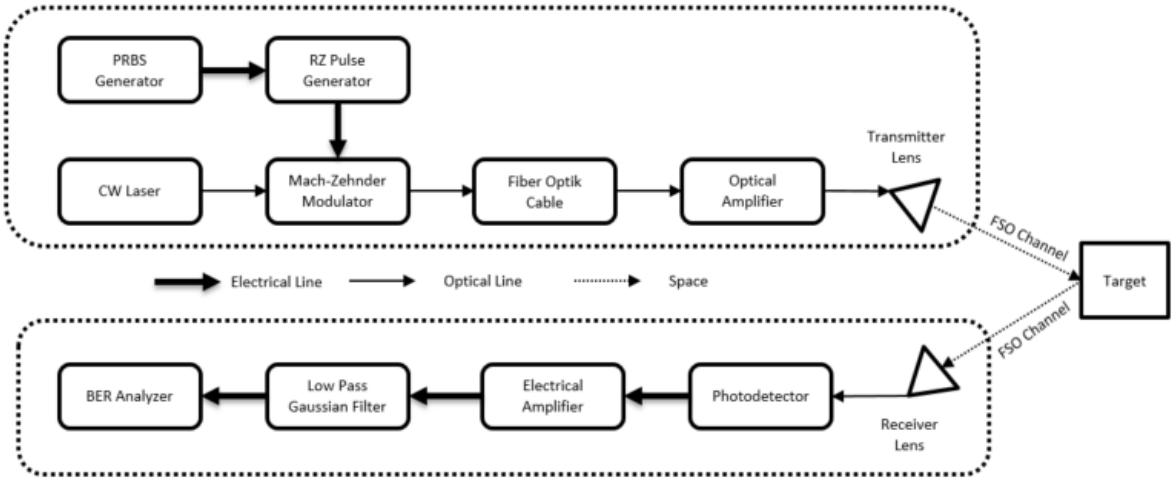

Fig. 1. LiDAR-FSO system model

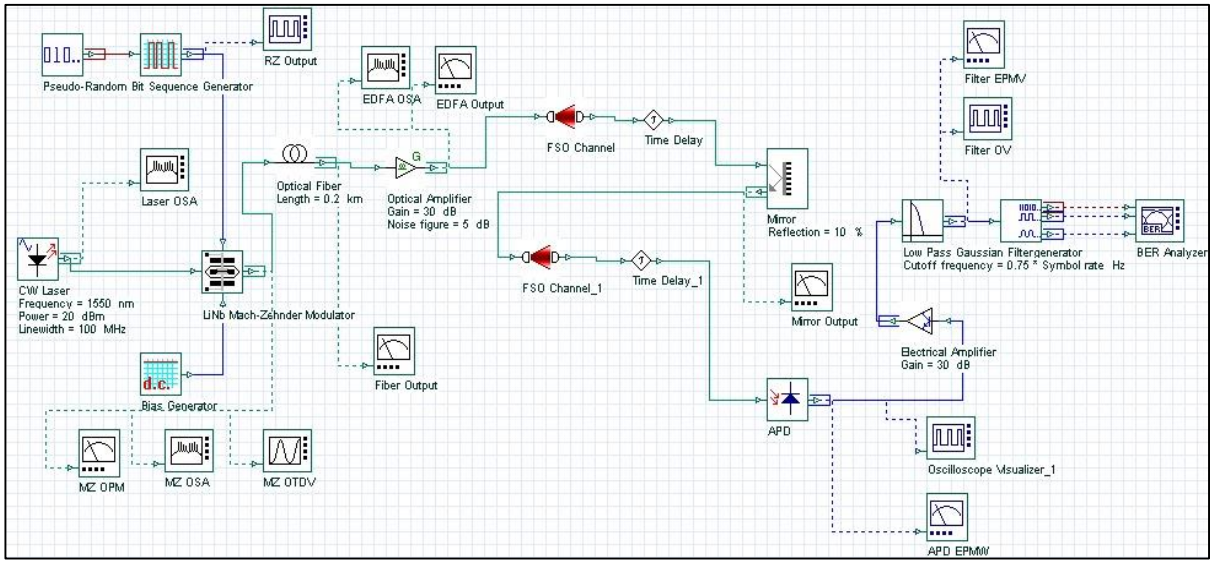

Fig. 2. LiDAR-FSO simulation schematics realized in OptiSystem V21.

Table 1. Subsystem specifications used in the simulations.

Product Name	Parameters	Its function in the LiDAR-FSO System
Pseudo-random bit sequence generator.	Bit rate: 1+E6 bit/s.	Provides PRBS data for modulation of the transmitted signal in the LiDAR-FSO system.
RZ-pulse generator.	Duty cycle: 0.01 bit.	It functions as a pulse shaper to generate RZ-type LiDAR pulses.
CW laser.	Wavelength : 1550 nm, output power: +20 dBm, linewidth: 100 MHz.	A CW laser source with a low loss and eye-safe wavelength in the atmosphere for LiDAR-FSO applications (1550 nm).
Mach-Zehnder modulator.	LiNbO3 MZ modulator with a variable bias input.	It allows generation of LiDAR pulses in the form of RZ-modulated PRBS data.
Optical amplifier (EDFA).	Gain: 30 dB, noise figure: 5 dB.	Enhances the optical LiDAR pulse power to compensate for the losses in the LiDAR-FSO channel.
Optical fiber.	Length: 0.2 km, standard single-mode fiber (S-SMF) link with attenuation of 0.2 dB/km and dispersion of 16.75 ps/nm/km.	It is used to transmit LiDAR pulses to the FSO transmitter.
FSO channel.	Distance: 20-30-40-50-60-70-80 m, attenuation: 1.875 - 12.5 - 18.75 dB/km. Transmitter and receiver aperture diameter: 0.125 mm (coreless fiber diameter).	It models the FSO link at optical frequencies under different atmospheric conditions resembling LiDAR systems.
Mirror reflector.	Reflection: 10% - 35% - 60% - 90% [20].	It simulates the back reflections arising from the other vehicles and obstacles in the LiDAR system.
APD (Avalanche photodiode).	High sensitivity and responsivity at 1550 nm.	It converts low pulse energy LiDAR pulses reflected back into electrical pulses.
Electrical amplifier.	30 dB gain.	Enhances the electrical LiDAR pulses.
Low pass filter.	Cut frequency: 0.75 x symbol rate.	Improves SNR in LiDAR signals by reducing out-of-band noise.
BER analyzer.	Bit error rate measurement.	It analyses the BER performance of the FSO channel resembling to LiDAR system.

2.1. FSO channel model

FSO Channel is a subsystem consisting of an FSO transmitter with a variable aperture, a free space link with variable atmospheric parameters, and an FSO receiver with a variable aperture. In the designed system, two FSO links were used resembling the links from the transmitter to the mirror reflector and from the mirror reflector to the receiver [3]. The FSO link parameters include the propagation distance between 20-80 m for one way, free space attenuation under different atmospheric conditions such as clear, rainy, and foggy weather, and transmitter and receiver aperture diameters. In the FSO channel, the transmitter and receiver aperture diameters were kept at 0.125 mm resembling a coreless fiber tip emitter/collector under the scenario of a fiber-coupled LiDAR system.

FSO channel has two main effects on the transmission of LiDAR pulses. The first parameter is power attenuation of the laser light in the atmosphere under different weather conditions. The second parameter is geometric loss and occurs due to the divergence of the transmitted beam between the transmitter and receiver. It is calculated using the aperture diameters of the transmitter and receiver and the beam divergence angle, as shown in Equation 1[3], and [21].

$$P_{Received} = P_{Transmitted} \cdot \frac{d_R^2}{[d_T+(D\cdot R)]^2} \cdot 10^{\left(-\frac{\alpha\beta}{10}\right)} \cdot 10^{\left(-\frac{TX}{10}\right)} \cdot 10^{\left(-\frac{RX}{10}\right)} \cdot 10^{\left(-\frac{AD}{10}\right)} \quad (1)$$

Where:

- $P_{Received}$: Received Power (W)
- $P_{Transmitted}$: Transmitted Power (W)
- d_T : Transmitter aperture diameter (m)
- d_R : Receiver aperture diameter (m)
- D : Beam divergence (mrad)
- R : Range (km)
- α : Atmospheric attenuation (dB/km)
- TX : Transmitter Loss (dB)
- RX : Receiver Loss (dB)
- AD : Additional Losses (dB)

In the simulations, the losses at the fiber-lens interface in the transmitter and lens-fiber interface in the receiver, i.e. coupling losses, are defined as transmitter loss (TX) and receiver loss (RX). Additional losses arising from scintillation, misalignment and other factors, is specified as Additional Losses (AD).

The propagation delay parameter enables to account the atmospheric turbulence effects between the transmitter and the receiver and therefore is included in the LiDAR-FSO model. To model atmospheric fading, which depends on intensity scintillation, a Gamma-Gamma distribution was used [21]. The probability of a given Intensity I is defined in Equation 2 [22].

$$P(I) = \frac{2(\alpha\beta)^{\frac{(\alpha+\beta)}{2}}}{\Gamma(\alpha)\cdot\Gamma(\beta)} \cdot I^{\frac{\alpha+\beta}{2}-1} \cdot K_{(\alpha-\beta)}\left(2\sqrt{(\alpha\beta I)}\right) \quad (2)$$

where, 1/α and 1/β represent the variances of small-scale and large-scale turbulence, respectively [21] as defined in Equations 3 and 4. [23] Γ(x) denotes the Gamma function, and $K_{\alpha-\beta}(x)$ represents the modified Bessel function of the second kind.

$$\alpha = exp\left[\frac{0{,}49\sigma R^2}{\left(1+0{,}69\sigma R^{\frac{12}{5}}\right)^{\frac{7}{6}}}\right] - 1 \quad (3)$$

$$\beta = exp\left[\frac{0{,}51\sigma R^2}{\left(1+0{,}69\sigma R^{\frac{12}{5}}\right)^{\frac{7}{6}}}\right] - 1 \quad (4)$$

The Rytov variance is calculated from:

$$\sigma R^2 = 1{,}23\, C_n^2\, k^{\frac{7}{6}}\, z^{\frac{11}{6}} \quad (5)$$

Here, the value of C_n^2 is the refractive index structure parameter, which ranges from 10^{-13} $m^{-2/3}$ for strong turbulence to 10^{-17} $m^{-2/3}$ for weak turbulence, k represents the optical wave number, and z is the parameter Range. Channel time variations are considered based on the theoretical quasi-static model, also known as the frozen channel model. According to this model, channel fading is assumed to remain constant over one symbol frame (coherence time) and changes to a new independent value from one frame to the next. [23]

2.2. Simulation results

In this study, firstly, the scenarios with different reflection ratios from the target surface (%10, %35, %60, and %90) were examined and the effect of reflection ratio on system performance was analyzed. During the simulations, the following parameters were used: a bit rate of 10 kbps, a duty cycle of 0.01, and a pulse width of 10 ns. The atmospheric attenuations based on weather conditions were determined as follows: 1.875 dB/km for clear weather, 12.5 dB/km for rainy weather, and 18.75 dB/km for dense foggy weather. The Q factor and BER variations obtained for different reflection ratios are given in Fig.3 as a function of mirror (target) distance. As shown in Fig.3, at a 10% reflection ratio, a reflecting pulse signal with a very low intensity was received from the target surface and hence this has caused a significant decrease in Q factor and an increase in BER value. It was observed that Q-Factor decreases to the accepted minimum value of 6 when the one-way distance (range) of the target was 60 m for clear weather, 55 m for rainy weather and 50 m for extremely foggy weather. The low reflection ratio of the target surface made the signal detection process more challenging as the distance increased, which, in turn, caused a considerable rise in bit error rates.

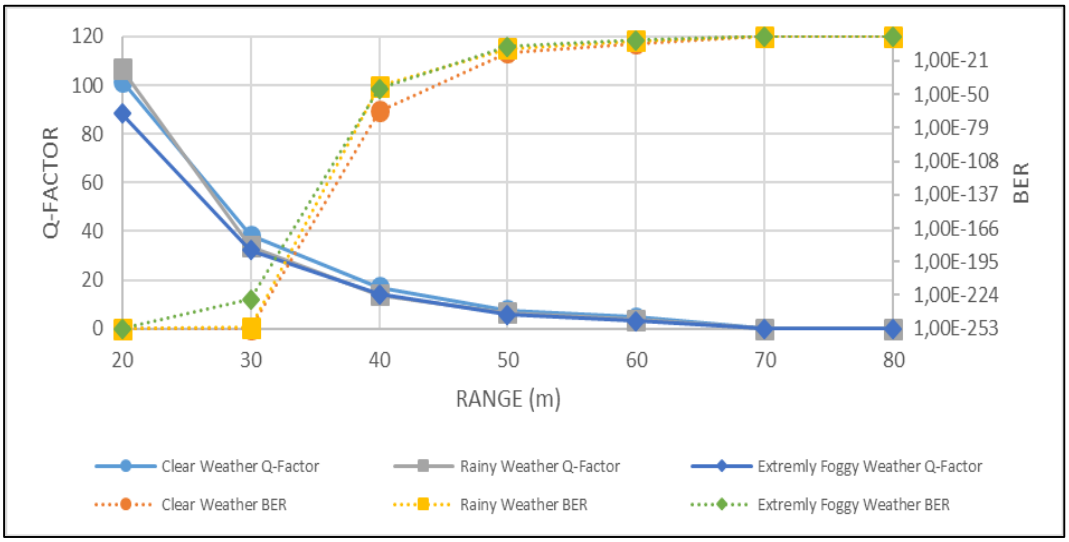

Fig. 3. Q-Factor and BER variation as a function of mirror (target) distance obtained under three atmospheric weather conditions (clear, rainy and extremely foggy weather) for the mirror reflection ratio of 10%.

Increasing the reflection ratio to 35% resulted in a significant improvement in system performance. As shown in Fig. 4, when the target's one-way distance (range) was 75m in clear weather, 65m in rainy weather, and 60m in extremely foggy weather, the Q-Factor was observed to drop to the minimum acceptable value of 6. This improvement was supported by an overall increase in Q-Factor and a decrease in BER value.

However, signal attenuation in rainy and extremely foggy weather conditions is higher. While the adverse effects on transmission performance were less pronounced compared to a 10% reflection rate, they still poses significant challenges to the system. Specifically, compared to the 10% reflection rate, difficulty in pulse detection has been reduced, and therefore BER performance improved. Nonetheless, it was evident that performance losses caused by environmental factors could not be eliminated.

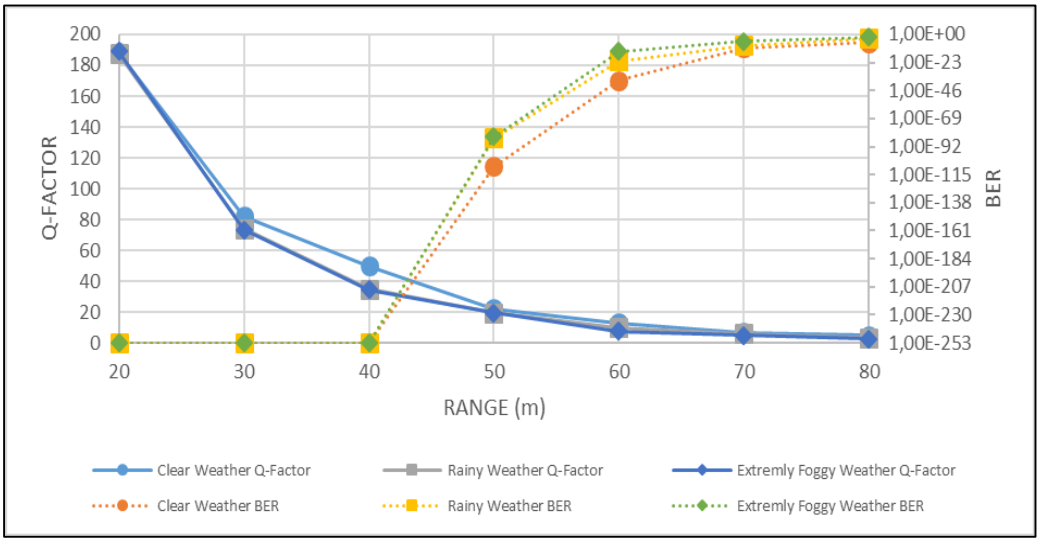

Fig. 4. Q-Factor and BER variation as a function of the mirror (target) distance obtained under three atmospheric weather conditions (clear, rainy and extremely foggy weather) for the mirror reflection ratio of 35%.

Increasing the mirror reflection ratio to 60% resulted in a significant improvement in signal transmission performance. As shown in Fig. 5, when the target's one-way distance (range) was 85m in clear weather, 80m in rainy conditions, and 75m in extremely foggy weather, the Q-Factor was observed to drop to the minimum acceptable value of 6.

Under clear weather conditions, Q-Factor values reached remarkably high levels, and the BER dropped to a minimum. In rainy weather, while transmission performance was more affected, Q-Factors and BER values have remained at acceptable levels. However, in extremely foggy weather condition, transmission performance continued to be adversely affected, leading to a significant decrease in Q factor and a noticeable increase in BER.

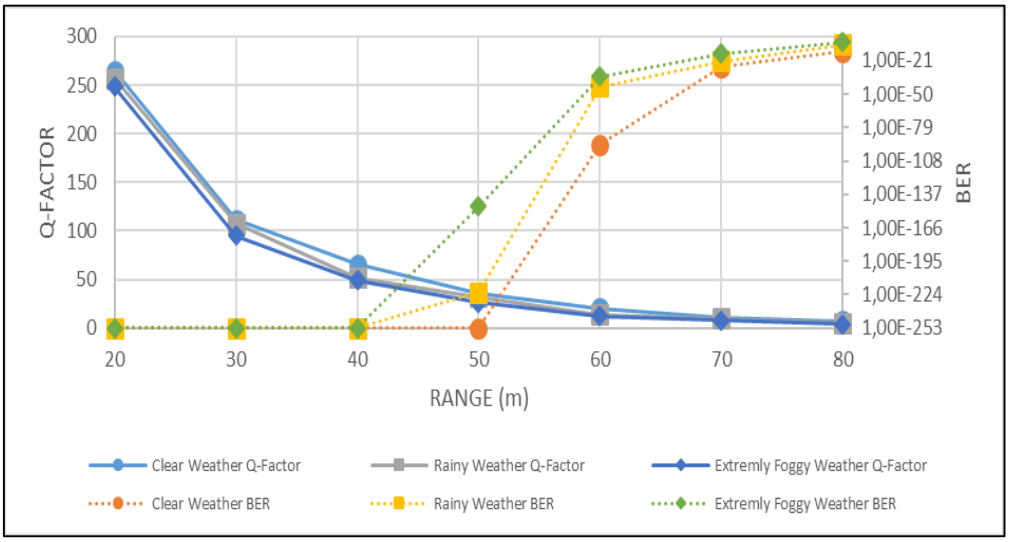

Fig. 5. Q-Factor and BER variation as a function of mirror (target) distance obtained under three atmospheric weather conditions (clear, rainy and extremely foggy weather) for the mirror reflection ratio of 60%.

Increasing the reflection ratio to 90% enabled perfectly receiving the strongly reflected pulses from the target surface, bringing transmission performance to its maximum level. As shown in Fig. 6, when the target's one-way distance (range) was 95m in clear weather, 85m in rainy conditions, and 80m in extremely foggy, the Q-Factor was observed to drop to the minimum acceptable value of 6.

Under clear weather conditions, Q-Factor values reached to maximum levels, and corresponding BER values have reduced to nearly zero. In rainy weather conditions, while system performance was slightly affected, it continued to operate with high Q factors. Even under extremely foggy conditions, the 90% reflection ratio has demonstrated an acceptable performance compared to less reflection ratios, with significantly improved signal detection and less BERs.

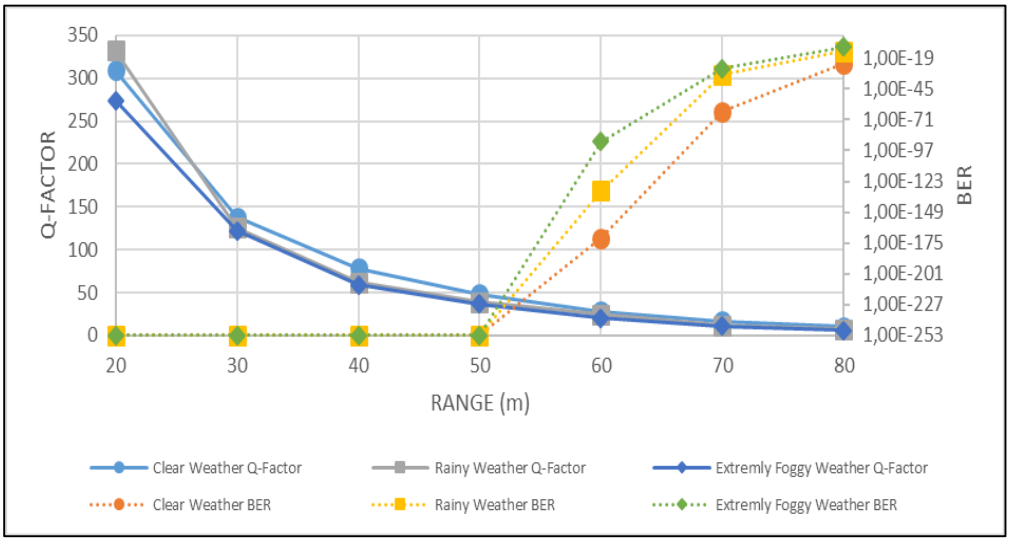

Fig. 6. Q-Factor and BER variation as a function of mirror (target) distance obtained under three atmospheric weather conditions (clear, rainy and extremely foggy weather) for the mirror reflection ratio of 90%.

In this study, secondly, the eye diagrams of the received pulses were obtained which play a critical role in evaluating signal quality under different LiDAR-FSO link conditions [15]. The received signal eye diagram was obtained under clear, rainy, and extremely foggy weather conditions together with the corresponding Q-Factors. Figures 7. a, b, c, and d display the eye diagrams of the received pulses under clear weather condition when the mirror reflection ratios are 10%, 35%, 60%, and 90%, respectively, for a target distance of 50 m. Measured Q factor and BER value are also given for each specific condition. The eye diagrams obtained show that an increase in the reflection ratio of the mirror leads to a significant improvement in back-reflected pulse quality, highlighting this parameter as a key factor influencing the performance of LiDAR-FSO systems. Although the level of obtained Q factors are sufficient for a reliable sensing of LiDAR back-reflected pulse, the intensity of the noise is significantly high for the reflection ratio of 10%.

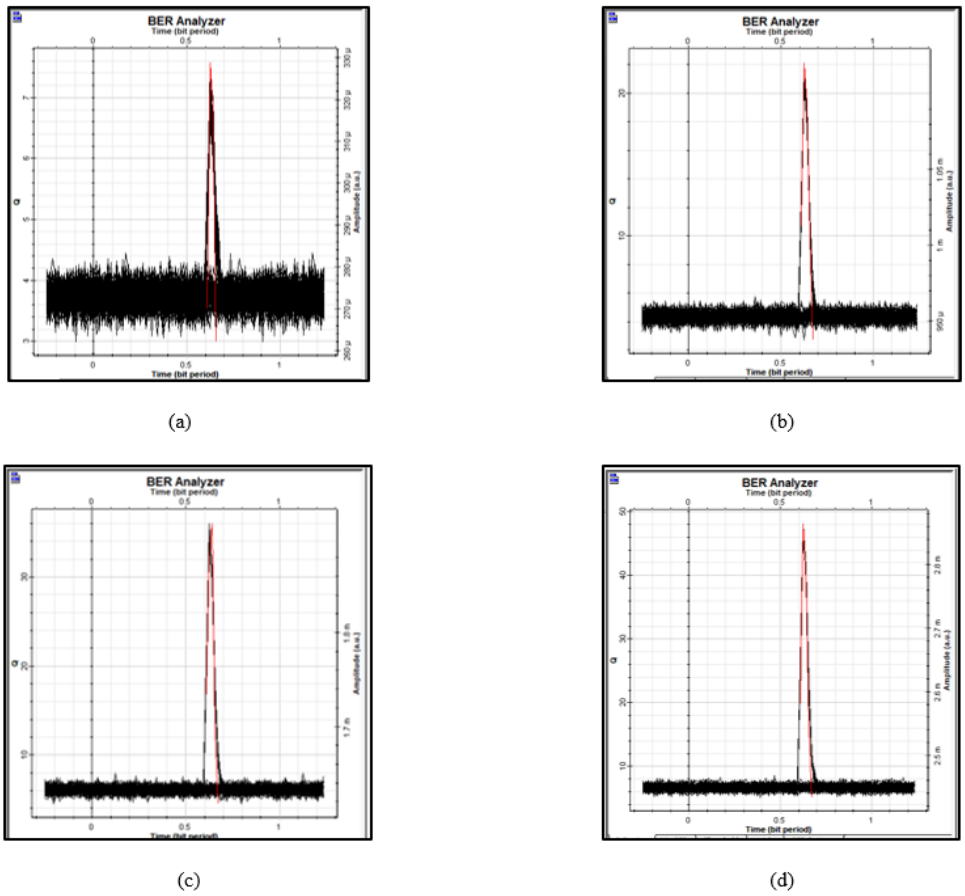

Fig. 7. (a). Eye diagram of the received signal obtained under clear weather condition for 10% reflection from the target, measured Q-Factor = 7.57, BER = 1.78e-14. (b). Eye diagram of the received signal obtained under clear weather condition for 35% reflection from the target, measured Q-Factor = 22.12, BER = 8.53e-109. (c). Eye diagram of the received signal obtained under clear weather condition for 60% reflection from the target, measured Q-Factor = 36.03, BER = 1e-253. (d). Eye diagram of the received signal obtained under clear weather condition for 90% reflection from the target, measured Q-Factor = 48.15, BER = 1e-253.

Under rainy weather conditions, Figures 8. a, b, c, and d illustrate the eye diagrams of pulses received at a 50 m target distance, with mirror reflection ratios of 10%, 35%, 60%, and 90%, respectively. The obtained eye diagrams clearly demonstrate that increasing the reflection ratio significantly improves back-reflected and received signal quality in rainy weather conditions, highlighting the critical role of this parameter in the performance of LiDAR-FSO systems.

While the Q-Factor achieved at each reflection ratio is sufficiently high for a reliable detection of the LiDAR back-reflected pulses, the noise intensity in rainy weather conditions is noticeably higher for all reflection ratios compared to clear weather. Specifically, at a 10% reflection rate, the noise level is significantly high, making the signal detection more challenging than under clear weather condition. These findings show that increasing the reflection ratio is not only crucial for optimizing LiDAR-FSO system performance in clear weather but also is required for improving received signal quality in rainy weather conditions.

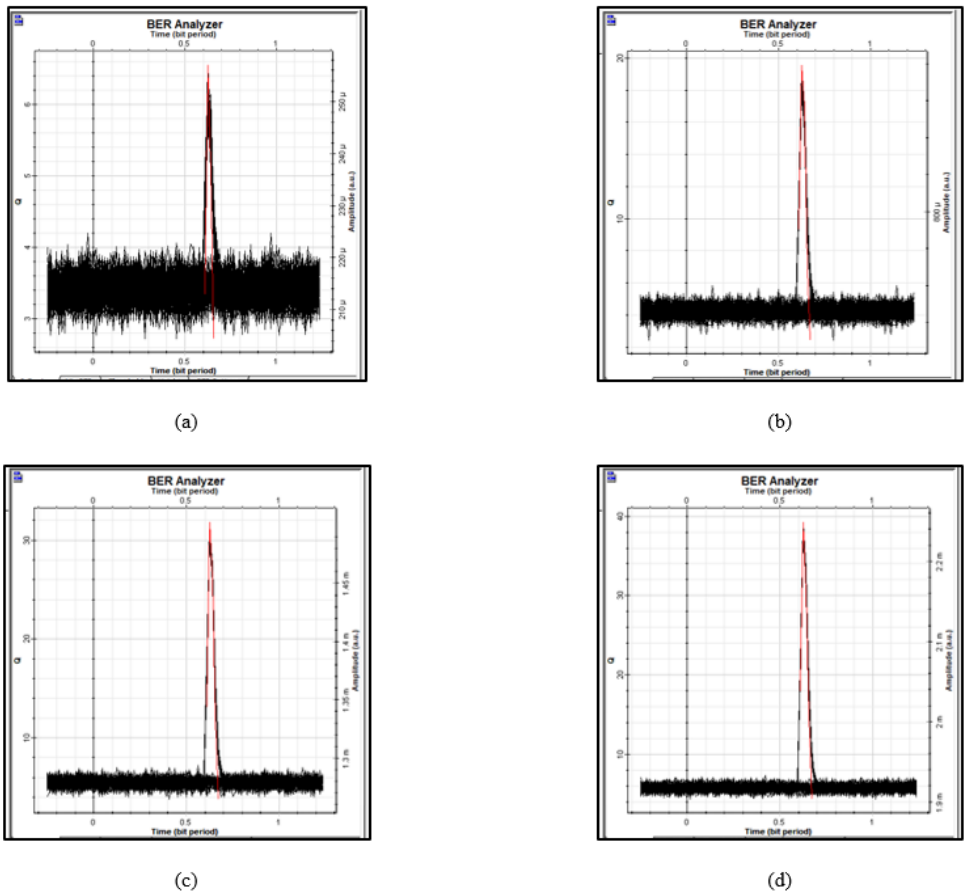

Fig. 8. (a) Eye diagram of the received signal obtained under rainy weather conditions for 10% reflection from the target, measured Q-Factor = 6.56, BER = 2.73e-11. (b) Eye diagram of the received signal obtained under rainy weather conditions for 35% reflection from the target, measured Q-Factor = 19.55, BER = 1.76e-85 (c) Eye diagram of the received signal obtained under rainy weather conditions for 60% reflection from the target, measured Q-Factor = 31.82, BER = 1.27e-222. (d) Eye diagram of the received signal obtained under rainy weather conditions for 90% reflection from the target, measured Q-Factor = 39.26, BER = 1e-253.

Under extremely foggy weather conditions, Figures 9. a, b, c, and d illustrate the eye diagrams of pulses received at a 50 m target distance, with mirror reflection ratios of 10%, 35%, 60%, and 90%, respectively. The obtained eye diagrams clearly demonstrate that increasing the reflection ratio improves optical received signal quality in extremely foggy weather conditions, highlighting the critical role of this parameter in the performance of LiDAR-FSO systems.

Although the Q-Factor achieved at each reflection ratio is sufficient for reliable detection of the LiDAR back-reflected pulse, it has been observed that the noise intensity in extremely foggy weather is significantly higher for all reflection ratios compared to clear and rainy weather conditions. Specifically, at a 10% reflection rate, the noise level increases further, making the signal detection process considerably more challenging than in clear or rainy weather.

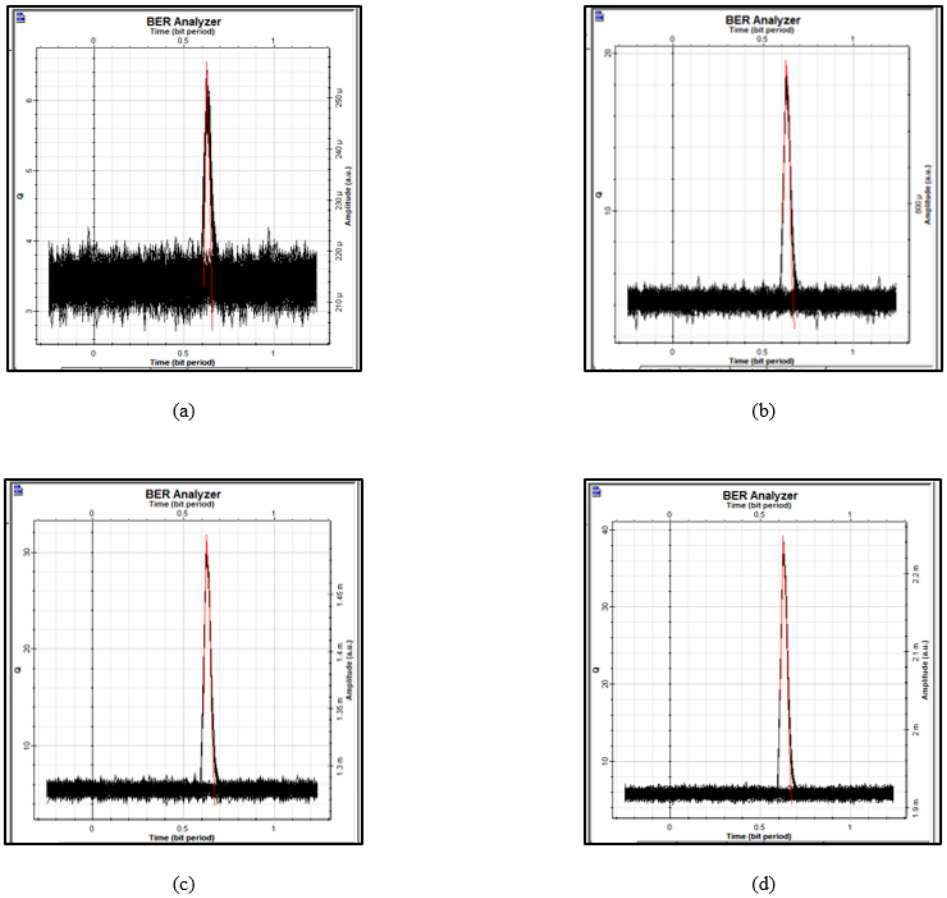

Fig. 9. (a) Eye diagram of the received signal obtained under foggy weather conditions for 10% reflection from the target, measured Q-Factor = 5.82, BER = 2.85e-9. (b) Eye diagram of the received signal obtained under foggy weather conditions for 35% reflection from the target, measured Q-Factor = 19.45, BER = 1.55e-84. (c) Eye diagram of the received signal obtained under foggy weather conditions for 60% reflection from the target, measured Q-Factor = 25.89, BER = 4.01e-148. (d) Eye diagram of the received signal obtained under foggy weather conditions for 90% reflection from the target, measured Q-Factor = 36.6, BER = 1e-253.

3. Potential applications and discussion

Although FSO systems have recently been widely studied in the context of optical wireless communication, their use in simulating the sensing performance of LIDAR systems has remained limited. In this study, a FSO system model was adapted not for analyzing the data transmission performance, but for evaluating the effects of atmospheric losses and target surface reflection characteristics on the performance of an optical fiber-based, lensless LiDAR architecture. This distinction highlights a novel analysis method of FSO applied to LiDAR system design and analysis. Based on the findings of this study, a distributed and phased-array fiber-optic LiDAR system is proposed for future implementation, utilizing a 1x4 fiber coupler at the transmitter side with optimized phased output fiber lengths. The transmitter and receiver fiber sides will have coreless fiber tips at the ends as pairs to emit and collect light through a constant aperture diameter of 0.125 mm to provide short-range sensing enhancement in autonomous vehicles. In this

design, the lensed structure used in conventional LiDAR systems will be eliminated and coreless fiber tips with constant aperture sizes will be used for emitting and collecting light. In this way, the need for precise optical alignment at the transmitter/receiver pairs will be alleviated and the compactness of the system will be enhanced, facilitating its integration into autonomous vehicles.

In literature, there are some studies exhibiting similar performance analyses for LiDAR systems comparable with the results presented here. Table 2 presents a general performance comparison of the proposed system with some existing systems although the proposed system has a fully fiber optical based and lensless structure with 0.125 mm coreless fiber tips as the transmitter and receiver. The proposed system has a moderate lidar range performance at 1550 nm signal wavelength, although it has the smallest aperture size and a very compact structure without a need to a lensed output design. The laser type for the proposed system can be fiber laser or fiber pigtailed diode laser operating at the most popular wavelengths of 905 nm, 940 nm, 980 nm or 1550 nm.

The simulations realized in the study have certain assumptions which can be seen as a shortcoming in performing precise modeling. Firstly, the FSO/LiDAR system model was constructed using the characteristics of high peak power pulsed laser sources. Although an erbium doped fiber amplifier (EDFA) was also used in the system to further increase the output power at 1550 nm and resemble to the practical pulsed diode laser powers, such amplifiers are not always necessary in practical applications due to the availability of commercial diode lasers operating at 900-1000 nm. Therefore, the dominant noise component of the system is usually laser source induced Relative Intensity Noise (RIN). In a different study presenting the experimental performance results of the proposed LiDAR system, dynamic variations, atmospheric turbulence fluctuations, multipath interference, ambient light noise, and sensor imperfections can be investigated in more detail. Secondly, the main objective of the study is to model the impact of optical signal attenuation on LiDAR system performance under challenging atmospheric conditions such as rain and fog. Advanced noise correction algorithms or signal processing techniques can be included at the receiver side of the system to further enhance the performance of an experimental system.

Table 2. General performance comparison.

Ref.	Wavelength (nm)	Pulse Width (ns)	Aperture size (mm)	Lens Usage	Laser Type	Range (m)
[24]	1550	1	6,5 mm collimator, 1,4 mm receiver.	Coaxial lens.	Fiber laser.	267,2
[25]	650	20	6.35	Aspherical lens.	Diode laser.	100
[26]	1550	69,4	Not specified.	Collimating lens.	Diode laser.	7
[27]	905	50	27	Condenser lens.	Diode laser.	0.35
[28]	1550	0.25	15	Telescope lens.	CW laser.	145
This study	1550	10	0.125	Coreless fiber.	Fiber laser or pigtailed diode laser.	80

4. Conclusion

In this study, the performance of a LiDAR system was analyzed through analogy with Free Space Optical (FSO) communication systems under different atmospheric conditions. The simulations evaluated the effects of reflection ratio (10%, 35%, 60%, and 90%) from the mirror (target) surface and distance between the transmitter/receiver and target on optical received signal performance under clear, rainy, and extremely foggy weather conditions. The pulse transmission performance of the LiDAR system was analyzed based on common FSO communication system

performance figures: Q factor, BER, and eye diagram. At clear weather conditions, the most favorable environment for a LiDAR-FSO transmission system was achieved exhibiting a perfect signal quality with a high Q-Factor and a low BER. Increasing the reflection ratio, particularly at the 90% level, maximized received signal quality. On the other hand, the rainy and extremely weather conditions caused higher signal attenuation and a significant decrease in LiDAR-FSO system performance. However, for the reflection ratios of higher than 35% leads to acceptable received signal qualities with high Q factor and low BER values. Extremely foggy weather conditions exhibited the most negative impact on optical signal quality in LiDAR-FSO system, specifically for low reflection ratios and limit the maximum sensing distance of LiDAR system. These results clearly demonstrate that atmospheric conditions and reflection ratios play a critical role on the LiDAR-FSO system performance. It was also shown for all weather conditions that increasing the sensing distance inversely affect the received pulse quality. In conclusion, the simulation results indicate that analyzing LiDAR system performance through analogy with FSO communication system can provide an effective method for understanding the effects of atmospheric conditions and system parameters. In real LiDAR system applications, rainy and extremely foggy weather conditions may be detrimental on received signal quality and may significantly limit the LiDAR sensing distance. Additional solutions to this problem, such as advanced signal processing techniques, more powerful laser sources or more efficient lens designs can be challenging.

4.1. Future work

This study has involved a LiDAR–FSO simulation structure modeled using coreless fiber tips with 0.125 mm cladding diameter at the ends of the transmission fibers. Experimental validation for the proposed structure has not yet been conducted. However, in the next phase, a distributed phased-arrayed fiber-optic LiDAR system will be experimentally designed using a 1x4 fiber coupler with phased output lengths and coreless fiber tip designs as transmitter and receiver apertures. Beside the experimental studies, dynamic variations, atmospheric turbulence fluctuations, multipath interference, ambient light noise, and sensor imperfections will be theoretically investigated in detail. The goal is to validate the simulation outputs under real atmospherical and environmental conditions. This validation study will aim to enhance the practical applicability of the proposed system and improve the reliability of the simulation results.

Acknowledgements

This research did not receive any specific grant from funding agencies in the public, commercial, or non-profit organizations.

Author Contribution

B.K., Conceptualization, methodology, simulation, data analysis, writing – original draft. A.A., Supervision, validation, writing – review & editing, project administration. Both authors read and approved the final version of the manuscript.

References

[1] F. Scotti et. al., "Dual use architecture for innovative lidar and free space optical communications," *Applied Optics*, vol. 56, no. 31, pp. 8811-8815, 2017, doi:10.1364/AO.56.008811.
[2] Bouchet, Olivier, et al. *Free-space optics: propagation and communication*. Vol. 91. John Wiley & Sons, 2010.
[3] S. Bloom, E. Korevaar, J. Schuster, and H. Willebrand, "Understanding the performance of free-space optics," *Journal of Optical Networking*, vol. 2, no. 6, pp. 178-200, June 2003.
[4] Wahab, Fauzi Abdul, et al. "Multiple transmitters & receivers for free space optical communication link performance analysis." *Journal of Telecommunication, Electronic and Computer Engineering (JTEC)*, vol.8, no.5, pp. 29-32, 2016, https://jtec.utem.edu.my/jtec/article/view/731.
[5] Ghassemlooy, Zabih, Wasiu Popoola, and Sujan Rajbhandari. *Optical wireless communications: system and channel modelling with Matlab®*.

CRC press, 2019.
[6] X. Zhu and J. M. Kahn, "Free-space optical communication through atmospheric turbulence channels," *IEEE Transactions on Communications*, vol. 50, no. 8, pp. 1293-1300, 2002.
[7] Wu, X., Liu, P. and Matsumoto, M., "A study on atmospheric turbulence effects in full-optical free space communication systems", *In 6th International Conference on Wireless Communications Networking and Mobile Computing (WiCOM)*, IEEE, 2010, pp. 1-5.
[8] X. Yang, W. Chunyang and L. Xuelian. "Research on the Attenuation Characteristics of LiDAR Transmission Energy in Different Atmospheric Environments." *Atmosphere*, vol.16, no.2/210, 2025, doi:10.3390/atmos16020210
[9] Al-Dabbagh, Rasha, and Hamed Al-Raweshidy. "Millimeter-wave transmission technologies over fiber/fso for 5g+ networks." *2021 IEEE 11th International Conference on Consumer Electronics (ICCE-Berlin)*. IEEE, 2021.
[10] Elfikky, Abdelrahman, et al. "Spatial diversity-based FSO links under adverse weather conditions: performance analysis." *Optical and Quantum Electronics*, vol.56, no.826, pp2-19, 2024, doi:10.1007/s11082-024-06625-y.
[11] Zhang, Yu-Ge, et al. "Study on laser scattering depolarization characteristics of typical aerosol particles." *Optics Communications*, 518:128183, 2022.
[12] L. You, and J. I. Guzman. "Lidar for autonomous driving: Theprinciples, challenges, and trends for automotive lidar and perception systems." *IEEE Signal Processing Magazine*, vol.37, no.4, pp. 50-61, 2020, doi: 10.1109/MSP.2020.2973615.
[13] Y. Li, P. Duthon, M. Colomb and J. Ibanez-Guzman, "What Happens for a ToF LiDAR in Fog?," *in IEEE Transactions on Intelligent Transportation Systems*, vol. 22, no. 11, pp. 6670-6681, Nov. 2021.
[14] M. Kutila, P. Pyykönen, W. Ritter, O. Sawade and B. Schäufele, "Automotive LIDAR sensor development scenarios for harsh weather conditions," *2016 IEEE 19th International Conference on Intelligent Transportation Systems (ITSC)*, Rio de Janeiro, Brazil, 2016, pp. 265-270.
[15] B. Kaya, A. Altuncu. "Analysis Of The Effect Of Transmitter And Receiver Lens Aperture On System Performance In An Fso Communıcatıon System" *14th International Congress On Engineering, Architecture And Design*. 28-29 December 2024.
[16] Lambert, Jacob, et al. "Performance analysis of 10 models of 3D LiDARs for automated driving." *IEEE Access*, vol.8, no.2169-3536, pp. 131699-131722. 2020, doi: 10.1109/ACCESS.2020.3009680.
[17] T. Zeng, J. Ji, L. Sun and Y. Song, "OCDMA-Based LiDAR Systems: Reducing False Alarm Probabilities in Autonomous Driving," *in IEEE Photonics Journal*, 2024. doi: 10.1109/JPHOT.2024.3524410.
[18] Moradi, Hassan, et al. "BER analysis of optical wireless signals through lognormal fading channels with perfect CSI." *2010 17th International Conference on Telecommunications*. IEEE, 2010.
[19] Otgonbayar, Zambaga, et al. "Designing LiDAR-Detectable Dark-Tone Materials with High Near-Infrared Reflectivity for Autonomous Driving: A Comprehensive Review." *Advanced Functional Materials*, vol.35 no. 2414876, pp.2-28, 2025, , doi:10.1002/adfm.202414876.
[20] Killinger, Dennis. "Free space optics for laser communication through the air." *Optics and photonics news*, vol.13, no.10, pp.36-42, 2002, doi:10.1364/OPN.13.10.000036.
[21] K. Hemani, V. K. Jain, and S. Kar. *Free space optical communication*. Vol. 60. ISSN, 1935-3847, New Delhi: Springer India, 2017.
[22] Farid, A.A., Hranilovic, S, "Outage Capacity Optimization for Free-Space Optical Links With Pointing Errors", *Journal of Lightwave Technology*, vol. 25, no. 7, pp. 1702-1710, July 2007
[23] Andrews, Larry C., and Ronald L. Phillips. "Laser beam propagation through random media." *Laser Beam Propagation Through Random Media: Second Edition*, 2005.
[24] Kim, Duck-Lae, Hyun-Woo Park, and Yoon-Mo Yeon. "Analysis of optimal detection range performance of LiDAR systems applying coaxial optics." *Heliyon*, vol.8, no.12, 2022, doi:10.1016/j.heliyon.2022.e12493.
[25] Nguyen, Thanh-Tuan, et al. "Improvement of accuracy and precision of the lidar system working in high background light conditions." *Electronics*, 11.1, 2021: 45.
[26] Mingshi, Zhang, et al. "Phase-modulated continuous-wave coherent ranging method for optical phased array lidar." *Optics Express*, vol.31, no.4, pp.6514-6528, 2023, doi:10.1364/OE.477952.
[27] Wang, Dingkang, et al. "A miniature LiDAR with a detached MEMS scanner for micro-robotics." *IEEE Sensors Journal*, vol.21, no.19, pp.21941-21946, 2021, doi: 10.1109/JSEN.2021.3079426.
[28] Sharma, Abhishek, et al. "Measurement of target range and Doppler shift by incorporating PDM-enabled FMCW-based photonic radar." *Optik*, vol.262, no. 169191, 2022, doi:10.1016/j.ijleo.2022.169191.

Contents lists available at *Dergipark*

Journal of Scientific Reports-A

journal homepage: *https://dergipark.org.tr/tr/pub/jsr-a*

E-ISSN: 2687-6167 ***Number 61, June 2025***

RESEARCH ARTICLE

Receive Date: 07.02.2025 *Accepted Date: 20.05.2025*

Investigation of photon ınteraction parameters of some premedication drugs

Halime ERZEN YILDIZ [a]*

[a]*Yuzuncu Yıl University, Vocational School of Health Care, Department of Medical Services and Techniques, 65200, Van, Turkey, ORCID: 0000-0002-0603-1815*

Abstract

Premedication, also known as the preparation phase, is the administration of drugs to patients before chemotherapy to reduce the side effects of chemotherapy in oncology patients. Metoclopramide, ranitidine and pheniramine are some of these drugs. Metoclopramide is a routine antiemetic for nausea and vomiting caused by antineoplastic drugs, especially cisplatin, due to its effect on the medulla chemoreceptor trigger zone. Ranitidine, which belongs to the histamine receptor 2 (H2) antagonist family, is a widely used drug clinically to control gastrointestinal symptoms. Pheniramine is an antagonist against allergic symptoms caused by inappropriate histamine release to reduce edema, pruritus and redness. Sometimes patients are given premedication drugs before radiological examination. In this study, photon interaction parameters of some premedication drugs (metoclopramide, ranitidine hydrochloride, and pheniramine) were investigated, namely mass attenuation coefficient (μ_ρ), effective atomic number (Z_{eff}), electron density (N_{el}), exposure and absorption accumulation factors (EBF and EABF). Maximum μ_ρ values for all drugs were found at low gamma energies. It was found that ranitidine hydrochloride has the highest Z_{eff} values in almost the entire energy range due to the presence of S and Cl. In addition, ranitidine hydrochloride showed the lowest EBF and EABF values, indicating that the material does not emit much radiation to the environment.

Keywords: Buildup factors; effective atomic number; mass attenuation coefficients; premedication drugs

*Corresponding author. Tel: +90-530-433-35-29

E-mail address: halimeyildiz@yyu.edu.tr

1. Introduction

Premedication, also known as the preparation phase, is the administration of drugs to the patient before chemotherapy to reduce the side effects of chemotherapy in oncology patients. Metoclopramide, ranitidine, and pheniramine are some of these drugs. Metoclopramide is a routine antiemetic for nausea and vomiting caused by antineoplastic drugs, especially cisplatin, due to its effect on the medulla chemoreceptor trigger zone [1-3]. It is also a drug used for stomach and esophageal problems. The chemical formula of metoclopramide is $C_{14}H_{22}ClN_3O_2$ [4].

Ranitidine, belonging to the histamine receptor 2 (H2) antagonist family, is a widely used drug clinically for the control of gastrointestinal symptoms. By blocking histamine receptors, ranitidine reduces the amount of acid produced by the stomach [5,6]. Ranitidine also has the potential to be used as an adjuvant therapy or preventive agent in breast cancer [7]. Its chemical formula is $C_{13}H_{22}N_4O_3S.HCl$ [8].

Pheniramine is an alkylamine derivative antihistamine used in the treatment of allergies and is taken more frequently than other antihistamines [9]. Alkylamine derivatives are among the most potent antihistamines, producing more stimulation and less sleepiness. Pheniramine acts as an antagonist against allergic symptoms resulting from inappropriate histamine release to reduce edema, pruritus, and redness [10, 11]. Its chemical formula is $C_6H_2ON_2$ [12].

Since radiation is used in many fields (medicine, biology, industry, nuclear power plants and radiation dosimetry), it is important to investigate the behavior of radiation in materials. X-rays and Gamma rays are used in diagnosis and treatment in medicine. Therefore, the behavior of radiation within the material must be accurately understood. The interaction of the material with radiation depends on the energy of the photon incident on the material, the density of the material and the atomic number of the elements [13]. There are studies in the literature on the interaction of drugs with radiation. In a study investigating the radiation protective effect of anti-inflammatory drugs, it was stated that radiation can inhibit the cell cycle and disrupt homeostasis. It has been determined that the prodromal, acute, and chronic effects of radiation are accompanied by overproduction of eicosanoids (prostacyclin, leukotrienes, prostaglandins, and thromboxanes), and anti-inflammatory drugs suppress prostaglandin/thromboxane synthesis [14]. In another study, it was reported that natural products such as Apigenin, caffeine, bergenin, coniferyl aldehyde, chlorogenic acid, curcumin, quinic acid and delphinidin are effective radioprotectors due to their low toxicity and quinic acid is the best radioprotector to protect from both thermal and fast neutrons [15]. According to a study on anti-HIV drugs (Kivexa, Combivir, Tenofovir, Lopinavir, and Nelfinavir), it is reported that Combivir, which has a relatively high heavy element content, has the highest radiation attenuation capacity, while Lopinavir has the lowest [16].

These premedication drugs (metoclopramide, ranitidine hydrochloride, pheniramine) are administered to the patient, especially before chemotherapy drugs and these patients may undergo some radiological examinations after taking the drugs. For example, it has been shown that the simultaneous application of chemotherapy and radiotherapy is beneficial in head and neck cancers (chemoradiotherapy) [17]. The spatial cooperation between radiotherapy and chemotherapy has been successfully used in the treatment of various tumors (such as Wilms tumor, acute lymphoblastic leukemia and breast cancer). In radiotherapy applications, when cancer cells are treated, irradiation of normal tissues surrounding the tumor may cause symptomatic damage. Ionizing radiation can interact with cellular macromolecules such as DNA (deoxyribonucleic acid), proteins and lipids (direct effect) or with water molecules in human tissues (indirect effect) and cause the formation of reactive oxygen species. For example, the Hydroxyl radical is highly reactive and damages cellular macromolecules. As a result of these effects, diseases such as organ inflammation, fibrosis, infertility, atrophy, vascular damage and secondary malignancies may occur [15,18].

When a substance is exposed to ionizing radiation, it is necessary to determine some coefficients characterizing the interaction of the radiation with this substance. The first of these parameters is the mass attenuation coefficient (μ_ρ), which characterizes the penetration effect of ionizing radiation. Two other important parameters, the effective atomic number (Z_{eff}) and the electron density (N_{el}), are used in medical radiation dosimetry and these coefficients are obtained using the $\mu\rho$ values. The ‘accumulation factors’, which indicate how radiation interacts with ‘living’ matter,

are divided into two types: the first is the absorption accumulation factor (EABF), where the amount of energy absorbed or deposited in the target is of interest and the detector response function is the absorption in the material (prodrug). The second is the exposure accumulation factor (EBF), where the amount of interest is the exposure and the absorption in air is the detector response function [19]. To the best of our knowledge, there is no detailed study evaluating the EBF and EABF values for commonly used premedication drugs. It is hoped that the current study will bridge this gap and provide insight into possible implications for radiologic practice.

2. Material and methods

This study aimed to calculate μ_ρ, Z_{eff}, N_{el}, EBF and EABF values in metoclopramide ($C_{14}H_{22}ClN_3O_2$), ranitidine hydrochloride ($C_{13}H_{22}N_4O_3S.HCl$) and pheniramine ($C_6H_2ON_2$) drugs. μ_ρ values were calculated theoretically in the wide gamma energy range (1 keV- 100 GeV) by using the WinXCom computer program. WinXCom calculates these values for compounds or mixtures (using the mixture rule). Z_{eff} and N_{el}'s values were obtained using the μρ's.

This study involves calculating various radiation shielding parameters for premedication drugs, using the WinXCom code and several related formulas to assess gamma radiation shielding effectiveness. The mass attenuation coefficient (μ_ρ), which represents how a material attenuates gamma radiation, was computed using the WinXCom software. This software calculates attenuation coefficients and cross sections in the energy range of 1 keV–100 GeV [20, 21]. For a given compound, the μρ value is calculated based on the mass attenuation coefficients of the constituent elements. The mass attenuation coefficient for a mixture is given by the weighted sum of the individual elements using the following formulas:

$$\mu_\rho = \sum_i w_i \left(\mu_\rho\right)_i \tag{1}$$

In Equation (1), w_i represents the weight of the ith element, and $(\mu_\rho)_i$ represents the mass attenuation coefficient. The w_i value for the composite can be calculated by Equation 2:

$$w_i = \frac{a_i A_i}{\sum_j a_j A_j} \tag{2}$$

A_i and a_i in equation (2) represent the atomic weight of the ith element and the number of formula units, respectively. The total molecular cross section is denoted by σ_m (barn/molecule) and is obtained by using the following formulas [22]:

$$\sigma_m = \frac{\left(\mu_\rho\right)}{N_A} M \tag{3}$$

$$M = \sum n_i A_i \tag{4}$$

Where; M is the molecular weight, N_A is the Avogadro number, and ni is the atomic number of the ith element. The total atomic cross section (σ_a (barn/atom)) and electronic cross section (σ_{el} (barn/electron)) values are calculated using equations (5) and (6) [22]:

$$\sigma_a = \frac{\sigma_m}{\sum n_i} \tag{5}$$

$$\sigma_e = \frac{1}{N_A} \sum \frac{A_i}{Z_i} f_i \mu_i \tag{6}$$

Where; f_i is the fractional abundance of the ith element and Z_i is the atomic number. This calculation provides insight into the overall interaction cross-section of the entire molecule, considering the contribution of each atom within the molecular structure. Z_{eff} and N_{el}'s values were derived as follows [22]:

$$Z_{eff} = \frac{\sigma_a}{\sigma_e} \tag{7}$$

$$N_{el} = \frac{(\mu_\rho)}{\sigma_e} \tag{8}$$

In the context of gamma radiation shielding, the concepts of Z_{eff} and N_{el} are used to assess and design materials that can effectively attenuate gamma radiation. These properties indicate how gamma photons interact with materials and how they affect their ability to attenuate radiation. In the context of radiation shielding, EABF and EBF are fundamental parameters for understanding their behavior in materials. Hila et al. [23, 24] introduced significant improvements to their spreadsheet-based program EpiXS, originally developed in their previous work. The updated version significantly improves its usability for photon shielding and shielding analysis by integrating the EPICS2017 and EPDL97 data libraries. These libraries provide detailed cross-section data for elements with atomic numbers 1 to 100 over a wide range of photon energies from 10 eV to 100 GeV. Thanks to these upgrades, EpiXS can reliably calculate theoretical parameters such as EBF and EABF, which are essential for accurate photon interaction modeling in various materials. These parameters play an important role in evaluating the shielding effectiveness of materials against photon radiation. They also provide the basis for the design of efficient and reliable radiation protection systems. These factors measure the rate of absorption or scattering of radiation within a material.

3. Results and discussion

The parameters μ_ρ, Z_{eff}, and N_{el} are concepts used in shielding calculations that determine the probability that a material will interact with gamma photons. Gamma radiation interacts with matter via the photoelectric effect, Compton scattering, and pair production, all of which depend on the Z value of the material. When the μ_ρ for the three examined drugs were evaluated, it was seen that the results were quite close to each other since the chemical contents of these drugs were similar. However, since ranitidine hydrochloride ($C_{13}H_{22}N_4O_3S.HCl$) drug has S and Cl elements, it was observed that mass attenuation values were high with a small difference (Fig. 1).

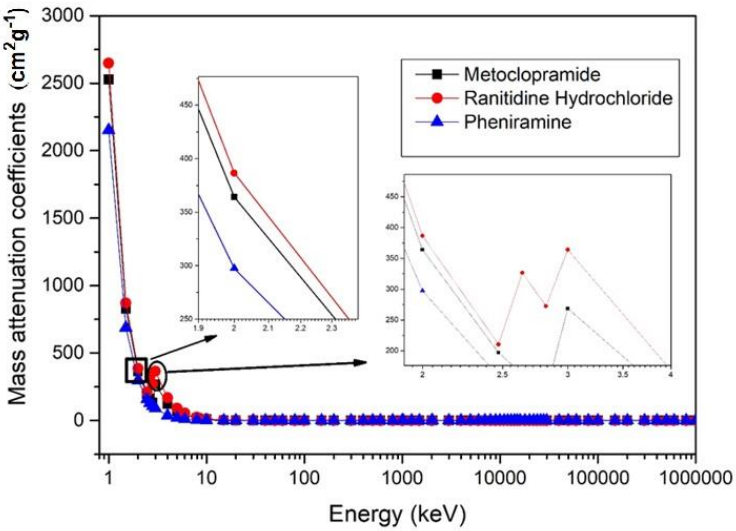

Fig. 1. μ_ρ values of metoclopramide, ranitidine, and pheniramine across 1 keV–100 GeV.

For gamma radiation shielding, the Z_{eff} value of a composite material or compound varies depending on the atomic numbers of the elements constituting that material and the energy of the gamma radiation. For drugs whose Z_{eff} values were examined at the same energy values, as can be seen from Figure 2, the results of the other two drugs, except pheniramine, have a similar tendency and rapid increases are seen in the low energy zone. The main reason for these two results is that these drugs contain elements with higher atomic numbers (S=16, Cl=17). In a study, the EMR (electromagnetic radiation) interaction parameters of some antihypertensive drugs (Fosinopril, Captopril, Losartan Potassium, Irbesartan, Ramipril, Telmisartan) were investigated, and it was found that Losartan Potassium had the largest MAC, Z_{eff} and N_{el} values and the lowest HVL, mfp and buildup factor values [25].

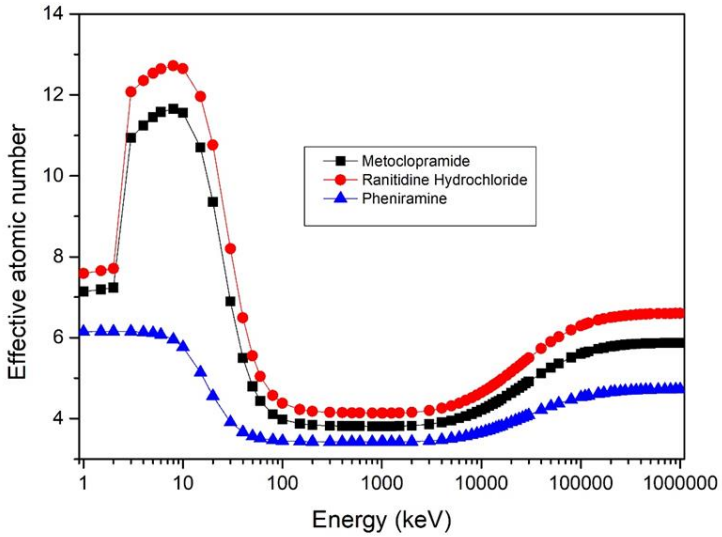

Fig. 2. Z_{eff} values of metoclopramide, ranitidine, and pheniramine across 1 keV–100 GeV.

Similarly, similar interpretations can be made for the N_{el} values. Figure 3 shows that the N_{el} values vary with gamma energy and drug type, and the results for metoclopramide and ranitidine hydrochloride are closer to each other. Cakir conducted a study that included the calculation of various radiation shielding parameters for iodinated contrast agents and the potential benefits of chemoradiotherapy for some tumors. In this study, the radiation interaction parameters (μ_ρ, Z_{eff} and N_{el}) of iodinated contrast agents (such as Iopamidol, Iodixanol, Iohexol, Iopromide, and Ioxagalet) were calculated using computer programs. The Z_{eff} and N_{el} values were found to be highest in the low energy range for all these iodinated contrast agents. The study findings showed that iodinated contrast agents have improved gamma radiation shielding properties, which is important for medical imaging techniques such as CT scans and other radiologic procedures, especially when used in low-energy radiation environments [26].

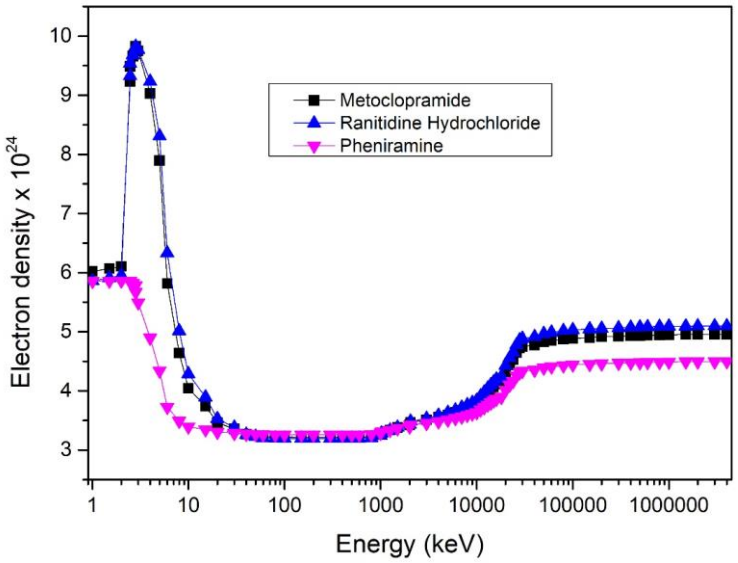

Fig. 3. N_{el} values of metoclopramide, ranitidine, and pheniramine across 1 keV–100 GeV.

In this study, the EpiXS program and the GP-Fitting approach were used together to calculate the equivalent atomic number (Z_{eq}), EABF and EBF parameters, which are the basic shielding parameters. The EBF and EABF parameters of the drugs were compared and discussed in the energy range of 0-15 MeV and penetration depths of 1-40 mfp (mean free path) (Figures 4-5). At low photon energies (typically below 100 keV), the dominant interaction process is the photoelectric effect. In this energy region, the absorption of a photon by an atom in the material results in the ejection of an electron from the inner shell. The probability of the photoelectric effect increases significantly with the Z value of the material and decreases with the energy of the photon (E) (the relationship is approximately proportional to $Z^4/E^{3.5}$).

At intermediate photon energies (100 keV- 10 MeV), the dominant interaction process shifts to Compton scattering. More scattering occurs at these energies, meaning that scattered photons are produced and contribute to both energy absorption and energy exposure. Both EABF and EBF values increase in this energy range because more scattered photons contribute to the total energy stored or exposure. EABF increases because the secondary photons generated by scattering contribute to the total energy absorbed in the material. EBF increases because the scattered photons that don't get absorbed still contribute to the overall exposure (the dose rate in the air or volume surrounding the material). This is where the EBF/EABF ratio tends to peak, as the material's shielding effectiveness is influenced by a combination of absorption and scattering.

At high photon energies (typically above 10 MeV), pair production begins to dominate. Pair production occurs when an incident photon has an energy above 1.022 MeV, the energy required to create an electron-positron pair, and interacts with the electric field of an atomic nucleus. The formation of an electron-positron pair results in the photon effectively being converted into matter. The probability of pair production increases with photon energy and Z, but only becomes significant at very high photon energies. The EABF and EBF decrease when the energy of the photon reaches very high values. The EABF is reduced because the dominant interaction is pair production, which provides a different energy deposition profile than Compton scattering. In pair production, instead of providing scattered gamma photons, a significant number of new particles (electrons and positrons) are produced.

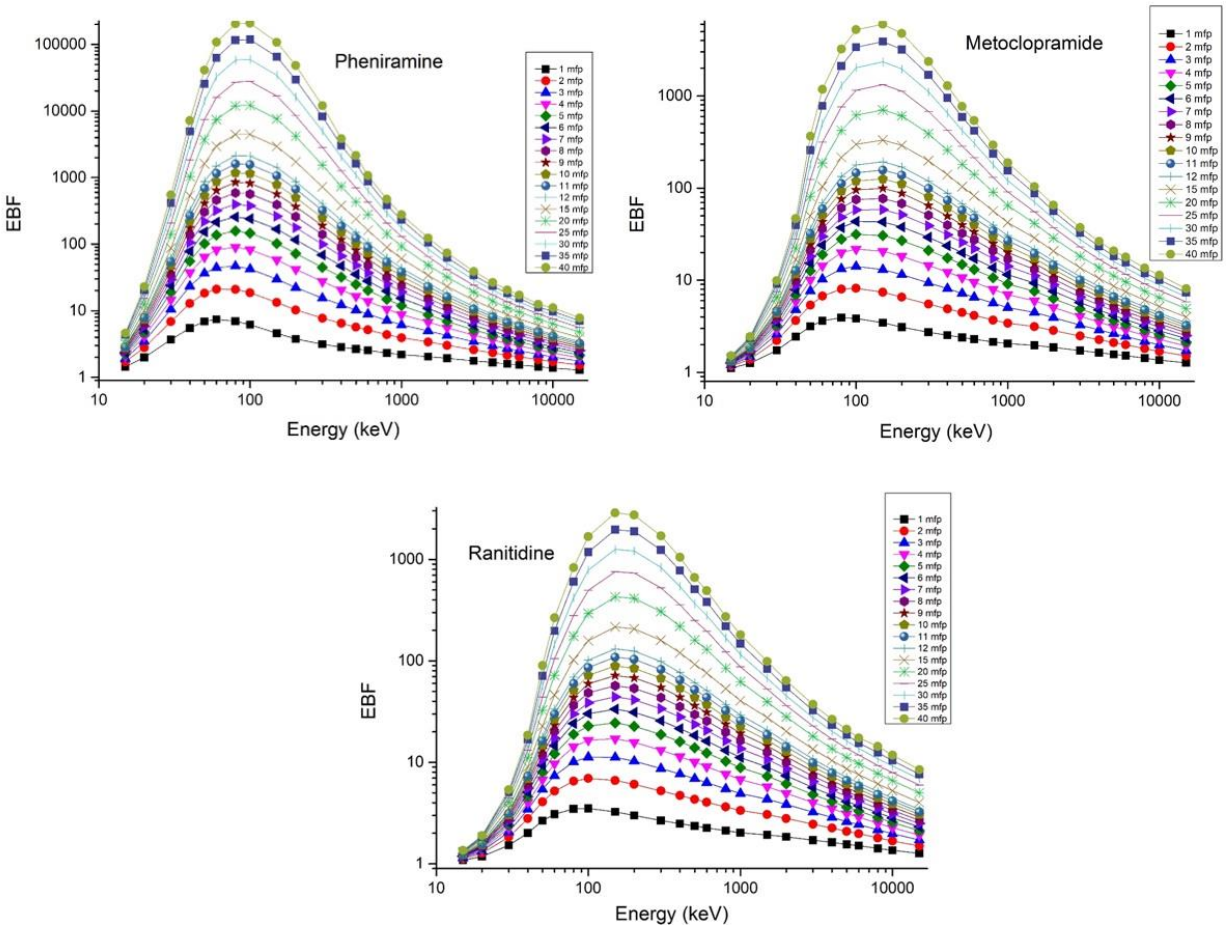

Fig. 4. Change of exposure buildup factors for metoclopramide, ranitidine, and pheniramine with different mfp values depending on photon energy.

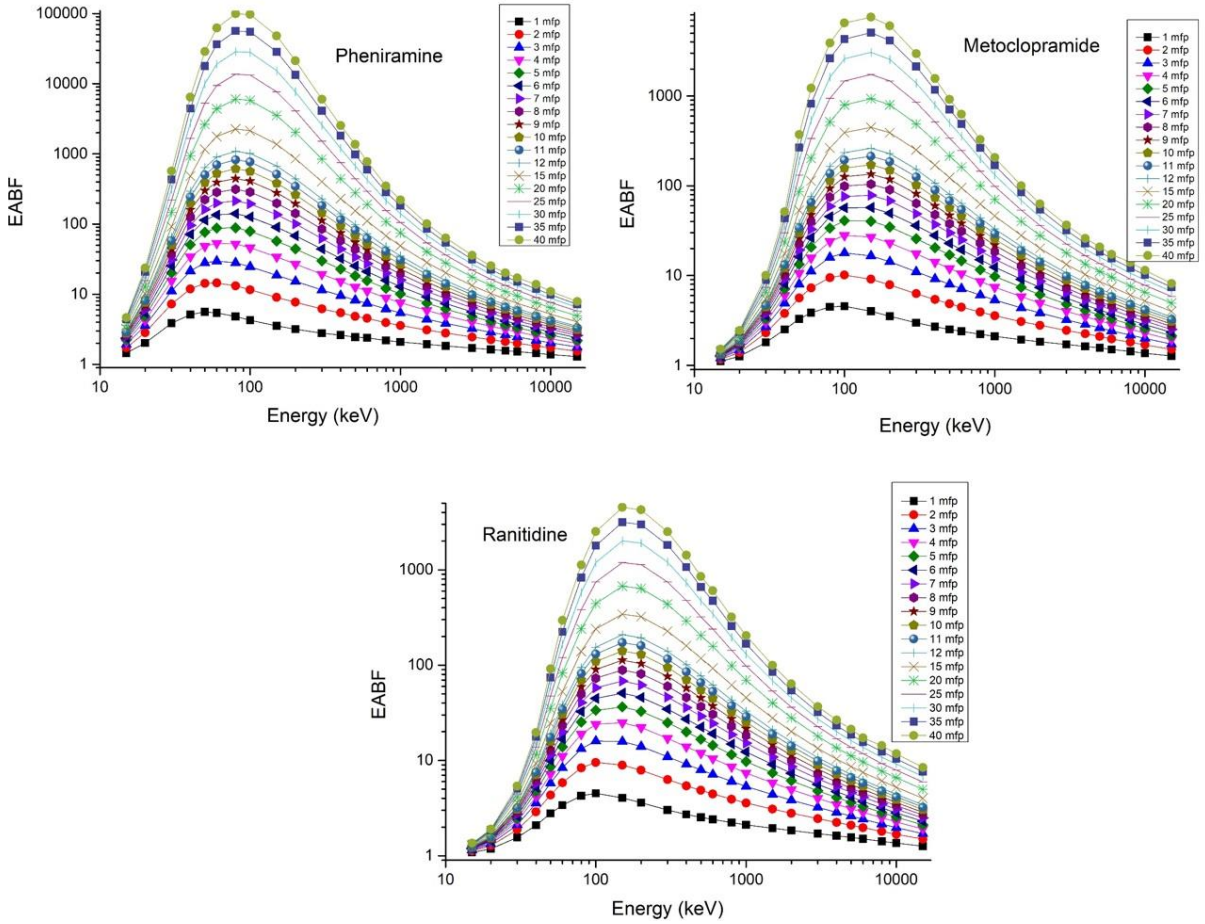

Fig. 5. Variation of absorption factors depending on photon energy for metoclopramide, ranitidine and pheniramine at different MFPs

Furthermore, graphical representations corresponding to a photon energy of 0.15 MeV, as a function of penetration depth, are provided in Figure 6. Ranitidine hydrochloride appears to attenuate gamma radiation more. In a study examining the gamma and neutron interaction parameters of diketone derivatives synthesized as potential anticancer agents (DKD1 (C17H10O5), DKD2 (C27H23NO4), DKD3 (C41H43NO4), DKD4 (C33H48O2), DKD5 (C30H34O2) and DKD6 (C32H35NO2)), it was determined that DKD1 (C17H10O5) showed lower EBF values and had better gamma absorption compared to other selected examples [27]. A similar result is also valid for our study, Ranitidine hydrochloride showed the lowest EBF value. This feature of Ranitidine may be evaluated as radioprotective in chemoradiotherapy.

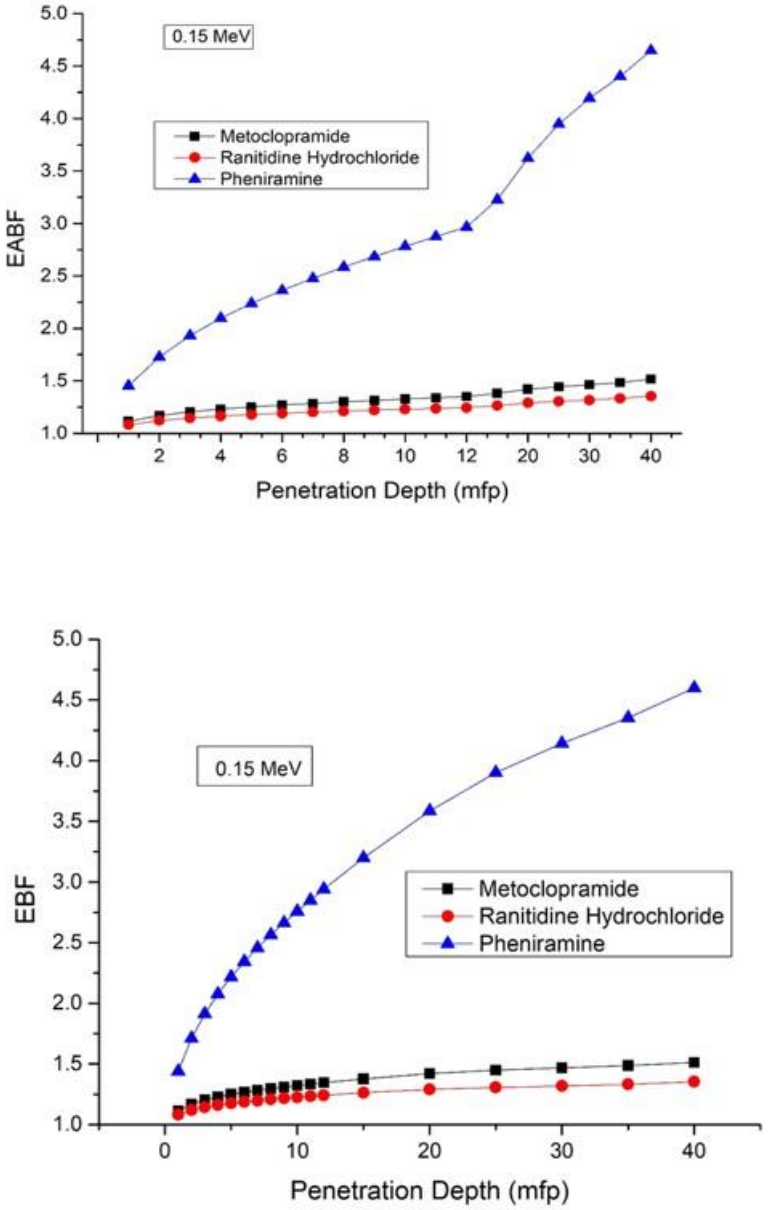

Fig. 6. Energy exposure buildup factor of metoclopramide, ranitidine, and pheniramine up to 40 mfp at 0.15 MeV energy

4. Conclusion

The maximum mass attenuation coefficient was obtained for all drugs at low gamma energies. This is attributed to the dominance of the photoelectric effect due to the probability of interaction with electrons. The μ_ρ parameters depend on the elemental composition of the drugs. At low photon energies, the atomic number of the elements involved strongly influences the photoelectric absorption cross section (the cross section behaves like Z^{4-5}). This

means that heavier elements (higher Z) are more efficient in absorbing low-energy photons. Due to the higher Z dependence, the $\mu\rho$ values are highest for drugs with high atomic number elements. Compton scattering is the dominant interaction mechanism for photons in the intermediate energy range. The attenuation coefficient μ_ρ decreases as the Z value of the material increases, since the Compton scattering cross section is approximately proportional to Z. In other words, for materials with higher atomic numbers, Compton scattering becomes less efficient at intermediate energies and the attenuation due to this mechanism decreases. Therefore, the results have the smallest values in this energy region. As the energy of the photon increases, the relative contribution of Compton scattering decreases. This is because at higher energies, pair production becomes the dominant interaction mechanism (the probability of pair production is proportional to Z^2). The results again appear to increase in this energy range. Ranitidine hydrochloride exhibited the highest effective atomic number (Z_{eff}) in almost the entire energy range due to the S and Cl content. The deposition factors (EBF and EABF) increase due to secondary interactions (scattering and photon production) within the shielding material. Ranitidine hydrochloride showed the lowest EBF and EABF values, indicating that the material does not reflect much radiation to the environment.

Acknowledgements

There is no conflict of interest.

References

[1] R. Albibi, R. W. McCallum, "Metoclopramide: pharmacology and clinical application,". *Annals of Internal Medicine*, vol. 98, no.1, pp. 86-95, 1983.

[2] Y. Chen, M. Zhang, X. Ji, J. Zhao, S. Qin, Y. Ji, R. Fan, Y. Liu, P. Lu, "The anti-cancer effect of metoclopramide on triple-negative breast cancer cells," *Die Pharmazie-An International Journal of Pharmaceutical Sciences*, vol. *76*, no.4, pp. 172-174, 2021. doi: 10.1691/ph.2021.0977

[3] E. M. McGovern, J. Grevel, S. M. Bryson, "Pharmacokinetics of high-dose metoclopramide in cancer patients," *Clinical pharmacokinetics*, vol. 11, pp. 415-424, 1986.

[4] S. Mishra, H. Soni, "Preformulation Studies of Metoclopramide Hydrochloride: Fundamental Part of Formulation Design," *EASJ Pharm & Pharmacol*, vol. *1*, *no*.6, pp. 164-169, 2019.

[5] R. D. Bezerra, M. M. Silva, A. I. Morais, J. A. Osajima, M. R. Santos, C. Airoldi, E. C. Silva Filho, "Phosphated cellulose as an efficient biomaterial for aqueous drug ranitidine removal," *Materials*, vol. *7*, *no*.12, pp. 7907-7924, 2014. doi:10.3390/ma7127907

[6] H.J. Kang, "Do Ranitidine and Nizatidine Increase the Risk of Gastrointestinal Cancer?" (Doctoral dissertation, Graduate School, Yonsei University), 2022.

[7] A. Vila-Leahey, S. A. Oldford, P. A. Marignani, J. Wang, I. D. Haidl, J. S. Marshall, "Ranitidine modifies myeloid cell populations and inhibits breast tumor development and spread in mice," *Oncoimmunology*,vol. *5*, no.7, pp. 1-13, 2016. https://doi.org/10.1080/2162402X.2016.1151591

[8] S. E. Dereci, "Investigation of coagulation removal properties of ranitidine and napro*xen,"* (Master's thesis, Institute of Science). 2010.

[9] N. A. Buckley, I. M. Whyte, A. H. Dawson, D. A. Cruickshank, "Pheniramine—a much abused drug," *Medical journal of Australia*, vol. *160*, no.4, pp. 188-192, 1994.

[10] O. Saatcioglu, C. Evren, "A case of pheniramine dependence. *Substance Abuse*," vol. *26*, no.1, pp. 45-47, 2006. doi:10.1300/J465v26n01_06

[11] F. Hacıoğlu, "Side-by-Side Chromatographic Analysis of Phenylephrine Hydrochloride, Pheniramine Maleate, Ascorbic Acid, Paracetamol and Related Compounds," Istanbul University Health Sciences Institute (Doctoral Thesis), 2022.

[12] H. S. Makhdoom, A. I. Abid, M. Mujahid, S. Afzal, K. Sultana, N. Hussain, K. Barkat, "Assessment of pheniramine in alternative biological matrices by liquid chromatography tandem mass spectrometry," *Forensic Science, Medicine and Pathology*, vol.20, pp. 1291-1302, 2024. https://doi.org/10.1007/s12024-024-00795-7

[13] T. Tuğrul, "Investigation of mass attenuation coefficients, effective atomic numbers, and effective electron density for some molecules: study on chemotherapy drugs," *Journal of Radiation Research and Applied Sciences*, vol. *13*1, pp. 758-764, 2020. https://doi.org/10.1080/16878507.2020.1838040

[14] A. S. Michalowski, "On radiation damage to normal tissues and its treatment: II. Anti-inflammatory drugs," *Acta Oncologica*, vol. 33, no. 2, pp. 139-157, 1994. https://doi.org/10.3109/02841869409098397

[15] G. B. Hiremath, N. H. Ayachit, N. M. Badiger, "Investigation of shielding properties of gamma and neutrons in some natural radioprotective drugs," *Radiation Effects and Defects in Solids*, vol.179, no. 3-4, pp. 344-357, 2024. https://doi.org/10.1080/10420150.2023.2278138.

[16] U. Akbaba, E. Şakar, M. I. Sayyed, B. Alim, Ö. F. Özpolat, "Evaluation of photon interaction parameters of Anti-HIV drugs," *Radiation Physics and Chemistry*, vol.*201*, no. 110441, 2022. https://doi.org/10.1016/j.radphyschem.2022.110441
[17] B. T. Hill, "*Antitumor drug radiation interactions*," CRC Press, 2018.
[18] H. B. Stone, C. N. Coleman, M. S Anscher, W. H. McBride, "Effects of radiation on normal tissue: consequences and mechanisms," *The lancet oncology*, vol.4, no. 9, pp. 529-536, 2003.
[19] M. I. Sayyed, S. A. Issa, S. H. Auda, "Assessment of radio-protective properties of some anti-inflammatory drugs," *Progress in Nuclear Energy*, vol. *100*, pp. 297-308, 2017. https://doi.org/10.1016/j.pnucene.2017.07.003
[20] L. Gerward, N. Guilbert, K. B. Jensen, H. Levring, "X-ray absorption in matter. Reengineering XCOM," *Radiation Physics and Chemistry*, vol.*60*, *no.*1-2, pp. 23-24, 2001. https://doi.org/10.1016/S0969-806X(00)00324-8
[21] L. Gerward, N. Guilbert, K. B. Jensen, H. Levring, "WinXCom—a program for calculating X-ray attenuation coefficients," *Radiation physics and chemistry*, vol. *71*, no.3-4, pp. 653-654, 2004. doi.10.1016/j.radphyschem.2004.04.040
[22] S. Gowda, S. Krishnaveni, R. Gowda, "Studies on effective atomic numbers and electron densities in amino acids and sugars in the energy range 30-1333 keV," Nucl. Instrum. Methods B, vol. 239, no.4, pp. 361–369, 2005. https://doi.org/10.1016/j.nimb.2005.05.048
[23] F. C. Hila, A. V. Amorsolo Jr, A. M. V. Javier-Hila, N. R. D. Guillermo, "A simple spreadsheet program for calculating mass attenuation coefficients and shielding parameters based on EPICS2017 and EPDL97 photoatomic libraries," *Radiation Physics and Chemistry*, vol. *177*, no. 109122, 2020. https://doi.org/10.1016/j.radphyschem.2020.109122
[24] F. C. Hila, A. Asuncion-Astronomo, C. A. M. Dingle, J. F. M. Jecong, A. M. V. Javier-Hila, M. B. Z. Gili, A. V. Amorsolo Jr, "EpiXS: A Windows-based program for photon attenuation, dosimetry and shielding based on EPICS2017 (ENDF/B-VIII) and EPDL97 (ENDF/B-VI. 8)" *Radiation Physics and Chemistry*,vol. *182*, no.109331,2021. https://doi.org/10.1016/j.radphyschem.2020.109331
[25] H. E. Yıldız, "Ionizing electromagnetic radiation interaction properties of some antihypertensive drugs. *Journal of Medicine and Applied Sciences*," vol. *2*, no.2, pp. 29-36, 2022.
[26] T. Çakır, "Determining the photon interaction parameters of iodine compounds as contrast agents for use in radiology," *Journal of Radiation Research and Applied Sciences*, vol. *13*, no.1, pp.252-259, 2020. https://doi.org/10.1080/16878507.2020.1731065
[27] G. B. Hiremath, G. V. Muddapur, H. T. Srinivasa, N. H. Ayachit, N. M. Badiger. "Investigation of gamma and neutron interaction parameters of synthesized diketone derivatives as potential anti-cancer," *Journal of Radioanalytical and Nuclear Chemistry*, vol. *333*, no.11, pp. 5425-5434,2024.

Contents lists available at Dergipark

Journal of Scientific Reports-A

journal homepage: https://dergipark.org.tr/tr/pub/jsr-a

E-ISSN: 2687-6167 ***Number 61, June 2025***

RESEARCH ARTICLE

Receive Date: 27.02.2025 *Accepted Date: 23.04.2025*

Optimization of material and process parameters in the injection molding of piezoresistive card-type pressure sensors using the finite element method

Fuat Tan[a*], Burak Birişik[b]

[a]*Balıkesir University, Faculty of Engineering, Mechanical Engineering, Balıkesir 10145, Türkiye, ORCID: 0000-0002-4194-5591*
[b]*Balıkesir University, Faculty of Engineering, Mechanical Engineering, Balıkesir 10145, Türkiye, ORCID:0009-0004-4978-7008*

Abstract

The purpose of this study is to determine the most suitable material and process parameters for piezoresistive card-type pressure sensors during the injection molding process. Simulation analyzes done with different engineering plastics Polyamide (PA), Polybutylene Terephthalate (PBT) and Polycarbonate (PC) focus on the optimization of critical parameters such as fill time, injection pressure, volumetric shrinkage and cooling efficiency during the production process. Cooling channel diameter was 10 mm, cooling water temperature was 25°C and Reynolds number was 10,000 designed to provide the minimum time of delivery from the mold by using idle times. Results indicate that PA has the shortest filling time of 0.0548 sec, PC has a volume shrinkage of 6.63%, among the lowest ones and PBT shows the best thermal stability of 252.8°C PA, which operates at lower injection pressure (132.3 MPa), increases throughput, while PBT has exhibited a proper balance between mechanical and thermal performance and PC is the most suitable material for high-dimensional accuracy applications. This study serves as a guide for optimizing the material selection and molding parameters in the production of plastic-based pressure sensors.

Keywords: Piezoresistive pressure sensor; FEM; injection molding; process parameters

1. Introduction

Injection molding technology is a manufacturing method where critical parts are produced by shaping thermoplastics and the type of materials used is getting richer every day [1]. Nowadays, this technique, which is widely used to mold plastic materials into parts with complex geometries [2], plays a critical role in automotive [3-4], medical devices [5], electronics [6] and many other industries, especially by offering fast and high-precision production [7].

Plastic card type pressure sensors are widely used in critical applications such as tire pressure monitoring systems [8] and airbags, especially in the automotive industry [9]. Boris Adam et al. investigated in detail the performance of a pressure sensor developed with APSM (Advanced Porous Silicon Membrane) technology for use in airbag systems. The

study focused on evaluating the effectiveness and application potential of the technology by analyzing the effects of this sensor on the pressure range and normalized differential pressure signal [10]. In the production of these sensors, material selection and optimization of process parameters are of great importance, since these parameters [11] directly affect the quality and performance of the final product [12-13].

Nan-Yang Zhao et al. conducted a study to reduce defects such as deformations and shrinkage encountered in injection molding processes. They explained how they are affected by process parameters such as injection rate, injection pressure, holding pressure, holding and cooling time. The paper comprehensively summarized recent progress on design of experiments approaches and four advanced methods (artificial neural networks, genetic algorithm, response surface methodology and Kriging model) [14].

Hsueh-Lin Wu and Ya-Hui Wang have conducted extensive studies to reduce the volumetric shrinkage in the injection molding process, especially in the chair bases, to solve this problem, which adversely affects the production quality and reduces the performance of the final product. These studies have enabled the optimization of various process parameters to minimize shrinkage and have made significant contributions to the improvement of production processes [15].

Modern simulation software offers effective tools to optimize various aspects of the injection molding process [16]. Using Moldflow software, heat transfer, injection pressure and filling times are optimized, resulting in significant improvements in product quality [17]. Fuat T. proposed a combined approach of Response Surface Methodology (RSM) and Grey Wolf Optimization (GWO) to optimize and model parameters such as polymer deformation, volumetric shrinkage and cycle time using Moldflow Insight software [18].

In their study, M.O.M Ali et al. used the Response Surface Method (RSM) to determine the optimum parameters on the filling time and explained that injection time is an important parameter that affects the filling time with 99% [19]. At the same time, the effects of cooling water temperature and Reynolds number on product quality were studied in detail by Fuat T. et al. using the Face Centered Cubic (FCC) experimental design approach [20].

Celio Fernandes et al. presented a comprehensive review of the mathematical modeling and optimization of the injection molding process, evaluating the effectiveness of artificial neural networks and evolutionary algorithms in this process. Their study highlighted the success of these methods in modeling and optimizing process parameters and made significant contributions to the development of injection molding technology [21].

Material selection is one of the most important aspects of the injection molding process. The viscoelastic properties and thermal behavior of different polymer materials significantly affect both the shape accuracy and mechanical strength of the final product. Markus Baum et al. studied various models involving the effects of temperature on viscosity and helped to systematically classify the models by creating mathematical structures that describe the complex viscous behavior of polymers in the filling stage of these models [22]. H.K. Lee et al. studied the residual stress distribution and surface replication performance in polymers in detail; while evaluating the residual stress state with photoelastic analysis methods, they verified the surface replication conditions with experimental findings [23].

The aim of this study is to investigate in detail the behavior of different plastic materials such as PC (Polycarbonate), PBT (Polybutylene Terephthalate) and PA (Polyamide) in the injection molding process through simulation and to identify the key factors affecting the quality of board type pressure sensors produced using these materials. The simulation process will help us understand the effects of critical parameters such as cooling water temperature and Reynolds number on filling times, injection pressure and surface deformation. The findings are intended to make significant contributions to both academic and industrial applications.

This paper demonstrates the potential of microinjection molding technology while presenting innovative methods that improve quality while reducing costs. The findings of the study will guide future research into optimizing material and process parameters to produce plastic board-type pressure sensors.

2. Method

Even if the desired product is standard, there may still be several production problems. These problems can be due to the size of the material and material characteristics. To remedy the problem, small changes in the production are employed. For example, optimization of the compressive force transfering the injection molding machine is one choice, while the design of sharp edges can be improved is another. These new features will make the production of hard-to-

manufacture parts that have complex shapes simpler.

It is certainly important that there is a capability of the plastic to shrink dimensionally after the process of cooling in the mold, that adequate cooling is given to make the component trouble-free and the surface roughness is requested to be within the acceptable range of limits and in the meantime the design of the gating system should be the right one. These aspects play a major role in the productivity of the production process and the product cycle.

The finite element method has a good and wise way of separating the production part into more fine parts so the study of its behavior could be done. The part was processed through the finite element method to simulate in-mold flow analysis. In this investigation, the in-mold flow simulation has been carried out by the use of Autodesk Moldflow Insight Synergy 2016 version software and the injection analysis was worked with the help of the Cool-Fill-Pack-Warpage module, designed for mold cooling and filling time. Fluid behavior was determined in these studies by the use of the following formulas:

Continuity Equation

$$\frac{\partial \rho}{\partial t} + \frac{\partial \rho u}{\partial x} + \frac{\partial \rho v}{\partial y} + \frac{\partial \rho w}{\partial z} = 0 \tag{1}$$

Momentum Conservation Equation

$$\frac{\partial^2}{\partial t} \nabla^2 \cdot (\rho V)^{\frac{1}{2}} = 0 + V^{\frac{1}{2}} \cdot \frac{\nabla^2}{\partial t} \rho + \rho V . V^{\frac{1}{2}} = 0 \tag{2}$$

Conservation of Energy Equation

$$P_c \frac{dt}{v_{dt}} = k \nabla^2 T + \emptyset \tag{3}$$

3. Material

We can find that by the literature review, the engineering plastics applied to the production of plastic board-type piezoresistive pressure sensors in the last ten years have attracted considerable attention for their high structural strength and stiffness as well as for their low cost and resistance to fatigue [24]. PA, PBT and PC materials were the predominantly used materials in the manufacture of piezoresistive pressure sensors using the card-type technology. Table 1 shows the thermophysical properties of the materials designated for injection analysis namely, the three engineering plastics used in the Moldflow Synergy Material Database and the trade names are Novarex PC, Valox PBT, Amoled PA.

Table 1. Physical characteristics table.

Material	**PA**	**PBT**	**PC**	
Physical Properties	**Value**	**Value**	**Value**	**Unit**
Melt Density	0.95273	1.0451	1.0579	g/cm^3
Melt Temperature	335	248	300	°C
Solid Density	1.2473	1.2585	1.397	g/cm^3
Surface Temperature	80	60	95	°C
Modulus of Elasticity E1	2410	2600	2280	MPa
Maximum Shear Stress	0.5	0.41	0.5	MPa

3.1. Model

The board type sensor is depicted in Figure 1 as a 2D technical drawing and 3D model. The piezoresistive film model

is 6.85 mm, 10.00 mm and 1.78 mm, respectively, having its X, Y and Z bases of piezoresistive card type pressure sensor solid model in a Cartesian coordinate system. Two inlets on the model are 3 mm apart and the internal hole diameter is 1.14 mm.

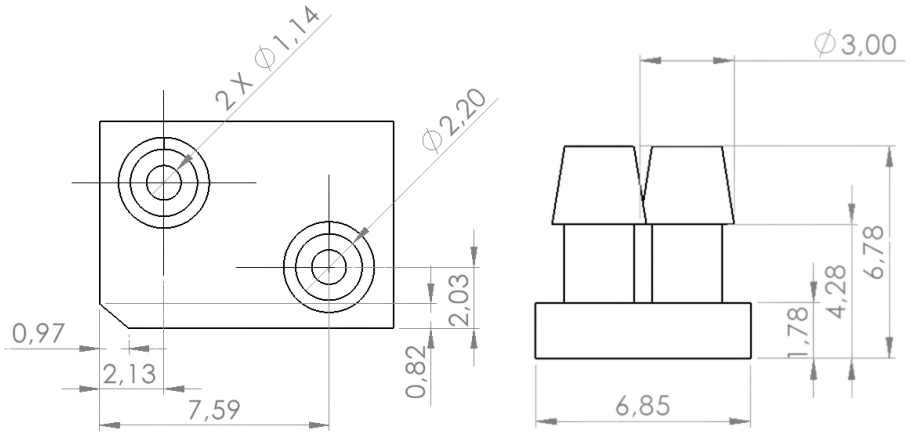

Fig. 1. Technical drawing dimensions of the model.

3.2 Mesh

The piezoresistive pressure gauge is designed with a flat structure when the triangular mesh lattice is used to cover the surface. The total number of the triangular mesh is 10798. This embodiment is designed to represent the geometric complexity of the model with high precision and to give a suitable mesh density for finite element analysis. The mesh element choice and the uniform mesh structure became efficient for the model's physical behavior simulation. The parameter specific to the proportion of the length-height width of a triangle to one of its angles (aspect ratio) which is an important one for the mesh and thus for the quality of the mesh structure, is maximum 3.69. Mesh representation of the model is shown in Figure 2.

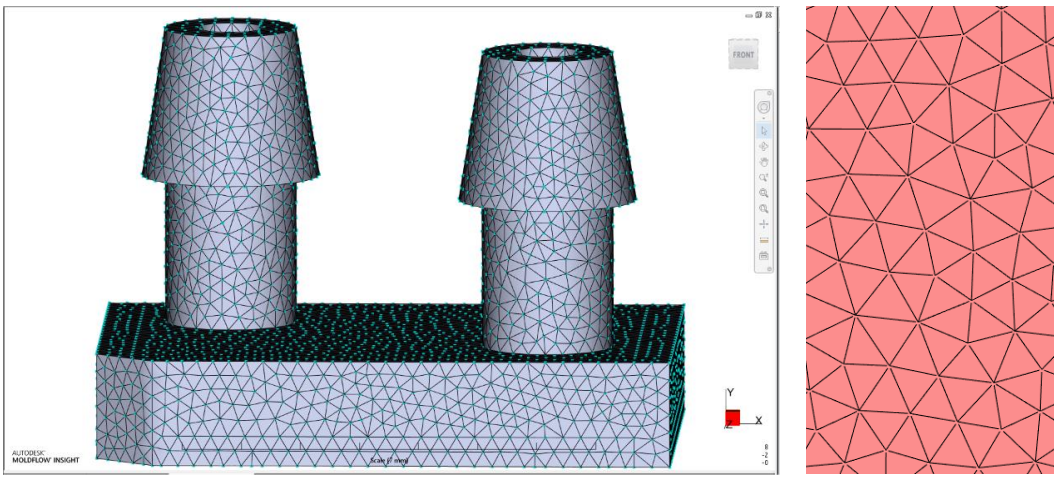

Fig. 2. Meshed model.

To improve the extent of precision within the simulation, localized mesh refinement was undertaken surrounding the important segments like injection gates, edges that are sharp and parts of the model that are thin. This method allowed

for a better representation of flow behavior and temperature distribution in the critical areas where disturbances are expected in the molding operations.

4. Modeling and analysis

The piezoresistive card type pressure sensor analyzed was simulated with SolidWorks commercial software program. It is crucial to simulate the appropriate mold design to create it. The mold designing of the model was done in the Moldflow Insight software.

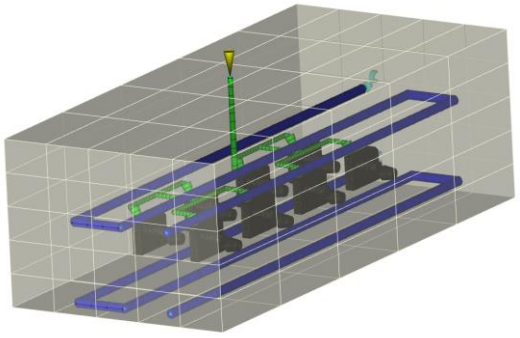

Fig. 3. Mold dimensions in Cartesian coordinates.

According to this 3D animation, the size of the mold measures 216, 50 and 200 mm for the X, Y and Z axes. The 3D representation of the mold is demonstrated in Figure 3. Tol steel P-20 was the used mold material. In this study, the Cool-Fill-Pack-Warpage analysis was completed and the recommended program values were input as the process settings.

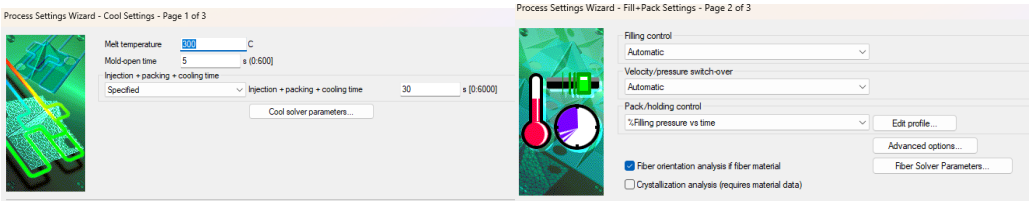

Fig. 4. Process settings view.

A process adjustment with adequate filling pressure was performed for 10 seconds and was limited to a maximum of 80% of the scope. The process controller was configured with the temperature control tab, the mold temperature control set as Uniform and 95°C was the criterion for the mold surface temperature. Besides this, the melt temperature reading was changed to 300°C as shown in Figure 4, while the room temperature was kept at 25°C. Summing up, the right time to fill the empty space (the open mold time) for starting is 5 seconds, the best cooling time is 20 seconds and a total of 30 seconds have been set as the enhanced time (injection + packing + cooling time) which was found to be the most effective configuration for the process.

4.1 Cooling circuit design

The vertical channels used for the cooling system were chosen to allow for the efficient design of the cooling system and the quality improvement of the product. From the sample of 8 pieces, it is possible to determine which heat channels have diameters and positions cooled by the dart. The rapid and uniform distribution of the heat and essential temperature

balancing were done by the diameters and positions of the cooling channels. By carrying out a uniform cooling process, the system runs at the highest efficiency and having the temperature profiles in the same position as the product. The cooling channels table is provided in Table 2.

Table 2. Cooling Duct Dimensions.

Part Size (X Axis) (mm)	68.04
Part Size (Y Axis) (mm)	20.34
Part Size (Z Axis) (mm)	6.85
Channel Diameter (mm)	10
Distance of the circuit to part (mm)	25
Channel Type	

These design features are shown in detail on the Figure 5 where the duct layout is. The picture is very evident of the way the optimization and the fixing of the ducts are to be made so that there is no one spot that is cooler than the others and thus ensured, the temperature control is done effectively.

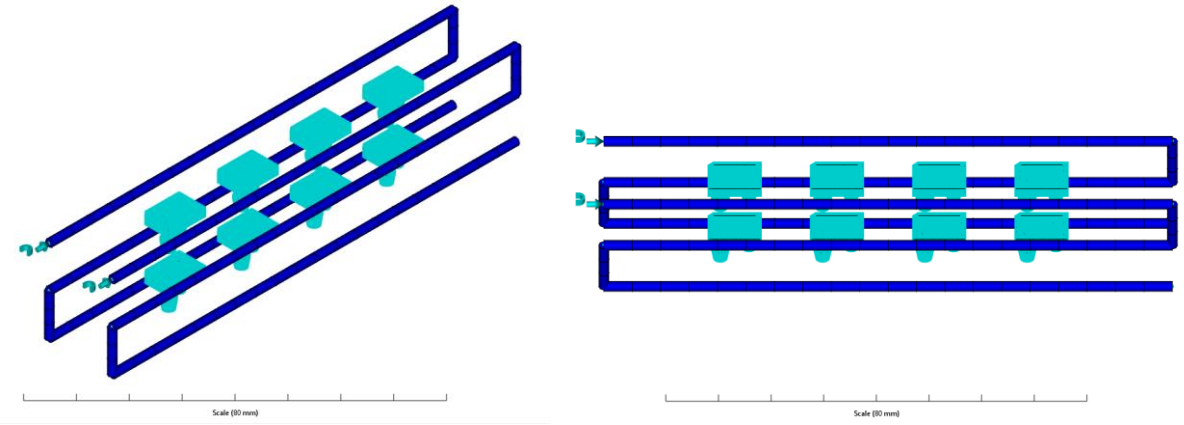

Fig. 5. Cooling circuit model.

Pure water was used as a coolant at 25° and the flow Reynolds number for the circulation was 10000. The fluid properties of the coolant in the analysis are given in Table 3.

Table 3. Fluid properties of the coolant.

Properties	**Value**	**Unit**
Coolant density	0.988	g/cm^3
Coolant specific heat	4180	J/kg-C
Coolant thermal conductivity	0.643	W/m-C

4.2 Gate location

The conformity issues resulted in a lack of and a very poor replication of the mold resulting in substantial flow defects like long gating systems and as such, were main sources of defects in the parts molded by that system. Therefore, part failure caused by shrinkage-induced warpage is a commonly known phenomenon. The detailed results of the flow resistance indicator and gate suitability analyses are visualized and presented in Figure 6. This approach is indispensable to the procedure of production optimization and the increase in the product's quality. The most suitable injection point was decided upon after the molding window and the gate location were determined through the use of a computer program which the results, in turn, are indicated in Figure 6.

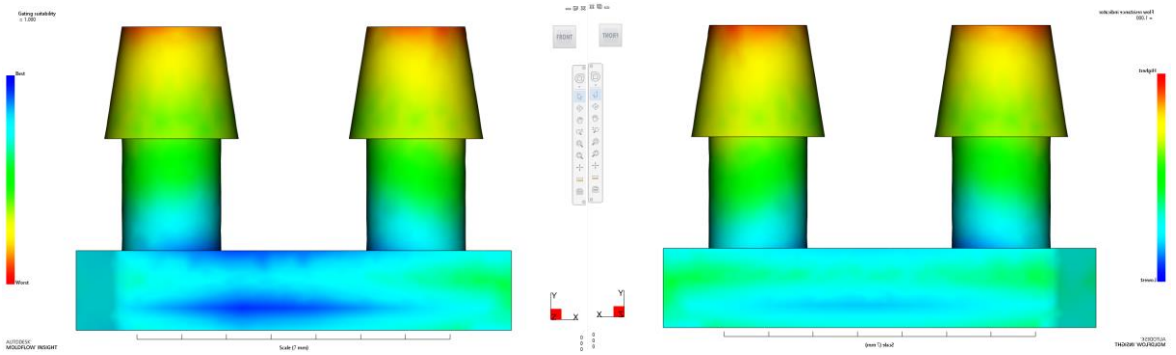

Fig. 6. a) Gating suitability. b) Flow resistance indicator analysis results.

Figure 6 illustrates the flow path system design for the piezoresistive card-type pressure sensor model. In Figure 6a, the overall layout of the runner system is depicted, pointing out the fact that the melt is driven uniformly to the eight identical cavities through the main and secondary runners. In Figure 6b, the material flow behavior within the runner system is presented through a simulation based analysis. The texture in Figure 6b symbolizes the distance and the progress of the melt moving as well as the distribution of the flow velocity, where warmer colors mainly red and orange indicate the speed of the flow and cooler colors, mainly blue and green, indicate no flow or regions with potential flow hesitation respectively.

4.3 Runner system

Injection molding flow path design depends not only on the filling time but also on the surface quality. The mold provided for the technological program has been carefully designed to provide and control the flow path that has thus resulted in eight piezoresistive solid models being manufactured at the same time. Additionally, this leads to the optimized flow pattern design and the flow path system layout that Figure 7 displays based on these design features.

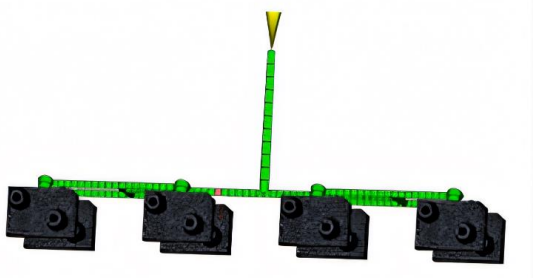

Fig. 7. Flow path system design.

To ensure all cavities were filled evenly and to minimize the internal stresses and the defects in the flow the design of the runner system was according to the rules of symmetry and balance. In the arrangement of eight sensor bodies simultaneously the manufacturing efficiency was notably increased.

The design of the runner system was well balanced and symmetrical for the even distribution of molten plastic within all cavities. This configuration made it possible to produce eight piezoresistive sensor bodies at the same time and without any defects which considerably increased manufacturing efficiency. The flow path optimization avoided the unfavorable occurrence of turbulence, air entrapment and surface defects during the filling operation. The simulation analyses indicated that material was smoothly directed to all the cavities via the main and secondary runners. This runner plan improved part quality while minimizing cycle time as a result of the optimization of production costs.

5. Results

The results achieved in this research are in line with the conclusions presented in the literature. One good case in point is that M.A.M. Ali et al. pointed out that filling time is the most important parameter that is affected by the injection process and if this parameter is optimized, then other factors that contribute to the production cycle time are not significant [19]. The analysis of this study revealed that PA had the shortest filling time (0.0548 s), thus confirming the idea that less viscous materials are more favorable for the process of mold filling. On the same note, Hsueh-Lin Wu and Ya-Hui Wang gave the proof of the fact that proper selection of materials and process conditions could potentially decrease volumetric shrinkage [15]. The result of our simulation also agreed with this, since PC material experienced the smallest volumetric shrinkage (6.63%) among all tested materials.

5.1 Fill time

Filling the time in the process is defined by the process of changing the material into the form of a product. According to the literature review, the study concluded that the time spent on the injection of the molds is the main parameter affecting the flow time [19]. The network model is set up by the operator who sets the proper gate location, material type and analysis parameters and the filling time analysis is executed. Figure 8 presents the details of the process when the material fills the model and the lines are the gameplay. The analysis result showed that PA is the material that best absorbs the filling time which gives the smaller time variant.

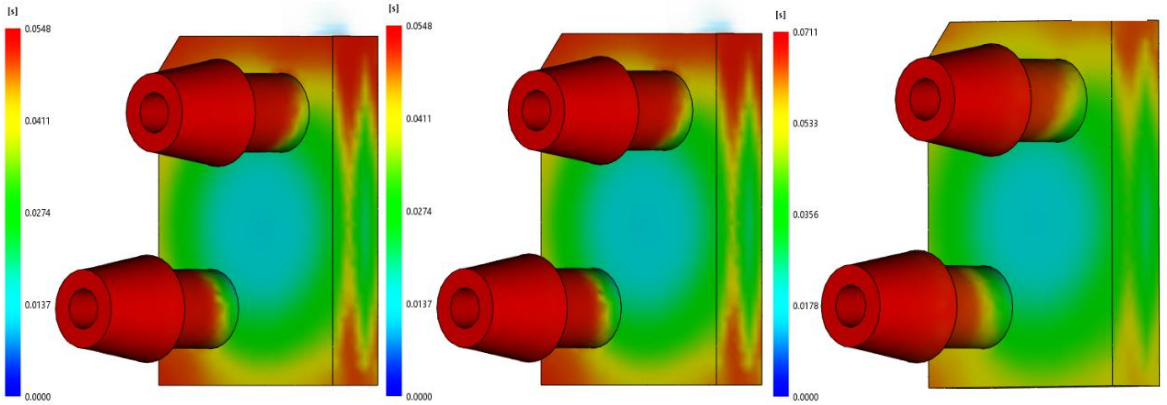

PA Time:0.0548s PBT Time:0.0987s PC Time:0.0711s

Fig. 8. Fill time results.

5.2 Pressure at v/p switchover

V/P switchover is a process that describes the point when the powders are transitioned from Speed control (injection process) to Pressure control (pressure holding process) at the moment at which the material is injected into the mold [25].

All raw material (PA, PBT and PC) were considered within a triad that was subjected to simulation. Based on the results of the Pressure at V/P Switchover procedure, PA is concluded as the material that seems to give the best results in production. The results of the analysis are presented in Figure 9.

The V/P switchover pressure is the key point of transition from filling to packing during the injection process, so it affects the surface quality and structural strength inside. In this research, PA was found to be the one with the least amount of V/P switchover pressure, efficient control of the in-mold pressure was also achieved and thus the energy consumption was minimized. Conversely, PBT and PC were found to have higher switchover pressures, which indicated that they had greater filling resistance. This parameter is a critical selection criterion for the material especially one required to achieve high precision. An internal mold stress reduction that's lower thresholded switchover pressure also aids in an easier and more uniform material flow.

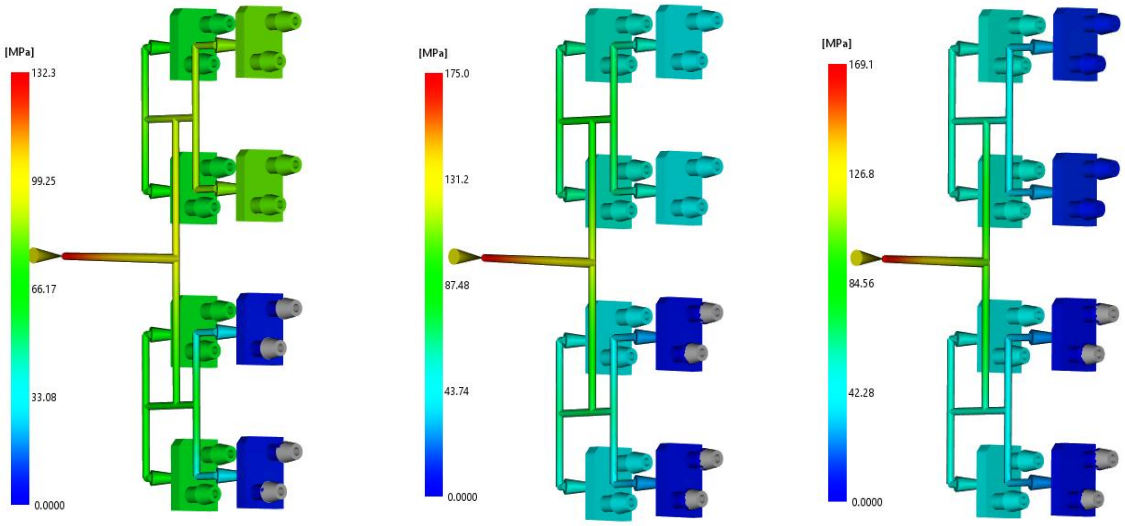

PA Pressure: 132.3 MPa PBT Pressure: 175 MPa PC Pressure: 169.1 MPa

Fig. 9. Pressure at v/p switchover results.

5.3 Temperature at front flow

In the analysis of cooling, in general, mold is put at a lower temperature than the melting material and the material temperature reduces during the filling process. The research found that PBT is the most suitable material for the selection of the optimum Temperature at Front Flow value. The results of the study are shown in Figure 10.

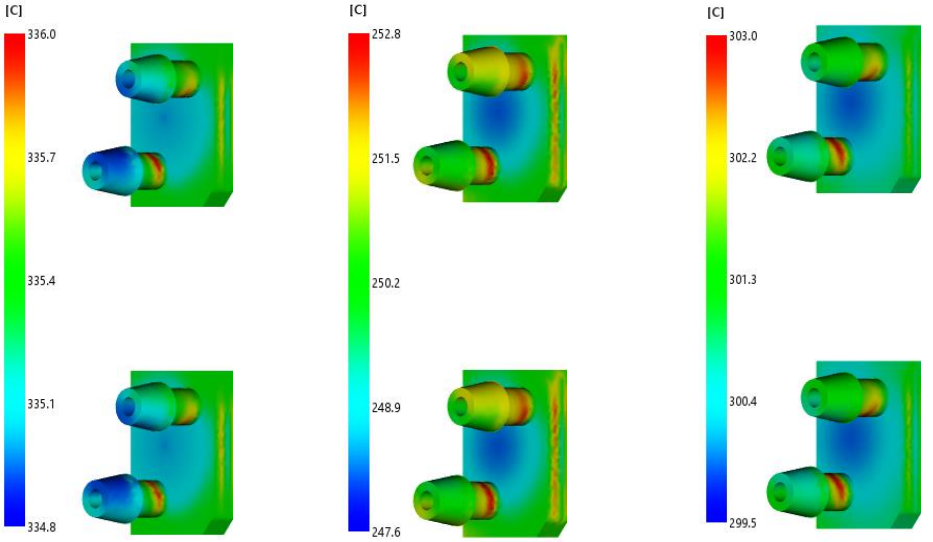

PA Temperature: 336°C PBT Temperature: 252.8°C PC Temperature:303°C

Fig. 10. Temperature at front flow analysis results.

The term "front flow temperature" denotes the temperature of the liquid polymer when it first reaches the cavity of the mold and acts as a major parameter for the control of surface quality, flow stability and thus for the prevention of filling defects. The results of this study show that PBT was characterized by the lowest front flow temperature as a result of its excellent thermal stability and its technical ability to minimize such trouble as burning, surface deformation and flash formation, which are the common problems in the molding of plastics. The temperature control was more effective, the filling process was smoother and more controlled and thus the overall product quality was improved. Therefore, PBT would remain the most suitable material for heat-sensitive components in particular.

5.4 Pressure at injection location: xy plot

The control of injection point pressure analysis, where three different materials were used for the produced parts in order to guarantee the optimum pressure control, is presented. These are PA, PBT and PC respectively. The results of the analysis are shown in Figure 11.

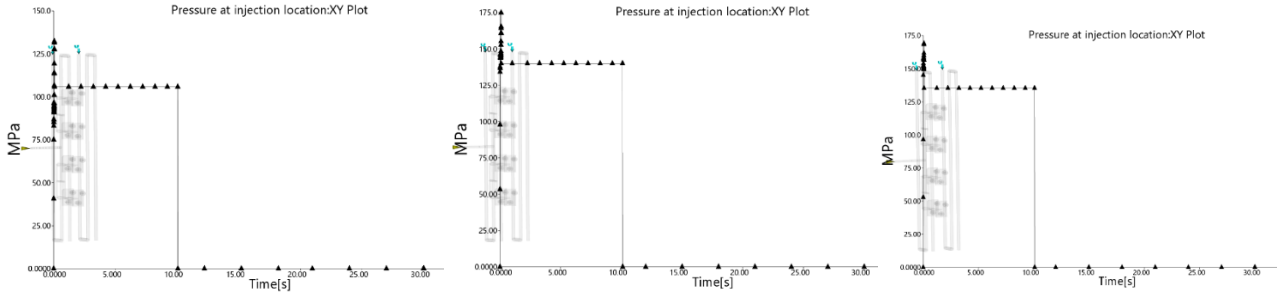

PA PBT PC

Fig. 11. Pressure at injection location: xy plot results.

When the injected material enters the mold, the pressure at the injection site is proportional to the resistance met by

the material through the mold and it is the prime factor in flow balance and distribution of internal stress. The analysis showed that the PA had the least amount of the injection pressure, meaning a more stable filling process, which is less energy consuming. On the other hand, PBT and PC received more pressure readings, which indicated the increased resistance of flow, primarily in narrow geometries and a more uneven pressure distribution in the mold. This finding emphasizes that adjusting the injection pressure not only rids the product of quality defects but also increases the efficiency of the whole process.

5.5 Volumetric shrinkage at ejection

The literature review has revealed that the process parameters have been optimized in respect of the volumetric shrinkage [26]. The study results noted that material that provides optimal volumetric shrinkage value was PC -6.63%. The analysis results are given in Figure 12 as PA, PBT and PC respectively.

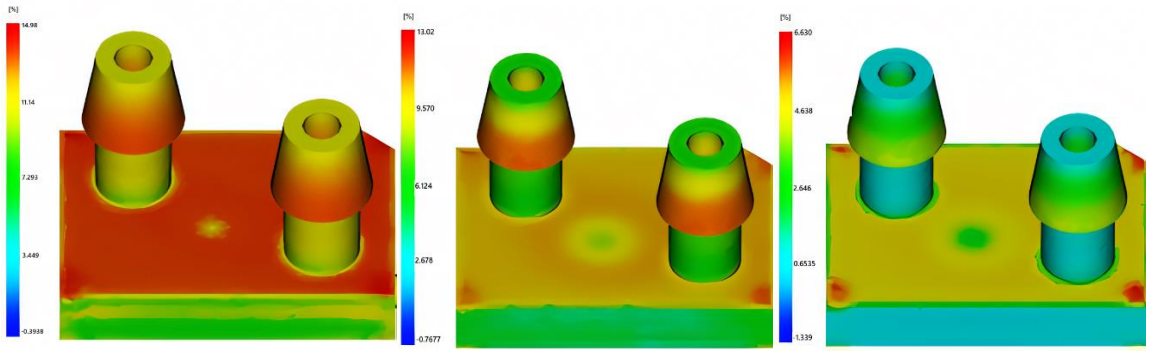

PA: 14.98% PBT: 13.02% PC: 6.63%

Fig. 12. Volumetric shrinkage values.

From the study it has been established that the lowest shrinkage rate is obtained with PC, thus making it the most suitable material for high precision applications. Conversely, chemicals such as PA and PBT were shown to have the highest shrinkage values which must be carefully taken into consideration in respect of warpage and dimensional deviations.

5.6 Time to reach ejection temperature

It is recognized that melt, mold and ejection temperature really influence the reduction of demolding time [27]. Based on the analytical results of Figure 13, it is clear that the material with the best demolding time is PA by time value of 2.214s.

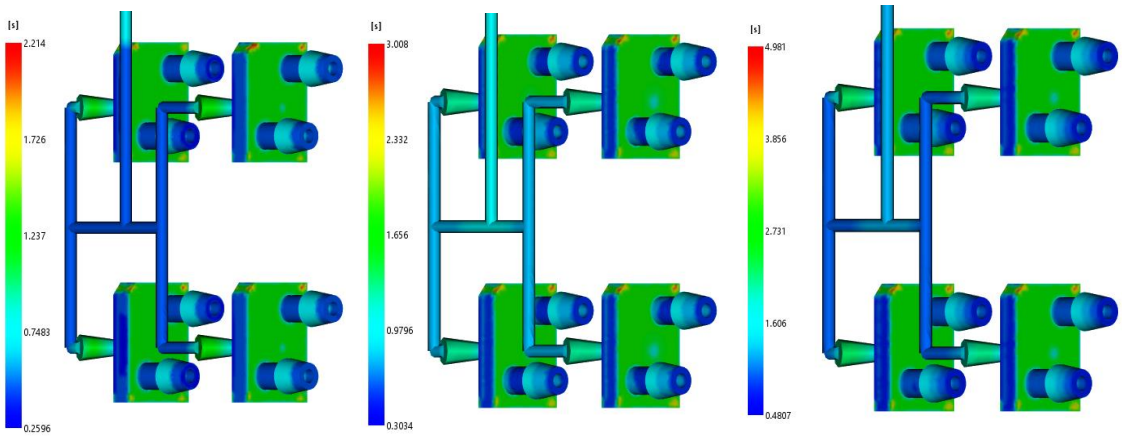

PA: 2.214s PBT: 3.008s PC: 4.981s

Fig. 13. Time to reach ejection temperature results.

The part needs to be cooled enough before, so we can remove it, the removal of the part must be safe. A comparative study of PA, PBT and PC materials was conducted with respect to the ejection temperature profile as the time taken by each to reach the ejection temperature was measured. The time took PA the least time, 2.214 seconds, faster than others, thus leading to the leading advantage of this type of material in rapid manufacturing processes. On the other hand, PBT and PC took much longer to reach this temperature hence leading to a possible elongation of the production cycle.

5.7 Bulk temperature at end of fill

As a part of bulk temperature analysis at the end of fill, the part temperature was monitored after the filling stage during injection. The material which was found to have the highest value was PBT which was 295 according to the analysis. The record is shown in Figure 14.

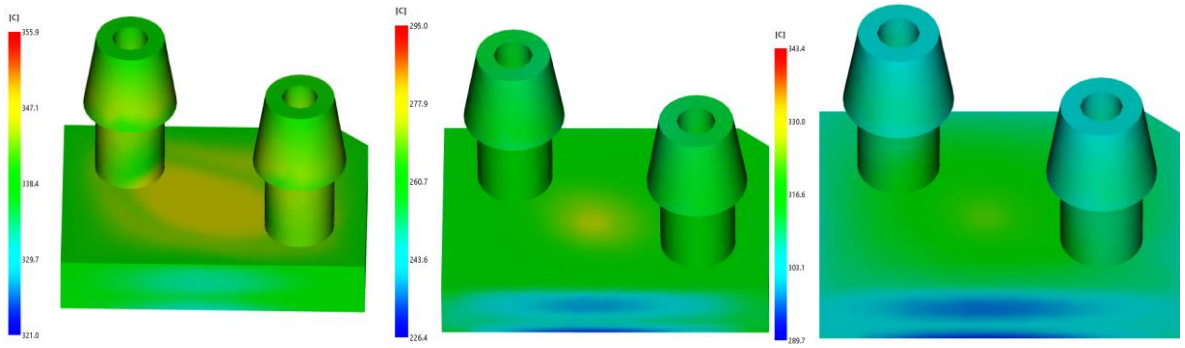

PA:355.9°C PBT: 295°C PC:343.4 °C

Fig. 14. Bulk temperature at end of fill results.

The bulk temperature measured at the end of the fill is a significant factor for evaluating the homogenous distribution and cooling of the molten material inside the mold. In this study, PBT which is the material we used reached the lowest average temperature of 295°C most likely due to better control of heating during the molding process. This property permits the choice of PBT in exact molding applications where the balance of heat is imperative.

5.8 Circuit pressure

Pressure Circuit analysis was done for determining the pressure on the cooling circuit and the results got from this analysis are shown in Figure 15. The molding process is strongly influenced by circuit pressure because it is a very important aspect of effective heat removal. Ensuring that the circuit pressure is well managed ensures that the coolant flows uniformly through the mold and that temperature variations and local shrinkage are minimal. The findings of this study's analysis show that the cooling circuit's pressure distribution was correctly designed and guaranteed effective heat transfer. The low pressure deviations indicate the thermal stability of the system and the good state of the overall part quality are achieved.

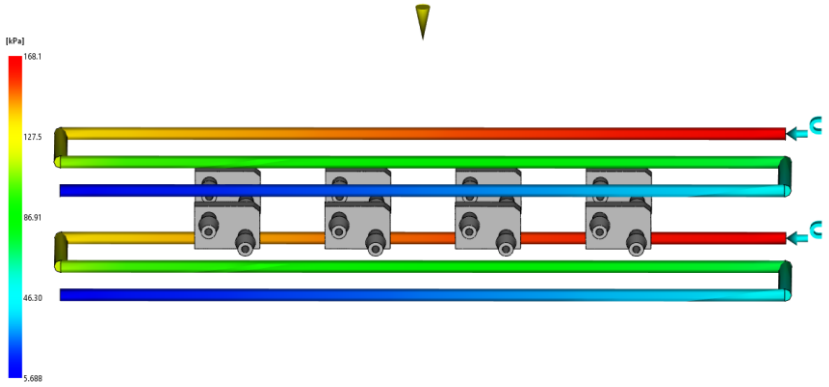

Fig. 15. Circuit pressure results.

5.9 Flow rate beams

The flow rate beams analysis included 3 different material types, considering the safe and stable flow control. These were PBT, PA and PC materials. The consequence of the study made it clear that of the three, PBT was able to satisfy production requirements in a more optimal way. Defining flow rate values is critical in determining whether or not the molten material penetrates the mold properly and evenly. As far as this research is concerned, PBT has proved to be the most effective in the control of filling process so that it becomes an even and uninterrupted process. Figure 16 displays the findings of the study.

The low and steady flow rate value (15.42 cm^3/s) of PBT ensured that rapid directional shifts that could cause turbulence in convoluted geometries were prevented. However, the higher flow rates of PA and PC materials at some locations indicated some regions were overpack and some potential surface defects were present. Thus, these defects may lead to increased cooling differentials and stress accumulations. The use of PBT caused a uniform flow pattern, which led to a more balanced temperature and pressure distribution in the full mold. This further proves that PBT is the best material in applications such as the one described above where precision is essential and high surface quality is a must.

A review of these analyses indicates that in the selection of materials, the characteristics of flow must be weighed equally with mechanical and thermal properties. The technique of flow rate control is the most crucial one in multi-cavity molds in achieving the equal filling of all cavities. The filling might be quicker at higher flow rates; however, such filling rates would also lead to a greater chance of defects such as air entrapment. The flow rate that was controlled by PBT was able to minimize such problems leading to the greater reliability of the molding process. The conclusions derived from these studies confirm that it is necessary that flow rate analysis must be a part of the design stage of injection molding operations.

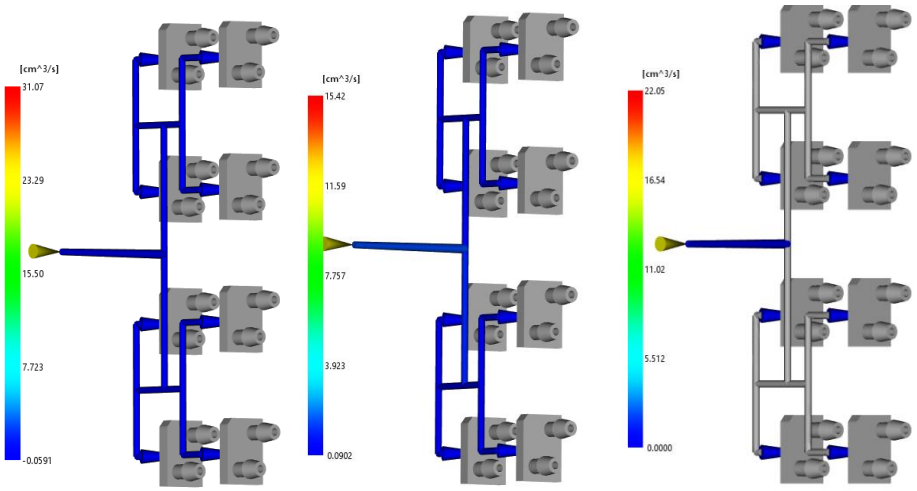

PA: 31.07[cm^3/s] PBT: 15.42[cm^3/s] PC: 22.05[cm^3/s]

Fig. 16. Flow rate beams results.

6. Conclusion

To determine the most suitable material and process parameters for the piezoresistive card type pressure sensors in the injection molding process, a comprehensive analysis has been carried out in this work. Three different engineering plastics, namely, PA, PBT and PC, have been evaluated and the impact of each material on the production process has been studied.

The simulation analysis results demonstrated that PA had the shortest filling time of 0.0548 s and the lowest mold disconnect time of 2.214 s, PC was the one with the lowest volumetric shrinkage of 6.63% and the one with the best thermal stability of 252.8°C was PBT. In addition, PA showed the lowest injection pressure value of 132.3 MPa whereas PBT showed optimum flow control leading to a balanced production process.

Accordingly, it is concluded that PA is advantageous in the rapid production of devices such as quick charging and energy efficient function whereas PC is useful in the applications where dimensional accuracy is critical and PBT is the best production choice if both mechanical and thermal stabilities are important. The study also identified that both mechanical as well as thermal stabilities are important factors in the production process and thus, PBT is a balanced solution. This proves its suitability and flexibility by further adding a product's market advantages.

The study is a comprehensive guide for the material selection and optimization of the injection molding parameters for the production of piezoresistive pressure sensors. The findings will contribute to the development of low cost, efficient and quality production processes that can be implemented in both academic and industrial applications. Although the study's findings significantly enlighten the understanding of the behavior of various engineering plastics in the process of injection molding, it would be advisable for the research in the future to be more focused on the verification of these findings of simulation with the help of experiments. The physical molding of PA, PBT and PC as well as the same process conditions of this study would enable one to conduct a direct comparison with the data gotten from the simulation. In addition to drawing the line between the simulations and the real injections, the findings would help to detect any kind of discrepancy due to the data feed into the machine, differences in the materials or the environment. Also, the part may need to undergo long term trials and mechanical tests to determine the service life and the fitness for pressure sensor applications. The co-use of the data from the experiments with the outputs of the simulation will, beyond a doubt, lift the method up to the stage of full reliability and industrial practicability.

Acknowledgements

There is no conflict of interest with any person/institution in the prepared article.

Author Contributions

F.T. and B.B. contributed to the design and implementation of the research, to the analysis of the results and to the writing of the manuscript.

References

[1] H. Fu *et al.*, "Overview of Injection Molding Technology for Processing Polymers and Their Composites," *ES Materials & Manufacturing*, vol. 8, no. 20, pp. 3–23, 2020, doi: 10.30919/esmm5f713.
[2] M. Czepiel, M. Bańkosz, and A. Sobczak-Kupiec, "Advanced Injection Molding Methods: Review," *Materials*, vol. 16, no. 17, p. 5802, Aug. 2023, doi: 10.3390/ma16175802.
[3] G. Wang, Y. Wang, and D. Yang, "Study on Automotive Back Door Panel Injection Molding Process Simulation and Process Parameter Optimization," *Advances in Materials Science and Engineering*, vol. 2021, no. 1, pp. 1–13, Jan. 2021, doi: 10.1155/2021/9996423.
[4] A. L. N. Vieira, R. D. S. G. Campilho, F. J. G. Silva, and L. P. Ferreira, "Increasing the Environmental Sustainability of an Over-Injection Line for the Automotive Component Industry," *Sustainability*, vol. 13, no. 22, pp. 1–23, Nov. 2021, doi: 10.3390/su132212692.
[5] S. S. Abubaker, S. A. Gashout, A. O. Alghazali, M. T. Albarouni, and A. M. Elbarouni, "Design and Simulation of Polymer Needles to Produce by Injection Molding Machine," *Surman Journal of Science and Technology*, vol. 6, no. 1, pp. 1–15, Jan. 2024
[6] C. Yang, G. Wang, J. Zhao, G. Zhao, and A. Zhang, "Lightweight and strong glass fiber reinforced polypropylene composite foams achieved by mold-opening microcellular injection molding," *Journal of Materials Research and Technology*, vol. 14, no. 1, pp. 2920–2931, Sep. 2021, doi: 10.1016/j.jmrt.2021.08.052.
[7] S. Ramesh *et al.*, "Simulation Process of Injection Molding and Optimization for Automobile Instrument Parameter in Embedded System," *Advances in Materials Science and Engineering*, vol. 2021, no. 1, pp. 1–10, Jan. 2021, doi: 10.1155/2021/9720297.
[8] S. Formentin, L. Onesto, T. Colombo, A. Pozzato, and S. M. Savaresi, "h-TPMS: a hybrid tire pressure monitoring system for road vehicles," *Mechatronics*, vol. 74, no. 1, p. 102492, Apr. 2021, doi: 10.1016/j.mechatronics.2021.102492.
[9] H. Soy and İ. Toy, "Design and implementation of smart pressure sensor for automotive applications," *Measurement*, vol. 176, p. 109184, May 2021, doi: 10.1016/j.measurement.2021.109184.
[10] B. Adam, T. Brandt, R. Henn, S. Reiss, M. Lang, and C. Ohl, "A New Micromechanical Pressure Sensor for Automotive Airbag Applications," in *VDI-Buch*, Berlin, Heidelberg: Springer Berlin Heidelberg, 2008, pp. 259–284. Accessed: May 07, 2025. [Online]. Available: https://doi.org/10.1007/978-3-540-77980-3_20
[11] C.-W. Su *et al.*, "Optimization process parameters and adaptive quality monitoring injection molding process for materials with different viscosity," *Polymer Testing*, vol. 109, no. 1, p. 107526, May 2022, doi: 10.1016/j.polymertesting.2022.107526
[12] J. Gim and L.-S. Turng, "A review of current advancements in high surface quality injection molding: Measurement, influencing factors, prediction, and control," *Polymer Testing*, vol. 115, no. 1, p. 107718, Nov. 2022, doi: 10.1016/j.polymertesting.2022.107718.
[13] R. Farooque, M. Asjad, and S. J. A. Rizvi, "A current state of art applied to injection moulding manufacturing process – A review," *Materials Today: Proceedings*, vol. 43, no. 1, pp. 441–446, 2021, doi: 10.1016/j.matpr.2020.11.967.
[14] N. Zhao, J. Lian, P. Wang, and Z. Xu, "Recent progress in minimizing the warpage and shrinkage deformations by the optimization of process parameters in plastic injection molding: a review," *The International Journal of Advanced Manufacturing Technology*, vol. 120, no. 1–2, pp. 85–101, Feb. 2022, doi: 10.1007/s00170-022-08859-0.
[15] H. L. Wu and Y. H. Wang, "Using Taguchi Method to Optimize Molding Process Parameters of Chair Base," *Applied Mechanics and Materials*, vol. 271–272, no. 1, pp. 1190–1194, Dec. 2012, doi: 10.4028/www.scientific.net/amm.271-272.1190.
[16] M. Zhiguo *et al.*, "Co-simulation technology of mold flow and structure for injection molding reinforced thermoplastic composite (FRT) parts," *Advanced Composites and Hybrid Materials*, vol. 5, no. 2, pp. 960–972, Jan. 2022, doi: 10.1007/s42114-021-00407-w.
[17] Q. Su, N. Zhang, and M. D. Gilchrist, "Precision injection moulding of micro components: Determination of heat transfer coefficient and precision process simulation," *International Journal of Mechanical Sciences*, vol. 269, no. 1, p. 109065, May 2024, doi: 10.1016/j.ijmecsci.2024.109065.
[18] F. Tan. "Experimental investigation of mechanical properties for injection molded pa66+ pa6i/6t composite using rsm and grey wolf optimization." *Al-Jazari*, vol. 7, no. 2, pp. 835-847, May. 2020, doi: 10.31202/ecjse.705212.
[19] M. A. Md Ali *et al.*, "Fill Time Optimization Analysis In Flow Simulation Of Injection Molding Using Response Surface Method," *Malaysian Journal on Composites Science and Manufacturing*, vol. 4, no. 1, pp. 28–39, Mar. 2021, doi: 10.37934/mjcsm.4.1.2839.
[20] F. Tan and A.K. Alkan. "Effect of Cooling Parameters on In-Mold Flow Behavior in the Microinjection Molding of Piezoelectric Pumps." *International Journal of Automotive Science and Technology*, vol. 8, pp. 467-475, December. 2024, doi: 10.30939/ijastech..1566495.
[21] C. Fernandes, A. J. Pontes, J. C. Viana, and A. Gaspar-Cunha, "Modeling and Optimization of the Injection-Molding Process: A Review," *Advances in Polymer Technology*, vol. 37, no. 2, pp. 429–449, Mar. 2016, doi: 10.1002/adv.21683.
[22] M. Baum, D. Anders, and T. Reinicke, "Approaches for Numerical Modeling and Simulation of the Filling Phase in Injection Molding: A Review," *Polymers*, vol. 15, no. 21, p. 4220, Oct. 2023, doi: 10.3390/polym15214220.
[23] H. K. Lee, J. C. Huang, G. E. Yang, and H. G. Kim, "Analysis of Residual Stress in Thin Wall Injection Molding," *Key Engineering Materials*, vol. 306–308, no. 1, pp. 1331–1336, Mar. 2006, doi: 10.4028/www.scientific.net/kem.306-308.1331.

[24] V. Chauhan, T. Kärki, and J. Varis, "Review of natural fiber-reinforced engineering plastic composites, their applications in the transportation sector and processing techniques," *Journal of Thermoplastic Composite Materials*, vol. 35, no. 8, pp. 1169–1209, Nov. 2019, doi: 10.1177/0892705719889095.
[25] Y. Xu *et al.*, "Self-optimization of the V/P switchover and packing pressure for online viscosity compensation during injection molding," *Polymer Engineering & Science*, vol. 62, no. 4, pp. 1114–1123, Jan. 2022, doi: 10.1002/pen.25910.
[26] L.L. Shu, J.-W. Zhou, M.-W. Wang, X.-H. Ye, D. Wu, and J.-W. Yu, "Optimization of Injection Molding Process Parameters for Left Front Bumper of Automobile Based on Entropy Weight Method," *Plastics Science & Technology/Suliao Ke-Ji*, vol. 51, no. 7, 2023, doi: 10.15925/j.cnki.issn1005-3360.2023.07.017.
[27] T. Lucyshyn, L.-V. Des Enffans d'Avernas, and C. Holzer, "Influence of the Mold Material on the Injection Molding Cycle Time and Warpage Depending on the Polymer Processed," *Polymers*, vol. 13, no. 18, p. 3196, Sep. 2021, doi: 10.3390/polym13183196.

Contents lists available at *Dergipark*

Journal of Scientific Reports-A

journal homepage: *https://dergipark.org.tr/tr/pub/jsr-a*

E-ISSN: 2687-6167 ***Number 61, June 2025***

RESEARCH ARTICLE

Receive Date: 19.03.2025 *Accepted Date: 28.04.2025*

Activated carbon production from black cumin pulp, walnut shell, almond kernel shell and apricot kernel shell

Kamil Mammadov[a], Salih Aydogan[b,*]

[a] *Azerbaijan Technical University, Departamen of Metallurgy and Materials Tecniolocy, Baku, Azerbaijan, ORCID: 0000-0001-6411-1090*
[b] *Konya Technical University, Departamen of Mining Engineering, Konya, Türkiye, ORCID: 0000-0001-6382-1488*

Abstract

Black cumin pulp, walnut shells, almond kernel shells and apricot kernel shells are plant residues from agricultural crops. Millions of tonnes of such biomass rich in carbon content are increasing every year in the world. In this study, the above-mentioned plant residues were collected and activated carbons were produced from these residues to be used in cyanide gold solution. The plant residues were subjected to carbonisation and then activation processes at different times and temperatures. As a result of carbonisation processes, products containing 68.80% C for black cumin pulp, 90.76% C for walnut shell, 89.10% C for almond kernel and 92.61% C for apricot kernel were obtained. BET and SEM analyses of these materials, which have sufficient carbon content for activated carbon production, were performed. As a result of BET analyses, it was determined that the surface area of activated carbon produced from apricot kernel shell increased up to 984 m²/g. SEM analyses showed that the activated carbon produced from almond shells had optimum porosity.

Keywords: Black cumin pulp; biomass; apricot kernel shell; almond shell; walnut shell; carbonisation; activation:

1. Introduction

In recent years, the rapid depletion of natural resources worldwide, the increase in environmental and atmospheric pollution and the recovery of depleted resources are becoming increasingly difficult. In order for humans and other

*Corresponding author. Tel.: +905359686160
E-mail address: saydogan@ktun.edu.tr

living creatures to survive in a healthy way, various solution proposals are being developed, and in this direction, it is aimed to popularise the understanding of 'environmental sustainability'.

Many issues from environmentally friendly products to renewable energy sources have gained importance within the framework of sustainability. Various adsorbent materials can be used to reduce water pollution and pollutants generated in industrial plants at the source. In this context, materials such as minerals, resins and activated carbon with adsorption capacity play an important role in controlling environmental pollution.

Activated carbon is a mainly amorphous solid with an extremely large internal surface area and a large pore volume [1]. Activated carbon is produced from materials containing high amounts of carbon and its composition usually contains 87-97% carbon. The remaining part may contain elements such as hydrogen, oxygen, sulphur and nitrogen. In addition, depending on the raw materials used and other chemicals added during the production process, activated carbon is known to contain different elements [2]. Activated carbons have the capacity to adsorb a wide range of substances and can act as adsorbents by attracting molecules to their inner surfaces. Generally, the pore volume of activated carbons is greater than 0.2 ml/g [3]. Activated carbons are widely used in many sectors such as medicine, environment, chemistry, energy, metallurgy, metallurgy, textile and food in processes such as separation, purification, removal and recovery. An important advantage of activated carbon is that it can be produced from various biomass wastes with high carbon content and low inorganic matter content and can be reused through regeneration [4].

Today, many agricultural residues can be used for activated carbon production. For example biomasses such as palm fibres [5], tea plant waste, almond shells [6], hazelnut and walnut shell [7], from the outer green shell of pistachios [8], sugar beet pulp [9], sunflower seed shells and trays [10] and pistachio shells [11] can be shown.

In order to develop lower cost activated carbons, there are many researches on cheap and easily available materials. Thanks to their high surface areas, microporous structures and surface chemical properties, activated carbons stand out as effective potential adsorbents for the removal of heavy metal ions in industrial wastewater. Activated carbon produced from apricot kernel, an agricultural waste, can be used as an effective adsorbent for the removal of heavy metal ions from aqueous solutions [12].

In this study, the carbonisation of black cumin pulp, almond shell, walnut shell and apricot kernel shells, which are biomasses to be used for gold adsorption in cyanide gold solutions, was carried out, the weight losses of the samples after carbonisation were examined and these materials were evaluated as raw materials for activated carbon production. The obtained samples were subjected to SEM tests to determine their morphological properties and BET tests to analyse their surface properties.

2. Experimental Studies

2.1. Material-Method

In this study, various biomasses such as black cumin pulp, walnut shell, almond kernel shell and apricot kernel shell were used (Figure 2.1). Carbonisation and activation processes were carried out in Nüve brand MF 201 model and Nevola brand muffle furnace. In the experiments, Merck brand potassium hydroxide (KOH) with CAS number 1.05033.1000 was used as activating agent, and in order to remove potassium from the environment, washing with Merck brand hydrochloric acid (HCl) with CAS number 1.00317.2500 was applied, followed by rinsing with pure water. The obtained samples were analyzed by SEM and BET and the results are shown in Table 6 and Figure 4.

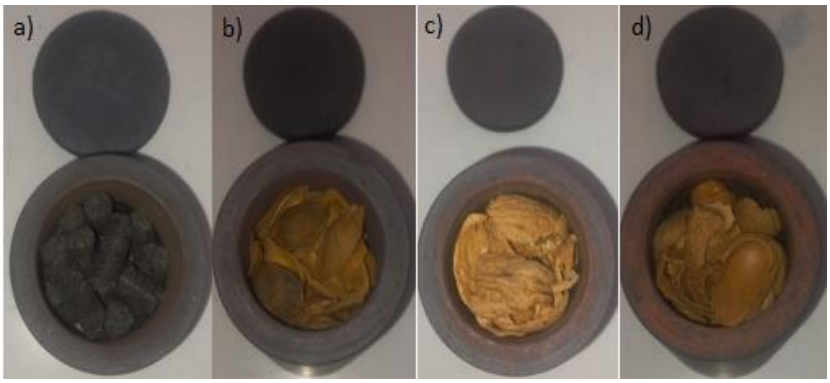

Fig. 1. Materials used in the carbonisation process: a- black cumin pulp, b- apricot kernel shell, c- walnut shell, d- almond shell.

Carbon (C) and sulphur (S) analyses of the obtained samples were carried out in LeCo CS 230 device before carbonisation and activation processes and the analysis results are given in Table 1.

Table 1. Crude C-S analysis results of almond shell, apricot kernel shell, walnut shell, black cumin pulp

Materials	Elements, %	
	C	S
Almond	46.4	0.001
Apricot	48.5	0.00131
Walnut	47.5	0.021
Black Cumin Pulp	----	----

Raw black cumin pulp showed a negative effect during the C and S analyses and the analyses could not be completed.

2.1.1. Carbonisation

The samples were carbonised in the muffle furnace at 600 °C, 700 °C and 800 °C for 2, 4 and 8 hours respectively. The samples in the crucibles were kept in the furnace without opening the lids to prevent contact with oxygen and allowed to cool down to room temperature. As a result of carbonisation processes, a weight loss of approximately 74-77.4% was observed in apricot kernel shell, 75.2-77.1% in almond kernel shell, 73.4-76.9% in walnut shell and 74.75-78.7% in nigella pulp. This weight loss indicates that impurities other than carbon in the structure were removed and a carbon-dominated material was obtained. Figure 2 details the weight loss of the materials during the carbonisation process.

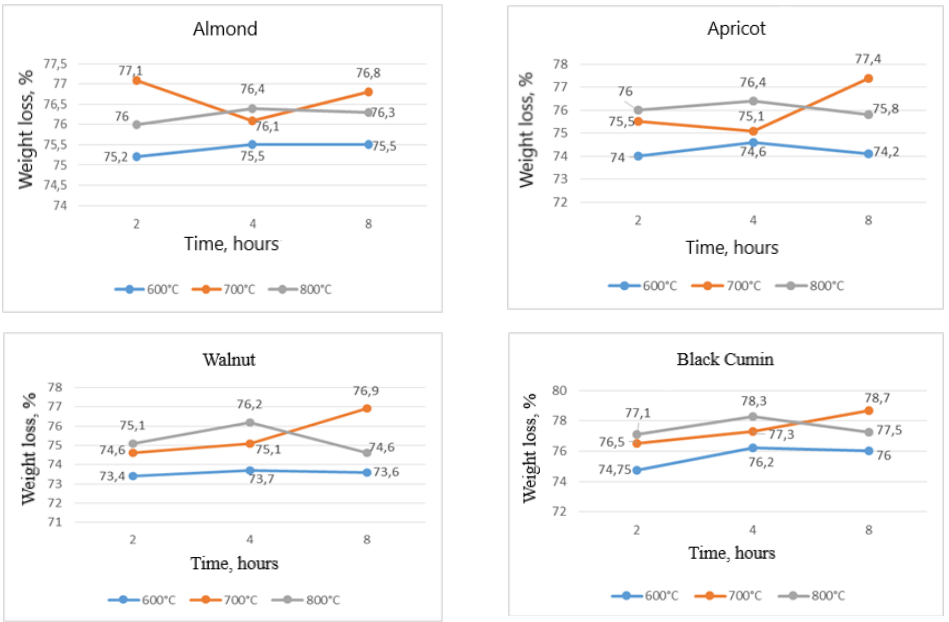

Fig. 2. Weight losses occurring in the structure of materials

After the carbonisation process was completed, the samples were removed from the furnace, weighed and stored in ziplock bags. Then, analyses were carried out to determine the carbon and sulphur contents.

When the analysis results of the carbonised products were examined, it was found that the carbon content of the almond shell treated at 800 °C for 4 hours was 89.1% and the sulphur content was 0.013% and these data are presented in Table 2.

Table 2. C-S analysis results of carbonised almond kernel shell

Material	Carbonisation temperature (°C)	Carbonisation time (hours)	Elements, %	
			C	S
Almonds	600	2	87.21	0.002
		4	88.23	0.015
		8	88.08	0.022
	700	2	87.8	0.04
		4	88.31	0.025
		8	88.4	0.016
	800	2	88.3	0.012
		4	89.1	0.013
		8	88.53	0.004

As a result of the carbonisation of apricot kernel shell, it was determined that the carbon content of the sample treated at 800 °C for 4 hours increased to 92.61% and the sulphur content decreased to 0.01%, and these results are presented in Table 3. These values represent the highest carbon yields reported for activated carbons derived from almond shells.

Table 3. C-S analysis results of carbonised apricot kernels

Material	Carbonisation temperature (°C)	Carbonisation time (hours)	Elements, %	
			C	S
Apricot	600	2	90.905	0.002
		4	91.91	0.022
		8	86.92	0.006
	700	2	91.44	0.016
		4	92.25	0.017
		8	87.35	0.013
	800	2	91.82	0.006
		4	92.61	0.01
		8	88.43	0.017

After the carbonisation process, the carbon content of walnut shells, which was 47.5% in raw form, increased to 90.76% in the sample treated at 800 °C for 8 hours. The sulphur content of the same sample was determined as 0.073% (Table 4).

Table 4. C-S analysis results of carbonised walnut shell

Material	Carbonisation temperature (°C)	Carbonisation time (hours)	Elements, %	
			C	S
Walnut	600	2	88.1	0.09
		4	88.25	0.035
		8	88.3	0.062
	700	2	88.94	0.079
		4	89.32	0.057
		8	89.3	0.087
	800	2	89.3	0.086
		4	90.72	0.086
		8	90.76	0.073

After the carbonisation of black cumin pulp, it was determined that the highest carbon content reached 68.8% in the sample treated at 800 °C for 2 hours. However, the sulphur content of this sample was quite high compared to the others and was determined as 0.37%. It is also shown in Table 5 that a decrease in carbon content was observed with increasing processing time.

Table 5. C-S analysis results of carbonised black cumin pulp

Material	Carbonisation temperature (°C)	Carbonisation time (hours)	Elements, %	
			C	S
Black Cumin Pulp	600	2	67.28	0.026
		4	65.21	0.101
		8	61.14	0.097
	700	2	68.2	0.345
		4	65.78	0.274
		8	62.52	0.35
	800	2	68.8	0.37
		4	66.46	0.43
		8	63.75	0.33

2.1.2. Activation

The activation studies were carried out on the samples obtained under the conditions yielding the highest carbon

content, as specified in the 'Carbonization' section. After the carbonization process, the carbonized product was crushed and sieved and the samples of -2;+1 mm size were subjected to activation process.

The carbonized products obtained from apricot kernel shell, walnut shell, almond kernel shell and black cumin pulp were activated by mixing with KOH at a ratio of 1/0.5 and 1/1. The activation process was carried out in a muffle furnace at 600 °C for 4 hours. The activated samples were cooled in the oven in a controlled manner to prevent contact with air.

Then 500 mL HCl solution was prepared per 50 g of material to remove KOH from the samples. This solution was prepared to contain 208 mL of 37% HCl (Merck) and the remaining volume was completed with distilled water. In order to bring the pH level to the desired range, the samples were subjected to sequential washing with distilled water and the washing process was continued using filter paper until the pH value reached 5.5-6. After the washing process was completed, the samples were subjected to drying and kept in an oven at 80 °C for 24 hours. Figure 3 shows the flow chart of the activated carbon production process.

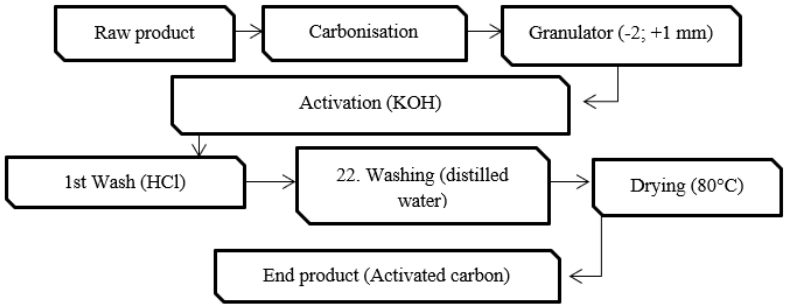

Fig. 3. Activated carbon production flow chart

Activated carbons were subjected to BET and SEM analyses. The results of BET analysis to determine the surface area of the activated carbon obtained as a result of activation processes and the description of the coded samples are presented in Table 6.

The production conditions of the activated carbons sent to BET analysis were determined as 600°C temperature and 4 hours as standard.

Table 6. BET surface area test results of the samples

Code of the material	Name of the material	Activator Ratio (Carbonized product / KOH)	Activation time, (h).	BET surface area (m2/g)
A1	Apricot	1/0.5	4	526
A2	Walnut	1/0.5	4	520
A3	Almond	1/0.5	4	274
A4	Black Cumin Pulp	1/0.5	4	109
B1	Apricot	1/1	4	984
B2	Walnut	1/1	4	712
B3	Almond	1/1	4	688
B4	Black Cumin Pulp	1/1	4	514

It was determined that the surface area of the activated carbon coded B1 produced from apricot kernel shell activated at 600 °C for 4 hours by mixing with KOH at a ratio of 1/1 had the highest surface area with 984 m^2/g compared to the other samples. SEM analysis images of the samples and the amount of activator ratio in the coded samples are shown in Figure 4.

A1 – Apricot (1/0.5)

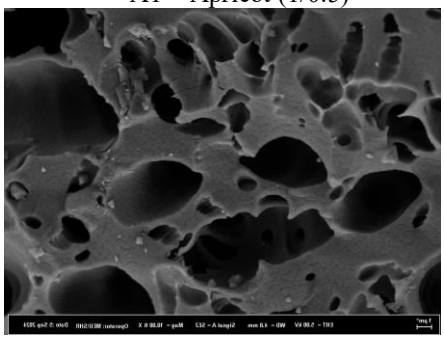

B1- Apricot (1/1)

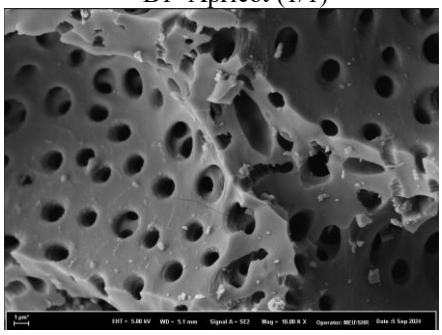

A2 – Walnut (1/0.5)

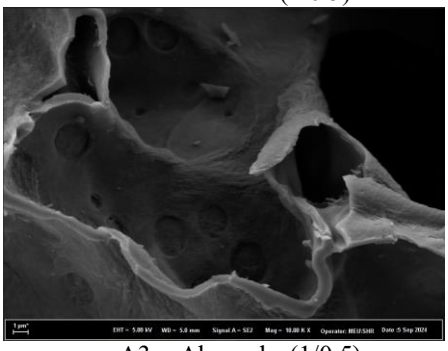

B2 – Walnut (1/1)

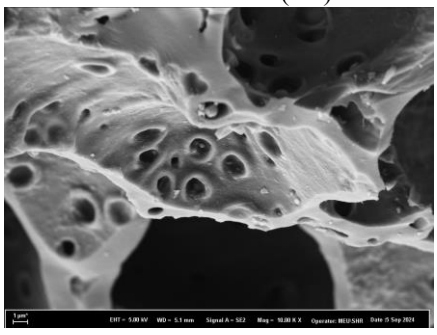

A3 – Almonds (1/0.5)

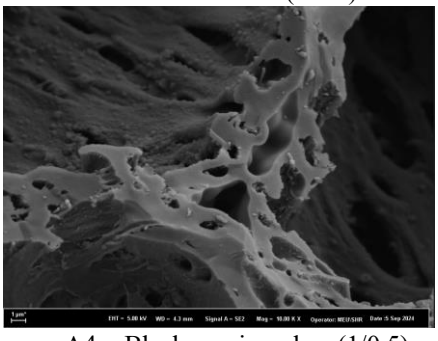

B3 – Almonds (1/1)

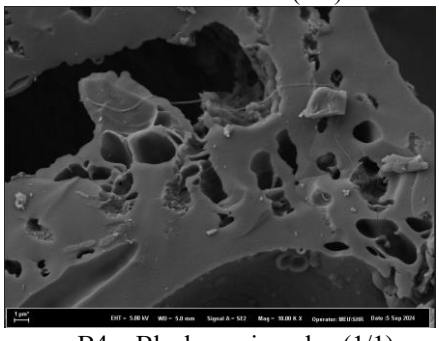

A4 – Black cumin pulps (1/0.5)

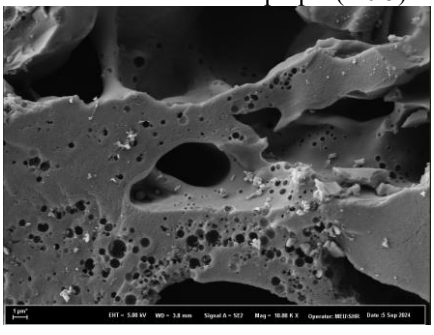

B4 – Black cumin pulps (1/1)

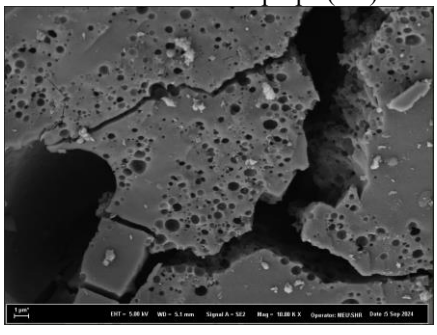

Fig. 4. SEM images of specimens magnified up to 1 µm, 10.00 K X.

3. Results

In this study, it was aimed to obtain high carbon content as a result of carbonisation processes of almond shell, apricot kernel shell, walnut shell and nigella pulp known as biomass wastes and to produce activated carbon from these products. BET and SEM analyses of activated carbons produced as a result of carbonisation and activation processes were carried out and the following results were obtained:

As a result of the carbonisation processes performed on almond shells, while the carbon content of the raw material of almond shells was 46.4%, the sample with the highest increase in carbon content after the carbonisation processes was the sample treated at 800 °C for 4 hours and the carbon content increased up to 89.1%. The sulphur content of the same sample was 0.013%. The BET surface area of activated carbon produced from almond shell increased to 274 m^2/g with the use of 1/0.5 activator ratio and to 688 m^2/g with the use of 1/1 activator ratio.

As a result of the carbonisation processes performed on apricot kernel shells, it was observed that the carbon content of the raw material was 48.5%, while the carbon content increased to 92.61% in the sample treated at 800 °C for 4 hours as a result of carbonisation processes. The sulphur content of the same sample decreased by 0.01%. The BET surface area of activated carbon produced from apricot kernel shell increased to 526 m^2/g with the use of 1/0.5 activator and to 984 m^2/g with the use of 1/1 activator.

While the carbon content of the walnut shells was 47.5% in the raw state, it was observed that the carbon content increased up to 90.76% in the sample treated at 800 °C for 8 hours as a result of the carbonisation processes. The sulphur content of the same sample was determined as 0.073%. The BET surface area of the activated carbon produced from walnut shell increased to 520 m^2/g with the use of 1/0.5 activator and 712 m^2/g with the use of 1/1 activator.

While the carbon content was 44.7% in the raw material of black cumin pulp, it was determined that the highest carbon content was obtained from the sample treated at 800 °C for 2 hours after carbonisation process and the carbon content could reach up to 68.8%. The sulphur content of the same sample was determined as 0.37%. The BET surface area of activated carbon produced from black cumin pulp increased to 109 m^2/g with the use of 1/0.5 activator ratio and to 514 m^2/g with the use of 1/1 activator ratio.

As a result of the carbonisation processes, it was observed that the best carbonisation process occurred in apricot kernel shells and the lowest carbonisation process occurred in black cumin pulp. In line with the analyses performed as a result of activation processes, SEM analyses showed that the best porosity occurred in activated carbons produced from almond shells. According to BET surface area analyses, the highest surface area values were obtained in activated carbons produced from apricot kernel shell. In these samples, it was determined that 526 m^2/g surface area was reached with the use of 1/0.5 activator ratio and 984 m^2/g surface area was reached with the use of 1/1 activator ratio.

In conclusion, the study demonstrated that biomass waste can be effectively utilized as a carbon source and holds significant potential as a precursor for the production of high-value activated carbon.

Acknowledgements

The author, Kamil Mammadov, wishes to express sincere thanks to his Ph.D. supervisor Prof.Dr. Salih Aydogan (Department of Mining Engineering, Faculty of Engineering and Natural Sciences, Konya Technical University) for his kind support and honest help.

Author Contributions

Kamil Mammadov: Research, Writing - review and editing, **Salih Aydogan:** Research, Writing – review and editing.

References

[1] Baker, F. S., Miller, C. E., Albert , J. R., & Donald Tolles, E. (2000, December 04). Activated Carbon. *Kirk-Othmer Encyclopedia of Chemical Technology*. doi:10.1002/0471238961
[2] Thcoboglanous , W. M. (1991). *Wastewater Engineering Treatment Disposal Reuse.* USA: Mcgraw-hill.
[3] Henning, K.-D., & von Kienle, H. (2021, April 16). Raw Materials, Production and Applications. *Industrial Carbon and Graphite Materials*, 491-531. doi:10.1002/9783527674046
[4] Balçık, E. Ü., Torun, M., & Nadeem, H. Ş. (2020, 01 15). Gıda Atıklarından Aktif Karbon Üretimi ve Aktif Karbonun Gıda Endüstrisinde Uyğulanmaları. *GIDA -The Journal of Food, 45*(2), 217-229. doi:10.15237/gida.GD19127
[5] Al-Bayatı, H. A. (2024). *Production of Activated Carbon Fibers from Date Palm for Industrial Wastewater Treatment.* Bolu: Bolu Abant İzzet Baysal University, Institute of Graduate Studies, Master Of Science.
[6] Süner, M. (2022). *Hidrotermal Karbonizasyon Yöntemi ile Çay Tesis Atıkları ve Badem Kabuklarından Aktif Karbon Üretimi.* Elazığ: Fırat Universitesi, Fenn Bilimleri Enstitüsü, Yüksek Lisans Tezi.
[7] Tünay, S. (2023). *Fındık ve Ceviz Kabuğundan Üretilen Aktif Karbon ile Diklofenak Sodyum, Siprofloksasin ve Sülfametoksazol Adsorpsiyonunun İncelenmesi.* Sakarya: Sakarya Universitesi, Fen Bilimleri Enstitüsü, Doktora Tezi.
[8] Öç, S. (2023). *Fıstığın Dış Yeşil Kabuğundan Farklı Yöntemlertle Elde Edilen Aktif Karbon ile Sulu Çözeltiden Metal Giderimi.* Siirt: Siirt Universitesi, Fen Bilimleri Enstitüsü, Yüksek Lisans Tezi.
[9] Güneş, S. (2024). *Şeker Pancarı Posasından Aktif Karbon Üretimi ve Gümüş Bazlı Biyokompozit Polilaktik Asit Filmlerde Uygulanması.* Sakarya: Sakarya Üniversitesi, Fen Bilimleri Enstitüsü, Doktora Tezi.
[10] Bozkurt, T. (2023). *Ayçiçeği Çekirdek Kabuğu ve Tablasından Aktif Karbon Üretimi ve Sulu Çözeltiden Kurşun (II) Giderimi.* Eskişehir : Eskişehir Osmangazi Üniversitesi, Fen Bilimleri Enstitüsü, Yüksek Lisans Tezi.
[11] Kuyucu, A. E. (2022). *Ceviz ve Antep Fıstığı Dış Kabuğundan Kimyasal ve Fiziksel Aktivasyon Yöntemleri ile Aktif Karbon Üretimi Uygulamaları ve Karakterizasyonu.* Van: Yüzüncü Yıl Üniversitesi, Fen Bilimleri Enstitüsü, Doktora Tezi.
[12] Kobya, M., Demirbas, E., Senturk, E., & Ince, M. (2005). Adsorption of Heavy Metal İons From Aqueous Solutions by Activated Carbon Prepared from Apricot Stone. *Bioresource Technology, 96*(13), 1518–1521.

Contents lists available at *Dergipark*

Journal of Scientific Reports-A

journal homepage: *https://dergipark.org.tr/tr/pub/jsr-a*

E-ISSN: 2687-6167 ***Number 61, June 2025***

RESEARCH ARTICLE

Receive Date: 27.03.2025 *Accepted Date: 16.06.2025*

Synthesis, characterization and biological studies of metal complexes of 4-iodo-*n*-(6-sulfamoylbenzothiazol-2-yl)benzamide

Halil İlkimen[a,*], Tuğçe Öztürk[b], Cengiz Yenikaya[c], Aysel Gülbandılar[d]

[a]*Kütahya Dumlupınar University, Faculty of Art and Sciences, Department of Chemistry, 43100 Kutahya, Türkiye, ORCID: 0000-0003-1747-159X*

[b]*Kütahya Dumlupınar University, Faculty of Art and Sciences, Department of Chemistry, 43100 Kutahya, Türkiye, ORCID: 0000-0003-1885-0700*

[c]*Kütahya Dumlupınar University, Faculty of Art and Sciences, Department of Chemistry, 43100 Kutahya, Türkiye, ORCID: 0000-0002-5867-9146*

[d]*Eskişehir Osmangazi University, Faculty of Agriculture, Department of Food Engineering, 26000 Eskişehir, Türkiye, ORCID: 0000-0001-9075-9923*

Abstract

In this study, the new 4-iodo-*N*-(6-sulfamoylbenzothiazol-2-yl)benzamide (**L3**) obtained from 2-amino-6-sulfamoylbenzothiazole (**L1**) and 4-iodobenzoyl chloride (**L2**) and Fe(II) {[Fe(**L3**)$_2$(SO$_4$)].H$_2$O (**1**)}, Ni(II) {[Ni(**L3**)$_2$(Ac)$_2$].2H$_2$O (**2**)} and Cu(II) {[Cu(**L3**)$_2$(Ac)$_2$].2H$_2$O (**3**)} complexes were synthesized. The structures were synthesized by elemental analysis for **L3** and **1-3**, infrared spectroscopy (IR) for **L3** and **1-3**, nuclear magnetic resonance (NMR) for **L3**, atomic absorption spectroscopy (AAS), molar conductivity, and magnetic susceptibility methods for **1-3**. As a consequence of spectroscopic evaluation, it was determined that compounds **1-3** exhibited a non-ionic and tetrahedral conformation. A comprehensive examination was conducted on the susceptibility of all substances to *C. albicans* (yeast), *L. monocytogenes, E. faecalis, E. coli, P. aeruginosa, S. aureus*, and *B. subtilis* (bacteria) were thoroughly investigated. The antimicrobial activities were contrasted with those of Ketoconazole, Fluconazole, Levofloxacin, Chloramphenicol, Vancomycin, and Cefepime.

Keywords: 4-Iodo-N-(6-sulfamoylbenzothiazol-2-yl)benzamide, 2-amino-6-sulfamoylbenzothiazole, 4-iodobenzoyl chloride, metal complex.

* Corresponding author. Tel.: +902744433096; fax: +902744430332
E-mail address: halil.ilkimen@dpu.edu.tr

1. Introduction

Amides are well-known important functional groups in biology and chemistry, and the formation of amide bonds is of great importance, especially in the synthesis of complex homogeneous glycoproteins [1]. Amides are extremely useful functional groups in organic synthesis. They also serve as precursors for many valuable compounds, including pharmaceuticals, agrochemicals, polymers, and organic materials [2]. Sulfonamides are generally expressed with the formula NH_2SO_2R and are bioisosteric derivatives of sulfamide group compounds. Compounds containing sulfonamide group have a very wide field of study in pharmaceutical chemistry [3-6]. The sulfonamide and benzothiazole derivatives are considered as a fundamental building block in the search for a novel class of drug molecules with diverse pharmacological activities [3-6]. *N*-(benzothiazol-2-yl)benzamide derivatives have antifungal [7], antiproliferative [8], antibacterial [9-16], antioxidant [5,6,17,17], anticancer [6,19-21], anti-Zika virus [22], antituberculosis [23], antiviral [24-26], anti-inflammatory [27,28], antiHIV [29], antiarteriosclerotic [30,31] and antitumor [32-34] activities. While 2-aminobenzothiazole-benzamide derivatives are synthesized abundantly in the literature [3-6,35], 2-amino-6-sulfonamidebenzothiazole-benzamide is very rare [36]. The simple or metal mixed-ligand complexes of *N*-(benzothiazol-2-yl)benzamide are few reports such as Cu(II) and Zn(II) of *N*-(benzothiazol-2-yl)benzamide [37], BF_2 of *N*-(benzothiazol-2-yl)benzamide, *N*-(benzothiazol-2-yl)-4-methoxybenzamide, *N*-(benzothiazol-2-yl)-4-(diphenylamino)benzamide and *N*-(benzothiazol-2-yl)-4-(dimethylamino)benzamide [38], Fe(III), Co(II) and Cr(III) of *N*-(benzothiazol-2-ylcarbamothioyl)benzamide [**Hata! Yer işareti tanımlanmamış.**], Pd(II) and Zn(II) of *N*-(benzothiazol-2-yl)-4-(octyloxy)benzamide [39], Pd(II) of *N*-(benzothiazol-2-yl)benzamide with 1,2-bis(diphenylphosphino)ethane [40] and Ru, Rh and Ir of *p*-isopropyltoluene, cyclopentadienyl and azide with *N*-(benzothiazol-2-yl)benzamide [5]. The metal complexes of 2-amino-6-sulfonamidebenzothiazole-benzamide have not been synthesized.

In this study, novel 4-iodo-*N*-(6-sulfamoylbenzothiazol-2-yl)benzamide (**L3**) of 2-amino-6-sulfamoylbenzothiazole (**L1**) and 4-iodobenzoyl chloride (**L2**) and the metal complexes were synthesized. The structures were suggested by elemental analysis for **L3** and **1-3**, IR for **L3** and **1-3**, NMR for **L3**, AAS, magnetic susceptibility and molar conductivity methods for **1-3**. The antimicrobial properties of all compounds against yeast and bacteria were thoroughly investigated. The antimicrobial efficacies were contrasted with those of Ketoconazole, Fluconazole, Levofloxacin, Chloramphenicol, Vancomycin, and Cefepime.

2. Experimental

*2.1. Preparation of **L1** and **L3***

According to the literature, for the synthesis of 2-amino-6-sulfamoylbenzothiazole (**L1**), firstly 4-thioureidobenzenesulfonamide (tbs) was obtained from the reaction of sulfanylamide (sa) with KSCN. Then, it was synthesized from the reaction of 4-thioureidobenzenesulfonamide with Br_2 [41].

1.1464 g (5 mmol) **L1** was dissolved in 50 mL of tetrahydrofuran in a flask. 1.3323 g (5 mmol) **L2** was added by dropwise in an ice bath at -5 degrees. After stirring at 25 ºC for three days, the solid precipitated in the reaction medium were filtered by using filter paper, washed with dry toluene, and dried at 25 ºC (**L3**, 1.8369 g, 80% yield, M = 459.28 g/mol) (Fig. 1).

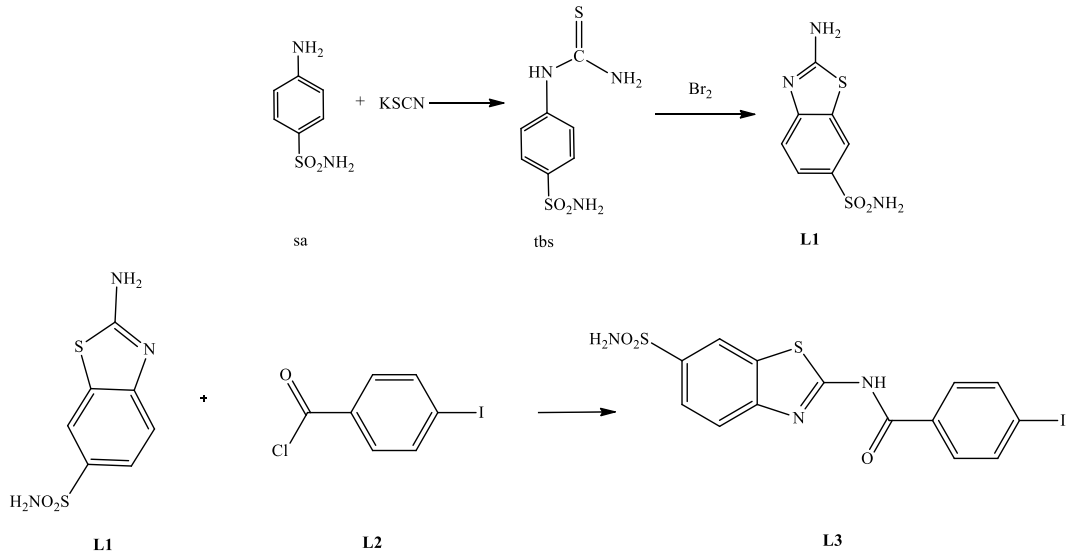

Fig. 1. The structure of **L3**.

*2.2. Preparation of **1-3***

0.278 g (1 mmol) $FeSO_4.7H_2O$ for **1** or 0.248 g (1 mmol) $Ni(Ac)_2.4H_2O$ for **2** or0.200 g (1 mmol) $Cu(Ac)_2.H_2O$ for **3** and 0.4593 g (1 mmol) **L3** was dissolved in water:ethanol (1:1) (50 mL) with stirring one week. The powdered solids obtained from the mixtures were filtered and dried {orange, 0.3538 g, 65% yield, M = 1088.49 g/mol for **1**, green 0.3677 g, 65% yield, M = 1131.38 g/mol for **2**, and brown, 0.3409 g, 60% yield, M = 1136.23 g/mol for **3**} (Fig. 1).

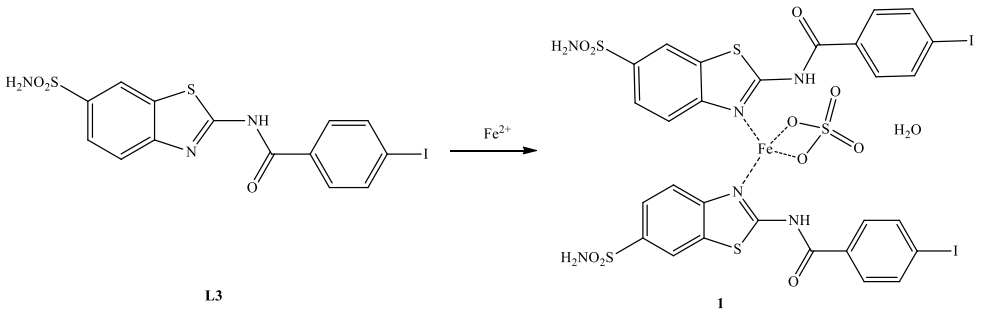

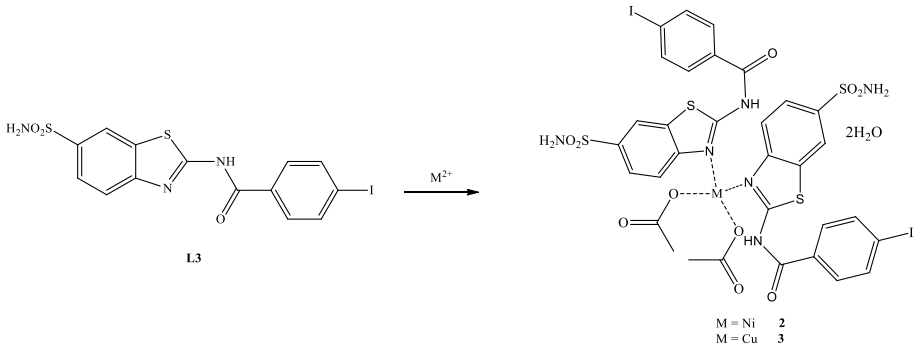

Fig. 2. The structures of **1**-**3**.

2.3. Antimicrobial study

In determining the antibacterial and antifungal activities of all compounds, the micro-tube dilution technique was applied to determine the lowest concentration value (MIC) that inhibits the growth of microorganisms [42,43]. Each microorganism culture was incubated in Müller Hinton Broth at 37 ºC overnight and adjusted to a concentration of approximately 10^8 cfu/mL (with 0.5 McFarland) in tubes containing 15 mL of double-strength Müller Hinton Broth (MBH). Dilutions of the compounds were prepared at a 1:1 ratio with 1000 µL of DMSO solution and 1000 µL of sterile distilled water, and 11 dilutions were made. Then, 100 µL of sterile distilled water was transferred to the 12th row of horizontal wells from 1 to 12 of sterile 96-well micro plates from top to bottom, and 100 µL of previously prepared dilutions were transferred to wells 11-1 from top to bottom, respectively, and 100 µL of single strength MHB medium was transferred to the wells in the last row of the horizontal row [42,43]. Finally, 100 µL of the microorganism suspension was added to each well. Reference antibiotic dilutions (Cefepime, Vancomycin, Levofloxacin, Chloramphenicol for bacteria and Fluconazole and Ketoconazole for yeast) were also performed in the same manner. The plates were incubated at 37 °C for 24 hours and the lowest concentration at which turbidity (growth) was not observed was determined as the MIC.

3. Results and discussion

*3.1. NMR result of **L3***

The NMR results of **L3** are given in Figures 3 and 4, and Table 1. In the ^{1}H NMR spectrum of **L3** (Fig. 3, Table 1), the protons were observed at 7.94 ppm (H^4 and H^5, 2H, doublet, $^3J_{H4\text{-}H5}$ = 7.59 Hz), 8.51 ppm (H^7, 1H, singlet), 13.15 ppm (H^{10}, 1H, singlet), 7.88 ppm (H^{13}, $H^{13'}$, H^{14} and $H^{14'}$, 4H, multiplet) and 7.36 ppm (H^{17}, 2H, singlet).

Table 1. ^{1}H-NMR and ^{13}C-NMR spectra peaks of **L3**.

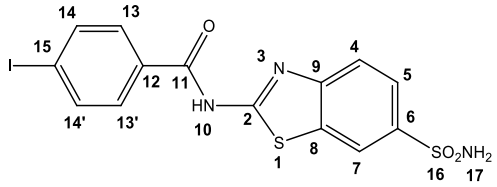

	^{1}H NMR		^{13}C NMR
H^4/H^5	7.94 (2H, d) [$^3J_{H4\text{-}H5}$ = 7.59 Hz]	C^2	166.346
H^7	8.51 (1H, s)	C^4	131.525

H^{10}	13.15 (1H, s)	C^{5}	124.432
$H^{13}/H^{13'}/H^{14}/H^{14'}$	7.88 (4H, m)	C^{6}	130.609
H^{17}	7.36 (2H, s)	C^{7}	120.918
		C^{8}	120.899
		C^{9}	120.668
		C^{11}	162.297
		C^{12}	138.038
		$C^{13}/C^{13'}$	131.963
		$C^{14}/C^{14'}$	131.591
		C^{15}	101.917

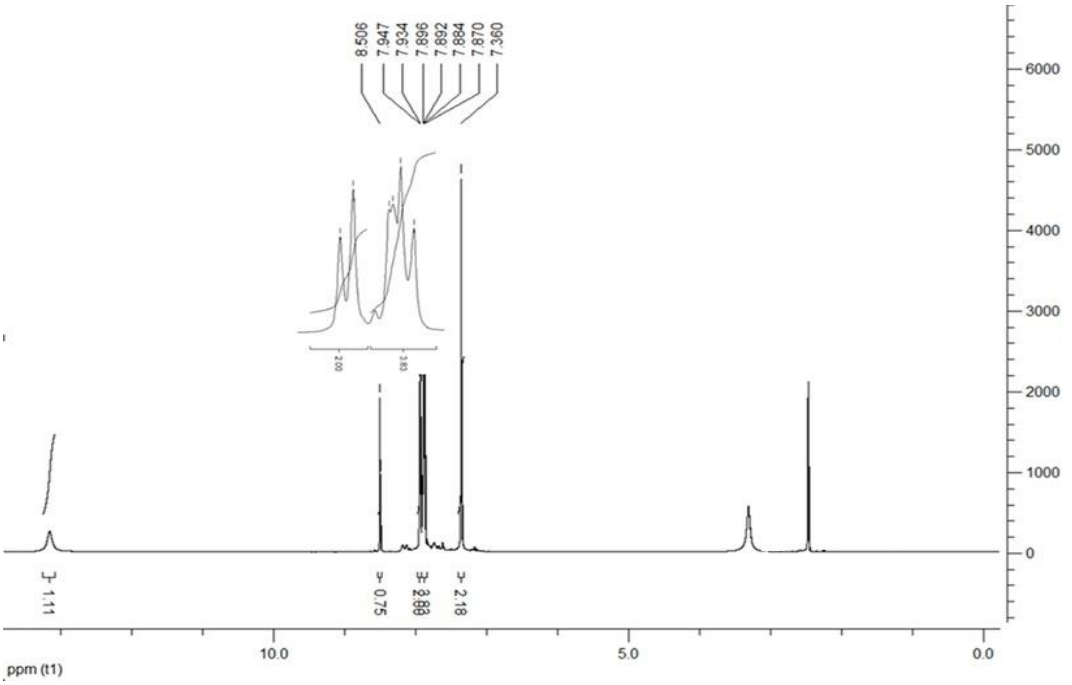

Fig. 3. ^{1}H NMR spectrum of **L3**.

^{13}C NMR spectrum of **L3** exhibits twelve signals (Fig. 4, Table 1) at 166.346 ppm (C^{2}), 131.525 ppm (C^{4}), 124.432 ppm (C^{5}), 130.609 ppm (C^{6}), 120.918 ppm (C^{7}), 120.899 ppm (C^{8}), 120.668 ppm (C^{9}), 162.297 ppm (C^{11}), 138.038 ppm (C^{12}), 131.963 ppm (C^{13}, $C^{13'}$), 131.591 ppm (C^{14}, $C^{14'}$) and 101.917 ppm (C^{15}).

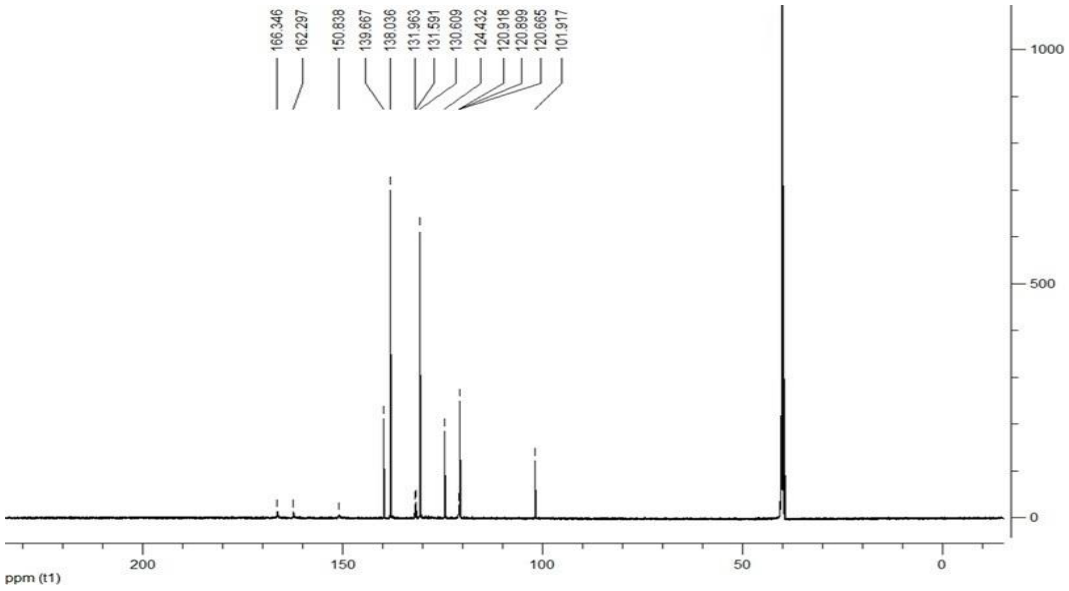

Fig. 4. ^{13}C NMR spectrum of **L3**.

3.2. AAS and Elemental analysis results

Results of AAS for **1-3** and elemental analysis for **L3** and **1-3** indicated that the metal:**L3** ratios for **1-3** were 1:1 (Table 2).

Table 2. Elemental analysis and AAS results of compounds **L3-3**.

Compound	Formula	Found% (Calculated%)				
		C	H	N	S	M
L3	$C_{14}H_{10}IN_3O_3S_2$	36.65(36.61)	2.20(2.19)	9.20(9.15)	13.95(13.96)	-
1	$C_{28}H_{22}FeI_2N_6O_{11}S_5$	30.90(30.90)	2.05(2.04)	7.75(7.72)	14.75(14.73)	5.10(5.13)
2	$C_{32}H_{30}I_2N_6NiO_{14}S_4$	33.90(33.97)	2.65(2.67)	7.45(7.43)	11.35(11.34)	5.20(5.19)
3	$C_{32}H_{34}CuI_2N_6O_{12}S_4$	33.80(33.83)	2.60(2.66)	7.50(7.40)	11.25(11.29)	5.60(5.59)

3.3. IR results

The IR spectra and IR data of **L3** and **1-3** are given in Figure 5 and Table 3, respectively. The ν(N-H) vibrations observed at 3424, 3314, and 3268 cm^{-1} for compound **L3**, 3483, 3411, and 3233 cm^{-1} for compound **1**, 3486, 3418, 3313, and 3265 cm^{-1} for compound **1**, and 3483, 3414, 3310, and 3270 cm^{-1} for compound **3**. The differential results (Δυ) between the symmetric and asymmetric vibrations of compounds **1** and **3** in the acetate group were found to be 218 (1618 and 1400 cm-1) for **1** and 219 (1619 and 1400 cm^{-1}) for **3**. These values indicate that the acetate group is monodentately bound to the metal ion [44]. The observed bands in the spectra of **L3** and **1-3** are observed region of 3551-3553 cm^{-1}, 3074-3114 cm^{-1}, 2852-2973 cm^{-1}, 1673-1676 cm^{-1}, 1448-1639 cm^{-1}, 1188-1390 cm^{-1}, 1056-1278 cm^{-1}, 607-630 cm^{-1} and 460-496 cm^{-1} for ν(O-H), aromatic *ν*(C-H), aliphatic *ν*(C-H) for compounds **1** and **3,** for $\nu(C{=}O)_{amide}$, *ν*(C=N)/*ν*(C=C), *ν*(C=O) for compounds **1** and **3**, *ν*(S=O), *ν*(M-O) (except compound **L3**) and *ν*(M-N) (except compound **L3**), respectively.

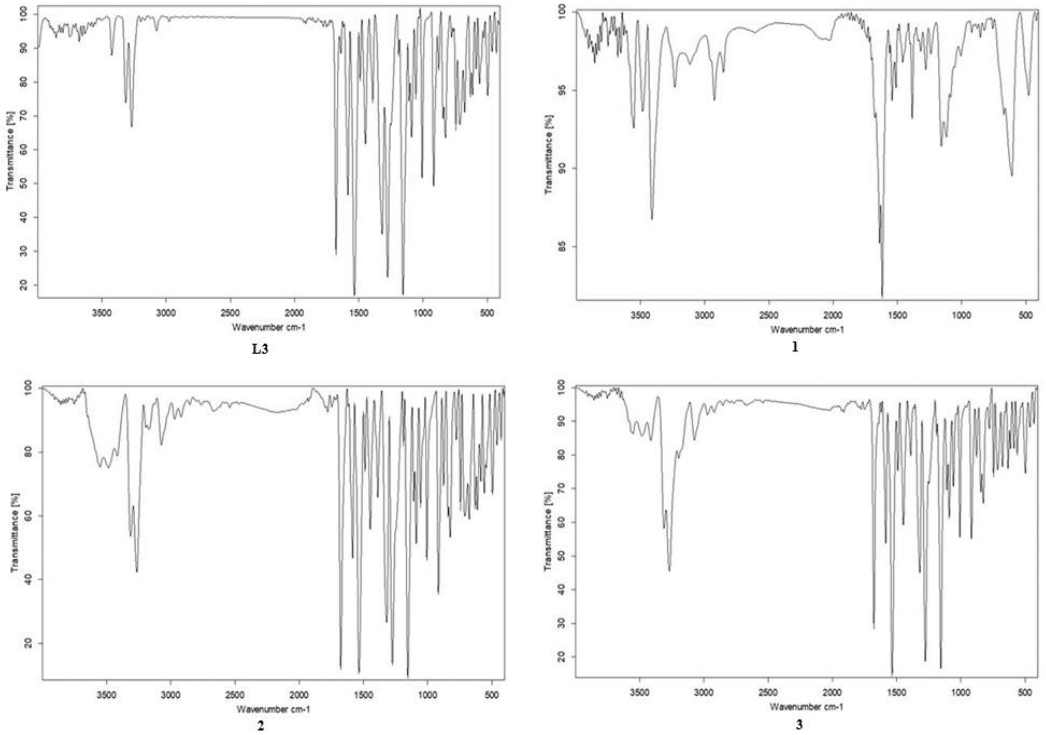

Fig. 5. IR spectra of **L3** and **1-3**.

Table 3. IR data of **L3** and **1-3** (cm^{-1})

	L3	**1**	**2**	**3**
ν(OH)	-	3553(br)	3551(br)	3552(br)
$\nu(NH_2)$	3424(m)	3483(m)	3486(m)	3483(m)
	3314(m)	3411(m)	3418(m)	3414(m)
	3268(m)	3233(m)	3313(m)	3310(m)
			3265(m)	3270(m)
$\nu(CH)_{Ar}$	3074(w)	3114(w)	3074(w)	3074(w)
$\nu(CH)_{Alp.}$	-	-	2971(w)	2973(w)
			2921(w)	2922(w)
			2852(w)	2852(w)
$\nu(C{=}O)_{acetate}$	-	-	1618(s)	1619(s)
			1400(s)	1400(s)
$\nu(C{=}O)_{amide}$	1676(s)	1673(s)	1676(s)	1676(s)
ν(C=N)	1639(s)	1638(s)	1584(s)	1584(s)
ν(C=C)	1619(s)	1618(s)	1535(s)	1535(s)
	1584(s)	1560(s)	1447(s)	1490(s)
	1534(s)	1541(s)		1447(s)
	1489(s)	1511(s)		
	1448(s)	1458(s)		
ν(C-O)	-	-	1388(s)	1390(s)
			1319(s)	1319(s)
			1188(s)	1188(s)
ν(S=O)	1275(s)	1278(s)	1274(s)	1275(s)

	1155(s)	1157(s)	1154(s)	1155(s)
	1056(s)	1118(s)	1089(s)	1090(s)
ν(M-O)	-	607(w)	630(w)	614(w)
ν(M-N)	-	477(w)	460(w)	496(w)

3.4. Results of UV-Vis measurements

The electronic spectra of **L3** and **1-3** (Fig. 6, in DMSO), π-π* and n-π* transitions are observed 285 nm (30900 $Lmol^{-1}cm^{-1}$) and 300 nm (37060 $Lmol^{-1}cm^{-1}$) for **L3**, 289 nm (28900 $Lmol^{-1}cm^{-1}$) and 300 nm (37000 $Lml^{-1}cm^{-1}$) for **1**, 285 nm (15900 $Lmol^{-1}cm^{-1}$) for **2** and 300 nm (38900 $Lmol^{-1}cm^{-1}$) for **3.** The sands for d-d transitions of tetrahedral complexes are observed at 702 nm (200 $Lmol^{-1}cm^{-1}$) for **1** [45], 6603nm (150 $Lmol^{-1}cm^{-1}$) for **2** [46] and 690 nm (100 $Lmol^{-1}cm^{-1}$) for **3** [47].

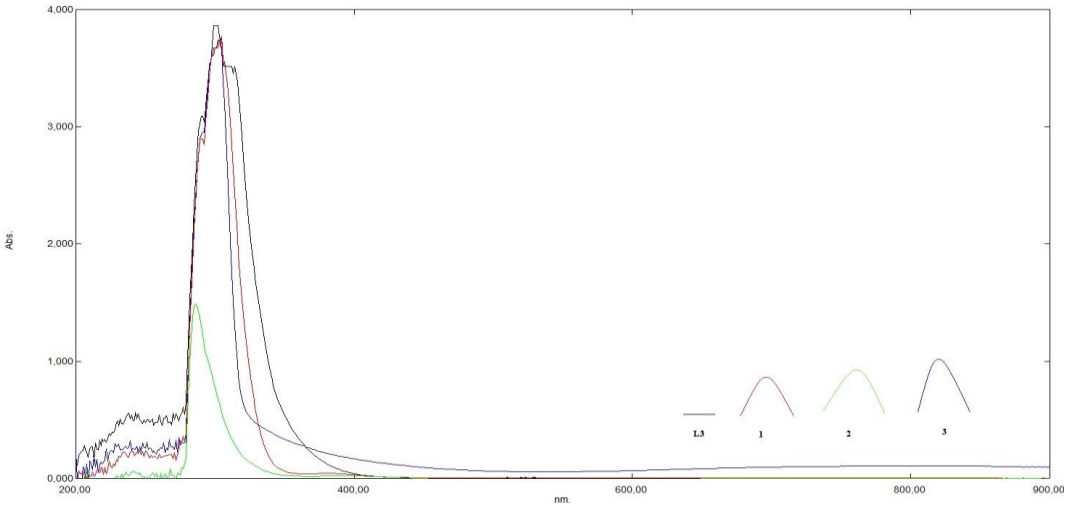

Fig. 6. UV-Vis spectra of **L3** and **1-3**.

*3.5. Magnetic susceptibilities and Molar Conductivity for **1-3***

The magnetic susceptibility measurements for compounds **1-3** were recorded as 4.80, 2.15, and 1.61 BM, respectively. These values indicate the presence of 4, 2, and 1 unpaired electron within the respective complexes. The magnetic moment associated with the metal ion in the tetrahedral configuration is also in agreement with these findings [48,49].

Conductivity assessments of compounds **1-3** (dissolved in DMSO) yielded values of 2.1, 5.0, and 2.1, respectively; consequently, these results indicate non-ionic behaviour for compounds **1-3** [50].

The highly effective technique of single-crystal X-ray diffraction analyses is not applicable for elucidating the structures of complexes **1–3** as a result of their particulate nature. The molecular formulas of the above mentioned complexes are elucidated based on the results from elemental analysis, AAS, spectral analyses (IR, UV-Vis), magnetic susceptibility and molar conductivity (Fig. 2).

3.6. Antimicrobial activity

The antimicrobial efficacy of Levofloxacin, Vancomycin, Chloramphenicol, Cefepime, Ketoconazole,

Fluconazole, sa, KSCN, tbs, and **L1-L3** and **1-3** were systematically examined utilizing the microdilution methodology. Minimum Inhibitory Concentration (MIC) values of the compounds against yeast and bacteria are given in Table 4.

Table 4. MIC values of all compounds (µg/mL)

	S. aureus	***B. subtilis***	***E. Coli***	***E. faecalis***	***L. monocytogenes***	***P. aeruginosa***	***C. albicans***
Vancomycin	31.25	31.25	125.00	31.25	125.00	62.50	
Levofloxacin	62.50	31.25	31.25	31.25	62.50	31.25	
Cefepime	31.25	62.50	31.25	62.50	62.50	31.25	
Chloramphenicol	62.50	62.50	62.50	62.50	62.50	125.00	
Fluconazole	-	-	-	-	-	-	62.50
Ketoconazole	-	-	-	-	-	-	62.50
sa	31.25	62.50	31.25	15.62	31.25	31.25	62.50
KSCN	31.25	62.50	31.25	62.50	31.25	31.25	62.50
tbs	62.50	31.25	62.50	62.50	62.50	31.25	62.50
L1	62.50	62.50	62.50	62.50	31.25	31.25	62.50
L2	62.50	62.50	62.50	62.50	62.50	62.50	62.50
L3	31.25	31.25	62.50	62.50	31.25	62.50	62.50
1	62.50	62.50	62.50	62.50	31.25	31.25	62.50
2	62.50	62.50	62.50	62.50	31.25	31.25	62.50
3	62.50	62.50	62.50	62.50	31.25	31.25	62.50

Cefepime, Levofloxacin, Vancomycin, and Chloramphenicol (antibacterial drugs) and all compounds have activity against *S. aureus:* sa, KSCN, and **L3** showed the same activity as Vancomycin and Levofloxacin, while other compounds showed the same effect as Cefepime and Chloramphenicol.

B. subtilis; while tbs and **L3** found the same effect as Vancomycin and Levofloxacin, other compounds showed Cefepime and Chloramphenicol, the other compounds found equally active.

E. coli; sa and KSCN were found to demonstrate activity comparable to that of Cefepime and Levofloxacin, while the remaining compounds exhibited effects akin to those of Chloramphenicol. Notably, all compounds demonstrated superior activity relative to Vancomycin.

L. monocytogenes; all compounds exhibited enhanced activity when compared to Vancomycin. All compounds (except tbs and **L2**) showed greater activity according to the other drug while tbs and **L2** showed the same activity according to the other drug.

E. faecalis; faecalis, sa exhibited a level of activity surpassing that of all tested drugs. The remaining compounds exhibited activity comparable to Cefepime and Chloramphenicol, while other compounds were determined to possess a lesser degree of efficacy relative to both Levofloxacin and Vancomycin.

P. aeruginosa; all compounds (except **L2** and **L3**) exhibited superior activity in comparison to Vancomycin, while compounds **L2** and **L3** were found to be equally effective. Although all compounds (apart from **L2** and **L3**) demonstrated equivalent efficacy, compounds **L2** and **L3** were identified as having a lesser degree of activity compared to Cefepime and Levofloxacin. Furthermore, all compounds exhibited greater activity than that observed with Chloramphenicol.

Ketoconazole and Fluconazole (antifungal drugs) both classified as antifungal agents, along with all other compounds, demonstrated efficacy against Candida albicans when the MIC values were compared; all compounds exhibited effects analogous to those of Ketoconazole and Fluconazole.

4. Conclusions

In this study, the novel compound 4-iodo-*N*-(6-sulfamoylbenzothiazol-2-yl)benzamide (**L3**) was synthesized from 2-amino-6-sulfamoylbenzothiazole, 4-iodobenzoyl chloride, and the complexes of Fe(II), Ni(II), and Cu(II) derived from compound **L3**. The structural elucidation of these compounds was accomplished through a combination of elemental analysis, IR, NMR, AAS, magnetic susceptibility measurements, and molar conductivity assessments. The results obtained from the spectroscopic analysis indicated that compounds **1-3** exhibited a non-ionic nature and a tetrahedral geometry. All synthesized compounds demonstrated antimicrobial activity against a spectrum of both bacterial and fungal microorganisms. Compound **L3** showed better activity in *S. aureus* and *B. subtilis* bacteria, while compounds **L3** and **1-3** showed the same activity in *E. coli* and *E. faecalis* bacteria and *C. albicans* yeast. Complex compounds (**1-3**) showed better activity in L. monocytogenes bacteria.

Acknowledgements

The authors acknowledge the assistance provided by the Kütahya Dumlupinar University Research Fund (Grant No. 2024/16).

Author contributions

H.I: Investigation, Writing- Reviewing and Editing, T.O: Investigation**,** C.Y: Investigation, and A.G: Activity Study.

References

[1] R. Pandya, M. Takashi, L. Tedeschi, A. G. M. Barrett, “Facile One-Pot Synthesis of Aromatic and Heteroaromatic Sulfonamides”. *J. Org. Chem.*, vol. 68, no. 21, pp. 8274-8276, 2003, doi: 10.1021/jo034643j.
[2] J. Gómez-Carpintero, J. D. Sánchez, J. F. González, J. C. Menéndez, “Mechanochemical synthesis of primary amides”. *J. Org. Chem.*, vol. 86, no. 20, pp. 14232-14237, 2021, doi: 10.1021/acs.joc.1c02350.
[3] R. Ali, N. Siddiqui, “Biological aspects of emerging benzothiazoles: a short review”. Academic Editor: Gabriel Navarrete-Vazquez, Kaustubha Mohanty, Indian Institute of Technology Guwahati, India, 2013, doi: 10.1155/2013/345198.
[4] P. S. Yadav, G. P. Senthilkumar, “Benzothiazole: different methods of synthesis and diverse biological activities”. *Int. J. Pharm. Sci. Drug. Res.*, vol. 3, no. 1–7, 2011, doi: 10.25004/IJPSDR.2011.030101.
[5] G. Achaiah, N. S. Goud, K.P. Kumar, P. Mayuri, “Review on 2-substituted benzothiazoles: diversity of synthetic methods and biological activities”. *Int. J. Pharm. Sci. Drug. Res.*, vol. 7, no. 4, pp. 1375-1382, 2016, doi: 10.13040/IJPSR.0975-8232.7 (4).1375-82.
[6] R. Yadav, D. Meena, K. Singh, R. Tyagi, Y. Yadav, R. Sagar, “Recent advances in the synthesis of new benzothiazole based anti-tubercular compounds”. *RSC* Adv., vol. 13, pp. 21890-21925, 2023, doi: 10.1039/D3RA03862A.
[7] M. Singh, H. Verma, P. Bhandu, M. Kumar, G. Narendra, S. Choudhary, P.K. Singh, O. Silakari, “Network analysis guided designing of multi-targeted anti-fungal agents: synthesis and biological evaluation”. *J. Mol. Struct.*, vol. 1272, 134128, 2023, doi: 10.1016/j.molstruc.2022.134128.
[8] X. Wang, M. Zhao, Y. Chang, S. Guan, M. Li, H. Yang, M. Sun, “Identification of novel benzothiazole derivatives as inhibitors of NEDDylation pathway to inhibit the progression of gastric cancer”. *Bioorg. Med. Chem. Let.*, vol. 100, pp. 129647, 2024, doi: 10.1016/j.bmcl.2024.129647
[9] N. A. Galieva, D. A. Saveliev, O. S. Eltsov, V. A. Bakulev, G. Lubec, J. Xing, Z. Fan, V. Beryozkina, “Antimicrobial activity of new benzazolyl *N*-sulfonyl amidines”. *Mendeleev Commun.*, vol. 31, no. 4, pp. 495-497, 2021, doi: 10.1016/j.mencom.2021.07.019.
[10] N. Sharma, N. Srivastava, A. Kaushal, B. Das, A. Vashistha, L. Kumar, R. Kumar, A. K. Yadav, “Synthesis, in silico study and biological evaluation of *N*-(benzothiazol/thiazol-2-yl)benzamide derivatives as quorum sensing inhibitors against pseudomonas aeruginosa”. *Chem. Biodiv.*, vol. 20, no. 9, pp. e202300647, 2023, doi: 10.1002/cbdv.202300647.
[11] L. Shadap, N. Agarwal, V. Chetry, K. M. Poluri, W. Kaminsky, M. R. Kollipara, “Arene ruthenium, rhodium and iridium complexes containing benzamide derivative ligands: Study of interesting bonding modes, antibacterial, antioxidant and DNA binding studies”. *J. Organomet. Chem.*, vol. 937, pp. 121731, 2021, doi: 10.1016/j.jorganchem.2021.121731
[12] E. S. Al-Farraj, A. Fetoh, “Synthesis of new Fe(III), Co(II), and Cr(III) complexes of *N*-(benzo[d]thiazol-2-ylcarbamothioyl)benzamide (H_2L_2): Structural characterization and biological activities”. *App. Organomet. Chem.*, vol. 37, no. 11, pp. e7248, 2023, doi: 10.1002/aoc.7248.
[13] S. Bonnett, J. Jee, S. Chettiar, Y. Ovechkina, A. Korkegian, E. Greve, J. Odingo, T. Parish, “Identification of 2-amino benzothiazoles with bactericidal activity against Mycobacterium tuberculosis”. *Microbio. Spect.*, vol. 11, no. 1, pp. 1-17, 2023, doi: 10.1128/spectrum.04974-22.

[14] J. Early, J. Ollinger, C. Darby, T. Alling, S. Mullen, A. Casey, B. Gold, J. Ochoada, T. Wiernicki, T. Masquelin, C. Nathan, P. A. Hipskind, T. Parish, "Identification of Compounds with pH-Dependent Bactericidal Activity against Mycobacterium tuberculosis". *ACS Infec. Dis.*, vol. 5, no. 2, pp. 272-280, 2019, doi: 10.1021/acsinfecdis.8b00256.
[15] H. M. Alazmaa, V. R. Avupati, C. Santiago, "Synthesis, characterization, in vitro biological evaluation of a series of benzothiazole amides as antibacterial agents". *Asian J. Chem.*, vol. 36, no. 4, pp. 963-968, 2024, doi: 10.14233/ajchem.2024.31299.
[16] S. R. Gurram, M. A. Azam, "Design, synthesis and biological evaluation of some novel N'-(1,3-benzothiazol-2-yl)-arylamide derivatives as antibacterial agents". *Chem. Papers*, vol. 75, no. 10, pp. 5435-5452, 2021, doi: 10.1007/s11696-021-01730-8.
[17] M. B. Taj, S. A. Tirmizi, A. Raheel, W. Alelwani, D. Hajjar, A. A. Makki, U. Ali, M. Darroudi, H. B. M. Ali, "Facile synthesis of *N*-phenyl benzamidine derivatives, their skin protecting, and anti-aging activity". *Russian J. Gen. Chem.*, vol. 88, no. 11, pp. 2425-2431, 2018, doi: 10.1134/S1070363218110270.
[18] I. Sovic, M. Cindric, N. Perin, I. Bocek, I. Novakovic, A. Damjanovic, T. Stanojkovic, M. Zlatovic, M. Hranjec, B. Bertosa, "Biological potential of novel methoxy and hydroxy substituted heteroaromatic amides designed as promising antioxidative agents: synthesis, 3D-QSAR analysis, and biological activity". *Chem. Res. Toxic.*, vol. 32, no. 9, pp. 1880-1892, 2019, doi: 10.1021/acs.chemrestox.9b00256.
[19] Y. Wei, M. Zhang, Z. Lyu, G. Yang, T. Tian, M. Ding, X. Zeng, F. Xu, P. Wang, F. Li, Y. Liu, Z. Cao, J. Lu, X. Hong, H. Wang "Benzothiazole amides as TRPC3/6 Inhibitors for gastric cancer treatment". *ACS Omega*, vol. 6, no. 13, pp. 9196-9203, 2021, doi: 10.1021/acsomega.1c00514.
[20] F. Ricci, A. Angeli, F. Mancuso, L. De Luca, C. T. Supuran, R. Gitto, "Screening campaign and docking ınvestigations in ıdentifying new hit compounds as ınhibitors of human carbonic anhydrases expressed in tumour cells". *ChemMedChem*, vol. 18, no. 20, pp. e202300330, 2023, doi: 10.1002/cmdc.202300330.
[21] J. T. Chiou, Y. Y. Wu, Y. C. Lee, L. S. Chang, "BCL2L1 inhibitor A-1331852 inhibits MCL1 transcription and triggers apoptosis in acute myeloid leukemia cells". Biochem. Pharm., vol. 215, pp. 115738, 2023, doi: 10.1016/j.bcp.2023.115738.
[22] R. F. C. Dias, B. M. R. M. Ribeiro, N. M. Cassani, D. N. Farago, G. A. Antoniucci, R. E. de Oliveira Rocha, F. de Oliveira Souza, E. J. Pilau, A. C. G. Jardim, R. S. Ferreira, C. O. R. Júnior, "Discovery and structural optimization of a new series of *N*-acyl-2-aminobenzothiazole as inhibitors of Zika virus". *Bioorg. Med. Chem.*, vol. 95, no. 15, pp. 117488, 2023, doi: 10.1016/j.bmc.2023.117488.
[23] "Substituted benzo-1,3-hetero-azoles useful in treatment of tuberculosis and their preparation". Assignee: Institute of Medicinal Biotechnology, Chinese Academy of Medical Sciences, China, CN103772376 A 2014-05-07.
[24] M. Dittmar, K. Whig, J. Miller, B. Kamalia, S. Suppiah, L. Perelygina, K. E. Sullivan, D. C. Schultz, S. Cherry, "Nucleoside analogs NM107 and AT-527 are antiviral against rubella virus". *PNAS Nexus*, vol. 2, no. 9, pp. 1-8, 2023, doi: 10.1093/pnasnexus/pgad256.
[25] H. Maus, F. Barthels, S. J. Hammerschmidt, K. Kopp, B. Millies, A. Gellert, A. Ruggieri, T. Schirmeister, "SAR of novel benzothiazoles targeting an allosteric pocket of DENV and ZIKV NS2B/NS3 proteases". *Bioorg. Med. Chem.*, vol. 47, pp. 116392, 2021, doi: 10.1016/j.bmc.2021.116392.
[26] E. S. Leal, M. G. Aucar, L. G. Gebhard, N. G. Iglesias, M. J. Pascual, J. J. Casal, A. V. Gamarnik, C. N. Cavasotto, M. Bollini, "Discovery of novel dengue virus entry inhibitors via a structure-based approach". *Bioorg. Med. Chem.*, vol. 27, no. 16, pp. 3851-3855, 2017, doi: 10.1016/j.bmcl.2017.06.049.
[27] M. Jyothi, V. L. Ranganatha, H. A. Khamees, M. J. N. Khadri, S. A. Khanum, "Design, synthesis, characterization and analysis of anti-inflammatory properties of novel *N*-(benzo[d]thiazol-2-yl)-2-[phenyl(2-(piperidin-1-yl)ethylamino]benzamides and *N*-(benzo[d]thiazol-2-yl)-2-[phenyl (2-morpholino)ethylamino]benzamides derivatives through in vitro and in silico approach". *J. Iranian Chem. Soc.*, vol. 20, no. 4, pp. 861-873, 2023, doi: 10.1007/s13738-022-02719-0.
[28] D. Muhammed Aziz, S. A. Hassan, A.A.M. Amin, M. N. Abdullah, K. Qurbani, S. B. Aziz, "A synergistic investigation of azo-thiazole derivatives incorporating thiazole moieties: a comprehensive exploration of their synthesis, characterization, computational insights, solvatochromism and multimodal biological activity assessment". *RSC Adv.*, vol. 13, no. 49, pp. 34534-34555, 2023, doi: 10.1039/D3RA06469G.
[29] M. B. Taj, A. Raheel, W. Alelwani, N. Babteen, S. Kattan, A. Alnajeebi, M. Sharif, R. H. Ahmad, Abbas, A. Hazeeq, S. A. Tirmizi, H. B. M. Ali, "One-Pot CuO-catalyzed green synthesis of *N*(*N*')-arylbenzamidines as potential enzyme inhibitors". *Russian J. Org. Chem.*, vol. 55, no. 7, pp. 1047-1052, 2019, doi: 10.1134/S1070428019070224.
[30] T. J. W. J. D. Lapierre, D. N. Farago, M. G. F. de Moura Lodi Cruz, D. de Melo Resende, A. C. R. de Oliveira, B. R. M. dos Santos, F. de Oliveira Souza, S. Michelan-Duarte, R. C. Chelucci, A. D. Andricopulo, L. L. G. Ferreira, E. J. Pilau, S. M. F. Murta, C. O. R. Júnior, "Evaluation and discovery of novel benzothiazole derivatives as promising hits against Leishmania İnfantum". *Chem. Bio. Drug Des.*, vol. 103, no. 4, pp. e14525, 2024, doi: 10.1111/cbdd.14525.
[31] "Amides as apolipoprotein A-I expression stimulators. Assignee: Shionogi and Co., Ltd., Japan, JP2001139550 A 2001-05-22.
[32] S. Ramos, A. Vicente-Blazquez, M. Lopez-Rubio, L. Gallego-Yerga, R. Alvarez, R. Pelaez, "Frentizole, a nontoxic ımmunosuppressive drug, and İts analogs display antitumor activity via tubulin inhibition". *Inter. J. Mol. Sci.*, vol. 24, no. 24, pp. 17474, 2023, doi: 10.3390/ijms242417474.
[33] M. G. Chini, A. Giordano, M. Potenza, S. Terracciano, K. Fisher, M. C. Vaccaro, E. Colarusso, I. Bruno, R. Riccio, A. Koeberle, O. Werz, G. Bifulco, "Targeting mPGES-1 by a combinatorial approach: ıdentification of the aminobenzothiazole scaffold to suppress PGE levels". *ACS Med. Chem. Let.*, vol. 11, no. 5, pp. 783-789, 2020, doi: 10.1021/acsmedchemlett.9b00618.
[34] Ajou University, Industry-Academic Cooperation Foundation. "Composition for preventing or treating neurofibrosarcoma". Korea, Republic of, KR1902845 B1 2018-10-02.
[35] "Preparation of aromatic and heterocyclic carboxamides as antineoplastic agents" Assignee: Pfizer Inc. European Patent Organization, EP343893 A1 1989-11-29.

[36] M. M. F. Ismail, H. G. Abdulwahab, E. S. Nossier, N. G. El Menofy, B. A.Abdelkhalek, "Synthesis of novel 2-aminobenzothiazole derivatives as potential antimicrobial agents with dual DNA gyrase/topoisomerase IV inhibition". Bioorg. Chem., vol. 94, pp. 103437, 2020, doi: 10.1016/j.bioorg.2019.103437.
[37] J. Angulo-Cornejo, M. Lino-Pacheco, R. Richter, L. Hennig, K.H. Hallmeier, L. Beyer, "Metal chelates of *N*-benzothiazol-2-yl-, *N*-benzoxazol-2-yl- and *N*-(1*H*-benzimidazol-2-yl)-benzamide". *Inorg. Chim. Acta*, vol. 305, no. 1, pp. 38–45, 2000, doi: 10.1016/S0020-1693(00)00109-2.
[38] H. Zheng, Y. X. Li, W. C. Xiong, X. C. Wang, S. S. Gong, S. Pu, R. Shi, Q. Sun, "Mechanistic insights into diversified photoluminescence behaviors of BF_2 complexes of N-benzoyl 2-aminobenzothiazoles". *Phys. Chem. Chem. Phy*., vol. 26, no. 15, pp. 11611-11617, 2024 doi: 10.1039/D4CP00101J.
[39] U. Caruso, B. Panunzi, A. Roviello, M. Tingoli, A. Tuzi, "Two aminobenzothiazole derivatives for Pd(II) and Zn(II) coordination". *Inorg. Chem. Commun*., vol. 14, no. 1, pp. 46-48, 2011, doi: 10.1016/j.inoche.2010.09.027.
[40] A. A. Irzoqi, F. A. Salman, Y. K. Alasadi, M. A. Alheety, "Synthesis and structural characterization of palladium(II) mixed-ligand complexes of N-(benzothiazol-2-yl)benzamide and 1,2-bis(diphenylphosphino)ethane". *Inorg. Chem*., vol. 60, no. 24, pp. 18854-18858, 2021, doi: 10.1021/acs.inorgchem.1c02584.
[41] G. Anderegg, E. Bottari "Pyridinderivate als komplexbildner VII. Uber die koordinationstendenz von substituierten dipicolinat-ionen". *Helvetica Chim. Acta*, vol. 48, no. 4, pp. 887-892, 1965, doi: 10.1002/hlca.19650480425.
[42] Z. A. Kaplancıklı, G. Turan-Zıtounı, G. Revial, K. Güven, "Synthesis and study of antibacterial and antifungal activitiesof novel 2-[[(benzoxazole/benzimidazole2yl)sulfanyl] acetylamino]thiazoles". *Arch. Pharm. Res.*, vol 27, no 11, pp. 1081-1085, 2004. doi: 10.1007/BF02975108.
[43] Z. A. Kaplancıklı, G. Turan-Zıtounı, A. Özdemir, G. Revial, K. Güven, "Synthesis and antimicrobial activity of some thiazolyl-pyrazoline derivatives". *Phosp. Sulf. Sili. Relat. Elem.*, vol. 182, no. 4, pp. 749-764. doi:10.1080/10426500601047529.
[44] K. Nakamoto, "Infrared and raman spectra of inorganic and coordination compounds". 5th ed. NewYork: Wiley-Interscience, pp. 232, (1997).
[45] S. Yelin, B. Cula, C. Limberg, "Low-coordinated iron(II) siloxide complexes – structural diversity and reactivity towards O_2 and oxygen atom transfer reagents". *Eur. J. Inorg. Chem*., pp. e202200078, 2022, doi: 10.1002/ejic.202200078.
[46] D. Sasi, V. Ramkumar, N.N. Murthy, "Bite-angle-regulated coordination geometries: tetrahedral and trigonal bipyramidal in Ni(II) with biphenyl-appended (2-pyridyl)alkylamine N,N-bidentate ligands". *ACS Omega*, vol. 2, no. 6, pp. 2474-2481, 2017, doi: 10.1021/acsomega.7b00119.
[47] I. Shimizu, Y. Morimoto, D. Faltermeier, M. Kerscher, S. Paria, T. Abe, H. Sugi-Moto, N. Fujieda, K. Asano, T. Suzuki, P. Comba, S. Itoh, "Tetrahedral Copper(II) complexes with a labile coordination site supported by a tris-tetramethylguanidinato ligand". *Inorg. Chem.*, vol. 56, no. 16, pp. 9634–9645, 2017, doi: 10.1021/acs.inorgchem.7b01154.
[48] M. Ameen, F. Ahmed, "Preparation and characterization of some complexes of nickel(II), copper (II), and zinc (II) with decylxanthate and their adducts with nitrogen base ligands, and their biological activity". *J. Turkish Chem. Soc. Sec. A: Chem.*, vol. 10, no. 4, pp. 975-84, 2023, doi: 10.18596/jotcsa.1311891.
[49] E. Canpolat, A. Aglamis, H. Şahal, M. Kaya, "Some transition metal complexes of NO type schiff base: preparation and characterization". *Fac. Sci. Cumhuriyet Univ.*, vol. 37, no. 1, pp. 65-73, 2016, doi: 10.17776/csj.38701.
[50] W. J. Geary, "The use of conductivity measurements in organic solvents for the characterisation of coordination compounds". *Coord. Chem. Rev.*, vol. 7, no. 1, pp. 81-122, 1971, doi: 10.1016/S0010-8545(00)80009-0.

Contents lists available at *Dergipark*

Journal of Scientific Reports-A

journal homepage: *https://dergipark.org.tr/tr/pub/jsr-a*

E-ISSN: 2687-6167 ***Number 61, June 2025***

REVIEW ARTICLE

Receive Date: 13.12.2024 *Accepted Date: 27.05.2025*

Types of cyber-attacks with using voice

Nursel Yalçın[a], Bilge Lale[b,*]

[a]*Gazi University, Gazi Faculty of Education, Department of Computer and Instructional Technologies Education, Ankara, Türkiye, ORCID: 0000-0002-0393-6408*

[b]*Gazi University, Department of Computer Forensics, Institute of Informatics, Ankara, Türkiye, ORCID: 0009-0005-1919-0929*

Abstract

Recently, attacks targeting individuals, organizations and even critical voice-activated systems have become widespread one after another. Basically, these are unauthorized access or control of a device using manipulated or synthesized voice commands to attack an identified vulnerability in voice technologies, usually supporting smart assistants and smart speakers. While such attacks are diversifying simultaneously with the regular implementation of voice technologies in daily life, the potential consequences of such attacks also increase their impact in cases where most users and organizations are not sufficiently aware. In this study, various voice-based cyber-attacks, such as voice phishing (vishing), voice command manipulation, attacks using ultrasonic sound waves, hard disk attacks via voice commands and acoustic eavesdropping attacks, their methods (e.g., synthesizing deceptive voice commands, using ultrasonic frequencies to bypass security systems, manipulating devices through inaudible commands, exploiting voice interfaces to access sensitive data on hard drives, capturing private conversations using sound waves) and possible effects are investigated and some legal situations related to these threats are also touched upon in the context of the current cyber security environment in Türkiye. This study aims to increase awareness by providing a comprehensive analysis of voice-based cyber-attacks and to better inform users and cybersecurity professionals about effective prevention and mitigation strategies. It serves as a comprehensive review of existing research in this field.

Keywords: Cybersecurity; cyber-attack; data breach; voice technologies; voice-based attacks

* Corresponding author. Tel.: +90-5395818598
E-mail address: bilge.lale@gazi.edu.tr

1. Introduction

Cyber-attacks are considered one of the huge threats of this digital era, as they pose a high risk to individuals' organizations and governments by destroying important information systems or networks, taking control of devices and illegally accessing personal data. There are various forms and methods of carrying out cyber-attacks, each of which differs depending on the attacker's goal and tools.

Cyber threats have grown considerably in recent years, boosted by the development of voice technologies. While voice assistants, smart speakers and all kinds of other devices that get turned on by the sound of one's voice started to be a feature in everyday life, so too they have increasingly turned out to be an attractive target for malicious actors. Most voice technology-based cyber-attacks rely on exploiting vulnerabilities of the systems using manipulated voice commands or phony voice recordings, which could be used to grant unauthorized access, data breach or system takeover.

While these emerging technologies are changing how humans interact with their devices, they come along with new risks of serious consequences in case manipulation to one's advantage ensues. Attacks on voice technology are among the most serious and fastest-growing attack vectors. Such risks are generally not well known and their potential impacts are worse in an environment where users are not well prepared for such an attack.

Most of the studies that have focused on voice-based cyber-attack vectors merely point to the fragmented treatment that this has received in the literature. Such kinds of studies focus on specific attack vectors; however, in this study some of them will be compiled into a comprehensive analysis of methodologies, objectives and results.

It also covers the legal frameworks of voice-based cyber-attacks within the context of cybersecurity and cybercrime legislation in Türkiye. Although challenges associated with voice technologies are relatively new, their legal counterparts have not yet been developed. This paper, therefore, will discuss recent developments regarding these types of attacks and will further propose how existing legal frameworks can be enhanced. Additionally, this study serves to set a basis of understanding changes in the technological and legal fronts concerning voice-based cyber-attacks and creates a demand for more stringent preventive measures in the face of constantly escalating cyber threats.

This study adopts a descriptive literature review methodology and aims to provide a structured and comprehensive overview of voice-based cyber-attack methods. The research was developed by examining up-to-date academic publications, technical reports and real case examples that reflect current attack techniques and defense mechanisms. Rather than generating new data, the goal is to synthesize existing knowledge in a thematically organized format. Literature was selected based on relevance, credibility and credibility. To ensure the comprehensiveness of the review, the search focused on publications between 2013 and 2024 sourced from academic databases including Scopus, ScienceDirect, IEEE Xplore and Web of Science. In addition, the most frequently discussed types of voice-based cyber-attacks identified in these sources were examined. These attack categories were selected based on their prevalence in the literature and their relevance to emerging cybersecurity challenges. While this method allows for broad contextualization of the topic, it also has limitations, such as the absence of empirical data and reliance on secondary sources, which may affect the granularity of the findings.

2. The concepts of voice and cyber-attacks

Voice is a form of physical energy and is produced by vibrations in a physical environment, the airway and atomic molecules. The vibrations produced originate from a sound source such as a musical instrument, a human voice or natural sound, causing the surrounding air molecules to move. These movements also propagate in the form of wave motions and are detected by the receiver's ear, allowing hearing to occur. The human voice is the sound generated by the vibration of the vocal cords while air from the lungs passes through the trachea. The frequency range for normal human voice, on average, ranges between 85-180 Hz for men and 165-255 Hz for women. This is the anatomic process by which speech can occur, whereby communication through speech, music and other sound signals is enabled. The frequency, amplitude and speed of sound waves determine the pitch, tone and intensity of the sound [1]. Voice plays

a critical role in the field of communication with applications ranging from music and speech to alarms and notifications commonly used in daily life. Recent developments in digital technologies have significantly affected various fields and have also affected audio technologies in many ways. Digital Signal Processing (DSP), for example, is one of them. DSP enables the conversion of audio signals into digital formats for processing and analysis. This field is widely used in audio engineering, music production, telecommunications technologies and numerous media applications [2]. Moreover, the increasing prevalence of voice-related technological advances has profound implications for cybersecurity. While voice data is widely used in devices, voice commands and voice assistants are increasingly vulnerable to threats related to the security of personal data [3].

Cyber-attacks are carried out through various methods that compromise the security of information systems. These attacks aim to disrupt the functionality of target systems, steal sensitive information, manipulate data or achieve financial gain [4]. Common types of cyber-attacks (Examples of some of these are also shown in Fig. 1.) include information theft, phishing, ransomware, malware and Distributed Denial of Service (DDoS) attacks.

Fig. 1. A diagram illustrating common types of cyber-attacks [5].

Information Theft refers to the unauthorized acquisition of personal data by an attacker. Cybercriminals often exploit vulnerabilities in target systems to steal this personal data, financial data or confidential corporate information [6].

Phishing attacks aim to trick users into giving their personal information to attackers through fake calls, emails or websites. Attackers use deceptive tactics called social engineering to steal sensitive information such as passwords or credit card information [7].

In ransomware attacks, attackers encrypt the files of target systems, deny access to the owner and attempt to charge users a fee. Such attacks can cause significant damage to both individuals and organizations [8].

There are many different types of malwares designed to harm computers or networks or steal information. These threats include viruses, trojans and worms.

DDoS attacks disrupt target systems, rendering them inoperable. These attacks are usually carried out over large-scale networks and can seriously reduce the availability of systems [9].

The convergence of voice technologies and cybersecurity has become increasingly significant in safeguarding information security and protecting personal data. Voice assistants and smart devices that collect and process vocal inputs to deliver various services introduce a range of security vulnerabilities. These devices and their associated voice commands can be exploited by malicious actors to access sensitive personal information. Of particular concern are the risks associated with the recording and processing of voice biometric data, which underscores the importance of

implementing comprehensive security measures for voice data within the broader context of cybersecurity. Biometric voice authentication systems are especially vulnerable and require heightened protection against cyber-attacks. Secure digital processing of voice data must be supported by robust cybersecurity protocols to maintain the integrity and confidentiality of these systems [10].

As a result of developing voice technologies and the proliferation of IoT (Internet of Things) devices, new types of attacks beyond traditional cyber-attacks are emerging.

The protection of voice data and the prevention of cyber-attacks in this area necessitate the strengthening of both technological and legal infrastructures. The connection between traditional cyber-attacks and voice-based attacks is important, especially in this period when voice technologies are developing, in terms of ensuring the security of the relevant systems. Because the basis of defense strategies is based on traditional cybersecurity methods.

3. Cyber-attacks utilizing voice

The rapid advancement of technology, especially in the field of voice technology, has led to the increased use of voice as a tool in cyber-attacks. Fig. 2 shows the stages of some of the attacks. Research conducted in various fields aims to clarify the effects of voice technologies on cybersecurity and to reveal the complexities and potential risks associated with voice-based attacks. Although there are many types, the most common voice-based cyber-attacks can be divided into two main types: voice phishing attacks (vishing) and system manipulations carried out through voice commands.

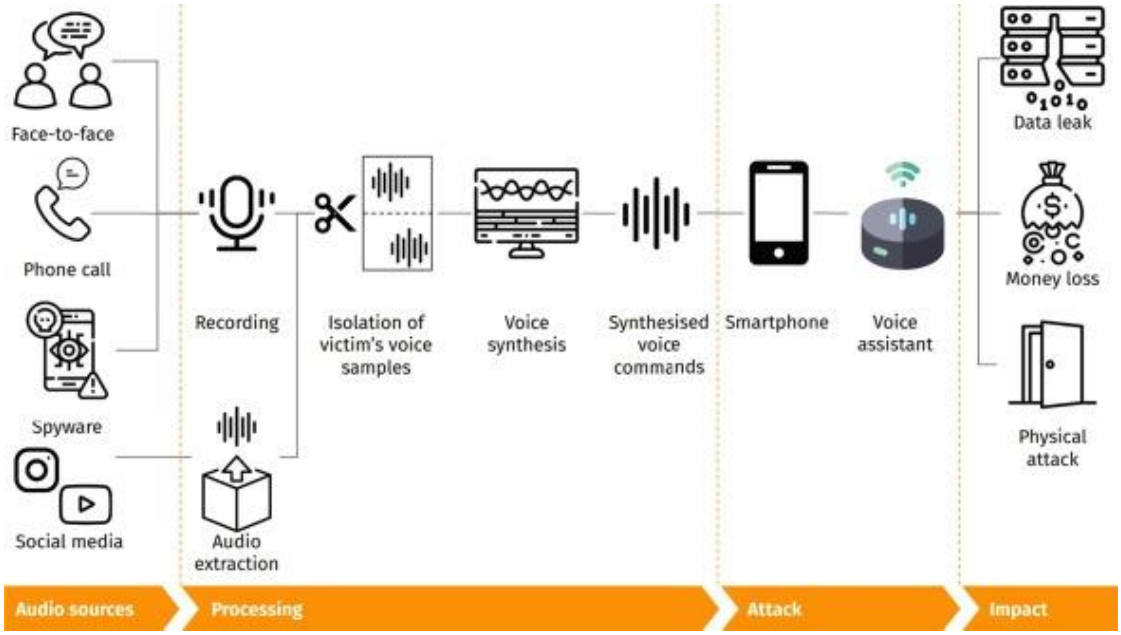

Fig. 2. An example of the stages involved in cyber-attacks executed using voice technology [11].

Voice phishing or vishing is the voice-driven counterpart of traditional phishing attacks, where attackers aim to steal users' personal data through phone calls or voice messages. Studies have revealed that during vishing attacks, perpetrators use social engineering techniques designed to establish an environment of trust with the target user, thus allowing personal data to be easily intercepted by unauthorized persons [3]. These types of attacks are extremely convincing and can often be designed specifically for specific individuals through software, taking advantage of

advances in voice analysis and speech synthesis technologies. For example, innovations in artificial intelligence and machine learning have significantly increased the possibility of deceiving target users by allowing attackers to produce almost one-to-one voice imitations through software [12].

Another common type of voice-based cyber-attack, system manipulations via voice commands, refers to the unauthorized control of smart devices using voice commands. These attacks exploit vulnerabilities in the microphones or voice assistants of the target devices. Smart home systems and personal assistants are important targets of this attack technique and pose significant risks in this regard. Research has shown that vulnerabilities in these devices can be exploited by malware, thus compromising personal and financial data [13]. For example, an attacker can steal data stored on a targeted smartphone, such as passwords, financial data, photos, messages, phone numbers and contacts, by issuing malicious commands through the voice assistant of this targeted smartphone [14].

The main purposes of voice-based attacks usually include stealing personal data, obtaining financial information or completely disabling the target information systems. As a result of developments in voice recognition and speech synthesis technologies, it has become easier for malware to spread through voice commands or voice messages and affect users. In particular, the fact that smart devices can be remotely controlled for malicious purposes without the user's knowledge via voice commands creates significant security problems [15]. Research shows that voice commands are frequently used to install malware on smart devices or to exploit system vulnerabilities [16]. Thus, attackers can easily harm the target user and their device and obtain various amounts of financial benefit from the user.

4. Types of cyber-attacks with using voice

Cyber-attacks with using voice can be carried out by using people's voices or by exposing devices to sound waves. These types of attacks aim to capture personal data, financial information, corporate data, trade secrets and other sensitive information that can cause a lot of damage. Voice-based cyber-attacks can be divided into several types, including vishing, voice command manipulation, voice identity theft, voice messaging attacks and attacks using ultrasonic sound waves. Each type of attack is carried out using different techniques and methods. As a result, different damage is caused to the targeted users, devices and information systems.

4.1. Voice phishing (vishing)

Voice phishing (vishing) is a social engineering technique that attackers use to collect personal and financial information from people through phone calls. These attacks usually begin with attackers using trust-building strategies. These attackers usually present themselves to the person they are talking to as representatives of familiar and trusted institutions such as financial institutions, government agencies or technical support companies [3]. To do this, attackers can easily imitate the voice of a different person who does not belong to them but is trusted by the target person by using special software to deceive the target person.

In addition, vishing attacks are carried out in a systematic approach to identifying and targeting specific audiences. Attackers usually collect personal data using corporate databases, social media platforms and various websites and can create comprehensive profiles of their victims. They initiate phone calls aimed at creating panic or imposing a sense of urgency on the target person by bringing together many different personal information, Fig. 3 shows a simple example of this attack. For example, victims may receive alarming voice calls regarding the security of their bank accounts, and attackers may direct them to immediately transfer sensitive information or a certain amount of money to them [17].

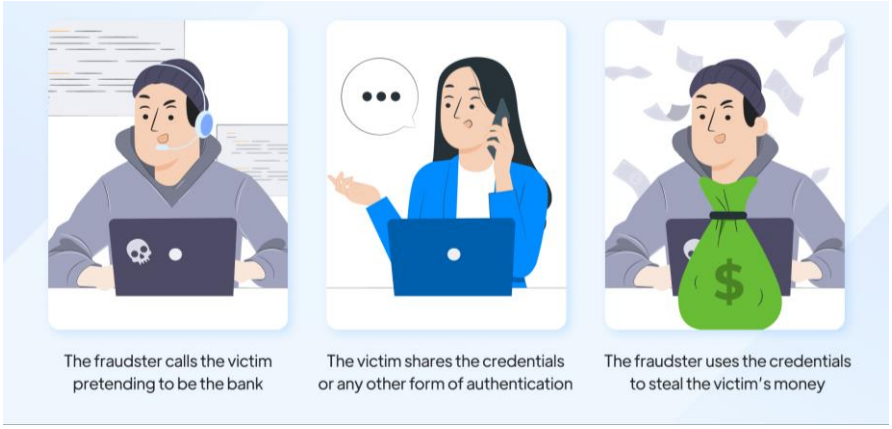

Fig. 3. The typical stages involved in a commonly executed vishing attack [18].

One of the most deceptive aspects with vishing concerns manipulation, in which the attacker distorts the perception of the authenticity of the call. By using an extremely simple voice-altering software, the attacker can make their voice sound like someone they can trust-a bank teller, family member or even coworker. This would sound incomparably more convincing for the targeted victim, who would be less likely to follow the request of an attacker. With the development of technology nowadays, voice synthesis or deepfake technology could enable hackers to imitate voices of people whom one really can trust; it also significantly blurs the line of which calls are legitimate and which ones are fake. Besides, during the call, an attacker may use a wide range of psychological manipulations and threats against the victims. They may also threaten the victim with consequences, such as the suspension of accounts or other legal actions, if financial information is not provided immediately. These types of threats may cost the victim losses in terms of finance and very fast, because one may be hoisted to a corner and made compulsorily to act accordingly upon the instructions given. Others may even claim that the victim has won some kind of reward and that the reward is to be given to the victim if a certain amount of money is given. They then use this to demand large amounts of money from them [12].

The effectiveness of vishing attacks and the variety of ways they are carried out are increasing with the use of rapidly developing technology, technological tools and methods in every field. For example, attackers can use the voice of a familiar or trusted person through software and in addition, they can display their phone numbers as caller ID. This deceptive practice can easily manipulate the target person, significantly reducing the likelihood that people will question the authenticity of the caller's identity. These techniques not only increase the probability of attackers' success, but also significantly weaken public trust in communication technologies.

As a result, vishing uses sophisticated social engineering techniques and psychological manipulation to target individuals. It is important for individuals to be aware of this type of attack and not to immediately establish trust. Financial institutions should also develop technological solutions to prevent vishing. Implementing robust security measures and conducting awareness campaigns to educate the public is an important step in reducing the risks associated with this sophisticated type of fraud and cyber-attack. Such preventive actions not only protect individuals, but also contribute to the broader goal of increasing societal safety and security.

4.2. Voice identity theft

Voice identity theft is a form of voice-based cyber-attacks in which attackers attempt to obtain victims' personal data through voice communication, a method involving phone calls, voice messages or even voice commands that

mimic the victim's or a trusted individual's voice. These attacks are carried out by creating the illusion that victims are interacting with a trusted person and by exploiting the victim's natural trust, which is often placed in public institutions. Attackers often impersonate financial entities, public officials or representatives of social media platforms to deceive individuals into disclosing sensitive personal information [19]. This manipulation, as in vishing attacks, effectively exploits the victim's psychological predisposition to trust familiar names, making it easier for attackers to reach their malicious targets.

Vishing is closely related to but distinct from voice identity theft - see a comparison in Fig. 4. While vishing is specifically carried out by tricking victims into giving personal information or tangible benefits via phone calls or voice messages, voice identity theft encompasses broader methods aimed solely at impersonating someone in order to extract personal data. These methods have also included the use of stolen personally identifiable information in fraud activities, such as opening new accounts or committing fraud via existing accounts, which is particularly vulnerable in voice communications and systems [20].

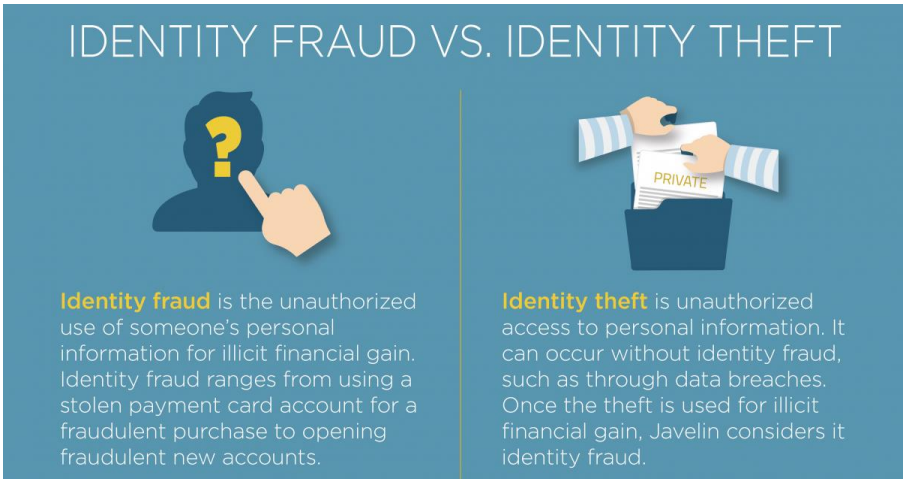

Fig. 4. A diagram illustrating the difference between identity fraud and identity theft [21].

As in vishing, voice identity theft attacks often involve the attacker pretending to be a familiar or trusted person. In this type of attack, the attacker can also abuse recorded voice samples or synthesized speech from a familiar or trusted person. This method becomes even more effective when attackers include specific details they have collected through previous research or social media, which can lead to financial data or even identity information falling into the hands of attackers [15]. Techniques such as requesting personal data under the pretext of "security verification" exploit the victim's instinct to protect their data, facilitating the attacker's goal of accessing critical information.

Despite vishing and voice identity theft sharing some superficial characteristics, such as the use of vocal communication as an attack vector, their core strategies, technological foundations and psychological mechanisms differ significantly. Table 1 summarizes their definitions, techniques, technological requirements, attack targets, real-world examples, and prevention strategies. This comparative analysis makes it easier to understand more fully how each attack works and what differentiates them from each other in reality.

Table 1. A general comparison of the characteristics of vishing and voice identity theft attacks.

Attack type	Vishing	Voice identity theft

Definition	A fraud method that uses social engineering techniques through phone calls or voice messages to trick victims into disclosing sensitive information.	The use of stolen voice samples to bypass identity verification systems or to commit fraud by impersonating the victim.
Purpose	To deceive the victim and obtain confidential data such as passwords, credit card details, and identity information.	To impersonate the victim by mimicking their voice in order to bypass biometric security systems or conduct fraudulent transactions.
Common techniques	• Impersonating a trusted figure (e.g., bank employee, police officer, government agent) • Creating a sense of urgency to force quick reactions • Using spoofed caller IDs	• Using AI-based voice cloning and deepfake technologies • Exploiting stored voice samples to deceive identity verification systems • Attacking biometric voice recognition mechanisms
Use of technology	Generally requires low technical skill, persuasive communication via phone is often sufficient.	Involves advanced technologies such as artificial intelligence, machine learning, and voice synthesis.
Target of the attack	Primarily focuses on human psychology and manipulating the victim emotionally.	Targets technological systems, especially biometric voice authentication mechanisms.
Prevention Methods	• Stay alert against suspicious calls • Verify the caller's identity before sharing personal data • Confirm that the phone number belongs to the real institution	• Implement multi-factor authentication in systems using voice biometrics • Avoid discussing sensitive topics in insecure environments • Use AI-based synthetic voice detection tools

As discussed in Section 4.1, plunderers create a sense of fear or urgency by applying psychological pressure to get their targets to take quick action. Thus, the victim suffers damage without realizing that the incident they are experiencing is an illusion. For example, attackers may claim that the victim's bank account will be blocked if action is not taken immediately and may force them to share personal data quickly without sufficient thought [22].

Raising awareness among individuals is of great importance in preventing voice identity theft. Victims should be careful about calls from unknown numbers and evaluate requests for personal information with suspicious approaches. Simple steps such as verifying the identity of the caller through official channels or not sharing personal data immediately can significantly reduce the risk of falling victim to these attacks. Financial institutions can also increase public awareness through user education programs and technological measures aimed at preventing fraud attempts, such as multi-factor authentication and caller verification systems.

In conclusion, voice identity theft attacks are an example of one of the risks posed by social engineering and psychological manipulation, which are widely used and pose a major threat in an increasingly digital environment.

The prevalence of both voice identity theft and related attacks and frauds are sophisticated tactics used by modern attackers, highlighting the need to be vigilant and take precautions to protect various personal and financial data.

4.3. Voice command manipulation

Manipulation of voice commands is a significant and current cybersecurity threat targeting smart homes, voice-activated virtual assistants and other voice-controlled technological systems. As the use of these systems in modern life becomes more widespread (from voice-activated personal assistants such as Amazon's Alexa, Google Assistant and Apple's Siri to voice-activated smart home systems), the potential for these systems to be exploited and exposed to security breaches also increases. These systems are based on voice recognition technology that can synthesize human speech according to the frequency, tone and amplitude of sound waves and generate various actions in response [3]. However, existing voice recognition technologies present some vulnerabilities. Attackers can also manipulate

these vulnerabilities in different ways to execute unauthorized voice commands, access private information or execute other malicious actions. Therefore, voice command manipulation is not only a significant security concern, but also a growing risk as multiple devices and user accounts are connected.

These attacks center on the voice recognition feature of smart devices, the working stages of this technique are illustrated in Fig. 5. The most common technique is voice spoofing, where attackers use pre-recorded voice samples and imitate a target's voice to give commands to a voice-activated smart device. In this technique, the attacker records the victim's voice and plays back the recorded audio to perform some action, such as opening doors or making unauthorized purchases [13].

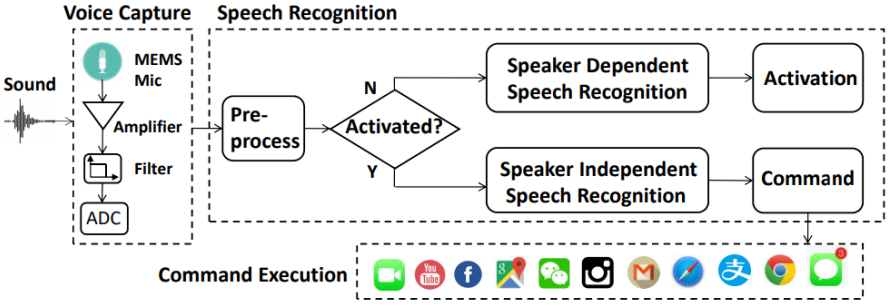

Fig. 5. Stages of a simple Voice Command Manipulation attack [23].

Although voice recognition systems are becoming increasingly sophisticated, they still fail to distinguish between a legitimate command and maliciously crafted speech, especially in basic speech recognition.

In addition to voice spoofing, acoustic attacks pose an advanced threat. These attacks use the physical properties of sound waves, especially frequencies that are outside the range of human hearing but can be detected by microphones in voice-activated devices. Attackers can use ultrasonic or subsonic sound waves, above 20 kHz and below 20 Hz, respectively, to send commands to the user's system without the user being aware of them. This technique can lead to serious risks that could allow an attacker to access personal data without the user knowing, open doors for smart homes or even control other smart devices in the home. Such attacks are carried out outside the detection capabilities of both users and devices, which makes this type of attack particularly dangerous.

Another danger is when malicious actors manipulate voice commands by interfering with the voice-to-text conversion process and modifying the voice and speech data before it is processed by the systems. In this case, attackers can intercept and modify a voice command while it is being transmitted, allowing a modified version of the command to be executed. This form of attack can lead to situations where, for example, a user intends to control their thermostat, but the attacker can instead execute a command to open a door or window or disable any security system.

Both technical and practical measures need to be taken to reduce these risks. From a technical perspective, the use of advanced biometric voice data is an important method for strengthening voice authentication systems. Voiceprint recognition is a more reliable method by analyzing not only the content of the speech but also the rhythm of the voice, speech patterns and speaker features such as phonetic details of the speaker [24]. However, biometric systems are not completely reliable and attackers are increasingly developing new techniques to imitate or defeat these systems and features. Therefore, combining voice recognition with multi-factor authentication (MFA), which requires users to verify their identity with a different form of authentication such as a PIN code or facial recognition, is a very important step in protecting systems against unauthorized access [25].

Other security measures depend on the regular updating of software and hardware so that all loopholes attacked by the attackers in the algorithms or software of voice recognition systems are patched. Users should update their devices because these manufacturers, such as Google, Apple and Amazon, provide regular updates for detecting these

vulnerabilities. Other potential risks can be mitigated by managing device and app permissions and settings with care regarding which applications should have access to voice data.

While voice-controlled and voice-guided technological gadgets increase, from voice assistants and smart homes to automotive systems, so does the potential danger regarding manipulation by voice command. For example, an attacker could use the voice control feature of a smart home system to disable security cameras or disable the alarm system. This would allow them to break into the security of a home using smart home technology based on the possible weaknesses in the voice recognition software. These kinds of security breaches demand further modification of hardware and software to ensure that these voice recognition systems are used correctly and securely. Educating people on how they can protect privacy and ensuring security in an ever-digitizing environment will also be necessary.

4.4. Voice messaging attacks

Voice Messaging Attacks are a serious cybersecurity threat where cybercriminals manipulate voicemail services to trick unsuspecting individuals into revealing sensitive personal information. Most attacks occur through fake voicemails that aim to extract confidential data such as account numbers, passwords and financial information. With the increasing use of automated voicemails by organizations for legitimate purposes, both in the field of analog telephone systems and modern messaging services such as WhatsApp and Facebook Messenger, the scope of voice messaging attacks has increased tremendously. For example, recently, cybercriminals utilized voicemails on Facebook Messenger to proliferate Trojans and other malware. In some instances, triggering the malware required merely hitting the button to play the voicemail. This has taken place all around the world as the attackers have gone so far as to target groups, sending multiple targets the fake messages. Clicking on the links may redirect users to attacker-controlled websites where the malware is hosted [26].

These attacks are also carried out based on psychological manipulation of the target. The language in such voicemails often contains emotional appeals that exploit cognitive judgments such as urgency or threat. Cognitive judgments are psychological shortcuts that people resort to when they act impulsively under stress or fear. Research has shown that many of these fear-based tactics, especially those that create a sense of urgency or personal threat, are highly effective in increasing stress levels and thus impairing decision-making abilities. A well-known feature of voice messasing attacks is the manipulation of tone and prosody. Attackers adopt a tone of voice that is similar to the tone, pace and formality of a professional organization that the target person trusts. These subtle vocal cues can positively enhance the perceived legitimacy of the message, thus making it harder to detect the scam. Using certain cultural words, pronunciations or excluding official language can further increase the credibility of the scam, especially if it targets certain demographic groups [22].

The primary protection against voice messaging attacks is again user education and awareness of the risks. First and foremost, people need to be somewhat sceptical when receiving unwanted voicemails, let alone those that demand urgent attention or even personal data. Users need training to recognize various manipulative cues, such as emotional language, unusual caller IDs or high-pressure tactics. The second step is for a person to verify the request for personal or financial information through independent contact with the organization, rather than responding directly to the message. This will help users be more resilient to voice messaging attacks and avoid falling victim to these increasingly common scams.

4.5. Deepfake technology and synthetic voice threats

Deepfake technology is one of the most complex and alarming threats in the contemporary digital world, supported by significant developments in artificial intelligence (AI) and machine learning techniques. The term "deepfake" is a combination of the words "deep learning" and "fake", which refers to the use of deep learning algorithms, especially generative adversarial networks (GANs), to create highly realistic and deceptive audio, video or other multimedia content. This includes not only altered visuals but also synthetic voices such as voice cloning, modification and

synthesis, all of which contribute to the increasing ability to impersonate individuals. Initially widely and popularly used in the entertainment field, deepfake technology has evolved over time, providing cybercriminals with new ways to impersonate people, manipulate media and personal data and conduct various fraudulent activities. Due to these threats, deepfake technology, particularly synthetic voice manipulation, has become a serious concern for cybersecurity experts, media organizations and individuals.

Attackers, scammers and malicious people are widely using deepfake technology to create realistic audio recordings or videos that mimic the voices and appearances of trusted people. This is basically done by following the steps in Fig. 6. Many new software tools are currently being developed for this purpose and through this software tools, the voice of each individual can be copied almost exactly and the content of their speech can be changed in seconds as the attackers want. These tools use AI and deep learning algorithms to convincingly mimic one's voice with high accuracy, allowing the changing of speech content in real time. For example, attackers can create a deepfake voice that mimics the voice of a CEO or senior manager in a company in seconds and use it to instruct employees to make unauthorized transactions or disclose important financial information. Using voice biometrics with AI-driven analysis, it becomes possible to identify and authenticate audio content, even detecting synthetic patterns in the voice. This helps in distinguishing between genuine and deepfake voices, ensuring security in communication systems.

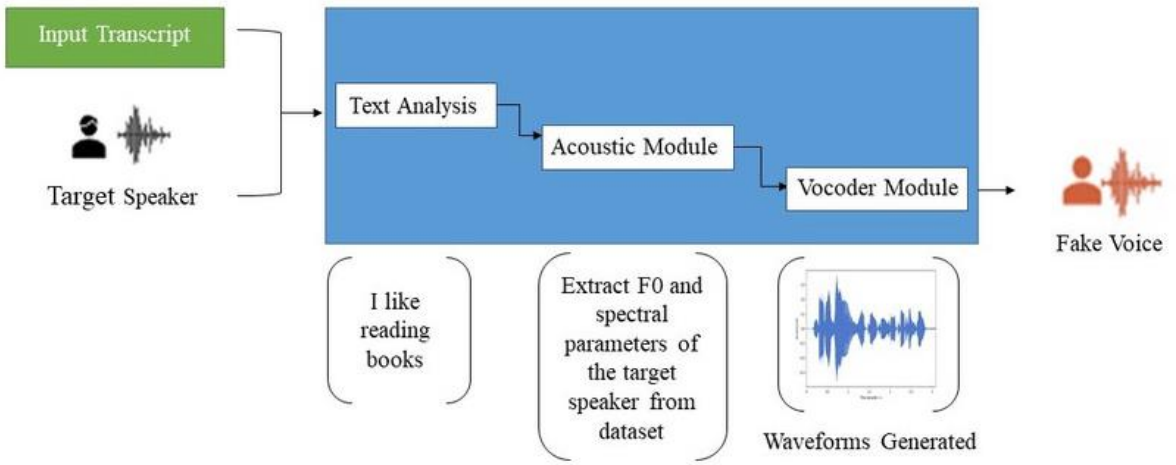

Fig. 6. A diagram showing how deepfake technology synthesizes a voice, segments of speech are analyzed and manipulated with sophisticated algorithms to fabricate a voice that sounds like the original speaker's tone and cadence [27].

In addition to individual financial fraud, deepfake technology also poses a significant threat to society. In high-risk scenarios such as elections, public health crises or international conflicts, deepfakes can be used to manipulate public opinion or destabilize social order. For example, deepfake videos or audio recordings of political leaders making false statements or behaving inappropriately can spread rapidly on social media, undermine trust in institutions and negatively impact public confidence. In 2024, cybercriminals targeted the global advertising giant WPP (World's Largest Advertising and Public Relations Group) by using a deepfake voice clone of CEO Mark Read. The fraudsters impersonated Read in a Microsoft Teams meeting, using a voice clone and YouTube footage to deceive employees into divulging sensitive information and money. While the attackers were not successful, the incident highlights the growing risk of deepfake technology in corporate environments, where it can be used to exploit trust and cause significant financial harm [28]. Such manipulations not only manipulate democratic processes, but also increase distrust in digital media and make it harder to distinguish truth from lies in the era of pervasive digital content.

The development of advanced detection mechanisms is increasingly important to mitigate the risks that deepfake technology may pose. Advanced deepfake detection methods rely on the effective use of machine learning and deep learning models. In particular, the MFCC-GNB XtractNet method, which combines MFCC (Mel-Frequency Cepstral Coefficients) and Gaussian Naive Bayes (GNB) models, has achieved a high accuracy rate in deepfake voice detection. This method extracts MFCC features from audio recordings, performs statistical analysis using the GNB model and then applies Non-Negative Matrix Factorization (NMF) to make the data more distinguishable. Studies have shown that this approach has achieved a remarkably high accuracy rate of 99.93%. With the advancement of deepfake technologies, the necessity of adopting such advanced detection mechanisms in the field of cybersecurity has become increasingly evident [29]. Today, researchers and cybersecurity experts focus on creating algorithms that can distinguish real and manipulated media. These detection methods often rely on subtle inconsistencies in content, such as unnatural eye blinking movements in the video or irregularities and distortions in tone and speech patterns. However, as deepfake creation techniques continue to evolve, detection tools must also evolve at the same pace. In addition to technological solutions, public awareness and education are critical components of a broader defense strategy. Media literacy campaigns aimed at helping individuals determine the reliability of deepfake content and creating scepticism about the authenticity of digital media can reduce the harm these attacks can cause.

In conclusion, deepfake technology is a multifaceted threat that constantly concerns both individuals and institutions and requires significant attention. The increasing sophistication of deepfakes necessitates the continued development of detection tools and public education to increase awareness of this growing threat. For voice deepfakes, methods such as forensic audio analysis and deep learning models help detect inconsistencies, such as unnatural speech patterns or audio artifacts. Verification of content authenticity is also essential and can be achieved through metadata validation, digital signatures or watermarking. Deepfake technologies are fast evolving; challenges lie ahead while manipulations in non-native languages create even more difficulties. Future research will be toward perfecting methods for detection across languages and explorations beyond the realm of manipulations of facial expressions into the domains of changes in body language and group dynamics [30]. By implementing robust detection systems and increasing public awareness, the negative impacts of deepfakes can be mitigated. By implementing robust security measures and creating a more informed public, the negative effects of manipulations through increasingly widespread deceptive media can be reduced [31]. It is also vital to keep up the tempo of technological innovation along with creating public awareness regarding the developments associated with deepfake technology as a way to reduce possible risks and avoid giving malicious actors opportunities.

4.6. Attacks using ultrasonic sound waves

Attacks using ultrasonic sound waves are the most sophisticated, since these voice-based cyber-attacks take advantage of technological vulnerabilities, especially in voice-activated smart systems. These attack modes deploy high-frequency sound waves above the range of human hearing-usually above 20 kHz-and thus are imperceivable to human ears. It is called "DolphinAttack"; the idea is to manipulate the voice-detection mechanisms of voice-controlled devices, which include not only smartphones and smart speakers but also voice-activated virtual assistants, to let the attackers' issue unauthorized commands without the user knowing about it. This range beyond the hearing of the human ear enables such an attack to carry out its processes completely hidden from the targeted user, thus setting serious risks for both users and manufacturers of voice-activated technologies. The attackers get an advantage wherein they manipulate the devices with sounds that cannot be heard by humans and make calls, send text messages or basically conduct any financial transaction without detection. The execution framework of DolphinAttack consists of two major parts: generating ultrasonic sound waves and manipulating the voice recognition system of the target device, as shown in Fig. 7. It employs specialized hardware and software tools which produce inaudible ultrasonic signals to the human ear but are easily detected by the target device. Such high-frequency signals can be modulated to fall within the range of frequencies at which the device's microphone is most sensitive, thus allowing attackers to easily transmit commands to the system. For example, an attacker can use ultrasonic waves to command a smartphone to send money

to an unknown person or to transfer it into a virtual account operated by the attacker without the victim's knowledge [32].

Fig. 7. Stages of a cyber-attack using ultrasonic sound waves [33].

One of the major vulnerabilities through which an attack can be made by ultrasonic sound waves lies in the sensitivity of voice-controlled devices. While most voice-activated smart devices are designed to respond to voice commands across a wide frequency spectrum, their systems are often ill-equipped to make out the difference between legitimate commands and those carried by ultrasonic waves. This is where one finds a critical vulnerability that can be exploited by an attacker. To reduce these risks, manufacturers need to set up sophisticated security features in voice detection systems of voice-activated devices. This may include the development of algorithms specifically designed to detect ultrasonic sound waves and the given device an ability to distinguish between normal voice commands and probably malicious commands. It can be further extended in developing voice mechanisms like biometric voiceprints for enhancement of the security features of the devices against access by unauthorized users, improvements should also be made in other mechanisms like multi-factor authentication.

However, besides the technological advancements, there is an equal requirement for increasing the awareness of the users in mitigating the attacks resulting from the ultrasonic sound waves. Users must be aware of such vulnerabilities and potential risks pertaining to the use of voice-activated technologies. This helps the user in understanding specific signs when systems are compromised, for example, unexpected behavior of their devices or execution of unauthorized actions. In addition, a user is expected to ensure the software on their device is updated since most companies release patches and security updates whenever a new vulnerability is found.

The after-effects of such an attack, like those with ultrasonic sound waves, range from individual security breaches to corporate integrity, public safety and even national security. With more devices beginning to be put into use in critical infrastructures, smart home automation systems and security protocols, the prevalence and rate of success of DolphinAttack are also on a rise. Attackers will be able to manipulate voice-activated systems in corporate environments in such a way that they steal sensitive company data, perform unauthorized financial transactions or even disrupt business operations. Afterwards, financial losses, reputational damage and erosion of customer trust follow, with the long-term effects of threatening the sustainability of an organization. Moreover, voice recognition is already being applied to some public systems nowadays, such as public services or security infrastructures of national importance; therefore, they are susceptible to manipulation with the aim of creating serious damage.

Considering the growing sophistication in attacks using ultrasonic sound waves, all this calls for a multi-pronged cybersecurity approach. Emphasis should fall on adaptive detection mechanisms that would identify and neutralize such threats before they can cause much harm. It is also very important to generate public awareness among users

about the potential risks of such kinds of attacks. In this regard, users are called upon to come up with scepticism and vigilance each time they have to deal with voice-controlled gadgets. Manufacturing companies, on their part, should work with regulatory agencies and experts in cybersecurity to lay down standards that will ensure that, if followed by all in the industry, a proper level of ultrasonic-based cyber-attack detection and prevention can be instituted. It is at such a time when the rate of technological innovation equips the establishment of security protocols and mass education on emerging threats, such as DolphinAttack and others of this nature, that the information environment within the digital world is best protected.

In conclusion, ultrasonic sound wave cyber-attacks are an example of the growing, insidious threat that needs constant vigilance and innovation. With the capabilities of voice-controlled systems continuing to expand, both manufacturers and users must remain proactive in identifying and addressing vulnerabilities. Since voice-activated technologies will compose an immense part of future cybersecurity, development should be collaboratively carried out with robust methods of detection and enhancement of system security, thereby enlightening the public about the risks of such emerging threats. Technology keeps evolving and since what malicious actors have been up to also evolves with time, this means continuous research and development and above all, cooperation by all parties concerned.

4.7. NUIT (Near-ultrasound inaudible trojan)

The Near-Ultrasound Inaudible Trojan (NUIT) is another very sophisticated and upcoming form of cyber-attack whose target analysis is voice-activated technologies such as voice assistants, smart speakers and other IoT devices. This attack mechanism uses waves from the audio spectrum in the frequencies of 16 kHz to 20 kHz, which are inaudible to humans with an audibility of approximately 20 Hz to 20 kHz but can still be detected by the microphones of many modern devices as shown in Fig. 8. These are designed to be inaudible to the human ear. However, since smart devices are designed to listen to user commands, these ultrasonic sounds are in the range that voice assistants can detect, making them a potential target for malicious actors.

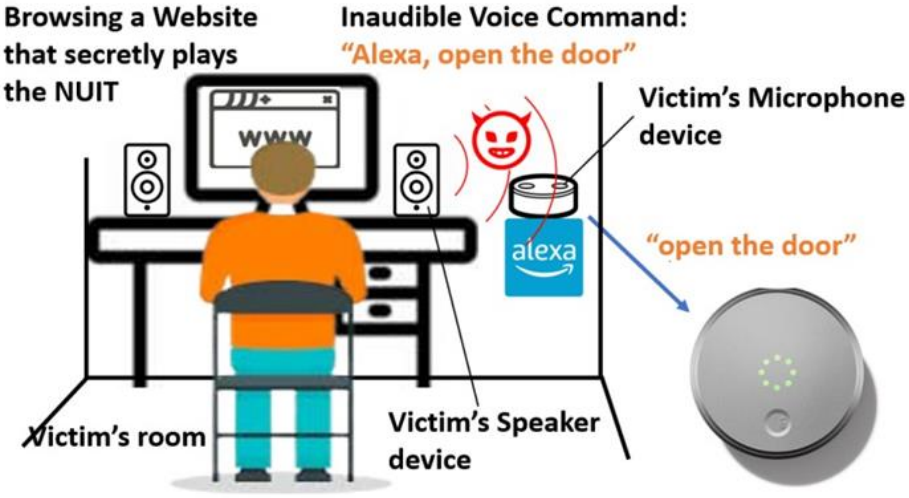

Fig. 8. A diagram illustrating how a NUIT attack is executed without the user's knowledge [14].

A classic example of how the operational mechanism of a NUIT attack can be carried out is the exploitation of ultrasonic signal coding. In this case, an attacker aims to insert complex instructions into the device using modulated sound waves. The sound waves are encoded with specific frequency patterns that can deceive speech recognition algorithms built into the device that mimic legitimate voice commands. For example, consider how researchers have successfully demonstrated how ultrasonic signals can be modulated into speech-like patterns that are recognized as commands after demodulation [33]. All these manipulations mostly occur without any trace of intrusion, because the attack exploits the device's existing microphone hardware as well as its normal listening capabilities.

This vulnerability arises because in many high-end voice-activated devices, from smartphones and smart televisions to smart assistants of all kinds, audio signals are processed without satisfactory distinction between audible and ultrasonic frequencies. When the malicious signal reaches the microphone, the speech recognition software does not recognize the frequency as an anomaly and thus the malicious action is successfully performed.

The consequences and impacts of these attacks by NUIT are enormous. One of the dangerous aspects of these attacks is that they are stealthy, leaving the victim completely unaware that their device has been compromised. There are several ways for a cybercriminal to gain control of a victim's device. For example, through this vulnerability, an attacker can remotely trigger certain unauthorized activities: opening smart locks, tampering with security cameras and performing financial transactions [34]. The attack can also be used to obtain sensitive personal information (passwords or credit card details) from voice-activated payment or communication platforms.

One of the most dangerous cases for NUIT could be focused attacks on people working in high-security environments: government facilities, prisons, research labs or corporate offices. Using a variety of voice-activated smart devices, attackers can bypass security protocols, for example and compromise sensitive information or even entire corporate networks. As IoT (Internet of things) devices proliferate, the scope of potential vulnerabilities related to ultrasonic attacks is growing, further increasing the risks to individuals and organizations.

Mitigating the risks posed by NUIT attacks requires initiatives from device manufacturers and users. In this context, the need to develop algorithms that can distinguish human voice commands from unusual ultrasonic signals stands out. Solutions range from dynamic filtering of the frequency to coding to discard certain frequency bands outside the audible range of the microphone, to developing voice recognition technologies that distinguish natural speech from artificial ultrasonic sound waves and somehow analyze the sound wave characteristics [33].

Moreover, voice-activated devices should be designed with much more serious security policies than in previous cases. This is possible by developing end-to-end encryption between voice assistants and back-end servers, anomaly detection systems and signalling that voice commands are unusual for such a user. Enabling these capabilities on devices ensures explicit consent of users before sensitive actions such as financial transactions and is an important measure to minimize the possibility of remote exploitation. This proactive security practice should be addressed at the end-user level. Permissions on devices should be reviewed from time to time and voice activation should be disabled when not in use. This can be done with Always Listening Mode for Voice Activated Payments and Transactions or Non-2FA Devices, preventing the possibility of unauthorized access. As a result, user education is extremely important in terms of ways to reduce exposure, as well as awareness of ultrasonic threats and recognition of potential vulnerabilities; this will greatly help to reduce vulnerabilities and prevent damage that may occur.

As voice-activated technologies become an increasingly important part of modern life, attacks like NUIT orchestrated by highly specialized attackers, are certain to become more sophisticated. Therefore, continuously evolving technical solutions and user education are highly recommended. The only way to reduce such risks in stealth attacks is to encourage manufacturers and consumers to develop good defenses against ultrasonic vulnerabilities. Sooner or later, more than just technological innovation will be required; a cultural shift will be required to create security awareness among users and smart devices to cope with the current emerging cybersecurity threats.

4.8. SurfingAttack

SurfingAttack technique is an advanced voice-based cyber-attack technique that uses the acoustic transmission properties of atomic structures of solid materials, especially focusing on the interaction of Micro-Electro-Mechanical Systems (MEMS) microphones in current and voice-controlled smart devices with high-frequency ultrasonic sound waves. This attack technique exploits the properties of MEMS microphones that are sensitive to sound frequencies, which are generally between 16 kHz and 100 kHz and are beyond the frequency range that humans can hear. These ultrasonic frequencies, which are not perceptible to the human ear, can be detected by MEMS microphones built into smart devices that are widely used by consumers, such as smartphones, smart speakers and other voice assistants. Attackers can manipulate these devices to establish covert communication, issue unauthorized commands or intercept sensitive data.

Attackers specifically use directed ultrasonic signals to interact with voice-controlled smart devices without requiring direct access to the device or its physical microphone. By exploiting the nonlinear nature of MEMS microphones (according to which the microphone's response to sound waves becomes more complex as the frequency increases), attackers send ultrasonic signals that are then demodulated by the device's speech recognition system and interpreted as a legitimate command [35]. This covert manipulation allows the attacker to issue commands to the device without the user's knowledge, such as unlocking the device, initiating transactions or accessing private data.

The SurfingAttack technique is based on the interaction between ultrasonic waves and the nonlinear properties of MEMS microphones. MEMS microphones are commonly found in mobile phones, voice assistants and other smart devices. These microphones easily convert high-frequency acoustic signals into electrical signals, which are then processed by the firmware as if they were legitimate voice commands. The problem is that MEMS microphones lack proper filtering mechanisms for ultrasonic signals; therefore, guided ultrasonic waves can manipulate them quite easily [36].

A modulated ultrasonic signal can be equipped with digital information such as commands or data that are inaudible to the victim and interpreted by the device. This signal can be transmitted over short distances - for example, from a hidden speaker or smartphone - and can be reflected by the transmission of atomic particles from surrounding surfaces such as walls, windows or furniture and as a result, it can be detected by the microphone connected to the voice assistant. It can then be transmitted to the device as a valid command by the microphone where it is detected. Thus, the attacker can remotely operate the device to perform many actions or obtain sensitive information from the device. In most scenarios, such attacks are also possible at extremely long ranges, assuming a suitable condition for ultrasonic wave propagation.

Another important factor that makes SurfingAttack dangerous is that it may work covertly, considering the acoustic properties of materials which usually reflect or absorb high-frequency sound waves. For instance, in a normal household environment, walls and furniture would serve as reflectors for ultrasonic signals, extending the attack range. This further benefits from the low energy required to transmit these ultrasonic signals, together with increased sensitivity in MEMS microphones; this therefore allows attacks that are power-efficient and difficult to detect.

Given the various threats mentioned, voice-activated smart device manufacturers should invest in advanced filtering technologies that distinguish legitimate voice commands from malicious ultrasonic signals. Various mitigation strategies can be developed, including:

- Ultrasonic Signal Detection: Improved signal processing algorithms allow devices to identify and eliminate non-human speech pattern ultrasonic signals. For example, active noise cancellation systems or DSPs can distinguish between high-frequency ultrasonic waves and standard voice commands.
- Frequency Range Limitation: One of the best measures in this regard is to limit the frequency range of the microphone so that it does not pick up ultrasonic frequencies. This can be done through hardware-based filters or software-based algorithms that simply ignore frequencies above 20 kHz and render ultrasonic commands ineffective.

- Two-Factor Authentication (2FA): For any high-risk activity, such as financial transactions or account changes, the integration of multi-factor authentication will reduce successful exploitation. Even if an attacker manages to issue a command via SurfingAttack, requiring secondary verification in the form of a PIN or biometric authentication can prevent unauthorized actions.
- Mic Sensitivity Controls: Devices would also be developed to support variable microphone sensitivity based on contextual information. For example, reducing the sensitivity of a microphone when a device is not active to listen for commands can prevent unnecessary ultrasonic waves from being detected.

Furthermore, users should be informed about the risks associated with acoustic attacks and why their voice-controlled devices need to be secured. Regularly updating device software, disabling voice assistants in public places and avoiding potentially sensitive voice commands in untrusted environments significantly reduce the potential for exploitation.

While the adoption of voice-activated devices increases, the technique of SurfingAttack points to an intrinsic vulnerability that requires both technological innovation and awareness. In other words, manufacturers can take long strides toward limiting the possibility of such exploits by dealing with the intrinsic security weaknesses in MEMS microphones and adopting effective strategies for detecting and mitigating such attacks. Similarly, user education and vigilance form the basis of safe and secure usage of voice-activated devices in daily life. In this manner, therefore, in a rapidly changing voice-activated technology environment, advanced security measures together with public awareness and smart device design are an integral component of protection against these and other emerging threats.

4.8.1. Piezoelectric transducers' role in SurfingAttack

One of the key components that makes attacks like SurfingAttack so effective is the use of piezoelectric transducers. These devices can convert mechanical stress (e.g. mechanical waves) into electrical stress and vice versa. Some materials, such as quartz, exhibit piezoelectricity; that is, an electrical charge is generated by mechanical perturbation and vice versa, the application of an electric charge causes mechanical oscillations. This is why these piezoelectric transducers are so effective in generating and controlling ultrasonic waves for covert communication.

In the context of SurfingAttack, piezoelectric transducers can emit high-frequency ultrasonic signals that are quite effective for manipulating MEMS microphones in voice-activated devices. Added to this are the advantages of compactness, low power consumption and high sound emission accuracy; these are exactly what SurfingAttack needs to be effective. This makes them an ideal tool for an attacker who wants to transmit high-frequency acoustic signals undetected over long distances from the target device. Ultrasonic transmitters using piezoelectric materials can be placed to interact with voice-activated devices either directly by transmission or by reflection from surrounding surfaces, thus increasing the range and effectiveness of the attack, as a diagram of how an attack is carried out is shown in Fig. 9.

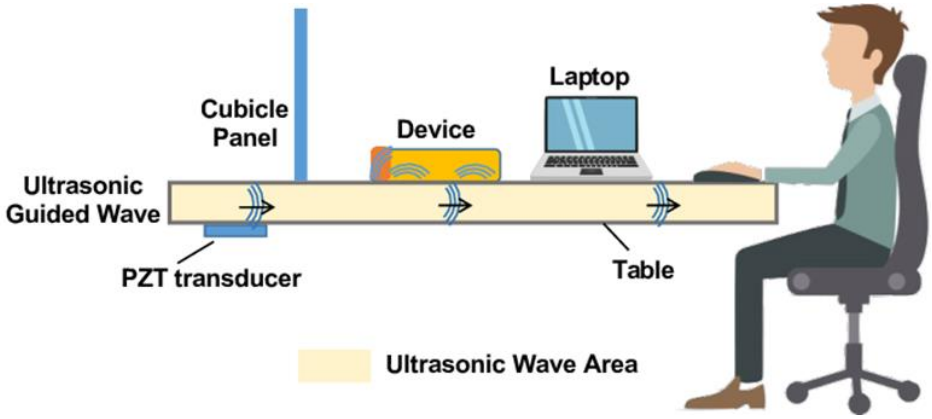

Fig. 9. A diagram illustrating how a simple SurfingAttack is carried out using a piezoelectric transducer [37].

Another important feature of piezoelectric materials is that they operate over a wide frequency range, giving an attacker tremendous opportunities to fine-tune ultrasonic signals to exploit specific vulnerabilities in voice-activated devices. For example, attackers can increase the probability of a successful exploit by emitting frequencies that correspond to the resonant frequency of materials or device components. The sensitivity and directionality provided to piezoelectric transducers make them effective in directing ultrasonic signals exactly where they need to go and do not spread into the environment [36]. In the case of an attacker, they can use the piezoelectric transducer to generate highly directed high-frequency waves ultrasonically and manipulate voice-activated devices in stealthy and difficult-to-detect ways.

With further developments in piezoelectric technology in terms of efficiency, size and power consumption, such devices are expected to be more widely used in cyber-attacks on acoustic interfaces in smart environments. Therefore, with the increasing awareness of the risks arising from such vulnerabilities, it is necessary to go a step further in countermeasures such as advanced measures such as filtering ultrasonic signals.

4.9. Hard disk attacks

Recent research has revealed a surprising and important new avenue for voice-based cyber-attacks: ultrasonic sound waves aimed at hard disk drives. Researchers at the University of Michigan and Zhejiang University have shown that high-frequency sound waves, far beyond human audible ranges, can severely damage the firmware of hard disk drives (HDDs) and instantly disable a device beyond repair [38]. These ultrasonic attacks exploit mechanical weaknesses in HDD components, particularly the highly sensitive disk platters and read/write heads, to perform sabotage. This interference by these waves results in data corruption, system crashes and sometimes irreversible hardware damage. This poses a new critical problem in cybersecurity, where an attacker can use sound as a powerful tool to manipulate hardware.

The mechanism of hard disk attacks using ultrasonic sound waves is to exploit the interaction between high-frequency sound waves and sensitive physical components inside the HDD. Therefore, when an ultrasonic signal is directed at a hard disk, it causes interference in the vibration movements that occur between the moving parts inside the device. Specifically, it targets the micro-mechanical components: the spindle motor, the read/write head and the disk platters. These components are critical to the accuracy of reading or writing data stored on magnetic platters. The delicate balance and accuracy involved here can be altered when exposed to ultrasonic sound waves, leading to incorrect data being read, written or lost.

In most such attacks, an action revolves around the generation of ultrasonic frequencies in the range of 16 kHz to 100 kHz - beyond the audibility of the human ear. The frequencies can penetrate the devices either through the air or through direct contact with surfaces. Once the attack begins, the sound waves can cause misalignment of the read/write heads or even induce micro-vibrations that physically damage the storage plates. In some cases, the vibrations are enough to cause the reading heads to come into contact with the platters, which may result in data loss or permanent hardware damage [38].

The effects of such attacks are extensive. An ultrasonic attack on the HDD can completely crash the entire system and therefore you cannot start the operating system or recover critical data. In such an environment where hard drives are used to store sensitive corporate or personal data, such attacks have disastrous consequences, ranging from irreversible data loss to compromise of confidential information.

The problem with ultrasonic sound wave attacks on HDDs is that they are undetectable when they tamper with the hardware. Often, the effects of an attack will not seem harmful at first; the system may slow down erratically, produce some errors or crashes and it will not be considered that these are due to malicious activity. This is the main reason why such an attack is almost impossible for a user or even an IT administrator to detect from the very beginning. In this case, critical data may become unrecoverable once the damage becomes apparent due to the lack of proper backups.

Additionally, ultrasonic attacks do not require local physical proximity; they can also be carried out remotely by directing ultrasonic waves at an HDD through acoustic reflections from the air or nearby surfaces. This makes such attacks stealthy and difficult to detect, especially if the system in question is in a secure and controlled environment such as a data center or office space. The use of piezoelectric actuators allows attackers to generate precise, high-frequency ultrasonic waves that target vulnerable components of the hard drive, which can make the attack more effective.

Another serious consequence of this attack would be data loss. Since modern HDDs store large amounts of critical data such as financial records, personal information and intellectual property, the loss of this data can be catastrophic for both individuals and organizations. Worse still, if these attacks occur against corporate storage systems or servers, the impact can easily range from simple individual data loss to corporate paralysis, financial loss and even reputational damage. Ultrasonic attacks are becoming an increasingly greater risk due to the continued reliance of companies on Hard Disk Drives and other such storage media for sensitive data.

The fact that technology is still improving means that the ultrasonic attacks, post-attack complications and the need to increase actions by individual users and organizations to protect the integrity of devices and hardware will also increase. Following are a few key measures which can reduce the effectiveness of such an attack and the damage caused: Periodic backup of sensitive information with remote servers or the cloud remains one of the most reliable security measures that could be employed against data loss by ultrasonic attacks.

The other security features that could be implemented are mainly when noise filtering and vibration dampening is highly advanced on a device containing critical data. Some of the hardware filtering techniques include the installation of high-frequency sound wave barriers or installation of software that may run in the device to detect any abnormal vibration or sound.

Firmware and security software need to be regularly updated to protect devices from newly discovered vulnerabilities that may also target the physical layer of the hardware. Software updates could enhance the capabilities of the firmware in terms of processing such external inputs and protecting it from ultrasonic manipulations.

This is the imminent danger to hard disks: an attack with the use of ultrasonic sound waves, which opens an entirely new dimension of cybersecurity vulnerabilities. With the rise of connectivity and sensitivity to environmental factors, there is an ever-increasing need for advanced detection systems against ultrasonic attacks on critical hardware components such as HDDs. While these systems are designed to protect many critical hardware, the vulnerability of HDDs due to their delicate mechanical components and wide usage for data storage makes their protection particularly important. Hence, this development of such detection systems is not only crucial for protecting HDDs but also for developing better security practices and awareness among users and organizations. Fully implemented data protection

policies consisting of regular backups, updated security software measures and physical security measures will go long towards making our digital assets much more difficult to breach for such advanced threats emanating from ultrasonic sound wave exploits.

Additionally, a general comparison of the types of cyber-attacks carried out with ultrasonic sound waves can be seen in Table 2 below.

Table 2. A general comparison of the types of cyber-attacks carried out with ultrasonic sound waves.

Attack type	Method	Target	Key feature	Primary challenge
DolphinAttack	Ultrasonic sound waves manipulate voice recognition systems	Voice-activated systems (e.g., smartphones, smart homes)	Uses inaudible ultrasonic signals to bypass audio filters	Difficult to detect due to inaudible frequency
NUIT	Electromagnetic pulses interfere with electronics	Voice-activated systems	Manipulates electromagnetic signals to issue commands	Requires specialized hardware for detection
SurfingAttack	Exploits MEMS microphones with high-frequency ultrasonic waves	Voice-activated smart devices (e.g., smartphones, smart speakers)	Uses ultrasonic waves to covertly issue commands via MEMS microphones without direct device access	Difficult to detect due to high-frequency sound, works over long distances and reflections from surfaces
HDD attacks	Ultrasonic sound waves damage mechanical components	Hard disk drives (HDDs)	Uses high-frequency sound to damage HDD's physical parts	Detection difficulty due to inaudible frequencies

4.10. Acoustic eavesdropping attacks

Acoustic eavesdropping attacks are a new and emerging type of voice-based cyber-attack in which attackers use sound to covertly collect sensitive information in specific environments. Aside from traditional eavesdropping methods that rely on physical access to devices or networks, acoustic eavesdropping attacks exploit vulnerabilities in the microphones and voice detection systems found in modern technology. The danger of such an attack has increased exponentially with the proliferation of smart devices and voice-activated technologies, making voice assistants, smartphones, laptops and other internet-connected devices extremely vulnerable targets. Designed to listen for specific commands by default, such devices can become unwitting aids in capturing a wide range of information, from passwords and personal information to financial data and sensitive conversations. The more people rely on these technologies in their daily lives, the more likely acoustic surveillance is to occur, but since most eavesdropping tools are already built into microphones that are commonly used, they are increasingly difficult to detect.

Different approaches can be used for acoustic eavesdropping, each relying on a different interpretation of sound selection and processing. The most common techniques are related to the compromise of smart devices by malware. Once the device is infected, it grants an attacker access to the microphone and remotely captures audio directly from an environment. These compromised devices are then used to record private conversations, monitor phone calls or even listen to keystrokes. These types of attacks are quite successful when used in conjunction with social engineering techniques. For example, some attackers may use social engineering tactics, tricking users into installing malicious apps or clicking on phishing links that give the attacker access to control of the device's microphone. When the device

is not actively being used, an attacker can simply use the built-in microphone to listen in on conversations around them or obtain sensitive information without the user's knowledge.

A much more sophisticated approach involves manipulating specific frequencies of sound waves. For example, the DolphinAttack attack mentioned above uses ultrasonic sounds to communicate with voice assistants or smart devices to issue voice commands or record audio without the victim being detected [39].

Another technique, such as Keylogger, will use acoustic reflections from physical surfaces. In this context, attackers will want to place microphones or voice recorders in certain strategic locations and then analyze the sound reflected off walls, tables or other objects in the vicinity. These reflected sound waves can leak keystroke patterns, thus

allowing an attacker to extract text input from typing sounds. Research has shown that keystroke extraction can be quite accurate when background noise levels are low, even when small differences in the sound produced between different keys can be analyzed to reconstruct typed text. This technique requires proper placement of the recording devices and involves extensive processing, but it represents a critical vulnerability for environments where sensitive information is written or discussed near any digital recording device.

Acoustic eavesdropping on individuals and organizations imposes potential hazards that need to be avoided by implementing prevention strategies that are layered in nature. Devices and communication must be secured in a multitude of ways. First, as simple as it may sound, perform constant reviews and modifications of the settings of devices, particularly the settings that regard the microphones. As well as controlling the sharing of the devices, turning off the unnecessary microphone functions of devices that are not used to participate in any conversation is a wise move that helps the situation from acoustic monitoring. Furthermore, checking the application that have the permission to microphones and only allow the trusted ones can prevent the resources from being a trap to a microphone via a virus.

Another one of the most significant steps to take is the implementation of the means of communications that are not easy to break. Take the case of the telephone call of voice-based devices for example, it is often the case of encrypted services, especially end-to-end encrypted messaging services that are used, which means that only the sender and the receiver are the parties who are able to listen to the content, even though the information is with a third party, who is in possession of the audio recording of the conversation. These methods make it impossible for third parties to hear the conversations even if a bug is placed in the microphone to send the signal outside the users. Besides, a peaceful place for face-to-face meetings or proper noise control techniques are sure factors that may significantly decrease the odds of unwanted acoustic interception of communications. Non-voice surroundings are also noise-free rooms or sound suppression techniques that are used to protect the larger coverage of the sound eavesdropping. Fig. 10 below shows simple examples of various types of Acoustic Eavesdropping Attacks.

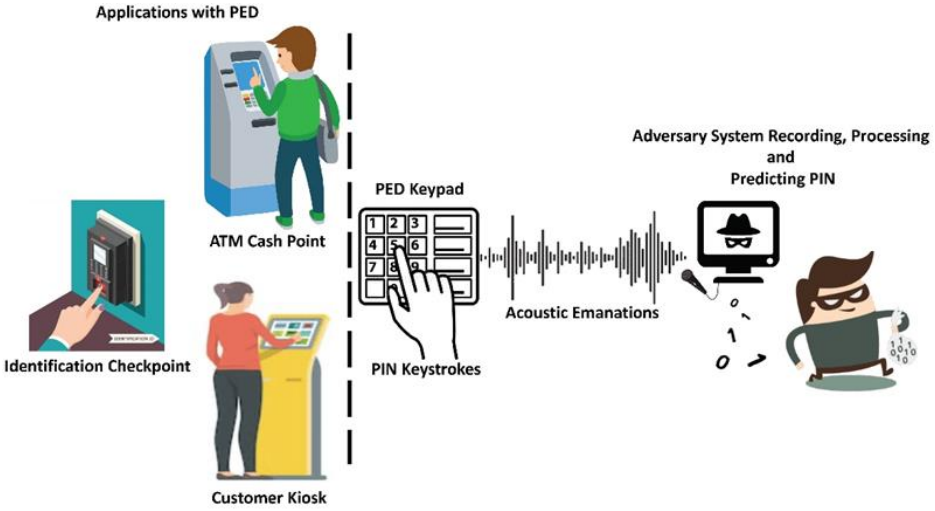

Fig. 10. Simple examples of various types of Acoustic Eavesdropping Attacks [40].

Acoustic devices as data manipulators can be something not so typical therefore, it is the responsibility of security personnel dealing with information and physical countermeasures to be aware of the associated risks. So far as practitioners are concerned, a proper mechanism such as a jamming device would in most occurrences be the one helpful in the affirmation of the acoustic threats. Suggestions on the measures taken to secure the audio such as the user's audio safety guidelines and thus the informed audio threat surveillance, help will set an organization in a good stand for a smart action taking company. In simple words, it means, that the various institutes, firms and businesses are required to implement efficient means, systems and strategies that will ensure customer Personally Identifiable Information (PII) and other confidential information is safe and made especially through data transmission within the organizations and outside.

While smart devices and voice-enabled technologies become increasingly integrated into our lives, the risk of eavesdropping attacks will also continue to increase. In such attacks, attackers take advantage of the microphones and voice detection system of these devices to intercept sensitive data, monitor conversations or even capture keystrokes without being detectable. It complicates the problem because it is sophisticated and kept secret, making it hard to identify the attack and defend oneself against it. However, it's possible to reduce a person's or organization's vulnerability to eavesdropping by means of control measures. This may be achieved through periodic review permissions for devices, utilization of encrypted communication devices and protection of the environment from within which one shares confidential information. The deep understanding of risks associated with cyber-attacks is critical to trying to maintain privacy and keep sensitive information from easy access as this field of cyber security continues to evolve.

4.11. Audio-delivered malware

Audio delivered malware is a new and highly advanced type of cyber-attack where malware is transmitted from one device to another via sound waves. Given the pervasive nature of sound in contemporary life, this method stands out as a new and sophisticated line in the evolution of cyber threats targeting the physical and digital interfaces of voice-activated systems, microphones and other audio input devices. The whole concept of voice-delivered malware aims to encode malicious payloads into sound and make them invisible to traditional security set up for network traffic and file-based threats [41]. Since malware signals in such attacks are usually placed using sophisticated obfuscation

techniques such as cryptography and steganography, the transmission of the malicious code becomes extremely stealthy, allowing attackers to carry out attacks without raising any obvious alarms.

The attack usually consists of two steps: first, the vocal transmission of the malware and then the activation of the malware upon reception. First, the attacker broadcasts sound waves at high frequencies, between 16 kHz and 100 kHz, which are inaudible to humans [42]. Therefore, the malware can be transmitted without alerting the user because the sound is not actually audible to humans. Certain modulation techniques will encode the malware into these sound waves, where the frequencies or patterns are used to encode the data in the audio signal. The problem with this type of concealment scheme is that the malicious code is guaranteed to be hidden in a file that looks and sounds like any normal audio file, which could include a song, a voice note or even an advertisement.

Later in the attack chain, after the sound waves are emitted, the target device receives the sound and decodes the malicious code embedded in it. The decoding process can be done through native audio processing systems on the device or other voice recognition technologies that can interpret these high-frequency audio signals as harmless sounds or instructions. Sometimes, malware can instantly and automatically execute commands encoded in the sound waves, such as downloading and installing them, changing system settings or opening backdoors for further attacks. The attack is complex because, in this case, the malware distribution tools, specifically voice-based tools and the entire chain of its activation are outside the scope of traditional security measures, which are very prone to looking at aspects of network traffic and file system scans. As a result, even the most careful security systems cannot detect this attack, since its structures are transmitted through information flow channels designed to bypass traditional detection mechanisms.

The implications of audio-delivered malware are broad. Since the use of voice-activated devices-such as smartphones, smart speakers and virtual assistants-is increasingly pervasive, so is the potential for such an attack. These devices are often equipped with always-on microphones, which listen continuously for commands, therefore making them ideal targets for attackers who want to inject code via sound. Apart from the infection of devices owned by individuals, audio-delivered malware has the potential for organizational network compromise: this depends on communication means such as Voice Over Internet Protocol (VoIP) or video conferencing applications or various remote collaboration platforms that are dependent on audio signals. An attack against such a system might result in information disclosure, disruption of services or the exploitation of network access for further malicious activity.

In fact, audio as a medium of transmission has brought cybersecurity professionals a whole new set of challenges. Other than traditional malware, most of which can be screened via scanning for files or network signatures, audio-delivered malware operates at a totally different dimension of attack surface. Due to the nature of audio encoding and signal modulation techniques, detecting malicious payloads requires further expertise and specific tools. For example, most of the audio-delivered attacks use steganographic methods so that the payload remains well hidden, invisible even within seemingly benign audio files. This in turn challenges traditional security frameworks, which might not be designed to inspect audio signals in real time.

Because of the increased threat of audio-delivered malware, proactive users and organizations go the extra mile to enhance their security posture. The most efficient way to ward off the attacks is a full turnout of patches in devices and software, updating them to their latest security updates. Quite obviously, frequent updates patch vulnerabilities in the device audio processing system or software before the attackers get a chance. Besides the updates, strong endpoint security solutions, like antivirus programs and firewalls, help in the detection of unusual or suspicious activity in malware execution. While these are not infallible, they nevertheless form a first line of defense against many common attack vectors.

Further, the user should be cautious when accessing audio from untrusted sources. Since malicious payloads in most of the recent malware attacks delivered through audio appear to the target as normal audio files, users must remain sceptical of opening unsolicited files or interacting with unfamiliar links that contain audio. Clearly, file integrity checks could be employed or specialized software designed to scan and analyze audio files for any hidden threats. It is also very important that organizations make employees aware of the risks posed by voice-based malware, especially in those contexts where the employees use voice-activated devices or systems to share sensitive information.

Another effective measure is disabling the microphone on devices while it is not in active use. Most microphones are always on-even when not in use from a range of devices from smartphones and laptops to IoT devices. An attacker would have to first exploit this as an entry point. Disabling microphone access for applications or services that do not need it may reduce the risk of voice-based threats. Highly sensitive settings may also consider anti-eavesdropping technologies or the adoption of secure channels of communication that make it nearly impossible for unauthorized people to get any kind of audio.

Considering the increasing sophistication of cyber-attacks, voice-transmitted malware is a particularly insidious threat as it can exploit widespread audio systems in modern devices. This introduces new complexity to the use of sound waves as a vehicle for malware delivery in security frameworks that are unable to control such innovations. With the increasing use of technology via voice-activated functions and voice-activated communication devices, awareness and defense mechanisms have become key. Keeping software up to date, being suspicious of the inclusion of audio files and using specialized security utilities go a long way in ensuring that users and organizations reduce their vulnerability to voice-transmitted malware and other evolving acoustic threats.

5. Legal frameworks and digital evidence in voice-based cyber-attacks under Turkish legislation

In order to solve the increasing incidents of cyber-attacks in the global society, various legal frameworks have been created to ensure the rights and security of people in online communities. The systems aim not only to prevent the occurrence of cybercrimes but also to mitigate the effects of damage caused to people. In Türkiye, legislative efforts have been made to redefine existing legal instruments to accommodate new forms of cyber threats, including voice technology. While voice assistants, smart home devices and voice-controlled devices become more and more prevalent in daily life, the demand for a legal explanation in this context has increased even more.

Although crime, penalty and security measures are rightly defined in the earliest concepts of Turkish criminal law, the law itself no longer always considers the unique nature of voice-based cyber-attacks. For this purpose, Turkish law rigorously adheres to "no crime without a law." In accordance with Article 2 of the Turkish Penal Code (Law No. 5237), no individual can be penalized for an act unless it has been explicitly delineated as a criminal offense [43]. This principle sets a structural limit in prosecuting actions under emerging technologies, particularly when the subject acts, such as ultrasonic attacks or voice-controlled interference, are not specifically addressed by current texts of law.

The usual objectives of cyber-attacks are to disrupt information systems, data theft or manipulation and financial fraud. These acts are provided for in Articles 243 to 245 of the Turkish Penal Code. Article 243 criminalizes illegal access into information systems and comes with penalties of one-year imprisonment. Article 244 widens the scope further by criminalizing destruction, alteration or hindering of system operation. Article 245 also criminalizes misuse of bank and credit card information with a view to attending to the monetary aspect of cybercrimes [44].

While these statutes represent a solid legal basis for the fight against traditional cybercrimes, they do not go far enough to be adequate to govern more advanced varieties of attack, e.g., the utilization of inaudible acoustic signals or the covert operation of voice-commanded machines. The legality of these emerging methods is, therefore, primarily an issue of judicial interpretation of terminology like "unauthorized access" and "information system." Consequently, existing law must be extended interpretatively or modified by statute to adequately encompass such emerging threats.

At the global level, there are a few conventions and treaties that provide a collaborative platform to combat cybercrime. The most prominent among them is the Budapest Convention, signed by the Council of Europe in 2001, which provides a comprehensive blueprint for transborder legal convergence on matters of cybersecurity. The treaty promotes the exchange of common legal standards and cooperation internationally in investigation and prosecution. Türkiye is a party to the convention and has pledged itself to the harmonization of its domestic law with its provisions, although controversy about its actual implementation exists among Turkish jurists [45].

Another relevant regulation as far as voice-based attacks are concerned is Law No. 6698 on Protection of Personal Data (according to its abbreviation in Turkish: KVKK). This act forms a full legal framework of processing, storage and safeguarding personal data. It imposes severe administrative sanctions in the event of non-compliance. Even

though protection of personal data is crucial to prevention of cyber-attacks, current provisions under KVKK do not include interception of voice data or voice-controlled system vulnerabilities, thereby showing a legislative gap.

In order to provide effective legal protection against advanced and dynamic cyber threats, continuous legislative adaptation and international cooperation covering voice technologies are required. Although Turkish legislation has a detailed framework to tackle cybercrime, the growing sophistication of attacks necessitates more targeted fine-tuning. Specifically, the incorporation of precise legal definitions of voice attacks in the Penal Code and related legislation would enhance the legal framework to effectively prosecute such offenses. With evolving cyber-attacks riding with advances in technology, law needs to be agile enough to sustain both human rights and cybersecurity in an ever-changing environment.

6. Detection and prevention of voice-based cyber-attacks

Detecting and preventing voice-based cyber-attacks is a major concern in today's complex, interconnected digital environment. The rapid adoption and use of voice-activated devices and technologies is increasing the risks associated with voice-based cyberthreats. Detection and prevention mechanisms will be crucial in reducing the losses that such attacks can cause, as they can sometimes lead to unauthorized access, data theft and manipulation of voice-controlled systems. Fig. 11 shows a flowchart illustrating the strategic stages of cybersecurity measures in general.

Fig. 11. A flowchart illustrating the strategic stages of cybersecurity measures in general. / Source: IWM Cybersec. (n.d.). Information security audit. Retrieved November 11, 2024, from https://iwmcybersec.com/information-security-audit/ [46].

These voice-based attacks are currently detected using machine learning algorithms, a central strategy. These sophisticated algorithms are tuned using large datasets of voice recordings to learn what normal voice patterns are and to recognize anomalies that may indicate malicious activity. Machine learning models that can analyze voice input in real time can detect subtle changes in frequency, tone or speech patterns that may indicate an attack. In this context, ML can be applied to the issue of voice command systems: detecting deviations in speech, abnormal intonations or unusual sentence structures that may indicate the presence of unauthorized commands or even maliciously crafted voices. These algorithms will increasingly learn and adapt to better build the ability of devices to compare legitimate

user inputs with any suspicious sounds. If the system predicts an attack, it will alert you for quick action that can reduce the risk of exploitation.

Along with machine learning, audio analysis is extremely important when it comes to identifying any voice-based threat. This analysis software uses advanced techniques such as frequency analysis and time domain analysis to examine the characteristics of sound waves in any environment. Therefore, frequency analysis can allow systems to measure the frequency capture range for certain commands based on known profiles. For example, if a voice command system is designed to be sensitive to a certain frequency range, sounds outside this range can indicate that the device is being manipulated using high-frequency sound waves that are inaudible to the human ear but detectable by the system. In contrast, time domain analysis focuses on the timing and rhythm of audio signals and can therefore identify unusual patterns, such as those produced by ultrasonic signals used in attacks like NUIT or SurfingAttack [38]. These analyses detect irregularities in the sound environment and enable the establishment of proactive defense mechanisms.

Most devices or even all, have pre-configured voice assistants and therefore there are only a few prevention techniques and methods that can be taken as precautions to reduce the possibility of such an attack. It is a good tool to combat cyber threats. Users need to be educated about the various techniques that attackers use in this attack. Users should be more careful and observant than before when communicating with a voice-activated device, as there is potential for some kind of risk. For example, making people aware of the risk of sensitive personal information being leaked by word of mouth, which can be used against a person if discovered by an attacker, is a good example [47]. Awareness of voice command security, for example, keeping microphones muted when not in use, can reduce the likelihood of devices being exploited. The second approach is to ensure that voice-activated systems strengthen their authentication mechanisms. Today's voice recognition systems verify them through spoken inputs or comparison of stored voiceprints/unique biometric features to ensure that only authorized individuals can access the system or perform certain sensitive operations. This means that when combined with other forms of biometric authentication such as passwords or fingerprints, the use of MFA in voice recognition can exponentially increase the overall security level of voice-based systems. This will also be important to help stop unauthorized access and minimize the scope of various attacks that may be directed at voice-activated devices.

Regular software updates, along with the installation of security patches, protect systems from newly identified vulnerabilities. Since attackers are always finding new ways to carry out cyber-attacks, it is critical that device manufacturers regularly update their various security measures and patch known vulnerabilities in voice recognition software. This ensures that devices are equipped with the latest defense mechanisms against emerging voice-based threats.

Because each of these threats requires a multi-layered defense strategy, including the latest technology, end-user training and corporate security controls, caution will be required by users and manufacturers amid the explosion of voice-activated technologies and increasing sophistication for cyber-attacks. All these combined—machine learning algorithms, advanced voice analytics, strong authentication methods, ongoing security updates and user awareness—can greatly reduce the likelihood of cyberthreats via voice.

7. Conclusion

While modern technology provides many comforts, voice-based cyber-attacks pose serious threats to security. This study examines various types of cyber-attacks using voice and discusses the methods and possible consequences of such attacks. From vishing, acoustic eavesdropping attacks, voice-delivered malware and special attack types such as NUIT and DolphinAttack, many types of attacks pose a real threat to cybersecurity and can violate people's privacy and security. The proliferation of these attacks is related to the increase in voice command systems and smart devices used by users. Nevertheless, the widespread lack of awareness of the vulnerability of voice command systems allows malicious individuals to carry out their activities to access personal information. Since voice-controlled devices are on the rise, more attention should be paid to manipulation using sound waves.

Voice-based cyber-attacks are a complex problem for users and organizations in general. The real attack exploits the inherent vulnerabilities in the same technologies that enable voice recognition and acoustic sensors to function. This type of attack is difficult to detect because most attacks use inaudible audio frequencies or transmit audio from hidden sources, which requires the creation of advanced detection techniques and prevention measures. Since cybercriminals are not standing still and new technologies continue to emerge every day, the security of voice-activated systems must also keep pace. Machine learning models, frequency analysis tools and voice filtering techniques are some of the most promising solutions to detect and mitigate these attacks so that immediate action can be taken in the event of suspicious activity.

Moreover, preventive measures cannot be limited to technological defenses. The complexities involved in voice-based attacks make extensive user education on their use important. Nevertheless, many people are still in the dark about the potential risks associated with this new generation of voice-activated devices and therefore can easily fall victim to attacks such as vishing, acoustic eavesdropping or malware-carrying audio files. This is because a lack of preparation paves the way for some form of interaction with digital assistants; such interaction is considered harmless but serves hidden villains. This means that manufacturing companies and software developers must take responsibility for embedding strong security measures in their products, including secure authentication mechanisms, periodic software updates and advanced encryption protocols for voice data.

Finally, voice-based cyber-attacks are detailed and multifaceted in their approach; they pose serious threats to users' security. It is time to inform users about the security protocols of voice command systems and to educate them about cybersecurity issues. Although the studies in literature generally focus on specific attack types, in this current study, the most common types of voice-based cyber-attacks were selected and each attack type was examined separately; a systematic study was prepared on the subject rather than a scattered structure. The issues require further research and study in-depth in order to create more robust security systems; hence, more literature is required in this aspect and the users of technology should be informed on the subject. In addition, device manufacturers need to produce systems that are resilient to such attacks and conduct training programs to increase users' awareness. In the future, more effective protection mechanisms and security measures, especially regarding voice-based cyber-attacks, will play an important role in ensuring cybersecurity at both individual and societal levels. In this context, research needs to be further supported to prevent and detect voice-based cyber-attacks with the aim of creating a single secure digital environment. Therefore, the increasing tendency for reliance on voice-activated devices and the ever-increasing level of cyber threats make the multi-layered security approach supported by technological innovation in a careful user a key factor in ensuring the security of digital systems.

Acknowledgements

This research was conducted independently without any external funding or financial support. Authors declare no conflicts of interest related to this work.

References

[1] T. D. Rossing, F. R. Moore, and P. A. Wheeler, *The Science of Sound*, 3rd ed. SF, USA: Addison Wesley, 2002.

[2] B. Mulgrew, P. Grant, and J. Thompson, *Digital Signal Processing: Concepts and Applications. London,* 1st ed. U.K.: Palgrave HE UK, 1999.

[3] B. Naqvi, K. Perova, A. Farooq, I. Makhdoom, S. Oyedeji and J. Porras, "Mitigation strategies against phishing attacks: A systematic literature review," *Comput. & Security*, vol. 132, p. 103387, 2023, doi: 10.1016/j.cose.2023.103387.

[4] W. Stallings, *Network Security Essentials: Applications and Standards*, 6th ed. Upper Saddle River, NJ, USA: Pearson, 2016.

[5] A. Saxena. "What is cybersecurity and why is it important?" Sprinto.com. https://sprinto.com/blog/importance-of-cyber-security/ (accessed Nov. 11, 2024).

[6] R. Anderson, *Security Engineering: A Guide to Building Dependable Distributed Systems.* Hoboken, NJ, USA: Wiley, 2021.

[7] M. E. Whitman and H. J. Mattord, *Management of Information Security*, 6th ed. Boston, MA, USA: Cengage Learning, 2018.

[8] V Malik, A. Khanna, N. Sharma, and S. Nalluri, (2024). Trends in Ransomware Attacks: Analysis and Future Predictions. *International Journal of Global Innovations and Solutions (IJGIS).* doi:10.21428/e90189c8.f2996624.

[9] J. Mirkovic and P. Reiher, (2004). "A taxonomy of DDoS attack and DDoS defense mechanisms," *ACM SIGCOMM Computer Communication Review,* vol. 34, no.2, pp. 39-53. doi:10.1145/997150.997156.

[10] P. Cheng and U. Roedig, "Personal voice assistant security and privacy-A survey," *IEEE J. Emerg. Sel. Top. Circuits Syst.,* vol. 10, no. 4, pp. 476–507, Apr. 2022, doi: 10.1109/JPROC.2022.3153167. https://doi.org/10.1109/JPROC.2022.3153167.

[11] D. Bilika, N. Michopoulou, E. Alepis, and C. Patsakis, "Hello me, meet the real me: Voice synthesis attacks on voice assistants," *Computers & Security,* vol. 137, p. 103617, 2024, doi: 10.1016/j.cose.2023.103617.

[12] A. G. Desetty, V. D. Jangampet, and S. R. Pulyala, "Phishing attacks: Evolving techniques, emerging trends, and countermeasure strategies," International Journal for Innovative Engineering and Management Research, vol. 9, no. 12, pp. 985–991, 2020. [Online]. Available: https://www.researchgate.net/profile/Vinay-Dutt/publication/376645699_Phishing_Attacks_Evolving_Techniques_Emerging_Trends_and_Countermeasure_Strategies/links/673eb65d440ad82b18a086fb/Phishing-Attacks-Evolving-Techniques-Emerging-Trends-and-Countermeasure-Strategies.pdf

[13] A. Ansari and M. Nazir. "Risk assessment of security vulnerabilities in smart home using CAPEC and defensive goals." *Advances in Data and Information Science*, vol 318, p. 705–722, 2022, doi:10.1007/978-981-16-5689-7_63.

[14] F. McKee and D. Noever, "Acoustic cybersecurity: Exploiting voice-activated systems," *Cryptography and Security,* vol. 2023, p. 2312.00039, 2023, doi:10.48550/arXiv.2312.00039.

[15] S. Hussain, P. Neekhara, S. Dubnov, J. McAuley and F. Koushanfar, "WaveGuard: Understanding and mitigating audio adversarial examples," in *Usenix Security 2021,* 2021, pp. 1–10, doi:10.48550/arXiv.2103.03344.

[16] D. Buil-Gil, S. Kemp, S. Kuenzel, L. Coventry, S. Zakhary, D. Tilley and J. Nicholson, "The digital harms of smart home devices: A systematic literature review," *Comput. in Hum. Behav.,* vol. 145, p. 107770, 2023, doi: 10.1016/j.chb.2023.107770.

[17] F. Toapanta, B. Rivadeneira, C. Tipantuña, and D. Guamán, "AI-Driven vishing attacks: A practical approach," *Engineering Proceedings,* vol. 77, no. 1, p. 15, 2024, doi: 10.3390/engproc2024077015.

[18] C. Dinu. "What is vishing? Unmasking voice phishing scams and techniques." TextMagic.com. https://www.textmagic.com/blog/what-is-vishing/ (accessed Nov. 11, 2024).

[19] N. Bhatnagar and M. Pry, "Student attitudes, awareness, and perceptions of personal privacy and cybersecurity in the use of social media: An initial study," *Information Systems Education Journal,* vol. 18, no. 1, pp. 48–58, 2020. [Online]. Available: https://files.eric.ed.gov/fulltext/EJ1246231.pdf

[20] C. S. Kayser, S. Back, and M. M. Toro-Alvarez, "Identity theft: The importance of prosecuting on behalf of victims," *Laws,* vol. 13, no. 6, pp. 68, 2024, doi: 10.3390/laws13060068.

[21] K. Marchini. "2018 Identity fraud: Fraud enters a new era of complexity." JavelinStrategy.com. https://www.javelinstrategy.com/research/2018-identity-fraud-fraud-enters-new-era-complexity (accessed Nov. 11, 2024).

[22] M.A. Siddiqi, W. Pak and M.A. Siddiqi, "A study on the psychology of social engineering-based cyberattacks and existing countermeasures," *Appl. Sci.,* vol. 12, p. 6042, 2022, doi: 10.3390/app12126042.

[23] G. Zhang, C. Yan, X. Ji, T. Zhang, T. Zhang and W. Xu, "DolphinAttack: Inaudible voice commands," in *ACM SIGSAC Conf. on Computer and Communications Security (CCS '17),* 2017, pp. 103–117, doi: 10.1145/3133956.3134052.

[24] H. Shah, M.Z. Rashid, M.F. Abdollah, M.N. Kamarudin, C.K. Lin and Z. Kamis, "Biometric voice recognition in security system," *Indian J. Sci. Technol.,* vol. 7, no. 1, pp. 104–112, Jan. 2014, doi: 10.17485/ijst/2014/v7i1.9.

[25] A. Hamed and N. Abdelbaki, "Acoustic attacks in iot era: Risks and mitigations," in *Proc. of the 2020 5th Int. Conf. on Cloud Computing and Internet of Things (CCIOT '20),* Okinawa, Japan, 2020, pp. 13–19, doi: 10.1145/3429523.3429530.

[26] European Parliamentary Research Service, "Data subjects, digital surveillance, AI and the future of work," in *Panel for the Future of Science and Technology,* Dec. 2020. [Online]. Available: https://www.europarl.europa.eu/RegData/etudes/STUD/2020/656305/EPRS_STU(2020)656305_EN.pdf

[27] A. Dixit, N. Kaur, and S. Kingra, "Review of audio deepfake detection techniques: Issues and prospects," *Expert Systems,* vol. 40, e13322, 2023, doi: 10.1111/exsy.13322.

[28] N. Robins-Early. "CEO of WPP Targeted by Deepfake Scam." TheGuardian.com. https://www.theguardian.com/technology/article/2024/may/10/ceo-wpp-deepfake-scam (accessed Jan. 9, 2025).

[29] M. U. Tanveer, K. Munir, M. Amjad, A. U. Rehman and A. Bermak, "Unmasking the fake: Machine learning approach for deepfake voice detection," in *IEEE Access*, vol. 12, pp. 197442-197453, Apr. 2024, doi: 10.1109/ACCESS.2024.3521026.

[30] Z. Cai, A. Dhall, S. Ghosh, M. Hayat, D. Kollias, K. Stefanov and U. Tariq, "1M-Deepfakes detection challenge," in *Proc. 32nd ACM Int. Conf. Multimedia (MM '24),* 2024, pp. 11355–11359, doi: 10.1145/3664647.3689145.

[31] J. R. Reeder and T. Hall, "Cybersecurity's Pearl Harbor moment: Lessons learned from the colonial pipeline ransomware attack," *The Cyber Defense Review,* vol. 6, no. 3, pp. 15–40, 2021. [Online]. Available: https://www.jstor.org/stable/48631153.

[32] S. S. Wang, "Integrated framework for information security investment and cyber insurance," *Pacific-Basin Finance Journal,* vol. 57, pp. 101173, 2019, doi: 10.1016/j.pacfin.2019.101173.

[33] Q. Xia, Q. Chen and S. Xu, "Near-ultrasound inaudible trojan (nuit): Exploiting your speaker to attack your microphone," in *Proc. 32nd USENIX Security Symp. (USENIX Security 23),* Anaheim, CA, 2023, pp. 4589–4606. [Online]. Available: https://www.usenix.org/conference/usenixsecurity23/presentation/xia.

[34] C. Yan, X. Ji, K. Wang, Q. Jiang, Z. Jin and W. Xu, "A survey on voice assistant security: Attacks and countermeasures," *ACM Comput. Surv.,* vol. 55, no. 4, Art. no. 84, Apr. 2023, pp. 1–36, doi: 10.1145/3527153.

[35] J. S. Lloyd, C. G. Ludwikowski, C. Malik and C. Shen, "Mitigating inaudible ultrasound attacks on voice assistants with acoustic metamaterials," *IEEE Access,* vol. 11, pp. 36464-36470, 2023, doi: 10.1109/ACCESS.2023.3266722.

[36] F. Hall, L. Maglaras, T. Aivaliotis, L. Xagoraris and I. Kantzavelou, "Smart homes: Security challenges and privacy concerns," in *Proc. 2020 arXiv Preprint,* Oct. 2020. [Online]. Available: https://arxiv.org/abs/2010.15394.

[37] Q. Yan, K. Liu, Q. Zhou, H. Guo and N. Zhang, "SurfingAttack: Interactive hidden attack on voice assistants using ultrasonic guided waves," in *Proc. Network and Distributed System Security Symposium (NDSS),* 2020. doi: 10.14722/ndss.2020.24068.

[38] C. Bolton, S. Rampazzi, C. Li, A. Kwong, W. Xu and K. Fu, "Blue note: How intentional acoustic interference damages availability and integrity in hard disk drives and operating systems," in *2018 IEEE Symposium on Security and Privacy (SP),* San Francisco, CA, USA, 2018, pp. 1048-1062, doi: 10.1109/SP.2018.00050.

[39] A. Kwong, W. Xu and K. Fu, "Hard drive of hearing: Disks that eavesdrop with a synthesized microphone," in *2019 IEEE Symposium on Security and Privacy (SP),* San Francisco, CA, USA, 2019, pp. 905-919, doi: 10.1109/SP.2019.00008.

[40] S. Panda, Y. Liu, G. P. Hancke and U. M. Qureshi, "Behavioral acoustic emanations: Attack and verification of PIN entry using keypress sounds," *Sensors,* vol. 20, no. 11, pp. 3015, Nov. 2020, doi: 10.3390/s20113015.

[41] X. Xu, Y. Liang, X. Zhang, Y. Wang, Y. Lin, B. Adebisi, H. Gacanin and G. Gui, "Self-evolving malware detection for cyber security using network traffic and incremental learning," in *Conference: 2022 9th International Conference on Dependable Systems and Their Applications (DSA),* 2022, pp. 454–463, doi: 10.1109/DSA56465.2022.00066.

[42] H. Ahmetoglu and R. Das, "A comprehensive review on detection of cyber-attacks: Data sets, methods, challenges and future research directions," *Internet of Things,* vol. 20, p. 100615, 2022, doi: 10.1016/j.iot.2022.100615.

[43] B. Akbulut, "The principle of legality in the law of misdemeanors and violation the measures taken due to Covid-19," *Journal of Penal Law and Criminology,* vol. 9, no. 1, pp. 197–253, 2021. doi: 10.26650/JPLC2020-837085.

[44] R. Erbaş, "Organized crime-related legislation in the Turkish criminal law," *Ceza Hukuku ve Kriminoloji Dergisi,* vol. 3, no. 1, pp. 275–311, Jun. 2015. [Online]. Available: https://dergipark.org.tr/tr/download/article-file/14682.

[45] Council of Europe. "Convention on Cybercrime." rm.coe.int. https://rm.coe.int/prems-105223-gbr-2023-convention-cybercrimininalite-a5-web-4-/1680ae7118 (accessed October 10, 2024).

[46] IWM Cybersec. "Information Security Audit." IWMCybersec.com. https://iwmcybersec.com/information-security-audit/ (accessed October 10, 2024).

[47] Z. Wang, L. Sun and H. Zhu, "Defining social engineering in cybersecurity," *IEEE Access,* vol. 8, pp. 85094–85115, Aug. 2020, doi: 10.1109/ACCESS.2020.2992807.